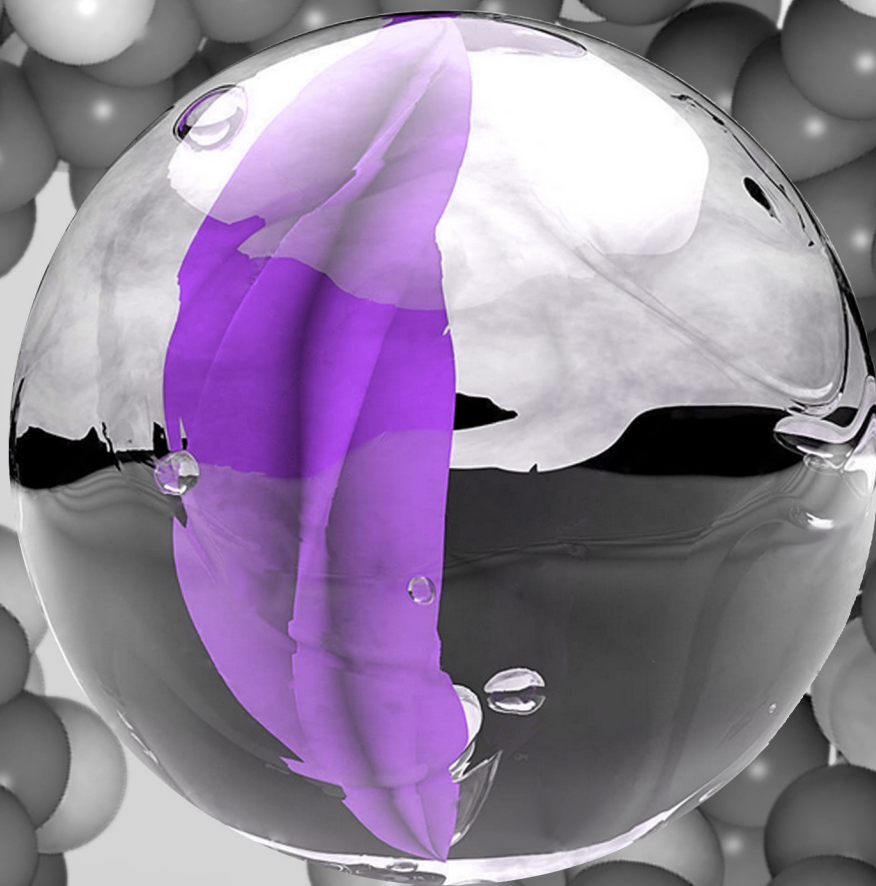# Porous Materials for Environmental Applications

Ana Martín Calvo

Faculty of Experimental Sciences,
University Pablo de Olavide

Faculty of Bioscience Engineering,
KU Leuven

POROUS MATERIALS FOR ENVIRONMENTAL APPLICATIONS

Ana Martín Calvo

Seville, March 2015

POROUS MATERIALS FOR ENVIRONMENTAL APPLICATIONS

SUPERVISORS

Sofía Calero Díaz

Profesora Titular de Universidad

Dpto. de Sistemas Físicos Químicos y Naturales

Universidad Pablo de Olavide

Johan A. Martens

Full Professor

Faculty of Bioscience Engineering

KU Leuven

Titus S. van Erp

Associated Professor

Dept. of Chemistry

Norwegian University of Science and Technology

Elena García Pérez

Investigadora Junior

Dpto. de Investigación

Abengoa Research

Work presented to obtain the degree of Doctor with International Mention

Ana Martín Calvo

Licenciada en Ciencias Ambientales

Departamento de Sistemas Físicos Químicos y Naturales

Universidad Pablo de Olavide

Sofía Calero Díaz, Profesora Titular de Universidad del Departamento de Sistemas Físicos, Químicos y Naturales de la Universidad Pablo de Olavide

CERTIFICA:

Que la presente memoria titulada "Porous Materials for Environmental Applications", que presenta Ana Martín Calvo para la obtención del título de Doctora, ha sido realizado bajo mi dirección en este departamento dentro del programa de Medio Ambiente y Sociedad y que cumple con los requisitos para poder optar a la Mención Internacional.

Sevilla, Enero de 2015

Sofía Calero Díaz

KU LEUVEN

FACULTY OF BIOSCIENCE ENGINEERING
DEPARTMENT OF MICROBIAL ANO MOLECULAR SYSTEMS
CENTER FOR SURFACE CHEMISTRY ANO CATALYSIS
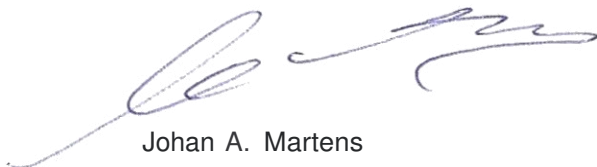KASTEELPARK ARENBERG 23 BOX 2461
3001 HEVERLEE, BELGIUM

Subject: Certification of thesis by Ana Martín Calvo

Heverlee, January 28th, 2015

To whom it may concern:

I would like to certify that I have been involved as co-supervisor in the PhD RESEARCH of Ana Martín Calvo.

After reading her thesis on porous materials for molecular separation and environmental applications, I can confirm the work is of excellent quality. It has already led to many publications in excellent scientific journals. I believe that there is no doubt that this thesis meets al requirements for Ana Martín Calvo to be honored with the title of doctor with international mention.

Johan A. Martens

Professor

Norwegian University of Science and Technology
Faculty of Natural Sciences and Technology
Department of Chemistry

Subject: Certification of thesis by Ana Martin Calvo

To whom it may concern:

With this letter I would like to certify that I have been involved as co-supervisor in the PhD project of Ana Martin Calvo. To my great satisfaction, after reading her thesis on porous materials for environmental applications, I can fully support this excellent work, which has already led to many high-standard publications. Therefore, I believe that there is no doubt that this thesis meets al requirements for Ana to honoured with the title of doctor with international mention.

Sincerely yours

Titus van Erp

Titus van Erp, Associated Proffessor
Applied Theoretical Chemistry
Department of Chemistry
Faculty of Natural Sciences and Technology
Norwegian University of Science and Technology (NTNU)
Høgskoleringen 5, Realfagbygget D3-117, 7491, Trondheim, Norway
+47 735 94142
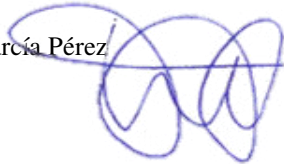
26 de Enero de 2015

Elena García Pérez, Dra. en Ciencias Ambientales por la Universidad Pablo de Olavide,

CERTIFICA:

Que la presente memoria titulada "Porous Materiales for Environrnental Applications", que presenta Ana Martín Calvo para la obtención del título de Doctora, ha sido realizada bajo mi co-dirección en el departamento de Sistemas Físicos, Químicos y Naturales, dentro del programa de Medio Ambiente y Sociedad y que cumple los requisitos para poder optar a la Mención Europea así como al doble título con la Universidad de Lovaina (KU Leuven).

Fdo.

Elena García Pérez

Doctoral Supervisors

      Prof. Sofía Calero Díaz

      Prof. Johan A. Martens

      Dr. Titus S. van Erp

      Dr. Elena García Pérez

Examination Committee

      Chair: Prof. José B. Parra Soto

      Secretary: Dr. Paula Gómez Álvarez

      Member: Prof. Tina Düren

      Member: Prof. Guillaume Maurin

      Member: Dr. Randy Mellaerts

External Committee

      Prof. Thijs J. H. Vlugt

      Dr. Juan M. Castillo

Contents

Appendixes

List of publications

Acknowledgements/Agradecimientos

1

Introduction

The use of porous materials as "molecular sieves" has been widely explored. Their pore size, shape and distribution make them very useful structures for adsorption and separation processes. Their porosity, strong interactions with the adsorbates, high surface area, ordered structure and stability are the main reasons that make these materials suitable for potential industrial applications such as purification of gases and liquids, removal of pollutants or storage and release of gases. Zeolites, clays, activated carbons or metal-organic frameworks (MOFs) are a few examples of materials with such applications. The origin of porous adsorbents can be natural or synthetic and the possibility of synthesising them opens a whole world of opportunities as tailored structures can be developed for specific purposes.

The number of structures reported increases every day[1,2]. The availability of a large amount of structures poses a challenge to experimentally screen all of them to identify the most adequate material for different processes. To characterise existing and new potential structures, simulation techniques become very useful tools[3]. With simulations it is possible to predict the behaviour of certain materials for specific processes. This knowledge provides hints on the desired characteristics of a given material for a better performance in the process under study. Furthermore, experimentalists can use these guide lines to synthesise structures that *a priori* will provide the best results.

In this work molecular simulation techniques are used to study the ability of porous materials to perform adsorption, diffusion and separations applied to processes of environmental relevance. Different materials under a variety of conditions are considered in order to study their behaviour for mixtures of greenhouse gases, pollutants and enantiomeric compounds.

1. Materials

Among the variety of materials used as molecular sieves, this thesis is focused on two of them: zeolites and metal-organic frameworks.

1.1. Zeolites

Zeolites are microporous materials with crystalline three-dimensional structure. They are based on TO_4 tetrahedra covalently bonded in which the central atom (T) can be either silicon or aluminium. These tetrahedra are the Primary Building Units (PBUs) that connect via corner-shared oxygen atoms, generating pore networks with different topologies (Figure 1). Depending on the topology, structures with channels and/or cavities can be found. Channels can appear under different distributions such as longitudinal, zig-zag, or interconnected. On the other hand, cavities can be connected by channels or windows. AlO_4 tetrahedra cannot be connected between them as the Löwenstein rule establish that oxygen atoms cannot be bonded to two aluminium atoms[4]. The difference of valence of silicon and aluminium generates a negative net charge in aluminosilicate zeolites that have to be compensated by the addition of extra-framework cations to the system.
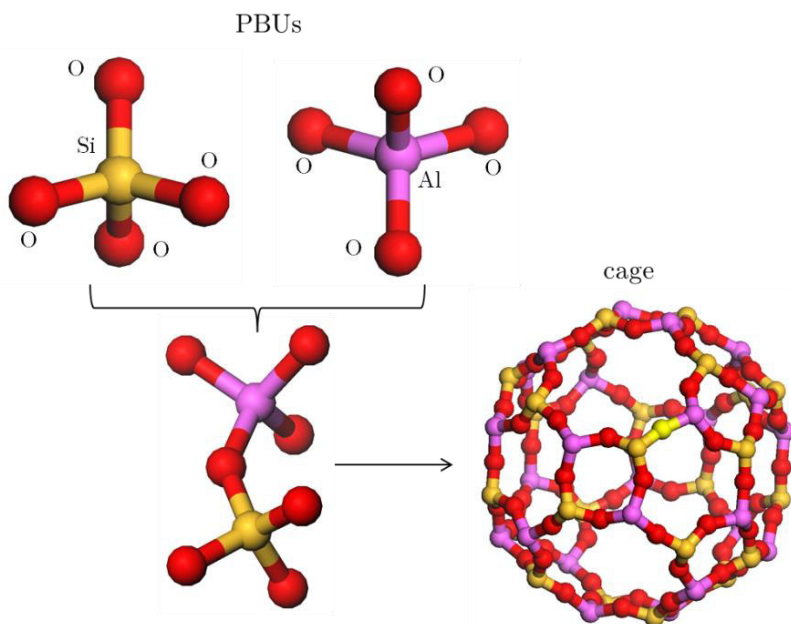
Figure 1. Representation of the coordination of silicon or aluminium tetrahedra via oxygen atoms to generate 3D zeolitic structures.

Other atoms than aluminium, such as B, Be, Zn, Ge, or S, can also substitute silicon atoms at the centre of the tetrahedra from the structure[5,6]. This type of atoms has been proved to favour the energetic stability of chiral zeolites. This characteristic is very important as only few zeolites are identified as chiral[7-10] and many studies have focussed on the creation of chiral zeolites resulting mostly as thermally unstable structures[6,11-13].

Zeolites can be found either in nature or synthesised in the laboratory. Over 200 different topologies have been already reported[1]. Nevertheless they have some common characteristics such as high surface area, thermal and chemical stability and durability. Pure silica zeolites are hydrophobic, while these with cations are hydrophilic, showing the latter high ion exchange capacity. All these characteristics give to zeolites a striking edge in industrial applications as selective adsorbents, ion exchangers, catalysts and more recently fuel cell[14-23].

1.2. Metal-Organic Frameworks

Metal-organic frameworks (MOFs) are synthetic nanoporous materials composed of metal centres or clusters, linked by organic ligands (Figure 2)[24-28]. These ligands behave as spacers resulting in structures with high pore volume and surface area, well defined cavities, high storage capacity and selectivity[29-40]. Since the discovery of MOFs by Yaghi *et al.* in the late nineties[40] thousands of new structures have been reported[2,24].
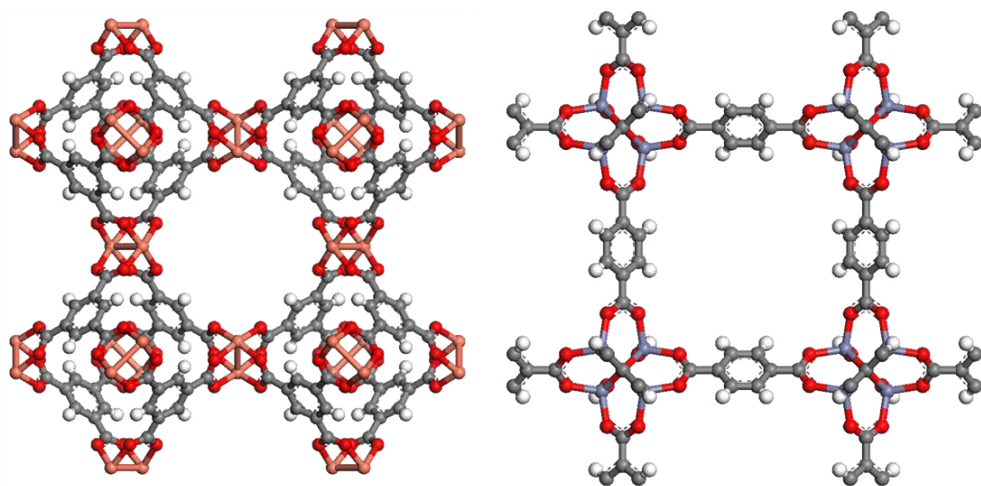
Figure 2. Atomic representation of two well-known metal-organic frameworks: Cu-BTC (left) and IRMOF-1 (right). Carbon, oxygen, and hydrogen atoms are depicted in grey, red and white, respectively, while copper and zinc metals are depicted in orange and blue.

Unlike zeolites, MOFs contain both organic and inorganic components which allow greater structural flexibility along with wide opportunities to customize specific properties[41]. The variety of structural features resulting from the combination of organic ligands and metallic centres give to these materials important industrial applications. Initially they were seen as potential storage materials for hydrogen and greenhouse gases[39,42-48]. Later on they were also used on adsorption, separation and purification processes[49-56], as well as catalysts[57-67], sensors[68,69], in fuel cells[70], as explosives[71] or for potential pharmaceutical and biomedical applications such as drug delivery, or cosmetic[72,73-76].

MOFs are generally thermally unstable upon removal of solvent molecules from the pores. The stability of these structures in water is also an open subject as in many cases water molecules attack the metallic centres breaking their crystalline structure[77-80]. It is for these reasons that among the huge amount of structures available in the Cambridge Crystallographic Data Center (CCDC)[2], only a small percentage remain capable for further exploration.

Structural flexibility is also an interesting feature of this type of materials[41]. The most common flexible behaviours studied are: a) *breathing*, change of the unit cell distances, angles, crystallographic space groups and volume as a result of the transition of MOFs during the displacement of the atoms of the framework[81-84]; b) *swelling*, enlargement of the unit cell volume without changes in the cell shape or in the space group[85,86]; c) *thermal expansion*, shrinking in absence of guest molecules[40,87]; d) *linker rotation*, linkers turn around a rotational axis, changing their spatial alignment, causing an expansion of the pore windows[88-90] and e) *subnetwork displacement*, drift, relocation or shift of the subnets in systems with individual networks that only interacts by weak forces, that includes interpenetrated 3D frameworks and interdigitated and stacked 2D frameworks[91-93].

The particular properties of MOFs and the capacity of tailoring these structures with specific goals in mind leaves the possibility of designing new materials still open[41].

2. Simulation methods

Molecular simulation is an essential tool in many fields and a perfect complement for experimental techniques. Molecular simulation consists on a set of techniques based on computational calculations to predict properties of physical, chemical and biological systems. Depending on the property under study the method used varies:

- <u>Monte Carlo</u> (MC): Statistical method to compute macroscopic properties of a system from the average of its microscopic states.
- <u>Molecular Dynamics</u> (MD): Deterministic method used to study the evolution of a system in time integrating the Newton's laws of motion.

In order to predict properties valid for extended crystal lattices, large systems are simulated. To avoid problems of systems with huge number of particles or surface effects, periodic boundary conditions are applied. For this purpose, the unit cell simulation box with all the atoms is infinitely replicated in the three directions of space[94].

2.1. Monte Carlo

To compute adsorption properties Monte Carlo (MC) method is used. This is a numerical statistic method which uses mathematical expressions to approximate complex and costly processes and to evaluate them accurately. It is based on the use of random numbers and probabilities to calculate macroscopic properties of a system. The tool used is the Markov Chain Monte Carlo (MCMC) method, providing average properties of systems with a large number of accessible states. System configurations are generated with a probability proportional to their statistical weight. The probability of a given microstate is proportional to the Boltzmann factor. Instead of the absolute probability of visiting states of a system, with the correct frequency, the MC method assumes that just the relative probability is needed[94].

The MCMC algorithm generates random trial moves from the current state (o) to a new state (n) which can be accepted or rejected. The probability of finding a system in the current or the new state is denoted as $P_B(o)$ and $P_B(n)$ respectively and the conditional probability to perform a trial move between states is denote as $\alpha(o \rightarrow n)$ and $\alpha(n \rightarrow o)$. Applying the condition of detailed balance, the probability of leaving a state by accepting a trial move $P_{acc}(o \rightarrow n)$, is the same as that of entering a new state $P_{acc}(n \rightarrow o)$.

$$P_B(o)\alpha(o \rightarrow n)P_{acc}(o \rightarrow n) = P_B(n)\alpha(n \rightarrow o)P_{acc}(n \rightarrow o) \qquad 1.1$$

Finally, according to the Metropolis algorithm[95], α is assumed as a symmetric matrix, $\alpha(o \rightarrow n) = \alpha(n \rightarrow o)$, so a possible acceptance probability is.

$$P_{acc}(o \rightarrow n) = \min\left(1, \frac{P_B(n)}{P_B(o)}\right) \qquad 1.2$$

Conventional Monte Carlo method requires high computational time when the molecules are bulky and large. To avoid this, the overlaps with the framework and to increase the number of successfully inserted molecules, Configurational Bias Monte Carlo method (CBMC) is used. With this method the molecule is grown inside the simulation box bead by bead as shown in Figure 3. For each bead k trial orientations are generated according to the internal energy (U^{int}), then based on the external energy (U^{ext}) the most favourable orientation is selected according to the expression.

$$P_i(j) = \frac{e^{-\beta U_i^{ext}(j)}}{\sum_{l=1}^{k} e^{-\beta U_i^{ext}(l)}} = \frac{e^{-\beta U_i^{ext}(j)}}{\omega_i}, \qquad\qquad 1.3$$

where $\beta = 1/(k_B T)$, k_B is the Boltzmann constant, T is the temperature and ω_i is the Rosenbluth weight.
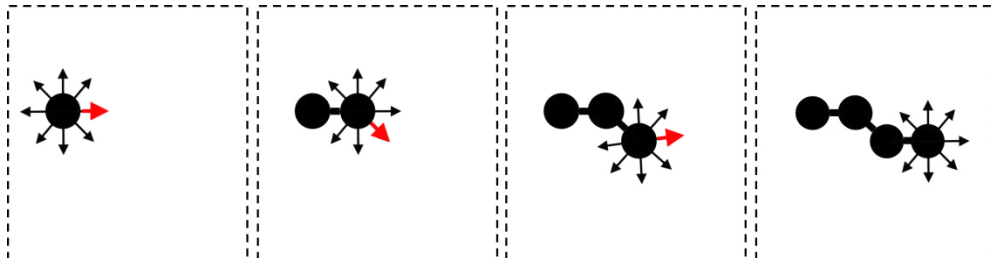
Figure 3. Schematic representation of the Configurational Bias Monte Carlo method.

Once the selected trial orientation is added to the chain and the procedure is repeated until the entire molecule is grown, it is necessary to calculate the Rosenbluth factor of the new configuration.

$$W = \prod_i \omega_i, \qquad\qquad 1.4$$

where ω_i is the Rosenbluth weight.

During Monte Carlo simulations several moves can be applied to a randomly selected molecule:

- Rotation: The selected molecule is randomly rotated around its centre of mass.
- Translation: A random displacement is given to the selected molecule.
- Regrow: The selected molecule is partially or completely regrown at a random position.
- Insertion: A molecule is grown at a random position.
- Deletion: The chosen molecule is removed from the simulation box.
- Identity change: This move is only applied for mixtures. A component is selected at random and changes its identity to another.
- ξ-replica exchange (Parallel Molar Fraction): A move used for simulations with more than one system at once. Two neighbouring systems with different molar fractions of their components are swapped (similar to parallel tempering).
- Chiral Inversion: Specific move for systems with chiral molecules. It changes all *S*-molecules in *R*-molecules and *vice versa*.

By varying the ensemble, different Monte Carlo simulations can be performed, depending on the property under study.

Vapour-liquid coexistence curve

To model the interactions between the adsorbates, van der Waals interaction parameters are obtained by fitting to the experimental vapour-liquid equilibrium curve. For the simulation of phase equilibria in fluids Monte Carlo simulations in the Gibbs ensemble are performed[94]. These simulations take place in two microscopic regions within the bulk phases away from the interface. Each region is simulated within standard periodic boundary conditions with images of itself. The thermodynamic requirements for phase coexistence are that each region should be in internal equilibrium and that the temperature, the pressure and the chemical potential of the components should be the same in the two regions. The values of temperature, total number of molecules and total volume are specified in advance and remain constant during the simulation.

The remaining three conditions are respectively satisfied by performing three Monte Carlo moves:

a) Displacement of the particles within each region, to satisfy internal equilibrium.
b) Fluctuations in the volume of the two regions, to satisfy equality of pressure.
c) Transfer of particles between regions, to satisfy equality of chemical potential.

Gibbs simulations are not so accurate when trying to obtain values near the critical point of the molecule. For this reason to obtain the critical parameters of the models of the molecules the density scaling law (T_c), the law of rectilinear diameters (ρ_c) and the Clausius-Clapeyron equation (p_c) are employed[96-99].

$$\rho_{liq} - \rho_{vap} = B \, (T - T_c)^\beta \qquad\qquad 1.5$$

$$\frac{(\rho_{liq} + \rho_{vap})}{2} = \rho_c + A \, (T - T_c) \qquad\qquad 1.6$$

$$\ln p = C + \frac{C'}{T}, \qquad\qquad 1.7$$

where ρ_{liq} and ρ_{vap} are the saturated liquid and vapour densities, A, B, C and C' are constants and $\beta = 1/3$ is the critical exponent.

Henry coefficients and heats of adsorption

Henry coefficients (K_H) and heats of adsorption (Q_{st}) provide information about the strength of the interaction of a molecule with a structure under diluted conditions. These properties are dependent on the temperature under study and can only be obtained in the low coverage regime. These values are obtained from Monte Carlo simulations in the canonical ensemble where the number of particles (N), the volume (V) and the temperature (T) are kept fixed. Due to the need of working at zero loading, the Widom test particle method can be applied[100-102]. This method consists on the insertion of a molecule in the system, computing its energy and its Rosenbluth factor before deleting it. The system is therefore left unaffected with this procedure.

Henry coefficients (K_H) are directly related to the excess free energy (or excess chemical potential) of the adsorbed molecule. Henry coefficients and Rosenbluth factors are related by:

$$K_H = \frac{1}{RT\rho}\frac{\langle W \rangle}{\langle W^{IG} \rangle}, \qquad\qquad 1.8$$

where R is the constant of gases, T is the temperature, ρ is the density of the host framework, $\langle W \rangle$ is the average Rosenbluth factor of a single molecule and $\langle W^{IG} \rangle$ is the average Rosenbluth factor of the molecule in the ideal gas[94].

Heat of adsorption (Q_{st}) is obtained from the average energies of the system.

$$Q_{st} = RT - \Delta U = RT - \left(\langle U_{hg} \rangle - \langle U_h \rangle - \langle U_g \rangle \right), \qquad\qquad 1.9$$

where R is the gas constant, T is the temperature of the system, $\langle U_{hg} \rangle$ is the average potential energy of the host-guest system, $\langle U_h \rangle$ is the average potential energy of the host and $\langle U_g \rangle$ is the potential energy of a single molecule. Two separated simulations are needed: (1) to calculate the energy of the molecule in the ideal gas phase and (2) to obtain the energy of the molecule inside the structure.

Adsorption isotherms

Adsorption isotherms are computed using Monte Carlo simulations in the grand canonical ensemble (GCMC). In this ensemble the chemical potential (μ), the volume (V) and the temperature (T) remain fixed, obtaining thereby the number of molecules adsorbed in the structure during the simulation (N). The molecules inside the system are susceptible to be exchanged with these from a reservoir with the same chemical potential[103]. The required equilibrium conditions of the gas in- and outside the system are equal temperature and chemical potential in both sides. The chemical potential of a gas (μ) is directly related to its fugacity (f) by:

$$\mu = \mu^0 + RT \ln\left(\frac{f}{f^0}\right), \qquad\qquad 1.10$$

where μ^0 and f^0 are the standard chemical potential and fugacity respectively, R is the ideal gas constant and T the temperature of the system. Fugacity (f) relates to pressure (p) through the fugacity coefficient (Φ) as $f = \Phi p$. For ideal gases or real ones below one bar of pressure, it is possible to assume fugacity as pressure ($\Phi = 1$). When this assumption is not affordable the fugacity coefficient has to be considered[94].

The output of this type of simulation is the total amount of molecules located inside the pores of the structure (absolute adsorption). Experimentally it is the excess adsorption the one that is measured, that means excluding the molecules that are in the pores without gas-solid interaction. For this reason, to compare simulated and experimental data it is necessary to convert absolute (n_{abs}) into excess (n_{exc}) adsorption using the following expression[104-107]:

$$n_{exc} = n_{abs} - V^g \rho^g, \qquad\qquad 1.11$$

where V^g is the pore volume of the adsorbent and ρ^g is the molar density of the bulk gas phase. The value of pore volume can be obtained experimentally or by simulation measuring helium adsorption[104].

2.2. Molecular Dynamics

Molecular Dynamics (MD) are performed to compute the diffusivity of the molecules in the structures from the mean square displacement (MSD). MD simulations are characterised by the generation of successive configurations of the systems which varies with time. Integrating Newton' laws of motion it is possible to predict the trajectories that describe the positions, velocities and acceleration. The most used method to integrate the equations of motion is the velocity Verlet algorithm[108,109].

$$r(t + \Delta t) = r(t) + v(t)\Delta t + \frac{f(t)}{2m}\Delta t^2 \qquad\qquad 1.12$$

$$v(t + \Delta t) = v(t) + \frac{f(t) + f(t + \Delta t)}{2m}\Delta t, \qquad\qquad 1.13$$

where $r(t)$, $v(t)$, $f(t)$ are the position, velocity and force vectors at time t, respectively, Δt is the time step used and m is the mass of the particle.

To compute the new forces, it is necessary to get new velocities, which can only be calculated after computing new positions. The actual measurements are performed on a previously equilibrated system by determining the average values properties from the trajectories of the particles.

Self-diffusion coefficients (D_s) measure the diffusive motion of a single particle. With the slope of the mean square displacement at long time it is possible to obtain the D_s in one direction $\alpha = x, y, z$ (D_s^α).

$$D_s^\alpha = \frac{1}{2N} \lim_{t \to \infty} \frac{d}{dt} \langle \sum_{i=1}^{N} \left(r_{i\alpha}(t) - r_{i\alpha}(t_0) \right)^2 \rangle, \qquad\qquad 1.14$$

where N is the number of molecules, t is the time and $r_{i\alpha}$ is the α-component of the center of mass of the molecule i.

The directionally averaged diffusion coefficient is given by:

$$D_s = \frac{D_s^x + D_s^y + D_s^z}{3}, \qquad\qquad 1.15$$

where D_s^x, D_s^y, D_s^z are the diffusion coefficients in the x, y and z.

MD simulations are performed in the canonical ensemble fixing the number of particles (N), the volume (V) and the temperature (T). To keep the temperature of the system constant during the equilibration and the production part of the simulation, the Nosé-Hoover thermostat is employed[94,110,111].

3. Force fields and models

Molecular simulations require models to define molecules and structures and force fields to reproduce the interactions that take place inside the systems. This work studies the behaviour of gases in confinement by classical calculations. Thus, the systems are defined by classical force fields. For this reason, models for the adsorbates, the adsorbents and their interactions are needed.

3.1. Force fields

To reproduce the interactions inside the system, the total energy (U^{total}) is obtained from bonded (U^{bonded}) and non-bonded atoms $(U^{non-bonded})$

$$U^{total} = U^{bonded} + U^{non-bonded} \qquad\qquad 1.16$$

The energy of the bonded interactions (U^{bonded}) is obtained from the binding and torsion energies of atoms directly connected to each other (Figure 4). It involves the energies between pairs of bonded atoms (U^{bond}), three linked atoms (U^{bend}) and the torsion of four consecutive atoms $(U^{torsion})$.

$$U^{bonded} = U^{bond} + U^{bend} + U^{torsion} \qquad\qquad 1.17$$
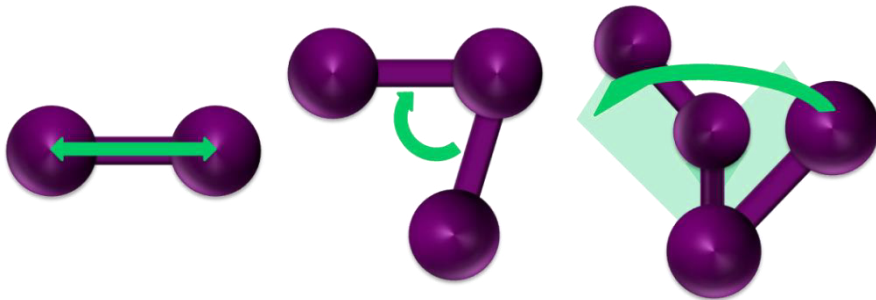
Figure 4. Schematic representation of the interatomic relations that contribute to the internal energy of the molecule (bond distance, bend angle and dihedral angle).

There are many functional forms to define the bonding energy between two connected atoms (U^{bond}). The function of interatomic distances used in this work is the harmonic potential.

$$U^{bond}(r_{ij}) = \frac{1}{2}k(r_{ij} - r_{eq})^2, \qquad\qquad 1.18$$

where k is the force constant, r_{ij} is the distance between the two atoms ($r_{ij} = r_j - r_i$) and r_{eq} is the equilibrium bond length.

The bend energy (U^{bend}) is related to the angle between three neighbouring atoms (θ_{jik}). Among the different functional potentials available to define this interaction, the harmonic potential is selected for this work.

$$U^{bend}(\theta_{jik}) = \frac{1}{2}k(\theta_{jik} - \theta_{eq})^2, \qquad\qquad 1.19$$

where k is the bend constant, θ_{jik} is the angle between three atoms and θ_{eq} is the equilibrium angle.

The last term to be considered in the bonded interactions is the torsion ($U^{torsion}$) which is related to the dihedral angle of four consecutive atoms (φ_{ijkl}). In this work both, proper and improper torsions are mainly defined by the TraPPE dihedral potential.

$$U^{torsion} = p_0 + p_1[1 + \cos(\varphi_{ijkl})] + p_2[1 - \cos(2\varphi_{ijkl})] + p_3[1 + \cos(3\varphi_{ijkl})], \qquad 1.20$$

where p_o, p_1, p_2, p_3 are fitted parameters and φ_{ijkl} is the dihedral angle.

The interactions between a) atoms of different molecules, b) atoms of the molecules with these from the structures, c) atoms of the structure (in rigid structures this value is zero) and d) atoms of the same molecule but separated by more than four atoms, are included in the non-bonded interactions ($U^{non-bonded}$). They are defined as a combination of van der Waals (U^{vDW}) and electrostatic interactions ($U^{electrostatic}$).

$$U^{non-bonded} = U^{vDW} + U^{electrostatic} \qquad \qquad 1.21$$

Van der Waals interactions are defined by pairs of Lennard-Jones potentials describing short-range interactions.

$$U^{vDW}(r_{ij}) = 4\varepsilon_{ij}\left[\left(\frac{\sigma_{ij}}{r_{ij}}\right)^{12} - \left(\frac{\sigma_{ij}}{r_{ij}}\right)^{6}\right], \qquad \qquad 1.22$$

where r_{ij} is the distance between two interacting particles, ε is the energy parameter and σ is the size parameter of the potential.

In general the values of ε and σ are defined for the interactions of identical atoms (ϵ_{ii} and σ_{ii}). Lennard-Jones interactions between different atoms are often computed using the Lorentz-Berthelot mixing rules[112].

$$\epsilon_{ij} = \sqrt{\epsilon_{ii} \cdot \epsilon_{jj}} \qquad \qquad 1.23$$

$$\sigma_{ij} = \frac{\sigma_{ii} + \sigma_{jj}}{2} \qquad \qquad 1.24$$

The long range interactions are considered within the electrostatic interactions ($U^{electrostatic}$) described according to Coulomb's law.

$$U^{electrostatic}(r_{ij}) = \frac{q_i q_j}{4\pi\varepsilon_0 \varepsilon_r r_{ij}}, \qquad \qquad 1.25$$

where q_i and q_j are the atomic charges, ε_0 is the electric constant of vacuum, ε_r is the relative dielectric constant of the medium and r_{ij} is the distance between the atoms.

To avoid extremely time consuming calculations and convergence problems, the cut-off distance chosen for the potentials is 12 Å. The Lennard-Jones potentials are cut and shifted at the cut-off distance. These interactions longer than the cut-off are omitted from the energy and force computations. The Ewald summation method is used to calculate the electrostatic energy in the periodic system[113].

3.2. Models for adsorbents

Pure silica zeolites are composed of oxygen and silicon atoms. In some zeolites silicon atoms can be substituted by aluminium forming aluminosilicates with different Si/Al ratio. In these cases, as a result of the different charge of both type of atoms (Si and Al) a negative net charge is generated in the system. This net charge has to be compensated by the addition of extra-framework cations. The structure of the frameworks is considered as rigid and therefore kept fixed during the simulation. Previous studies demonstrate that flexibility of the framework has a minor effect on the adsorption of small gases[114,115]. The atomic positions are taken from the crystallographic position of the atoms of the dehydrated structures. Regarding their interaction parameters, all the atoms involved have their own partial charge however the Lennard-Jones distribution differs. As the silicon or aluminium atoms are surrounded by four oxygen atoms, it is possible to assume that the dispersive interaction of the atoms of the structure with the adsorbates is described by that of the oxygen atoms. Specific adsorbate-adsorbent interactions are usually defined for zeolites for an accurate fitting to experimental data, but when this interactions are not established, generic mixing rules can be applied. In this case all the atoms in the structure must have their own effective potential. In the literature many force fields can be found for zeolites[116-119], but due to the need of specific interactions between zeolites and gases, only a few of them are able to reproduce experimental results and even less are transferable to other zeolites[114,120-122].

MOFs are porous materials composed of metal ions or clusters linked to organic ligands. Despite the fact that some MOF structures exhibit framework flexibility, the ones used in this work are considered non-flexible structures, as it has been proved that for these structures flexibility is not relevant in some adsorption processes and it reduces the computational time[123]. Similarly to zeolites, their structures are considered rigid as well and the atomic positions are obtained from experimental data. Both Lennard-Jones and partial charges are assigned to each framework atom. Due to the lack of specific force fields for this type of structures, the use of mixing rules to describe the interactions with the adsorbates is quite extended. We use Lorentz-Berthelot mixing rules. Contrary to zeolites, there are several generic force fields available to define the interactions in MOFs such as UFF, DREIDING or CVFF[124-127].

3.3. Models for extra-framework cations

The charge imbalance generated by the presence of aluminium in the framework is compensated by the addition of extra-framework cations. The nature, number and distribution of these extra-framework cations affect the ion exchange properties of zeolites, as well as the basicity and the electric field in their cavities. The initial distribution of the extra-framework cations in the structure has an important role

into the adsorption process[115]. Therefore it is necessary to identify the crystallographic position of these atoms. In some structures such as LTA zeolites, the location of the extra-framework cations is well known[128,129]. However their distribution is not so clear for FAU zeolites, as it highly depends on humidity or the nature of the adsorbate[130-132]. Another factor to consider is the mobility of the cations. It was not until the late nineties that mobility of extra-framework cations was taken into account in molecular simulations[133,134]. Previous publications completely ignored cation mobility[135], but later studies demonstrated that this mobility, together with the cation density, are essential factors during the adsorption process in certain zeolites[115].

3.4. Models for adsorbates

The adsorbates or guest molecules are defined using classical models. There are two main characteristics related to these models:

a) <u>Rigid or flexible</u>: It is possible to define the specific position of the atoms in such a way that the model has no internal energy (rigid). A more detailed definition is also possible by specifying the bond lengths, angles and torsions of the interactions as well as their functional forms (flexible). Depending on the molecule under study one type of definition or another is used. One should balance the efficiency of the selected model based on the requirements of the studied property.

b) <u>Full atom or united atom:</u> The most detailed way of defining a molecule is by considering interaction parameters for all the atoms involved (full atom). For some molecules it is possible to use united atom (UA) models, in which a group of atoms, also named as pseudo-atom, is treated as a single interaction centre. Interactions are easier to compute with UA models and in most cases lead to the same results as the full atom models.

In this thesis a variety of molecules with environmental relevance has been studied. A detailed description of all the adsorbates considered can be found below.

Hydrocarbons (CH_4, C_2H_6 and C_3H_8): These molecules are described using united atom models. Each CH_x group is considered as one pseudo-atom and therefore is treated as a single interaction centre with its own effective potential. No partial charges are considered for these alkanes. Molecules with more than one pseudo-atom are defined as flexible models using TraPPE parameters[97,136]. The Lennard-Jones parameters are taken from a previous work of Dubbeldam *et al.* where the interactions have been optimized to reproduce the vapour-liquid coexistence curve[120].

Air components (O$_2$, N$_2$ and Ar): Oxygen and nitrogen are described using rigid full atom models. The models of oxygen and nitrogen are based on these proposed by Stogryn and Murthy respectively[137,138]. They are modelled as two interaction centres with Lennard-Jones and partial charges. To reproduce the quadrupole moment of the molecules a third point charge is located at their centre of mass. The molecule of argon is defined as a non-polar molecule. Detailed information about Lennard-Jones parameters and partial charges of the molecules are discussed in chapters 2 and 4.

Greenhouse gases and pollutants (CO$_2$, CO, and CCl$_4$): Carbon dioxide is one of the most studied molecules in zeolites and MOFs, therefore a variety of models have been reported for this molecule[122,139]. Different models are also found for carbon monoxide where the charge distribution of the molecule varies from two to four sites.[140-142] In this work carbon dioxide and carbon monoxide are both defined as full atom models. All the atoms of these two linear molecules have their own effective potential and partial charge. For carbon monoxide a third point charge is used to reproduce the experimental dipole moment of the molecule. The model of carbon dioxide is based on this developed by Harris and Yung[139]. In contrast carbon tetrachloride (CCl$_4$) is defined as a single interaction centre. Lennard-Jones parameters and partial charges for carbon dioxide are discussed in chapters 2 and 6, these of carbon monoxide can be found in chapter 5 and the parameters for carbon tetrachloride are fitted in chapter 4.

Water: This is the most controversial molecule among all the adsorbates under study, due to the huge amount of available models[143-151]. Models with three, four and five sites have been reported, each of them designed to mimic a specific property or behaviour, however none of them is able to reproduce them all simultaneously. The Tip5pEw model is the one used in this work since it is the model that reproduces better the properties of water in the bulk at the conditions studied and has been parameterized to use Ewald summations[152].

Enantiomers (CHClFBr and LA): Chlorofluorobromomethane (CHClFBr) is selected as it can be considered one of the smallest chiral molecules and therefore the simplest for a first approach study in confined systems. It has been defined as a rigid model, using the OPLS force field[153]. The lactic acid molecule (LA), a carboxylic acid with a hydroxyl group, has been defined as a flexible full atom model. Harmonic potentials for bond and bend and TraPPE potentials for proper and improper torsions are used. The energy constant of the interactions are based on CVFF force fields[126,127].

4. Outline and scope of the thesis

In this thesis we use molecular simulations to study adsorption and diffusion properties of gases in nanoporous materials. We focus on gases with environmental relevance and study them in processes that can be used to reduce the emission of certain pollutants. We use zeolites and MOFs as adsorbents. These materials are well known and have many industrial applications making them good candidates for the processes under study. In our simulations we make use not only of available force fields in the literature but we also develop new ones. We study the mechanisms that rule the adsorption and diffusion behaviours as well as the distribution of molecules inside the structures. All the studies have been performed using the methods and models described in section 3.

Influence of the topology in adsorption and separation processes of greenhouse gases and pollutants (Chapters 2 and 3)

In chapter 2 we use previously published force fields and models to study the adsorptive separation of a natural gas mixture in MOFs. For that purpose we study the adsorption behaviour of the main components of natural gas (CH_4, C_2H_6, C_3H_8, CO_2, N_2) in two well-known metal-organic frameworks (Cu-BTC and IRMOF-1). Based on the different topologies and the distribution of the molecules inside these two structures, each of them will be suitable for a different purpose.

Once the efficiency of Cu-BTC in separation processes is proved, in chapter 3 we study the performance of this material on the separation of CCl_4 from air. To this aim, we study adsorption and diffusion properties of these molecules inside the structure. In addition, we propose a selective blockage of the structure to enhance its selectivity in the separation process.

Effect of humidity into adsorption and separation processes (Chapters 4 and 5)

To progress further with the study of removal of CCl_4 from air, in chapter 4 we discuss the effect of relative air humidity on the separation process. To this aim, we first discuss the models of the molecules under study. Then we analyse the influence of different percentages of relative air humidity in the removal of CCl_4 using Cu-BTC from the adsorption and diffusion behaviours of the gas mixture.

In chapter 5 we investigate the effect of water on the adsorption of CO in metal-organic frameworks. After discussion of the available models of CO and their adsorption behaviour in Cu-BTC, IRMOF-1 and MIL-47, we propose a new model for CO. Finally, we study the influence of water in both Cu-BTC and IRMOF-1 during the adsorption process.

Adsorption of gases in presence of extra-framework cations (Chapters 6 and 7)

In chapter 6 we study the adsorption of CO_2 in zeolites containing aluminium. Depending on the Si/Al ratio complexes between CO_2 and the extra-framework cations are formed interacting with the structure. In this work we investigate such effect in FAU and LTA zeolites by combining experimental and simulation techniques. From the simulation point of view we use an available transferable force field to define the interactions of CO_2 with the structures and provide a new set of parameters to reproduce these interactions when complexes are formed.

Not many transferable force fields are available in the literature to study the adsorption of some molecules in zeolites. In chapter 7 we use previously available models for CH_4 and Ar and provide new ones for O_2, N_2 and CO to study their adsorption behaviour in both pure silica and aluminosilicates.

Separation of enantiomers (Chapters 8 and 9)

Another separation process of industrial interest is the separation of enantiomers from racemic mixtures. In chapter 8 we investigate the enantioselective behaviour of zeolites during the adsorption of small polar molecules, such as CHClFBr. From previous works with non-polar molecules the need for cations to induce a selective behaviour in MFI zeolite was observed. Hence, we study the same effect along with topological effects of adsorption on MFI, MEL, FER and TON zeolites.

In chapter 9 we use the knowledge obtained from the previous chapter to describe the mechanisms that govern adsorption behaviour of enantiomeric mixtures of lactic acid in MFI zeolites.

Finally, chapter 10 compiles some specific conclusions extracted from each chapter, as well as the main conclusions of this thesis.

Bibliography

(1)   Baerlocher, C.; McCusker, L. B.   Database of Zeolites Structures: http://www.iza-structure.org/databases.

(2)   Allen, F. H. *Acta Crystallographica Section B-Structural Science* **2002**, *58*, 380.

(3)   Li, Y.; Yu, J. *Chemical Reviews* **2014**, *114*, 7268.

(4)   Loewenstein, W. *American Mineralogist* **1954**, *39*, 92.

(5)   Baburin, I. A.; Leoni, S.; Seifert, G. *Journal of Physical Chemistry B* **2008**, *112*, 9437.

(6)   Li, Y.; Yu, J. H.; Wang, Z. P.; Zhang, J. N.; Guo, M.; Xu, R. R. *Chemistry of Materials* **2005**, *17*, 4399.

(7)   Higgins, J. B.; Lapierre, R. B.; Schlenker, J. L.; Rohrman, A. C.; Wood, J. D.; Kerr, G. T.; Rohrbaugh, W. J. *Zeolites* **1988**, *8*, 446.

(8)   Rajic, N.; Logar, N. Z.; Kaucic, V. *Zeolites* **1995**, *15*, 672.

(9)   Rouse, R. C.; Peacor, D. R. *American Mineralogist* **1986**, *71*, 1494.

(10)   Gier, T. E.; Bu, X. H.; Feng, P. Y.; Stucky, G. D. *Nature* **1998**, *395*, 154.

(11)   Blaser, H. U.; Muller, M. *Stud. Surf. Sci. Catal.*, 1991; Vol. 59, 73-92.

(12)   Tang, L.; Shi, L.; Bonneau, C.; Sun, J.; Yue, H.; Ojuva, A.; Lee, B.-L.; Kritikos, M.; Bell, R. G.; Bacsik, Z.; Mink, J.; Zou, X. *Nature Materials* **2008**, *7*, 381.

(13)   Sun, J.; Bonneau, C.; Cantin, A.; Corma, A.; Diaz-Cabanas, M. J.; Moliner, M.; Zhang, D.; Li, M.; Zou, X. *Nature* **2009**, *458*, 1154.

(14)   Reut, S.; Prakash, A. *Fuel Processing Technology* **2006**, *87*, 217.

(15)   Chambellan, A.; Chevreau, T.; Khabtou, S.; Marzin, M.; Lavalley, J. C. *Zeolites* **1992**, *12*, 306.

(16)   Davis, M. E. *Nature* **2002**, *417*, 813.

(17)   Hampel, I.; Jacobi, U. *Monatshefte Fur Veterinarmedizin* **1986**, *41*, 238.

(18)   Hedstrom, A. *Journal of Environmental Engineering-Asce* **2001**, *127*, 673.

(19)   Martinez, C.; Corma, A. *Coordination Chemistry Reviews* **2011**, *255*, 1558.

(20)   Corma, A. *Journal of Catalysis* **2003**, *216*, 298.

(21)   Corma, A.; Martinez, A. *Advanced Materials* **1995**, *7*, 137.

(22)   Yeung, K. L.; Han, W. *Catalysis Today* **2014**, *236*, 182.

(23)   Li, K.; Valla, J.; Garcia-Martinez, J. *Chemcatchem* **2014**, *6*, 46.

(24)   Long, J. R.; Yaghi, O. M. *Chemical Society Reviews* **2009**, *38*, 1213.

(25)   Mueller, A. *Nature Chemistry* **2009**, *1*, 13.

(26)   Ferey, G. *Chemical Society Reviews* **2008**, *37*, 191.

(27)   James, S. L. *Chemical Society Reviews* **2003**, *32*, 276.

(28)   Meek, S. T.; Greathouse, J. A.; Allendorf, M. D. *Advanced Materials* **2011**, *23*, 249.

(29)   Pan, L.; Adams, K. M.; Hernandez, H. E.; Wang, X. T.; Zheng, C.; Hattori, Y.; Kaneko, K. *Journal of the American Chemical Society* **2003**, *125*, 3062.

(30)   Yaghi, O. M.; O'Keeffe, M.; Ockwig, N. W.; Chae, H. K.; Eddaoudi, M.; Kim, J. *Nature* **2003**, *423*, 705.

(31)   Dybtsev, D. N.; Chun, H.; Yoon, S. H.; Kim, D.; Kim, K. *Journal of the American Chemical Society* **2004**, *126*, 32.

(32)   Fletcher, A. J.; Cussen, E. J.; Bradshaw, D.; Rosseinsky, M. J.; Thomas, K. M. *Journal of the American Chemical Society* **2004**, *126*, 9750.

(33)   Ohmori, O.; Kawano, M.; Fujita, M. *Angewandte Chemie-International Edition* **2005**, *44*, 1962.

(34)   Rowsell, J. L. C.; Yaghi, O. M. *Microporous and Mesoporous Materials* **2004**, *73*, 3.

(35)   Snurr, R. Q.; Hupp, J. T.; Nguyen, S. T. *Aiche Journal* **2004**, *50*, 1090.

(36)   Chen, B. L.; Eddaoudi, M.; Hyde, S. T.; O'Keeffe, M.; Yaghi, O. M. *Science* **2001**, *291*, 1021.

(37)   Cheetham, A. K.; Rao, C. N. R. *Science* **2007**, *318*, 58.

(38)   Zhao, X. B.; Xiao, B.; Fletcher, A. J.; Thomas, K. M.; Bradshaw, D.; Rosseinsky, M. J. *Science* **2004**, *306*, 1012.

(39)   Eddaoudi, M.; Kim, J.; Rosi, N.; Vodak, D.; Wachter, J.; O'Keeffe, M.; Yaghi, O. M. *Science* **2002**, *295*, 469.

(40)   Li, H.; Eddaoudi, M.; O'Keeffe, M.; Yaghi, O. M. *Nature* **1999**, *402*, 276.

(41)   Schneemann, A.; Bon, V.; Schwedler, I.; Senkovska, I.; Kaskel, S.; Fischer, R. A. *Chemical Society Reviews* **2014**, *43*, 6062.

(42)   Kondo, M.; Shimamura, M.; Noro, S.; Minakoshi, S.; Asami, A.; Seki, K.; Kitagawa, S. *Chemistry of Materials* **2000**, *12*, 1288.

(43)   Kesanli, B.; Cui, Y.; Smith, M. R.; Bittner, E. W.; Bockrath, B. C.; Lin, W. B. *Angewandte Chemie-International Edition* **2005**, *44*, 72.

(44)   Bourrelly, S.; Llewellyn, P. L.; Serre, C.; Millange, F.; Loiseau, T.; Ferey, G. *Journal of the American Chemical Society* **2005**, *127*, 13519.

(45)   Thomas, K. M. *Dalton Transactions* **2009**, 1487.

(46)   Sumida, K.; Rogow, D. L.; Mason, J. A.; McDonald, T. M.; Bloch, E. D.; Herm, Z. R.; Bae, T.-H.; Long, J. R. *Chemical Reviews* **2012**, *112*, 724.

(47)   Millward, A. R.; Yaghi, O. M. *Journal of the American Chemical Society* **2005**, *127*, 17998.

(48)   Rowsell, J. L. C.; Yaghi, O. M. *Angewandte Chemie-International Edition* **2005**, *44*, 4670.

(49)   Duren, T.; Snurr, R. Q. *Journal of Physical Chemistry B* **2004**, *108*, 15703.

(50)   Keskin, S.; Sholl, D. S. *Journal of Physical Chemistry C* **2007**, *111*, 14055.

(51)   Bourrelly, S.; Moulin, B.; Rivera, A.; Maurin, G.; Devautour-Vino, S.; Serre, C.; Devic, T.; Horcajada, P.; Vimont, A.; Clet, G.; Daturi, M.; Lavalley, J.-C.; Loera-Serna, S.; Denoyel, R.; Llewellyn, P. L.; Ferey, G. *Journal of the American Chemical Society* **2010**, *132*, 9488.

(52)   Lee, J. Y.; Olson, D. H.; Pan, L.; Emge, T. J.; Li, J. *Advanced Functional Materials* **2007**, *17*, 1255.

(53)   Van de Voorde, B.; Bueken, B.; Denayer, J.; De Vos, D. *Chemical Society Reviews* **2014**, *43*, 5766.

(54)   Qiu, S.; Xue, M.; Zhu, G. *Chemical Society Reviews* **2014**, *43*, 6116.

(55)   DeCoste, J. B.; Peterson, G. W. *Chemical Reviews* **2014**, *114*, 5695.

(56)   Chaemchuen, S.; Kabir, N. A.; Zhou, K.; Verpoort, F. *Chemical Society Reviews* **2013**, *42*, 9304.

(57)   Lee, J.; Farha, O. K.; Roberts, J.; Scheidt, K. A.; Nguyen, S. T.; Hupp, J. T. *Chemical Society Reviews* **2009**, *38*, 1450.

(58)   Yang, Q.; Zhong, C.; Chen, J.-F. *Journal of Physical Chemistry C* **2008**, *112*, 1562.

(59)   Ma, L.; Abney, C.; Lin, W. *Chemical Society Reviews* **2009**, *38*, 1248.

(60)   Fujita, M.; Kwon, Y. J.; Washizu, S.; Ogura, K. *Journal of the American Chemical Society* **1994**, *116*, 1151.

(61)   Seo, J. S.; Whang, D.; Lee, H.; Jun, S. I.; Oh, J.; Jeon, Y. J.; Kim, K. *Nature* **2000**, *404*, 982.

(62)   Wang, C.-C.; Li, J.-R.; Lv, X.-L.; Zhang, Y.-Q.; Guo, G. *Energy & Environmental Science* **2014**, *7*, 2831.

(63)   Zhang, T.; Lin, W. *Chemical Society Reviews* **2014**, *43*, 5982.

(64)   Liu, J.; Chen, L.; Cui, H.; Zhang, J.; Zhang, L.; Su, C.-Y. *Chemical Society Reviews* **2014**, *43*, 6011.

(65)   Zhao, M.; Ou, S.; Wu, C.-D. *Accounts of Chemical Research* **2014**, *47*, 1199.

(66)   Leus, K.; Liu, Y.-Y.; Van Der Voort, P. *Catalysis Reviews-Science and Engineering* **2014**, *56*, 1.

(67)   Dantas Ramos, A. L.; Tanase, S.; Rothenberg, G. *Quimica Nova* **2014**, *37*, 123.

(68)   Harbuzaru, B. V.; Corma, A.; Rey, F.; Atienzar, P.; Jorda, J. L.; Garcia, H.; Ananias, D.; Carlos, L. D.; Rocha, J. *Angewandte Chemie-International Edition* **2008**, *47*, 1080.

(69)   Hu, Z.; Deibert, B. J.; Li, J. *Chemical Society Reviews* **2014**, *43*, 5815.

(70)   Ren, Y.; Chia, G. H.; Gao, Z. *Nano Today* **2013**, *8*, 577.

(71)   Zhang, Q.; Shreeve, J. n. M. *Angewandte Chemie-International Edition* **2014**, *53*, 2540.

(72)   Horcajada, P.; Chalati, T.; Serre, C.; Gillet, B.; Sebrie, C.; Baati, T.;
        Eubank, J. F.; Heurtaux, D.; Clayette, P.; Kreuz, C.; Chang, J.-S.; Hwang,
        Y. K.; Marsaud, V.; Bories, P.-N.; Cynober, L.; Gil, S.; Ferey, G.; Couvreur,
        P.; Gref, R. *Nature Materials* **2010**, *9*, 172.

(73)   Horcajada, P.; Serre, C.; Maurin, G.; Ramsahye, N. A.; Balas, F.; Vallet-
        Regi, M.; Sebban, M.; Taulelle, F.; Ferey, G. *Journal of the American
        Chemical Society* **2008**, *130*, 6774.

(74)   Mueller, U.; Schubert, M.; Teich, F.; Puetter, H.; Schierle-Arndt, K.; Pastre,
        J. *Journal of Materials Chemistry* **2006**, *16*, 626.

(75)   Keskin, S.; Kizilel, S. *Industrial & Engineering Chemistry Research* **2011**, *50*,
        1799.

(76)   Bernini, M. C.; Fairen-Jimenez, D.; Pasinetti, M.; Ramirez-Pastor, A. J.;
        Snurr, R. Q. *Journal of Materials Chemistry B* **2014**, *2*, 766.

(77)   Canivet, J.; Fateeva, A.; Guo, Y. M.; Coasne, B.; Farrusseng, D. *Chemical
        Society Reviews* **2014**, *43*, 5594.

(78)   Furukawa, H.; Gandara, F.; Zhang, Y. B.; Jiang, J. C.; Queen, W. L.;
        Hudson, M. R.; Yaghi, O. M. *Journal of the American Chemical Society*
        2014, *136*, 4369.

(79)   Greathouse, J. A.; Allendorf, M. D. *Journal of the American Chemical
        Society* **2006**, *128*, 10678.

(80)   Gul-E-Noor, F.; Jee, B.; Poeppl, A.; Hartmann, M.; Himsl, D.; Bertmer, M.
        Physical Chemistry Chemical Physics **2011**, *13*, 7783.

(81)   Loiseau, T.; Serre, C.; Huguenard, C.; Fink, G.; Taulelle, F.; Henry, M.;
        Bataille, T.; Ferey, G. *Chemistry-a European Journal* **2004**, *10*, 1373.

(82)   Millange, F.; Guillou, N.; Walton, R. I.; Greneche, J.-M.; Margiolaki, I.;
        Fereya, G. *Chemical Communications* **2008**, 4732.

(83)   Serre, C.; Millange, F.; Thouvenot, C.; Nogues, M.; Marsolier, G.; Louer, D.;
        Ferey, G. *Journal of the American Chemical Society* **2002**, *124*, 13519.

(84)   Mowat, J. P. S.; Seymour, V. R.; Griffin, J. M.; Thompson, S. P.; Slawin, A.
        M. Z.; Fairen-Jimenez, D.; Dueren, T.; Ashbrook, S. E.; Wright, P. A. *Dalton
        Transactions* **2012**, *41*, 3937.

(85)   Mellot-Draznieks, C.; Serre, C.; Surble, S.; Audebrand, N.; Ferey, G. *Journal
        of the American Chemical Society* **2005**, *127*, 16273.

(86)   Surble, S.; Serre, C.; Mellot-Draznieks, C.; Millange, F.; Ferey, G. *Chemical
        Communications* **2006**, 284.

(87)   Chui, S. S. Y.; Lo, S. M. F.; Charmant, J. P. H.; Orpen, A. G.; Williams, I.
        D. *Science* **1999**, *283*, 1148.

(88)   Fairen-Jimenez, D.; Moggach, S. A.; Wharmby, M. T.; Wright, P. A.; Parsons, S.; Dueren, T. *Journal of the American Chemical Society* **2011**, *133*, 8900.

(89)   Garberoglio, G.; Taioli, S. *Microporous and Mesoporous Materials* **2012**, *163*, 215.

(90)   Fairen-Jimenez, D.; Galvelis, R.; Torrisi, A.; Gellan, A. D.; Wharmby, M. T.; Wright, P. A.; Mellot-Draznieks, C.; Dueren, T. *Dalton Transactions* **2012**, *41*, 10752.

(91)   Kitagawa, S.; Kitaura, R.; Noro, S. *Angewandte Chemie-International Edition* **2004**, *43*, 2334.

(92)   Maji, T. K.; Matsuda, R.; Kitagawa, S. *Nature Materials* **2007**, *6*, 142.

(93)   Bureekaew, S.; Sato, H.; Matsuda, R.; Kubota, Y.; Hirose, R.; Kim, J.; Kato, K.; Takata, M.; Kitagawa, S. *Angewandte Chemie-International Edition* **2010**, *49*, 7660.

(94)   Frenkel, D.; Smit, B. *Undesrtanding Molecular Simulation: From Algorithms to Applications*; Academic Press: San Diego. C.A., 2002.

(95)   Metropolis, N.; Rosenbluth, A. W.; Rosenbluth, M. N.; Teller, A. H.; Teller, E. *Journal of Chemical Physics* **1953**, *21*, 1087.

(96)   Atkins, P. W. *Physical Chemistry*; Oxford Higher Educations: New York, 1990.

(97)   Martin, M. G.; Siepmann, J. I. *Journal of Physical Chemistry B* **1998**, *102*, 2569.

(98)   Rowlinson, J. S.; Swinton, F. L. *Liquids and Liquid Mixtures*; Butterworhts: London, 1982.

(99)   Rowlinson, J. S.; Widom, B. *Molecular Theory of Capillarity*; Oxford University Press: New York, 1989.

(100)   Vlugt, T. J. H.; Garcia-Perez, E.; Dubbeldam, D.; Ban, S.; Calero, S. *Journal of Chemical Theory and Computation* **2008**, *4*, 1107.

(101)   Vlugt, T. J. H. *Molecular Simulation* **1999**, *23*, 63.

(102)   Widom, B. *Journal of Chemical Physics* **1963**, *39*, 2808.

(103)   Liu, J.; Culp, J. T.; Natesakhawat, S.; Bockrath, B. C.; Zande, B.; Sankar, S. G.; Garberoglio, G.; Johnson, J. K. *Journal of Physical Chemistry C* **2007**, *111*, 9305.

(104)   Talu, O.; Myers, A. L. *Aiche Journal* **2001**, *47*, 1160.

(105)   Duren, T.; Sarkisov, L.; Yaghi, O. M.; Snurr, R. Q. *Langmuir* **2004**, *20*, 2683.

(106)   Myers, A. L. *Aiche Journal* **2002**, *48*, 145.

(107)   Myers, A. L.; Monson, P. A. *Langmuir* **2002**, *18*, 10261.

(108)   Verlet, L. *Physical Review* **1967**, *159*, 98.

(109) Verlet, L. *Physical Review* **1968**, *165*, 201.

(110) Nosé, S. *Journal of Chemical Physics* **1984**, *81*, 511.

(111) Hoover, W. G. *Physical Review A* **1985**, *31*, 1695.

(112) Allen, M. P.; Tildesley, D. J. *Computer Simulation of Liquids* Oxford Clarendon Press, 1987.

(113) Ewald, P. P. *Annalen Der Physik* **1921**, *64*, 253.

(114) Garcia-Perez, E.; Dubbeldam, D.; Maesen, T. L. M.; Calero, S. *Journal of Physical Chemistry B* **2006**, *110*, 23968.

(115) Calero, S.; Dubbeldam, D.; Krishna, R.; Smit, B.; Vlugt, T. J. H.; Denayer, J. F. M.; Martens, J. A.; Maesen, T. L. M. *Journal of the American Chemical Society* **2004**, *126*, 11377.

(116) Hagler, A. T.; Ewig, C. S. *Computer Physics Communications* **1994**, *84*, 131.

(117) Halgren, T. A. *Journal of the American Chemical Society* **1992**, *114*, 7827.

(118) Burchart, E. D.; Jansen, J. C.; Vanbekkum, H. *Zeolites* **1989**, *9*, 432.

(119) Allinger, N. L.; Yuh, Y. H.; Lii, J. H. *Journal of the American Chemical Society* **1989**, *111*, 8551.

(120) Dubbeldam, D.; Calero, S.; Vlugt, T. J. H.; Krishna, R.; Maesen, T. L. M.; Smit, B. *Journal of Physical Chemistry B* **2004**, *108*, 12301.

(121) Garcia-Perez, E.; Parra, J. B.; Ania, C. O.; Dubbeldam, D.; Vlugt, T. J. H.; Castillo, J. M.; Merkling, P. J.; Calero, S. *Journal of Physical Chemistry C* **2008**, *112*, 9976.

(122) Garcia-Sanchez, A.; Ania, C. O.; Parra, J. B.; Dubbeldam, D.; Vlugt, T. J. H.; Krishna, R.; Calero, S. *Journal of Physical Chemistry C* **2009**, *113*, 8814.

(123) Greathouse, J. A.; Kinnibrugh, T. L.; Allendorf, M. D. *Industrial & Engineering Chemistry Research* **2009**, *48*, 3425.

(124) Rappe, A. K.; Casewit, C. J.; Colwell, K. S.; Goddard, W. A.; Skiff, W. M. *Journal of the American Chemical Society* **1992**, *114*, 10024.

(125) Mayo, S. L.; Olafson, B. D.; Goddard, W. A. *Journal of Physical Chemistry* **1990**, *94*, 8897.

(126) Gaedt, K.; Holtje, H. D. *Journal of Computational Chemistry* **1998**, *19*, 935.

(127) Dauber-Osguthorpe, P.; Roberts, V. A.; Osguthorpe, D. J.; Wolff, J.; Genest, M.; Hagler, A. T. *Proteins-Structure Function and Genetics* **1988**, *4*, 31.

(128) Pluth, J. J.; Smith, J. V. *Journal of the American Chemical Society* **1980**, *102*, 4704.

(129) Firor, R. L.; Seff, K. *Journal of the American Chemical Society* **1978**, *100*, 3091.

(130) Olson, D. H. *Zeolites* **1995**, *15*, 439.

(131) Mortier, W. J.; Vandenbossche, E.; Uytterhoeven, J. B. *Zeolites* **1984**, *4*, 41.

(132) Fitch, A. N.; Jobic, H.; Renouprez, A. *Journal of Physical Chemistry* **1986**, *90*, 1311.

(133) Jaramillo, E.; Auerbach, S. M. *Journal of Physical Chemistry B* **1999**, *103*, 9589.

(134) Bandyopadhyay, S.; Yashonath, S. *Journal of Chemical Physics* **1996**, *105*, 7223.

(135) Vitale, G.; Mellot, C. F.; Bull, L. M.; Cheetham, A. K. *Journal of Physical Chemistry B* **1997**, *101*, 4559.

(136) Martin, M. G.; Siepmann, J. I. *Journal of Physical Chemistry B* **1999**, *103*, 4508.

(137) Stogryn, D. E.; Stogryn, A. P. *Molecular Physics* **1966**, *11*, 371.

(138) Murthy, C. S.; Singer, K.; Klein, M. L.; McDonald, I. R. *Molecular Physics* **1980**, *41*, 1387.

(139) Harris, J. G.; Yung, K. H. *Journal of Physical Chemistry* **1995**, *99*, 12021.

(140) Piper, J.; Morrison, J. A.; Peters, C. *Molecular Physics* **1984**, *53*, 1463.

(141) Straub, J. E.; Karplus, M. *Chemical Physics* **1991**, *158*, 221.

(142) Sirjoosingh, A.; Alavi, S.; Woo, T. K. *Journal of Physical Chemistry C* **2010**, *114*, 2171.

(143) Jorgensen, W. L.; Chandrasekhar, J.; Madura, J. D.; Impey, R. W.; Klein, M. L. *Journal of Chemical Physics* **1983**, *79*, 926.

(144) Jorgensen, W. L.; Madura, J. D. *Molecular Physics* **1985**, *56*, 1381.

(145) Berendsen, H. J. C.; Grigera, J. R.; Straatsma, T. P. *Journal of Physical Chemistry* **1987**, *91*, 6269.

(146) Mahoney, M. W.; Jorgensen, W. L. *Journal of Chemical Physics* **2000**, *112*, 8910.

(147) Wu, Y. J.; Tepper, H. L.; Voth, G. A. *Journal of Chemical Physics* **2006**, *124*.

(148) Levitt, M.; Hirshberg, M.; Sharon, R.; Laidig, K. E.; Daggett, V. *Journal of Physical Chemistry B* **1997**, *101*, 5051.

(149) Horn, H. W.; Swope, W. C.; Pitera, J. W.; Madura, J. D.; Dick, T. J.; Hura, G. L.; Head-Gordon, T. *Journal of Chemical Physics* **2004**, *120*, 9665.

(150) Abascal, J. L. F.; Vega, C. *Journal of Chemical Physics* **2005**, *123*.

(151) Stilling.Fh; Rahman, A. *Journal of Chemical Physics* **1974**, *60*, 1545.

(152) Rick, S. W. *Journal of Chemical Physics* **2004**, *120*, 6085.

(153) CostanteCrassous, J.; Marrone, T. J.; Briggs, J. M.; McCammon, J. A.; Collet, A. *Journal of the American Chemical Society* **1997**, *119*, 3818.

Molecular Simulations for Adsorption and Separation of Natural Gas in IRMOF-1 and Cu-BTC Metal-Organic Frameworks

Ana Martín-Calvo, Elena García-Pérez, Juan Manuel Castillo and Sofía Calero

2

We use Monte Carlo simulations to study the adsorption and separation of the natural gas components in IRMOF-1 and Cu-BTC metal-organic frameworks. We computed the adsorption isotherms of pure components, binary and five-component mixtures analysing the sitting of the molecules in the structure for the different loadings. The bulk compositions studied for the mixtures were 50:50 and 90:10 for CH_4/CO_2, 90:10 for N_2/CO_2 and 95:2.0:1.5:1.0:0.5 for the $CH_4/C_2H_6/N_2/CO_2/C_3H_8$ mixture. We choose this composition because it is similar to an average sample of natural gas. Our simulations show that CO_2 is preferentially adsorbed over propane, ethane, methane and N_2 in the complete pressure range under study. Longer alkanes are favoured over shorter alkanes and the lowest adsorption corresponds to N_2. Though IRMOF-1 has a significantly higher adsorption capacity than Cu-BTC, the adsorption selectivity of CO_2 over CH_4 and N_2 is found to be higher in the latter, proving that the separation efficiency is largely affected by the shape, the atomic composition and the type of linkers of the structure.

1. Introduction

Methane (CH_4) is one of the cleanest carbon fuels due to its low carbonaceous and particle emissions after combustion. It is also attractive for its low emissions of greenhouse gases per kW generated in industrial and energy production applications. Natural gas is composed of around 95% methane, traces of heavier gaseous hydrocarbons such as ethane (C_2H_6) and propane (C_3H_8) and other light gases such as CO_2 and N_2. To obtain a cheap and clean fuel from natural gas it is important to purify it since the presence of CO_2 reduces the combustion power efficiency and contributes to greenhouse gas emissions[1,2].

Metal-organic frameworks (MOFs) are turning into promising materials for storage, separation and purification of natural gas mixtures by adsorption. They are a new class of porous materials consisting of metal-oxide clusters and organic linkers[3-9] that can form pores and cavities of a desired shape and size by selecting linkers of specific length and metals of suitable coordination[7,9-20]. Experimental and simulation studies based on the adsorption and separation of natural gas and its components in MOFs are still scarce and most of them are focused on the adsorption isotherms of CO_2, methane, N_2 and on CO_2/CH_4 binary mixtures[21-31].

The adsorption and separation processes of CO_2, methane and ethane were analysed using molecular simulations by Wang et al.[21] in Cu-BTC, by Babarao et al.[22], Keskin and Sholl[23] and Walton et al.[24] in IRMOF-1 and by Yang and Zhong[25-27] in both Cu-BTC and IRMOF-1 structures. Liu et al.[28] used experimental and theoretical methods to study the adsorption behaviour of N_2 in Cu-BTC and Wang et al.[29] investigated the sorption properties of Cu-BTC for N_2, CO_2, methane, ethane and CO_2/CH_4 mixtures by a series of experimental methods. Zhou et al.[30] measured adsorption isotherms for CH_4 in IRMOF-1 over a large temperature and pressure range and Millward and Yaghi[31] compared the volumetric CO_2 capacity for a variety of MOFs. In this work we go one step forward by analysing the molecular sitting during the adsorption of the main components of natural gas and their mixtures. We use molecular simulations to obtain information about the performance of two highly porous MOFs, Cu-BTC and IRMOF-1, in the natural gas separation process. Cu-BTC (BTC: benzene-1,3,5-tricarboxylate) has garnered a good deal of attention since it was first reported by Chui et al.[32] in 1999. Its framework is a metal coordination polymer based on copper as the metal centre and benzene-1,3,5-tricarboxylate as the linker molecule. It is formed by primary building blocks connected to form a face-centred cubic crystal framework, and secondary building blocks forming octahedron-shaped pockets accessible for small molecules through small windows. IRMOF-1 belongs to the family of isoreticular metal-organic frameworks (IRMOFs) and was first synthesised by

Yaghi and co-workers[12,13]. IRMOF-1 structure consists of a cubic array of $Zn_4O(CO_2)_6$ units connected by phenylene links. The linkage of the Zn_4O complexes is forced to alternate between linkers pointing outwards and inwards, resulting in a structure with two alternating type of cavities. Small cavities of about 10.9 Å and larger cavities of about 14.4 Å diameter[13].

This work analyses the storage capacity and adsorption behaviour of CH_4, C_2H_6, N_2, CO_2, C_3H_8 and the separation of their mixtures in Cu-BTC and IRMOF-1. We focus not only on the adsorption capacities and selectivities but also on the preferential adsorption sites of the components as a function of pressure. In section 2 we describe the simulation methods and the models used for the MOFs and the adsorbates. The obtained adsorption isotherms, molecular sitting and occupancies for pure components and mixtures are presented in section 3, followed by some concluding remarks in section 4.

2. Simulation methods and models

Absorption isotherms were performed using grand canonical Monte Carlo (GCMC) simulations, where the chemical potential, the temperature, and the volume are kept fixed. The fugacity, related directly to the imposed chemical potential[33], is obtained from the value of pressure using the Peng-Robinson equation of state. We used at least 10^7 MC cycles that consist of translation, rotation, regrow in random positions and change of identity for mixtures[34]. For comparison with experimental isotherms, absolute

adsorption was converted to excess adsorption[18,35].

Atomic interactions were described by Lennard-Jones and Coulomb potentials computed with the Ewald summation technique, using a relative precision of 10^{-6}. The Lennard-Jones potential is cut and shifted with a cut-off distance of 12 Å. The parameters for methane, ethane and propane were taken from the united atom TraPPE model[36] in which the CH_x beads are considered as single, charge-less interaction centres. The beads are connected using a harmonic bond-potential $U = 0.5\ k\ (r - r_0)^2$ with $k/k_B = 96500$ K and $r_0 = 1.54$ Å and a harmonic bend potential $U = 0.5\ k\ (\theta - \theta_0)^2$ with $k/k_B = 62500$ K and $\theta_0 = 114^O$. CO_2 and N_2 were considered as small rigid molecules, using the model proposed by Harris et al.[37] for CO_2 and the model proposed by Murthy et al.[38] for N_2. The partial charges of N_2 and CO_2 are distributed along each molecule to reproduce the experimental quadrupole moment. These models and potentials have been successfully employed to describe the adsorption in zeolites[39-41].

Cu-BTC and IRMOF-1 frameworks are considered rigid with Lennard-Jones parameters taken from the DREIDING[42] force field except these for Cu and Zn, that were taken from the UFF[43] force field. Lorentz-Berthelot mixing rules were used to calculate mixed Lennard-Jones parameters and the atomic charges for the MOFs were taken from Frost et al. and Dubbeldam et al.[44]. One unit cell of IRMOF-1 (a = b = c = 25.832 Å) and one unit cell of Cu-BTC (a = b = c = 26.343 Å) were used

during the simulations. We obtained a helium void fraction of 0.82 for IRMOF-1 and 0.76 for Cu-BTC. The crystal structure of Chui et al. includes axial oxygen atoms weakly bonded to the Cu atoms, which correspond to water ligands. Our simulations have been performed on the dry Cu-BTC with these oxygen atoms removed. The complete set of parameters and charges used in this work for adsorbates and adsorbents is listed in Appendix 1 (Table A1).

The method used for the analysis of preferential adsorption sites in MOFs is similar to this used on the locations and occupancies of ions in zeolites[40,45]. We have defined eight individual adsorption sites for IRMOF-1 and four for Cu-BTC, based on previous works that studied the adsorption sites of argon and nitrogen in IRMOF-1[46,47] and hydrogen in Cu-BTC[28]. The IRMOF-1 unit cell contains 8 Zn_4O tetrahedral clusters and 24 linker molecules, defining 4 small cavities and 4 large cavities (see Figure A1 in Appendix 1). Five of the sites defined for IRMOF-1 are close to the Zn_4O cluster and the linker molecules (Sites I to V) and the other three form a second layer in the pores (Sites VI to VIII). Sites I and II are located in the large and small cages, respectively. Site III is located in the region that separates both types of cages. Sites IV and V are close to the linker molecules, above and beneath the centre of the phenyl ring (site IV) and on the edges of it (site V). Sites VI and VII forming a layer above site IV, and site VIII located at the centre of the small cage, above site II and surrounded by site V.

Cu-BTC is composed by benzene-1,3,5-tricarboxylate (BTC) ligands coordinating copper ions, forming big cavities and small octahedral cages (see Figure A2 of Appendix 1). We have defined four adsorption sites on this structure; the sites labelled I, II and III described by Liu *et al.* as preferential adsorption sites for H_2 and one additional site that we labelled I'. Sites I and I' are located at the big central cavities, in the centre (site I') or close to the Cu^{2+} atoms (site I) and sites II and III are located at the centre and at the windows of the small octahedral cages, respectively. More details about the structure and adsorption sites for IRMOF-1 and Cu-BTC can be found in Appendix 1 (Figures A3, A4 and A5).

3. Results

The adsorption isotherms and preferential adsorption sites in Cu-TC and IRMOF-1 were obtained at 298 K for 1) pure component methane, ethane, propane, nitrogen and carbon dioxide, 2) 50:50 and 90:10 CH_4/CO_2 binary mixtures, 3) 90:10 N_2/CO_2 binary mixture and 4) 95:2:1.5:1:0.5 five component mixture of methane, ethane, nitrogen, carbon dioxide and propane.

Adsorption of pure components

Simulated and available experimentally measured adsorption isotherms of pure methane, ethane, and propane in Cu-BTC and IRMOF-1 as a function of pressure are shown in Figures 1a and 1b, respectively. The simulated isotherms are in good agreement with previous simulation results and experimental data[22,26,27,29,30,35,44,48-50].

The adsorption of hydrocarbons increases with the number of carbon atoms in both structures for the complete pressure range under study. This is due to a size entropic effect[51]. At much higher pressures near saturation (not shown here) methane would absorb more as a consequence of a shape entropic effect[51] (methane fits better than ethane and propane into the partially occupied cavities). Adsorption isotherms of CO_2 and N_2 are shown in Figure 2a (Cu-BTC) and Figure 2b
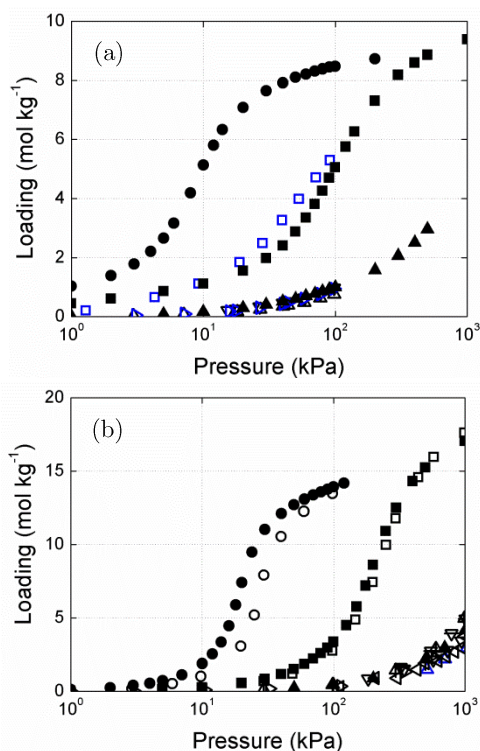

Figure 1. Adsorption isotherms of pure methane (triangles), ethane (squares) and propane (circles) in (a) Cu-BTC and in (b) IRMOF-1 at 298 K. Our simulated isotherms (full symbols) are compared with previous experimental data[29,30] (blue empty symbols) and simulation data[22,26,27,35,44,48-50] (black empty symbols).
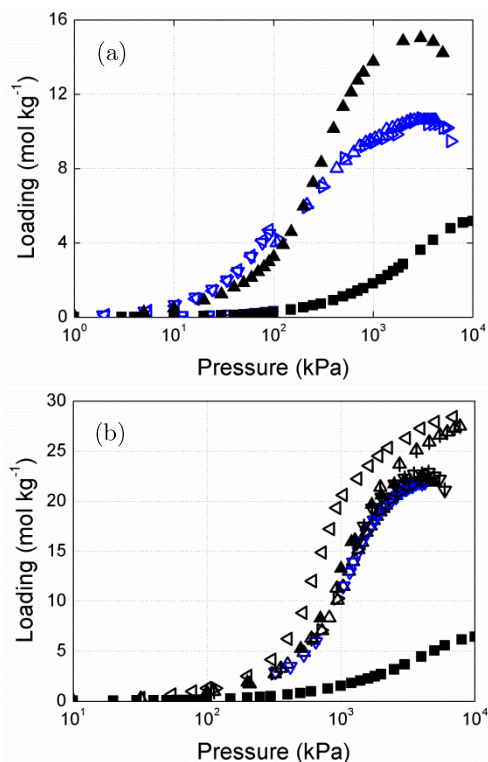
Figure 2. Adsorption isotherms of pure CO_2 (triangles) and N_2 (squares) in (a) Cu-BTC and in (b) IRMOF-1 at 298 K. Our simulated isotherms (full symbols) are compared with previous experimental data[29,31] (blue empty symbols) and simulation data[22,27,44,50] (black empty symbols).

(IRMOF-1). The simulation results obtained for IRMOF-1 are in very good agreement with previous experimental values[29,31]. The agreement is also good for Cu-BTC at low pressures[22,26,31,44,50,52] though deviations are observed at higher pressures, where simulation data overestimate measured values for CO_2. These deviations can be attributed to the force field accuracy and also to the fact that our framework is a rigid and perfect material, whereas experimental samples are flexible and they generally

contain water and organic residues after synthesis leading to a decrease in the storage capacity. The partially charged CO_2 has stronger interaction with the framework than N_2 and therefore higher adsorption. For the same reason, the extent of CO_2 adsorption is larger than the one of methane in both MOFs over the entire pressure range under study, in which saturation is not reached. Direct comparison of the obtained adsorption isotherms for hydrocarbons and for N_2 and CO_2 for both structures proves that Cu-BTC is the best adsorbent at the lower pressures and IRMOF-1 – with a larger pore volume and therefore more storage capacity- is the best adsorbent at the higher pressures (see Figures A6a y A6b in Appendix 1). This can be attributed to entropic effects since the molecular packing is more efficient in the small octahedral cages of Cu-BTC – preferential adsorption sites at low pressures– than in the big cavities of IRMOF-1. Appendix 1 contains movies taken directly from our simulations that illustrate the molecular sitting as a function of pressure (Movies 1 and 2). The adsorption behaviour of carbon dioxide and methane as a function of pressure in Cu-BTC is depicted in Figures 3a and 3b. At low pressures methane preferentially adsorbs in the small octahedral cages of Cu-BTC (site II), while CO_2 not only adsorbs in the cages but also in the windows (site III). The adsorption of N_2 in the big cages (site I') is as important as in the octahedral cages and the windows are also occupied (site III) but in a lower extent. Site II is also preferential adsorption site for longer alkanes at low pressures and the increase on the

number of carbon atoms in the chain progressively reduces the adsorption on site III, being almost zero for propane. At higher pressures and once the octahedral cages are partially filled, the molecules adsorb more in the big cage (site I') and in the windows (site III). Site I, defined by Liu *et al.* as a preferential adsorption position for hydrogen[53] remains empty for all adsorbates over the entire range of pressures.

A similar study was done for IRMOF-1, identifying the large cages (site I) and the region that separates large and small cages (site III) as preferential adsorption sites for pure component adsorption. Site III shows the highest occupation, followed by site I. Site II (small cages) was found almost empty. Most of the adsorbed molecules close to the linkers are found above and beneath the centre of the phenyl ring (site IV) and only a few molecules are on the edges of the linkers (site V). Two out of the three additional sites described by Rowsel *et al.* for argon molecules[46] show very little adsorption in all cases. These are the sites labelled as VI and VII that form a layer above the phenyl ring. The third additional site (site VIII) is almost empty at low pressures but a significant increase of adsorption is observed at higher pressures. Tables summarizing the occupancies of the sites by all pure components at 298 K in Cu-BTC and IRMOF-1 can be found in Appendix 1 (Tables A2 and A3).
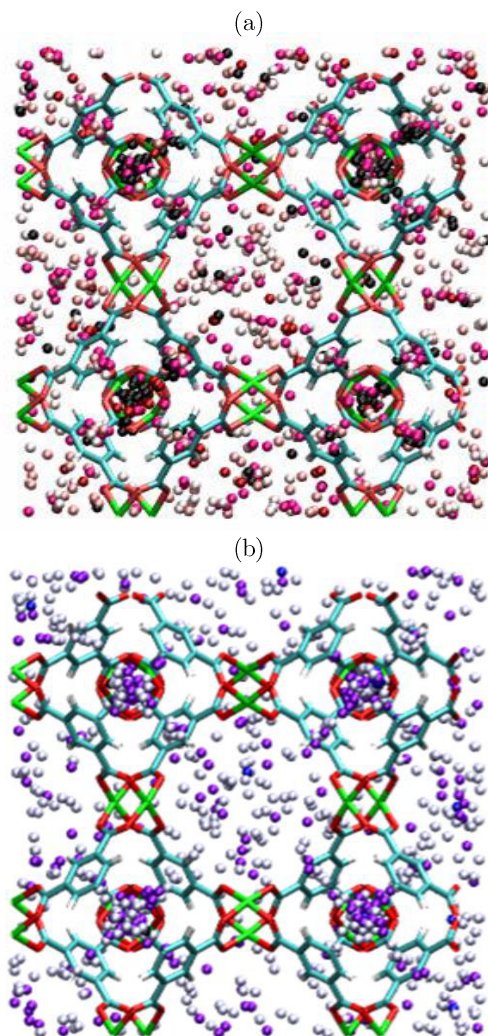
Figure 3. Centre-of-mass distributions of (a) carbon dioxide and (b) methane molecules adsorbed in Cu-BTC at 298 K for 2 kPa, 20 kPa, 200 kPa, 1000 kPa and 5000 kPa. The centre of mass changes from darker to lighter colour with calculations performed using one (2 kPa), two (20 kPa) and four million (200 to 5000 kPa) MC steps. The snapshots are taken every 5000 steps for 2 kPa, 10000 steps for 20 kPa and 20000 steps for the three higher pressures.

Adsorption of CH_4 and CO_2 binary mixtures

Figure 4 shows the computed adsorption selectivity for CO_2 relative to CH_4 defined as $(x_{CO2}/y_{CO2})/(x_{CH4}/y_{CH4})$, where x_{CO2} and x_{CH4} are the molar fractions in the adsorbed phase and y_{CO2} and y_{CH4} are the molar fractions in the bulk phase. Selectivities were computed for the 50:50 and for the 10:90 CO_2/CH_4 mixtures. The selectivity in Cu-BTC is the highest among the two adsorbents.

CO_2 preferentially adsorbs in both MOFs due to the stronger interactions between the CO_2 molecules and the surfaces. Previous simulation data[22,23,26] –only available for the 50:50 equimolar mixture– were added for comparison, showing very good agreement for IRMOF-1. The selectivity for Cu-BTC obtained by simulations show similar trends than the published one, but the deviation is larger than for IRMOF-1. The force field used in this work is less accurate for Cu-BTC than for IRMOF-1 and a very small deviation in the number of adsorbed molecules may result in a larger deviation in selectivity. The selectivity in Cu-BTC is the highest among the two adsorbents despite the deviations, suggesting that this structure is a potentially good candidate to separate CO_2 and CH_4.

The analysis of adsorption sites for the previous mixtures in Cu-BTC shows that at low pressures methane preferentially adsorbs in the octahedral cages displacing an important fraction of CO_2 molecules to the windows. At higher pressures and once the octahedral cages are full, site I' becomes
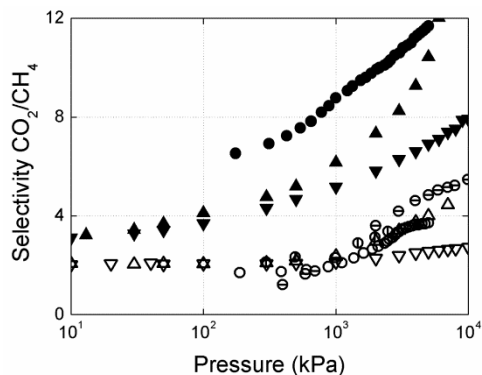
Figure 4. Selectivity for CO_2 from the equimolar and the 10:90 mixtures of CO_2 and methane in Cu-BTC (full symbols) and IRMOF-1 (empty symbols) at 298 K. Our simulation results (up triangles for the equimolar and down triangles for the 10:90 mixture) are compared with previous simulation data[22,23,26] (different style of circles) available only for the equimolar mixture.

the preferential adsorption site. The equilibrium snapshots are depicted in Figure 5. The sitting of methane and CO_2 molecules during adsorption of the binary mixture in IRMOF-1 shows the same trend as the pure components, being the large cages and the region that separates the large and the small cages the preferential adsorption sites. Appendix 1 contains movies taken directly from our simulations that illustrate the molecular sitting as a function of pressures, and tables summarizing the occupancies of the sites by the components of the mixtures at 298 K. (Tables A4 to A7 and Movie 3).

Figure 5. Adsorption of molecules in Cu-BTC at 2 kPa and 298 K. Snapshots were taken every 5000 steps in a simulation of one million MC steps, and all the molecules in them were plotted. Only the centre of mass of the molecules are drawn, CO_2 in red and methane in blue. (a) Pure CO_2, (b) pure methane, (c) 50:50 mixture CO_2/methane and (d) 10:90 mixture CO_2/methane.
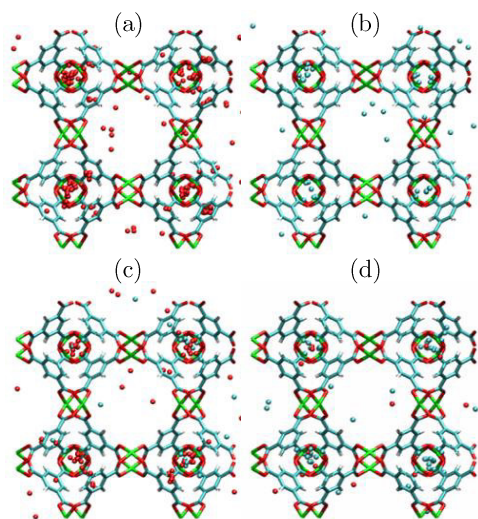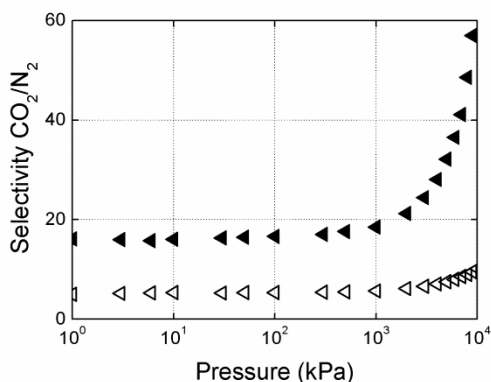

Figure 6. Selectivity for CO_2 from the 10:90 binary mixture of CO_2 and N_2 in Cu-BTC (full symbols) and IRMOF-1 (empty symbols) at 298 K.

Adsorption of CO_2 and N_2 binary mixtures

Figure 6 shows simulated adsorption selectivities for CO_2 relative to N_2 for the 10:90 CO_2/N_2 binary mixture in both structures. The complete excess adsorption isotherms can be found in Appendix 1 (Figure A7). Our results confirm a very strong preferential adsorption of CO_2 over N_2. This selectivity is much higher in Cu-BTC than in IRMOF-1 but the general trend is similar in the two materials and remains constant with pressure for the range that spans from 1 to 10^2 kPa. The selectivity of carbon dioxide from the binary mixture increases at higher pressures and this increase is sharper in Cu-BTC than in IRMOF-1. This can be attributed to the differences in structure. The pores of Cu-BTC are smaller than these of IRMOF-1, leading to stronger confinement effects for CO_2 and favouring its packing.

The analysis of the adsorption sites in Cu-BTC for this mixture shows competition for the octahedral cages. At low pressures, the order of preferential adsorption for carbon dioxide is site II > site III> site I', whereas for nitrogen is site I' > site II > site III. At the highest pressures the octahedral cages and the windows are already full increasing then the adsorption in the big cages (site I'). The sitting of CO_2 and N_2 in IRMOF-1 is similar to this for the pure components. The molecules preferentially adsorb in the large accessible cages and in the region that separates both types of cages and most of the molecules adsorbed close to the linkers are located above and beneath

Figure 8. Selectivity CO_2/CH_4 from the equimolar binary mixture (squares) and the 10:90 binary mixture (triangles) compared with the selectivity CO_2/CH_4 from the five components mixture (rhombus) in Cu-BTC (full symbols) and IRMOF-1 (empty symbols) at 298 K. The CO_2/CH_4 composition ratio in the bulk for the five components mixture is 1:95.

Figure 7. Excess adsorption for the 95:2.0:1.0:0.5:1.5 mixture of methane (black circles), ethane (red triangles), N_2 (green left triangles), CO_2 (pink rhombus) and propane (blue squares) in (a) Cu-BTC and (b) IRMOF-1 at 298 K.

the centre of the phenyl ring (see Tables A8 and A9 in Appendix 1).

Adsorption of the five-component mixture

Figure 7 shows the adsorption of a five-component mixture of methane, ethane, nitrogen, carbon dioxide and propane in Cu-BTC (Figure 7a) and IRMOF-1 (Figure 7b) at the bulk partial fugacity ratio of 95:2.0:1.5:1.0:0.5. The isotherms show similar adsorption for all components but methane in both MOFs. At high pressures the amount of methane adsorbed in IRMOF-1 is larger than in Cu-BTC since the cavities of the former are bigger than these of the latter. The selectivity between carbon dioxide and methane is similar to this of the corresponding binary systems as shown in Figure 8. Again carbon dioxide adsorption in Cu-BTC is much larger than in IRMOF-1, with a clearer increase with increasing pressure. This can be attributed to the combination of two effects; first, the electrostatic interactions between carbon dioxide and the framework - that enhances CO_2 adsorption in both structures - and second, the strong confinement effects in the octahedral cages of Cu-BTC - that enhances the selectivity of carbon dioxide in this structure.

The analysis of the adsorption sites in Cu-BTC and IRMOF-1 for this mixture was further performed and shows that the molecular sitting for the mixture is similar to this observed for the pure components in both structures. The detailed distribution is listed in Tables A10 and A11 in Appendix 1.

Conclusions

We have investigated the adsorption behaviour of the main components of natural gas in Cu-BTC and IRMOF-1 using Monte Carlo simulations. We computed adsorption isotherms at 298 K for pure components and mixtures, and analysed the preferential adsorption sites on these two MOFs. The detailed study of the sitting of the molecules in both structures provided an explanation for the high adsorption capacity of IRMOF-1 and for the high adsorption selectivity towards carbon dioxide of Cu-BTC. On the basis of our observations, IRMOF-1 seems a good material for the storage of the different components of natural gas, whereas Cu-BTC could be a promising material for their separation.

Bibliography

(1) Brasseur, G. P.; Orlando, J. J.; Tyndall, G. S. *Atmospheric Chemistry and Global Change*; University Press., 1999.
(2) Heinsohn, R. J.; Kabel, R. L.; Prentice Hall: 1999.
(3) Dybtsev, D. N.; Chun, H.; Yoon, S. H.; Kim, D.; Kim, K. *Journal of the American Chemical Society* **2004**, *126*, 32.

(4) Fletcher, A. J.; Cussen, E. J.; Bradshaw, D.; Rosseinsky, M. J.; Thomas, K. M. *Journal of the American Chemical Society* **2004**, *126*, 9750.
(5) Ohmori, O.; Kawano, M.; Fujita, M. *Angewandte Chemie-International Edition* **2005**, *44*, 1962.
(6) Pan, L.; Adams, K. M.; Hernandez, H. E.; Wang, X. T.; Zheng, C.; Hattori, Y.; Kaneko, K. *Journal of the American Chemical Society* **2003**, *125*, 3062.
(7) Rowsell, J. L. C.; Yaghi, O. M. *Microporous and Mesoporous Materials* **2004**, *73*, 3.
(8) Snurr, R. Q.; Hupp, J. T.; Nguyen, S. T. *Aiche Journal* **2004**, *50*, 1090.
(9) Yaghi, O. M.; O'Keeffe, M.; Ockwig, N. W.; Chae, H. K.; Eddaoudi, M.; Kim, J. *Nature* **2003**, *423*, 705.
(10) Fletcher, A. J.; Thomas, K. M.; Rosseinsky, M. J. *Journal of Solid State Chemistry* **2005**, *178*, 2491.
(11) Rowsell, J. L. C.; Yaghi, O. M. *Angewandte Chemie-International Edition* **2005**, *44*, 4670.
(12) Eddaoudi, M.; Kim, J.; Rosi, N.; Vodak, D.; Wachter, J.; O'Keeffe, M.; Yaghi, O. M. *Science* **2002**, *295*, 469.
(13) Li, H.; Eddaoudi, M.; O'Keeffe, M.; Yaghi, O. M. *Nature* **1999**, *402*, 276.
(14) Eddaoudi, M.; Li, H. L.; Yaghi, O. M. *Journal of the American Chemical Society* **2000**, *122*, 1391.
(15) Eddaoudi, M.; Moler, D. B.; Li, H. L.; Chen, B. L.; Reineke, T. M.; O'Keeffe, M.; Yaghi, O. M. *Accounts of Chemical Research* **2001**, *34*, 319.
(16) Chen, B. L.; Eddaoudi, M.; Hyde, S. T.; O'Keeffe, M.; Yaghi, O. M. *Science* **2001**, *291*, 1021.
(17) Wong-Foy, A. G.; Matzger, A. J.; Yaghi, O. M. *Journal of the American Chemical Society* **2006**, *128*, 3494.

(18) Duren, T.; Sarkisov, L.; Yaghi, O. M.; Snurr, R. Q. *Langmuir* **2004**, *20*, 2683.

(19) Pan, L.; Liu, H. M.; Lei, X. G.; Huang, X. Y.; Olson, D. H.; Turro, N. J.; Li, J. *Angewandte Chemie-International Edition* **2003**, *42*, 542.

(20) Lee, J. Y.; Pan, L.; Kelly, S. R.; Jagiello, J.; Emge, T. J.; Li, J. *Advanced Materials* **2005**, *17*, 2703.

(21) Wang, S.; Yang, Q. Y.; Zhong, C. L. *Separation and Purification Technology* **2008**, 30.

(22) Babarao, R.; Hu, Z. Q.; Jiang, J. W.; Chempath, S.; Sandler, S. I. *Langmuir* **2007**, *23*, 659.

(23) Keskin, S.; Sholl, D. S. *Journal of Physical Chemistry C* **2007**, *111*, 14055.

(24) Walton, K. S.; Millward, A. R.; Dubbeldam, D.; Frost, H.; Low, J. J.; Yaghi, O. M.; Snurr, R. Q. *Journal of the American Chemical Society* **2008**, *130*, 406.

(25) Yang, Q. Y.; Xue, C. Y.; Zhong, C. L.; Chen, J. F. *Aiche Journal* **2007**, *53*, 2832.

(26) Yang, Q. Y.; Zhong, C. L. *Journal of Physical Chemistry B* **2006**, *110*, 17776.

(27) Yang, Q. Y.; Zhong, C. L. *Chemphyschem* **2006**, *7*, 1417.

(28) Liu, J. C.; Culp, J. T.; Natesakhawat, S.; Bockrath, B. C.; Zande, B.; Sankar, S. G.; Garberoglio, G.; Johnson, J. K. *Journal of Physical Chemistry C* **2007**, *111*, 9305.

(29) Wang, Q. M.; Shen, D. M.; Bulow, M.; Lau, M. L.; Deng, S. G.; Fitch, F. R.; Lemcoff, N. O.; Semanscin, J. *Microporous and Mesoporous Materials* **2002**, *55*, 217.

(30) Zhou, W.; Wu, H.; Hartman, M. R.; Yildirim, T. *Journal of Physical Chemistry C* **2007**, *111*, 16131.

(31) Millward, A. R.; Yaghi, O. M. *Journal of the American Chemical Society* **2005**, *127*, 17998.

(32) Chui, S. S. Y.; Lo, S. M. F.; Charmant, J. P. H.; Orpen, A. G.; Williams, I. D. *Science* **1999**, *283*, 1148.

(33) Beerdsen, E.; Smit, B.; Calero, S. *J. Phys. Chem. B* **2002**, *106*, 10659.

(34) Krishna, R.; Smit, B.; Calero, S. *Chem. Soc. Rev.* **2002**, *31*, 185.

(35) Duren, T.; Snurr, R. Q. *Journal of Physical Chemistry B* **2004**, *108*, 15703.

(36) Martin, M. G.; Siepmann, J. I. *J. Phys. Chem. B* **1998**, *102*, 2569.

(37) Harris, J. G.; Yung, K. H. *Journal of Physical Chemistry* **1995**, *99*, 12021.

(38) Murthy, C. S.; Singer, K.; Klein, M. L.; McDonald, I. R. *Molecular Physics* **1980**, *41*, 1387.

(39) Garcia-Perez, E.; Parra, J. B.; Ania, C. O.; Garcia-Sanchez, A.; Van Baten, J. M.; Krishna, R.; Dubbeldam, D.; Calero, S. *Adsorption-Journal of the International Adsorption Society* **2007**, *13*, 469.

(40) Dubbeldam, D.; Calero, S.; Vlugt, T. J. H.; Krishna, R.; Maesen, T. L. M.; Beerdsen, E.; Smit, B. *Physical Review Letters* **2004**, *93*, 088302.

(41) Dubbeldam, D.; Calero, S.; Vlugt, T. J. H.; Krishna, R.; Maesen, T. L. M.; Smit, B. *Journal of Physical Chemistry B* **2004**, *108*, 12301.

(42) Mayo, S. L.; Olafson, B. D.; Goddard, W. A. *Journal of Physical Chemistry* **1990**, *94*, 8897.

(43) Rappe, A. K.; Casewit, C. J.; Colwell, K. S.; Goddard, W. A.; Skiff, W. M. *Journal of the American Chemical Society* **1992**, *114*, 10024.

(44) Dubbeldam, D.; Walton, K. S.; Ellis, D. E.; Snurr, R. Q. *Angewandte Chemie-International Edition* **2007**, *46*, 4496.

(45) Calero, S.; Lobato, M. D.; Garcia-Perez, E.; Mejias, J. A.; Lago, S.; Vlugt, T. J. H.; Maesen, T. L. M.; Smit, B.; Dubbeldam, D. *Journal of Physical Chemistry B* **2006**, *110*, 5838.

(46) Rowsell, J. L. C.; Spencer, E. C.; Eckert, J.; Howard, J. A. K.; Yaghi, O. M. *Science* **2005**, *309*, 1350.

(47) Dubbeldam, D.; Frost, H.; Walton, K. S.; Snurr, R. Q. *Fluid Phase Equilibria* **2007**, *261*, 152.

(48) Garberoglio, G.; Skoulidas, A. I.; Johnson, J. K. *Journal of Physical Chemistry B* **2005**, *109*, 13094.

(49) Jiang, J. W.; Sandler, S. I. *Langmuir* **2006**, *22*, 5702.

(50) Skoulidas, A. I.; Sholl, D. S. *Journal of Physical Chemistry B* **2005**, *109*, 15760.

(51) Krishna, R.; Calero, S.; Smit, B. *Chem. Eng. J.* **2002**, *88*, 81.

(52) Yang, Q. Y.; Zhong, C. L.; Chen, J. F. *Journal of Physical Chemistry C* **2008**, *112*, 1562.

(53) Liu, Y.; Brown, C. M.; Neumann, D. A.; Peterson, V. K.; Kepert, C. J. *Journal of Alloys and Compounds* **2007**, *446*, 385.

On the Performance of Cu-BTC Metal-Organic Framework for Carbon Tetrachloride Gas Removal

Sofía Calero, Ana Martín-Calvo, Said Hamad
and Elena García-Pérez

3

The performance of Cu-BTC metal-organic framework for carbon tetrachloride removal from air has been studied using molecular simulations. According to our results, this material shows extremely high adsorption selectivity in favour of carbon tetrachloride. We demonstrate that this selectivity can be further enhanced by selective blockage of the framework.

1. Introduction

Carbon tetrachloride had extensive industrial applications in the early 20th century, but it was phased out in the 2nd Montreal Protocol's revision in 1992 due to its adverse health effects. However, still today we find significant concentrations of carbon tetrachloride on air since it is being involved in current industrial processes either for the lack of replacements or as undesirable by-products of other reactions. For this reason it is interesting to explore the possibilities to reduce the amount of carbon tetrachloride being released into the environment. Several recent reviews have reported the use of metal-organic frameworks (MOFs) for treatment and remediation of pollutants and greenhouse gases in the environment[1-5]. MOFs are a new class of highly porous crystalline materials formed by metal-oxide units that are joined by organic linkers through strong covalent bonds[6-8].

Selective adsorption based mainly on the molecular sieving effect has been confirmed in several MOFs. Among them, with large surface area and high thermal stability, copper benzene tricarboxylate ($Cu_3 (BTC)_2$ or Cu-BTC) has great potential as adsorbent in industrial applications. In particular, this MOF has been suggested as useful for carbon dioxide capture and separation[9,10], removal of tetrahydrothiophene odorant from natural gas[5], or for the separation of polar components from nonpolar gases[11].

Although application of Cu-BTC to gas separation and to high-density gas storage is being widely studied[2-5], no work has been undertaken to analyse its capacity for carbon tetrachloride separation from air. Here we report a series of simulation studies that establish benchmark for adsorption capacity in Cu-BTC across carbon tetrachloride and main air-component gases. These studies will serve to evaluate the potential of Cu-BTC as a

material to be used in end-of-pipe technologies, especially for those processes in which clean technologies cannot be directly applied. Furthermore, they will provide insights into the properties of Cu-BTC that could make it most suited for this type of processes.

Cu-BTC was first reported in 1999 and named HKUST-1[12]. Its framework is composed of dimeric cupric tricarboxylate units with a short Cu-Cu inter-nuclear separation. Each metal completes its pseudo-octahedral coordination sphere with an axial water ligand opposite to the Cu-Cu vector[13]. After removing water from the framework, it becomes an open three-dimensional porous structure with main channels of a square cross-section of about 9 Å diameter and tetrahedral side pockets of about 5 Å, which are connected to the main channels by triangular windows of about 3.5 Å in diameter. In this study we analyse adsorption based on four preferential sites. Site I, in the largest cavity close to the copper atoms, site II, at the center of the octahedral cages and site III, at the windows that communicate the octahedral cages and the main cavities. These sites were identified by Liu *et al.* [14] for hydrogen adsorption. Most recently García-Pérez *et al.*[15], have identified an additional adsorption site, site I´, which is located at the center of the main cavities.

2. Simulation methods and models

The computed adsorption isotherms were obtained from grand canonical Monte Carlo simulations. Pressure was transformed into fugacity using the Peng-Robinson equation of state. Henry coefficients and energies of adsorption were computed using Monte Carlo in the NVT ensemble at 298 K. Detailed information about these methods can be found elsewhere[15]. Cu-BTC was modelled as a rigid structure with Lennard-Jones parameters taken from DREIDING force field[24] except these for Cu that were taken from the UFF force field[25]. Atomic charges were taken from reference 26 and Lorentz-Berthelot mixing rules were used to calculate mixed Lennard-Jones parameters. One unit cell of Cu-BTC (a = b = c = 26.343 Å) was used in our simulations. We obtained a helium void fraction of 0.76. The interactions between guest molecules (Ar, N_2, O_2 and CCl_4) with Cu-BTC host framework are modelled by Lennard-Jones and Coulombic potentials. The Coulombic interactions in the system were calculated with Ewald summations. The Lennard-Jones potential was cut and shifted with the cut-off distance set to 12 Å. Adsorbates were considered as rigid molecules. For Ar, N_2 and O_2 we used models and potentials that have been successfully employed to describe the adsorption in Cu-BTC[10,15]. The Lennard-Jones parameters for Ar, O_2, N_2 and CCl_4 were fitted to reproduce the vapour-liquid equilibrium curve. Table 1 in Appendix 2 collects the charges and intermolecular parameters used in this work.

3. Results

We used grand canonical Monte Carlo simulations to compute single and multicomponent adsorption for carbon tetrachloride, argon, nitrogen and oxygen at 298 K. The obtained isotherms for single argon, nitrogen and oxygen are in very good agreement with available experimental and simulation data[10,15-23] as shown in Figure 1. The special arrangement of channels in MOF Cu-BTC together with open metal ligand sites offers a dual type sorption behaviour for these three molecules. Analysis of the occupancies of the individual adsorption sites indicates that argon adsorbs preferentially in the same sites as nitrogen and oxygen, i.e. in the octahedral cages (site II), in the big cages (site I') and in a lower extent in the windows of the octahedral cages (site III). As previously observed for nitrogen and oxygen[15], Site I remains empty over the entire range of pressures that we have analysed for argon. The computed adsorption isotherm for carbon tetrachloride shows a steep curve that might be attributed to condensation in the Cu-BTC pores (Figure 1, inset). The obtained saturation value corresponds to 60 molecules of carbon tetrachloride per unit cell, all of them adsorbed in the main channels. To our knowledge, neither single nor multicomponent adsorption data involving carbon tetrachloride in Cu-BTC have been previously reported.

Some insights into the adsorption mechanism in Cu-BTC can be gleaned by observing the average occupation
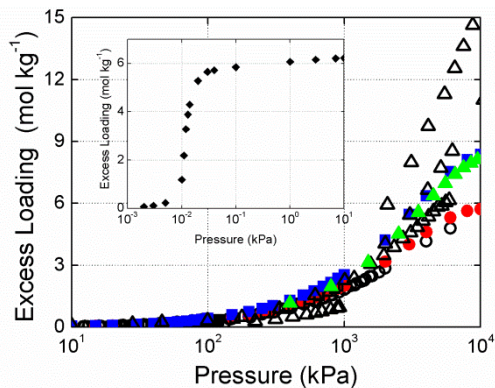
Figure 1. Comparison of simulated and previous adsorption isotherms of N$_2$ (circles), O$_2$ (squares) and argon (triangles) in Cu-BTC at 298 K. Our simulation results are represented by full symbols and available previous data[10, 15-23] by empty symbols. Absolute adsorption was converted to excess adsorption[24,25] for comparison with experimental values. Inset figure provides the computed adsorption isotherm of CCl$_4$ at 298 K.

profiles for the adsorbed molecules. The profiles for carbon tetrachloride (Figure 2) confirm that the preferential adsorption sites for this molecule are the big cages. At low pressures the molecule adsorbs preferentially in the centre of the big cages (site I'). However, at medium and high pressures the average occupation profiles reveal an additional site at the big cages, blocking the access to the windows that communicate these cages with the octahedral pockets. Direct comparison of these profiles with the ones obtained for oxygen, nitrogen, and argon, show reverse adsorption trends for the latter. These three types of molecules firstly adsorb in the octahedral cages, once they are filled they adsorb in the windows and finally they populate the big cages.
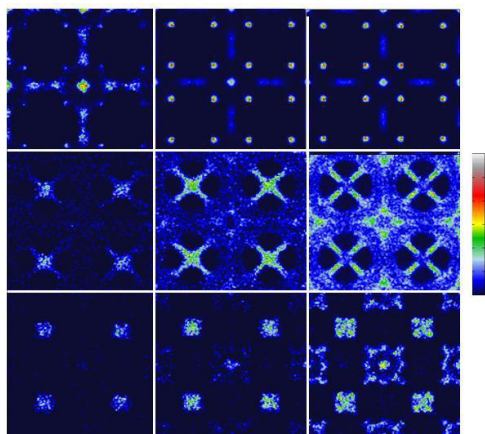
Figure 2. Average occupation profiles in Cu-BTC obtained (from left to right) at low, medium and high pressures for single carbon tetrachloride adsorption (top), single oxygen adsorption (middle) and oxygen in the $O_2/N_2/Ar/CCl_4$ mixture at a bulk partial fugacity ratio of 20.979 : 77.922 : 0.999 : 0.1 (bottom). The figure shows the average values of the projections of the centre of mass coordinates over the x-y plane. Due to the cubic symmetry of Cu-BTC, the profile projected over the x-y plane is the same than the profiles obtained projecting the coordinates over the x-z and y-z planes. The relation between colour and occupation is shown in the bar situated on right side of the figure. The same colour gradation (from dark blue to white) is employed in all figures, although the total number of molecules present in the unit cell is different for each calculation.

The adsorption isotherms in Cu-BT for a four component mixture of oxygen, nitrogen, argon and carbon tetrachloride were also computed at 298 K (see Appendix 2). To mimic a sample of air containing carbon tetrachloride as contaminant the following composition was used for the mixture: 20.979% O_2, 77.922% N_2, 0.999% Ar and 0.1% CCl_4. While the average occupation profiles

for carbon tetrachloride obtained from the mixture are very similar to these obtained for the single component, we found important differences for oxygen, nitrogen and argon. Figure 2 compares the average occupation profiles for oxygen as single component and in the multicomponent mixture. Nitrogen follows the same filling sequence as oxygen and for the four component mixture; argon adsorption in Cu-BTC is negligible.

In the multicomponent mixture, the adsorption of oxygen, nitrogen and argon are highly influenced by the presence of carbon tetrachloride adsorbing only in the sites that are not occupied by the latter. This combined with the very low mole fraction of argon in the mixture lead to negligible adsorption of this component in Cu-BTC. As for oxygen and nitrogen, the main differences in adsorption are found at the windows that communicate the octahedral cages with the main cages (now blocked by carbon tetrachloride molecules) and also at the main cages (now filled with carbon tetrachloride molecules).

The self-diffusion coefficients for the different components of the quaternary mixture were computed by taking the slope of the mean-squared displacement at long times. Calculations were performed for the molecular loading obtained at 1000 kPa and 298 K. i.e. 3 molecules of oxygen, 7 molecules of nitrogen, 0 molecules of argon and 59 molecules of carbon tetrachloride per unit cell. At 298 K the diffusion of 3 molecules of oxygen per unit cell (1.38 $\pm$ 0.02 10^{-8} m^2/s) is lower than the
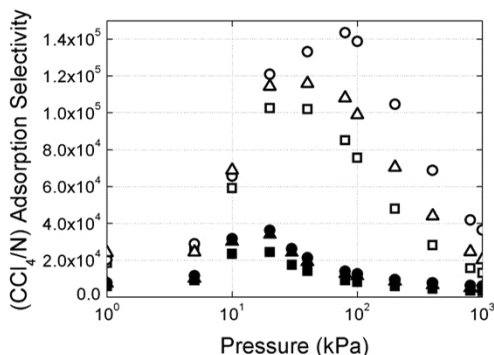
Figure 3. Adsorption selectivity of carbon tetrachloride over the different components of air at 298 K. The adsorption selectivity is defined as $[x_{CCl4} / y_{CCl4}] / [x_N / y_N]$, where x_i are the molar fractions in the adsorbed phase, y_i the molar fractions in the bulk phase and N indicates O_2 (squares), N_2 (circles) or Ar (triangles). The selectivity was obtained for the Cu-BTC structure with (empty symbols) and without (full symbols) selective blockage of the octahedral cages.

diffusion obtained for the 7 molecules of nitrogen ($1.91 \pm 0.04 \ 10^{-8} \ m^2/s$). This behaviour reverses in the quaternary mixture, though the diffusion coefficients for the two components slow down by three orders of magnitude. The computed diffusion for oxygen and nitrogen in the quaternary mixture is $4.0 \pm 0.1 \ 10^{-11} \ m^2/s$ and $1.6 \pm 0.1 \ 10^{-11} \ m^2/s$, respectively.

The slopes of the mean-squared displacements obtained for the 59 molecules of carbon tetrachloride at long times were almost zero, indicating very low self-diffusivity values for this molecule compared with the other two components.

Based on the differences on preferential adsorption sites for carbon tetrachloride

and air components, fine-tuning of the framework could be achieved for optimizing separation capacities. Hence, selective blockage of the octahedral pockets leads to extremely high adsorption selectivity in favour of carbon tetrachloride, as shown in Figure 3.

Conclusions

We conclude this work by highlighting that an effective adsorption material with long term viability in pollutants removal should combine (1) periodicity in the structure and (2) flexibility to achieve chemical functionalisation and fine-tuning at a molecular level. Based on these properties, our results provide evidence of the Cu-BTC efficiency in carbon tetrachloride removal from air. We demonstrate that this efficacy can be further enhanced by selective blockage of the framework. Many technological processes require pollutants capture from air. Our results open an area of investigation in the field and indicate the potential of Cu-BTC metal-organic framework to complement and eventually replace other materials as dynamic adsorption media.

Bibliography

(1) Britt, D.; Tranchemontagne, D.; Yaghi, O. M. *Proceedings of the National Academy of Sciences of the United States of America* **2008**, *105*, 11623.
(2) Czaja, A. U.; Trukhan, N.; Muller, U. *Chemical Society Reviews* **2009**, *38*, 1284.

(3) Li, J. R.; Kuppler, R. J.; Zhou, H. C. *Chemical Society Reviews* **2009**, *38*, 1477.

(4) Ma, S. Q.; Zhou, H. C. *Chemical Communications* **2010**, *46*, 44.

(5) Mueller, U.; Schubert, M.; Teich, F.; Puetter, H.; Schierle-Arndt, K.; Pastre, J. *Journal of Materials Chemistry* **2006**, *16*, 626.

(6) Li, H.; Eddaoudi, M.; O'Keeffe, M.; Yaghi, O. M. *Nature* **1999**, *402*, 276.

(7) Yaghi, O. M.; O'Keeffe, M.; Ockwig, N. W.; Chae, H. K.; Eddaoudi, M.; Kim, J. *Nature* **2003**, *423*, 705.

(8) Eddaoudi, M.; Li, H. L.; Yaghi, O. M. *Journal of the American Chemical Society* **2000**, *122*, 1391.

(9) Cavenati, S.; Grande, C. A.; Rodrigues, A. E. *Industrial & Engineering Chemistry Research* **2008**, *47*, 6333.

(10) Martin-Calvo, A.; Garcia-Perez, E.; Castillo, J. M.; Calero, S. *Physical Chemistry Chemical Physics* **2008**, *10*, 7085.

(11) Castillo, J. M.; Vlugt, T. J. H.; Calero, S. *Journal of Physical Chemistry C* **2008**, *112*, 15934.

(12) Chui, S. S. Y.; Lo, S. M. F.; Charmant, J. P. H.; Orpen, A. G.; Williams, I. D. *Science* **1999**, *283*, 1148.

(13) Prestipino, C.; Regli, L.; Vitillo, J. G.; Bonino, F.; Damin, A.; Lamberti, C.; Zecchina, A.; Solari, P. L.; Kongshaug, K. O.; Bordiga, S. *Chem. Mat.* **2006**, *18*, 1337.

(14) Liu, Y.; Brown, C. M.; Neumann, D. A.; Peterson, V. K.; Kepert, C. J. *Journal of Alloys and Compounds* **2007**, *446*, 385.

(15) Garcia-Perez, E.; Gascon, J.; Morales-Florez, V.; Castillo, J. M.; Kapteijn, F.; Calero, S. *Langmuir* **2009**, *25*, 1725.

(16) Liu, J. C.; Culp, J. T.; Natesakhawat, S.; Bockrath, B. C.; Zande, B.; Sankar, S. G.; Garberoglio, G.; Johnson, J. K. *Journal of Physical Chemistry C* **2007**, *111*, 9305.

(17) Chowdhury, P.; Bikkina, C.; Meister, D.; Dreisbach, F.; Gumma, S. *Microporous and Mesoporous Materials* **2009**, *117*, 406.

(18) Garberoglio, G.; Skoulidas, A. I.; Johnson, J. K. *Journal of Physical Chemistry B* **2005**, *109*, 13094.

(19) Karra, J. R.; Walton, K. S. *Langmuir* **2008**, *24*, 8620.

(20) Skoulidas, A. I. *Journal of the American Chemical Society* **2004**, *126*, 1356.

(21) Skoulidas, A. I.; Sholl, D. S. *Journal of Physical Chemistry B* **2005**, *109*, 15760.

(22) Wang, Q. M.; Shen, D. M.; Bulow, M.; Lau, M. L.; Deng, S. G.; Fitch, F. R.; Lemcoff, N. O.; Semanscin, J. *Microporous and Mesoporous Materials* **2002**, *55*, 217.

(23) Yang, Q. Y.; Xue, C. Y.; Zhong, C. L.; Chen, J. F. *Aiche Journal* **2007**, *53*, 2832.

(24) Mayo, S. L.; Olafson, B. D.; Goddard, W. A. *Journal of Physical Chemistry* **1990**, *94*, 8897.

(25) Rappe, A. K.; Casewit, C. J.; Colwell, K. S.; Goddard, W. A.; Skiff, W. M. *Journal of the American Chemical Society* **1992**, *114*, 10024.

(26) Farrusseng, D.; Daniel, C.; Gaudillere, C.; Ravon, U.; Schuurman, Y.; Mirodatos, C.; Dubbeldam, D.; Frost, H.; Snurr, R. Q. *Langmuir* **2009**, *25*, 7383.

Effect of Air Humidity on the Removal of Carbon Tetrachloride from Air Using Cu-BTC Metal-Organic Framework

Ana Martín-Calvo, Elena García-Pérez, Almudena García-Sánchez, Rocío Bueno-Pérez, Said Hamad and Sofía Calero

4

We have used interatomic potential-based simulations to study the removal of carbon tetrachloride from air at 298 K, using Cu-BTC metal-organic framework. We have developed new sets of Lennard-Jones parameters that accurately describe the vapour-liquid equilibrium curves of carbon tetrachloride and the main components from air (oxygen, nitrogen and argon). Using these parameters we performed Monte Carlo simulations for the following systems: a) single component adsorption of carbon tetrachloride, oxygen, nitrogen and argon molecules, b) binary Ar/CCl_4, O_2/CCl_4 and N_2/CCl_4 mixtures with bulk gas compositions 99:1 and 99.9:0.1, c) ternary $O_2/N_2/Ar$ mixtures with both, equimolar and 21:78:1 bulk gas composition, d) quaternary mixture formed by 0.1% of CCl_4 pollutant, 20.979% O_2, 77.922% N_2 and 0.999% Ar and e) five-component mixtures corresponding to 0.1% of CCl_4 pollutant in air with relative humidity ranging from 0 to 100%. Carbon tetrachloride adsorption selectivity, self-diffusivity and preferential sitting of the different molecules in the structure are studied for all the systems.

1. Introduction

Carbon tetrachloride was originally synthesised in 1839 by reaction of chloroform with chlorine. In the early 20th century, it had extensive applications as dry cleaning solvent, lava lamps, fire extinguishers, refrigerants and pesticides. Some years later, it was proved that the exposure to carbon tetrachloride had several adverse health effects. The exposure to a high concentration of CCl_4 affects both the liver and kidneys, which can lead to a coma and even death, after prolonged exposure. In addition, carbon tetrachloride plays a role in ozone depletion and in the greenhouse effect. For all these reasons, carbon tetrachloride was phased out in the 2nd Montreal Protocol's revision in 1992. However the main problem is the half life time of carbon tetrachloride, between 30 and 100 years. This coupled with many industries which continue using this molecule due to the lack of replacements, or that appears as a by-product of other reactions, explains why today we still find significant concentrations of carbon tetrachloride on air.

An optimal material able to remove carbon tetrachloride from air would be a very good starting point for a new generation of materials that could be employed, not only for the removal of this substance but also for the removal of other halogenated hydrocarbons with

similar physical and/or chemical properties.

Metal-organic frameworks (MOFs) are a relatively new class of highly porous crystalline materials, formed by metal-oxide units which are joined by organic linkers through strong covalent bonds[1]. Several recent reviews have reported the use of MOFs for treatment and remediation of pollutants and greenhouse gases in the environment[2-4]. Selective adsorption based mainly on differences in affinities has also been confirmed for some of these materials[4-12]. In particular, Cu-BTC is one of the most promising MOFs for selective adsorption. This MOF is being studied as a molecular sieve to separate the main compounds from gasoline by selective adsorption[13-17] and also as a porous structure to be used in environmental processes related to the capture and sequestration of carbon dioxide and to its removal from flue gas and natural gas[6-8,18-20]. Nowadays, there is a growing interest on studying the separation properties of Cu-BTC from mixtures such as CO_2/CH_4, $CO_2/CH_4/H_2$, CH_4/C_2H_6, CO_2/C_2H_6, C_2H_6/C_2H_4, C_3H_8/C_3H_6, CO_2/N_2, CH_4/N_2, CO_2/CO and it has been found that Cu-BTC is a potentially good material for their separation due to the presence of accessible side pockets on its structure[8,21-24]. The application of Cu-BTC to purify air effectively[25] (removing carbon monoxide and nitrous oxide), to purify low-sulphur gasoline and diesel fuels[26] (removing SO_x) and, to remove ammonia vapours[27] has also been investigated. To our knowledge, there are no experimental data available about molecular diffusivities in Cu-BTC

and there are only a few molecular simulation studies on the diffusion processes within the Cu-BTC structure. On these studies the authors use atomistic simulations to investigate the effect of Cu-BTC structure on the separation of light gas mixtures, determining the self-, corrected- and transport- diffusivities as a function of pore size. Previous works show that the diffusion coefficients of molecules in Cu-BTC are similar in magnitude to the analogous diffusion coefficients in zeolites[12][28-31]. Recently we demonstrated that adsorption selectivity in favour of carbon tetrachloride can be further enhanced by selective blockage of the Cu-BTC framework[12]. This short communication is to date the only work that analyses the capacity of Cu-BTC to separate carbon tetrachloride from air. The aim of this work is to cover the gap with an extensive simulation study, which provides a detailed analysis on the adsorption, diffusion and separation of carbon tetrachloride from dry and humid air, using Cu-BTC.

The structure Cu-BTC, also known as HKUST-1, was first reported in 1999 by Chiu *et al.*[32]. The structure is characterised by metal cores consisting of copper atoms, bounded by organic ligands 1,3,5-benzenetricarboxilate (BTC). This creates a three-dimensional network in which one can distinguish main channels of 9 Å in diameter in the centre of the structure and next to them 5 Å side octahedron. These side cavities are communicated with the central cage through a triangular window of 3.5 Å of diameter. To perform molecular simulations, the structure is replicated periodically in space. Figure 1a shows a

scheme of the unit cell used, which is cubic with a side length of 26.343 Å. The framework is composed of copper, oxygen, hydrogen and carbon atoms, as shown in Figure 1b. The carbon atoms are classified in three types: C_a, which are linked to another carbon atom, C_b, which binds to oxygen atoms and C_c, which binds to hydrogen atoms. On previous studies of hydrogen adsorption[33] and with a similar method reported for zeolites in the location and occupation of ions [34], there have been identified three characteristics sites of adsorption in Cu-BTC. Site I, which is located in areas close to the copper atoms, site II, located at the centre of the octahedral frames and site III, at the windows that communicate the octahedron with the central cavity. Most recently we have identified an additional adsorption site, site I´, which is located at the centre of the largest cages[5,9]. Based on these studies we have considered the four preferential sites of adsorption in Cu-BTC that are depicted

in Figure 1c.

In this work we use Monte Carlo and Molecular Dynamics simulations to study adsorption and diffusion of oxygen, nitrogen, argon and carbon tetrachloride molecules as pure components and mixtures in Cu-BTC. The adsorption selectivity of carbon tetrachloride is also analysed for air with relative humidity ranging from 0 to 100%. Firstly, we provide accurate sets of Lennard-Jones parameters that we fitted to reproduce the experimental vapour-liquid equilibrium curves of all molecules under study except these for argon and water, which have been previously reported[9,35]. Secondly we analyse the computed adsorption isotherms, Henry coefficients, energies and entropies of adsorption for these molecules, comparing our results with previous available data. Thirdly we discuss the preferential sites of adsorption and the adsorption selectivity obtained for the different systems. The differences observed on
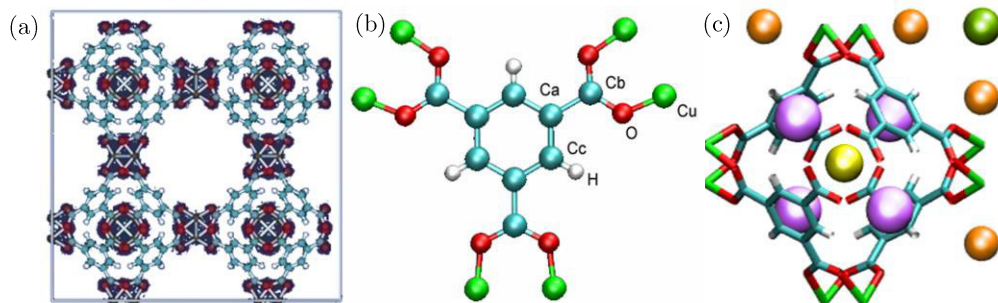
Figure 1. (a) Cu–BTC structure in which are represented in red the oxygen atoms, in brown the copper atoms, hydrogen atoms are represented in white and in blue the carbon atoms; (b) detailed classification of the atoms from the Cu–BTC structure. Copper atoms (Cu) are represented in green, oxygen atoms (O) in red, hydrogen atoms (H) in grey and light blue is for the carbon atoms (C_a, C_b and C_c); (c) diagram with the location of the preferential adsorption sites in Cu–BTC considered in this work. Site I is represented in orange (near to copper), site I´ in green (centre of big cage), site II in yellow (centre of octahedral cage) and site III in purple (windows).

the self-diffusion of carbon tetrachloride in Cu-BTC as pure component and as part of a multi-component mixture are also discussed. Finally we present some concluding remarks.

2. Simulation methods and models

Cu-BTC was modelled as a rigid framework with a = b = c = 26.343 Å. The computed helium void fraction is 0.76 and the obtained pore volume 13871.816 Å^3 per unit cell. We additionally computed the surface areas with the molecules under study. Lennard-Jones parameters for the Cu-BTC atoms were taken from DREIDING generic force field[36], except these of copper, which were taken from UFF force field[37]. The Lennard-Jones potential was cut and shifted with the cut-off distance set to 12 Å.

In this work we compute pure adsorption isotherms and mixtures containing carbon tetrachloride, argon, oxygen, nitrogen and water. The adsorption of carbon tetrachloride and argon (modelled as non-charged molecules) is not affected by the set of point charges used for Cu-BTC. Oxygen and nitrogen are modelled with point charges to reproduce their quadrupole moment, but their dipole moment is zero Therefore they are not very sensitive to the set of charges either[5,8]. The adsorption of polar molecules such as water is very sensitive to the set of charges used for the structure[9,38-41]. The influence of the atomic charges of Cu-BTC on the adsorption of water was examined in detail in reference 9. This work reported that water adsorption

was extremely selective to the set of charges used and differences lower than 6% in the charge values could lead to adsorption values up to 600 times lower than the experimental data. Based on these findings we selected the set of charges that, according to reference 9, provides the best agreement with experimental values of water adsorption on Cu-BTC. The computed surface areas and the parameters used for Cu-BTC are compiled in Appendix 3 (Tables A1 and A2). The adsorbates were considered as rigid molecules. The molecule of oxygen is modelled as two oxygen atoms at a distance of 1.2 Å. To reproduce the molecular quadrupole moment of 0.39 DÅ[42], we placed a negative point charge of -0.112 e$^-$ in each oxygen atom and a positive point charge of 0.224 e$^-$ at the centre of mass of the molecule. Nitrogen is modelled as two nitrogen atoms, separated by a distance of 1.1 Å[43] and negative point charges of -0.405 e$^-$, which are offset by a positive point charge 0.810 e$^-$ located at the centre of mass of the molecule. Using this model we obtain a molecular quadrupole moment of 1.17 DÅ that is very similar to the previously reported value 1.2 DÅ[43]. Argon and carbon tetrachloride were defined as single interaction centres and for water we used the Tip5pEw model that was parameterized for use with the Ewald summation method[9,44].

Table 1. Point charges, initial[47–49,59] and final sets of Lennard-Jones parameters used for oxygen, nitrogen, argon and carbon tetrachloride molecules.

Adsorbed molecules

Atoms	Charge (e-)	Initial Set		Final Set	
		ε/k_B (K)	σ (Å)	ε/k_B (K)	σ (Å)
O (O$_2$)	-0.112	44.500	3.090	53.023	3.045
Dummy (O$_2$)	0.224	-	-	-	-
N (N$_2$)	-0.405	36.400	3.318	38.298	3.306
Dummy (N$_2$)	0.810	-	-	-	-
Ar	-	124.070	3.420	124.070	3.380
CCl$_4$	-	424.730	5.240	519.730	5.140

Previous works reported the importance of reproducing the experimental vapour-liquid equilibrium curve in order to accurately perform adsorption studies[5,34,45,46]. For this reason we refitted available Lennard-Jones parameters for oxygen[47], nitrogen[48] and carbon tetrachloride[49] molecules to the experimental vapour-liquid equilibrium curves, obtaining the new sets of parameters listed in Table 1. For argon we took the parameters from reference 35. The vapour-liquid equilibrium curves were computed using Gibbs ensemble Monte Carlo and the obtained results are compared with the experimental values[50], as shown in Figure 2.
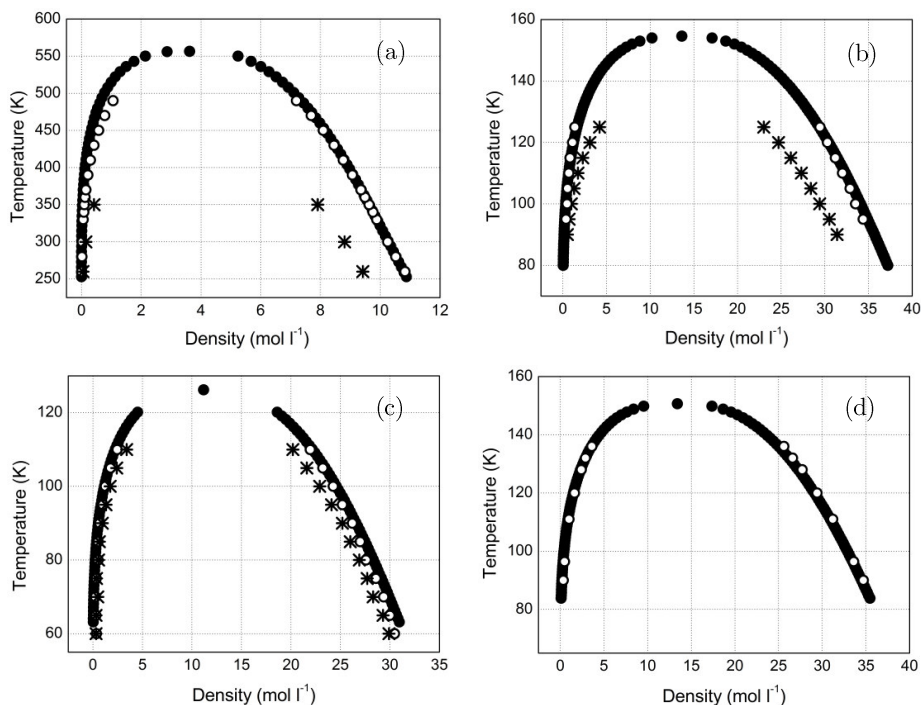
Figure 2. Experimental and computed vapour-liquid equilibrium curves for (a) carbon tetrachloride, (b) oxygen, (c) nitrogen and (d) argon. Experimental values[50] are represented by full circles. The computed data obtained with the initial set of parameters and with the new set of parameters are plotted by asterisks and empty symbols, respectively. The error bars are within the symbol size.
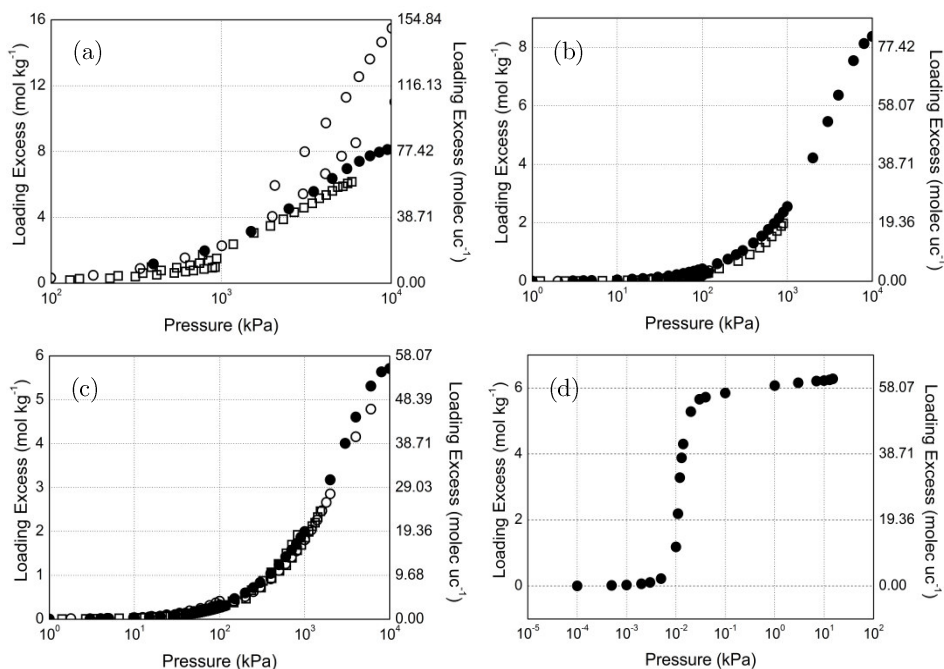
Figure 3. Computed adsorption isotherms of (a) argon, (b) oxygen, (c) nitrogen and (d) carbon tetrachloride in Cu–BTC at 298 K. Our simulation data (full circles) are compared with available experimental[5,52–55](empty squares) and simulation data [5,29,30,53,54,56,57] (empty circles). The error bars are within the symbol size.

The interactions of adsorbed molecules with other adsorbates and the Cu-BTC framework are modelled by Lennard-Jones and Coulombic potentials. For the adsorbate-adsorbent interactions, we used Lorentz-Berthelot mixing rules. The computed adsorption isotherms were obtained from grand canonical Monte Carlo simulations. Pressure was transformed into fugacity using the Peng-Robinson equation of state. Henry coefficients and energies of adsorption were computed using Monte Carlo in the NVT ensemble at 298 K. Self-diffusion coefficients for the different components and mixtures were computed by calculating the slope of the mean-squared displacement at long

times. Detailed information about these methods can be found elsewhere[5,51].

3. Results

We report a simulation study of carbon tetrachloride removal from air using Cu-BTC metal-organic framework. Below, we discuss the obtained results that are divided into five sections: adsorption of single components, adsorption of binary and ternary mixtures, adsorption of quaternary mixtures, adsorption of five-component mixtures and self-diffusivities.

Adsorption of single components

Figure 3 shows the computed adsorption isotherms for argon (a), oxygen (b),

nitrogen (c) and carbon tetrachloride (d) molecules in Cu-BTC at 298 K. The results obtained for the first three molecules are in agreement with previous experimental [5,52-55] and simulation data [5,29,30,53,54,56,57]. The adsorption isotherm for carbon tetrachloride was computed for a range of pressure that spans from 10^{-4} to 10^2 kPa. To our knowledge there are not experimental values reported in the literature for comparison. The adsorption isotherm obtained for carbon tetrachloride (Figure 3d) shows a deep rise at 10^{-2} kPa, which might be attributed to clustering in the Cu-BTC pores[58]. We found saturation at about 60 carbon tetrachloride molecules per unit cell. Figure 4 depicts the average occupation profiles obtained for the single components in the low, medium and high pressure regimens. These profiles are obtained from the average values (averaged over the whole number of configurations of the simulations) of the projections of the centre of mass coordinates over the x-y plane. The relation between colour and occupation is shown in the bar situated at the bottom of the figure. It is worth noting that, due to the symmetry of the system, the profile over the x-y plane is the same than the profiles obtained projecting the coordinates over the x-z or y-z planes. The average occupation profiles obtained for carbon tetrachloride verify that the octahedral cages are not accessible to carbon tetrachloride. At low pressures, this component is preferentially adsorbed in the centre of the big cages (site I´). However, at medium and high pressures we identify an additional site at the big cages, blocking the access to the
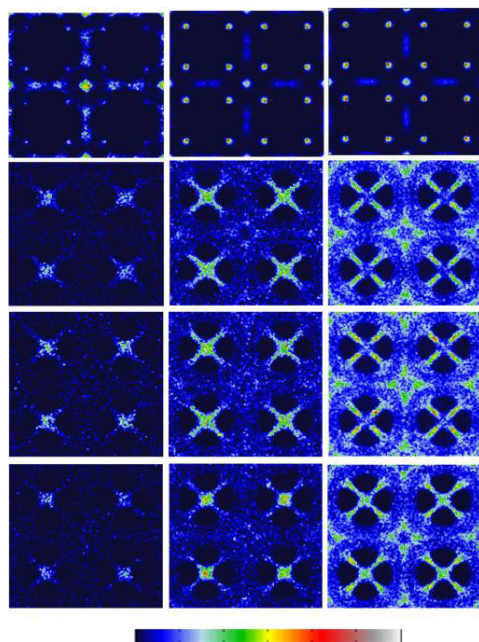
Figure 4. Average occupation profiles in Cu–BTC obtained (from left to right) at low, medium and high pressures for (from top to bottom) carbon tetrachloride, oxygen, argon and nitrogen as pure components at 298 K. The same colour gradation (from dark to light) is employed in all figures, although the total number of molecules present in the unit cell is different for each calculation.

windows that communicate these cages with the octahedral pockets (site III). The average occupation profiles for oxygen and argon show that the preferential adsorption sites in both cases are: site II, at low pressures, sites II and III at intermediate pressures and sites III and I´ at high pressures. Nitrogen follows similar behaviour than oxygen and argon at low pressures, adsorbing preferentially in the octahedral pockets, but as opposed to the oxygen and argon, site II remains the most populated region at

Table 2. Henry coefficients, entropies and energies of adsorption computed at zero coverage for the different sites of Cu-BTC at 298 K. Number in brackets gives the statistical errors in the last digits.

Site	K_H (mol/kg/Pa)	dH (kJ/mol)	dS (J/K/mol)	dU (kJ/mol)	dA (kJ/mol)	dG (kJ/mol)
Oxygen						
Cu-BTC	$4.9\ 10^{-6}$ (2)	-12.7 (2)	-22.7 (7)	-12.7 (2)	-5.9 (1)	-8.4 (1)
I´	$1.7\ 10^{-6}$ (4)	-7.1 (1)	-13.0 (2)	-7.1 (1)	-3.2 (7)	-5.7 (7)
II	$1.4\ 10^{-6}$ (1)	-16.5 (2)	-46.0 (6)	-16.5 (2)	-2.8 (2)	-5.3 (2)
III	$1.7\ 10^{-7}$ (3)	-14.0 (5)	-55.2 (2)	-14.0 (5)	-2.4 (4)	-0.1 (4)
II+III	$2.9\ 10^{-6}$ (2)	-16.2 (1)	-38.8 (8)	-16.2 (1)	-4.6 (1)	-7.1 (1)
Nitrogen						
Cu-BTC	$3.8\ 10^{-6}$ (2)	-11.7 (3)	-21.6 (8)	-11.7 (3)	-5.2 (1)	-7.7 (1)
I´	$1.6\ 10^{-6}$ (1)	-7.0 (1)	-13.2 (2)	-7.0 (1)	-3.1 (2)	-5.5 (2)
II	$1.2\ 10^{-6}$ (1)	-16.3 (2)	-46.7 (7)	-16.3 (2)	-2.4 (3)	-4.9 (3)
III	$8.8\ 10^{-8}$ (2)	-13.4 (2)	-58.2 (7)	-13.2 (2)	4.1 (5)	1.6 (5)
II+III	$1.9\ 10^{-6}$ (1)	-15.7 (1)	-32.8 (4)	-13.3 (1)	-3.5 (1)	-6.0 (1)
Argon						
Cu-BTC	$4.3\ 10^{-6}$ (1)	-11.7 (2)	-20.5 (6)	-11.7 (2)	-5.6 (1)	-8.1 (1)
I´	$1.6\ 10^{-6}$ (2)	-6.7 (1)	-11.9 (2)	-6.7 (1)	-3.2 (3)	-5.6 (3)
II	$1.6\ 10^{-6}$ (1)	-15.6 (1)	-42.2 (5)	-15.6 (1)	-3.1 (2)	-5.5 (2)
III	$3.2\ 10^{-7}$ (5)	-13.4 (2)	-47.8 (6)	-13.4 (2)	0.8 (4)	-1.6 (4)
II+III	$2.5\ 10^{-6}$ (2)	-15.2 (1)	-36.9 (2)	-15.2 (1)	-4.2 (2)	-6.7 (2)
Carbon tetrachloride						
Cu-BTC	$2.8\ 10^{-2}$ (1)	-35.7 (3)	-104.8 (8)	-35.7 (3)	-4.5 (1)	-7.0 (1)
I´	$2.8\ 10^{-2}$ (1)	-35.7 (2)	-104.8 (6)	-35.7 (2)	-4.5 (1)	-7.0 (1)

intermediate pressures and finally sites III and I´ are populated at the highest pressures. Computed Henry coefficients, energies and entropies of adsorption at zero coverage and 298 K corroborate that the centre of the big cage is the preferential adsorption site for carbon tetrachloride and the centres of the octahedral cages are the preferential sites for oxygen, nitrogen and argon at low loading. The obtained values for the big cages, the octahedral cages, the windows and for the whole structure are listed in Table 2.

Adsorption of binary and ternary mixtures

In this section we analyse the computed adsorption isotherms of binary mixtures containing carbon tetrachloride and ternary mixtures containing the main components of air. In particular, we computed the adsorption isotherms for Ar/CCl_4, N_2/CCl_4 and O_2/CCl_4 (Figures A1a-c in Appendix 3) at bulk partial fugacity ratios of 99:1 and 99.9:0.1. Figure 5 shows the adsorption selectivity of carbon tetrachloride over nitrogen, defined as $(x_{CCl_4}/y_{CCl_4})/(x_{N_2}/y_{N_2})$, where x_{CCl_4} and x_{N_2} are the molar fractions in the
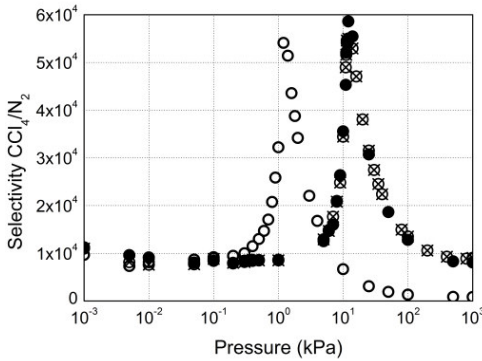
Figure 5. Adsorption selectivity of carbon tetrachloride over nitrogen obtained from the computed adsorption isotherms of N_2/CCl_4 mixtures at bulk partial fugacity ratios of 99 : 1 (empty symbols), 99.9 : 0.1 (full symbols) and 77.922 : 0.1 (crossed symbols).

adsorbed phase and y_{CCl4} and y_{N2} are the molar fractions in the bulk phase. The figure shows high selectivities in favour of carbon tetrachloride, that reach a maximum at 1.2 kPa for the bulk partial fugacity ratio 99:1 and at 12 kPa for the bulk partial fugacity ratio 99.9:0.1. These two maxima correspond to the pressure at which carbon

tetrachloride isotherms initiate the steep curve in the Cu-BTC pores (see Figure A1 in Appendix 3). The selectivities of carbon tetrachloride over oxygen are similar to these obtained over nitrogen (Figure A2 in Appendix 3).

To analyse the preferential adsorption sites of the main components of dry air in Cu-BTC we computed the adsorption isotherms for the equimolar $O_2/N_2/Ar$ mixture and for the mixture that mimics a general sample of air, i.e. with a bulk partial fugacity ratio 21:78:1. As shown in Figure 6a, the adsorption of the three components in Cu-BTC is very similar in the case of the equimolar mixture, though at the highest pressures the loading of nitrogen decreases. Figure 6b shows the adsorption isotherms of the mixture $O_2/N_2/Ar$ with ratio 21:78:1. For this mixture the adsorption of argon in Cu-BTC is negligible as a consequence of its low proportion in the bulk (1%). Following the same reasoning, nitrogen (78%) adsorbs more than oxygen (21%) in this structure.

Figure 6. Adsorption isotherms of ternary mixtures composed by oxygen (squares), nitrogen (circles) and argon (triangles) in Cu–BTC at 298 K. (a) equimolar mixture; (b) $O_2/N_2/Ar$ mixture with a bulk partial fugacity ratio of 21 : 78 : 1.

(a)   (b)
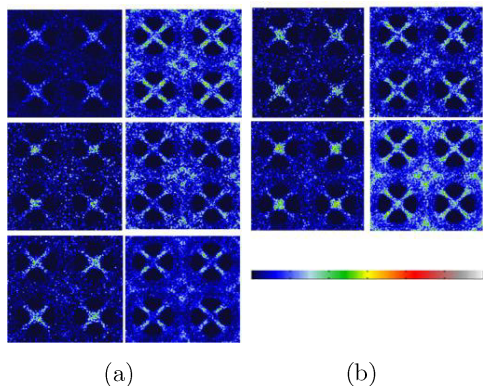
Figure 7. Comparison of the average occupation profiles of oxygen (top), nitrogen (middle) and argon (bottom) in Cu–BTC for the adsorption of (a) an equimolar ternary mixture and (b) an $O_2/N_2/Ar$ ternary mixture with partial fugacity ratio 21 : 78 : 1. The pro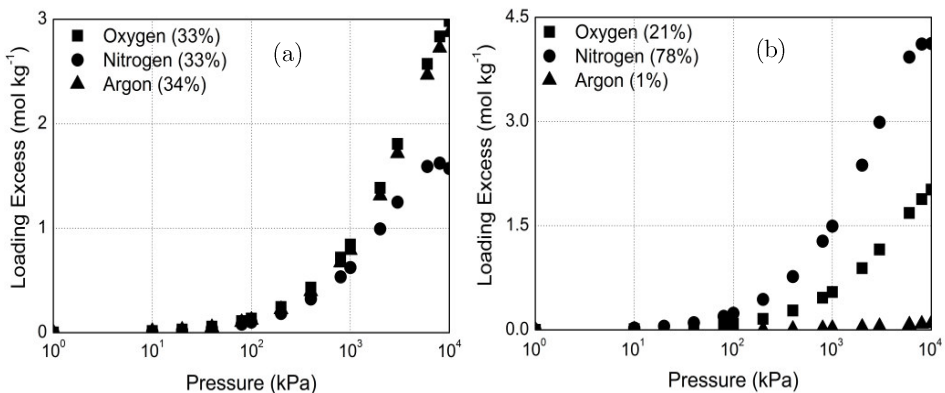files were obtained at 1000 kPa (left) and 10 000 kPa (right). The same colour gradation (from dark to light) is employed in all figures, although the total number of molecules present in the unit cell is different for each calculation.
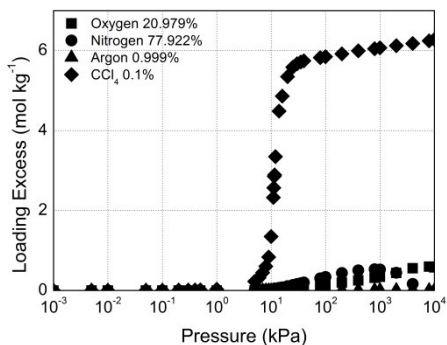
Figure 8. Adsorption isotherms of the quaternary mixture with ratio 20.979 : 77.922 : 0.999 : 0.1 in Cu–BTC at 298 K with oxygen (squares), nitrogen (circles), argon (triangles) and carbon tetrachloride (rhombus).

The preferential adsorption sites are also similar for the three components (Figure 7). The analysis of the results obtained for the equimolar ternary mixture shows that at low pressures (not shown in the Figure), argon, nitrogen and oxygen preferentially adsorb in the octahedral cages. At medium pressures the molecules also adsorb in the windows and in the big cages and finally, at the highest pressures and once the octahedral cages and windows are completely full, the molecules populate the big cages (Figure 7a). The decrease of the adsorption observed for nitrogen at high pressure might be explained in terms of a double competition; at high pressures, when the loading of molecules in the structure is already quite high, the smallest molecule (argon) fits better in the available empty space and, simultaneously, the molecule with higher quadrupole moment (nitrogen) packs worse in the structure. This competition is balanced for the adsorption of the system with a partial fugacity ratio 21:78:1, where nitrogen is by far the major component of the mixture in the bulk (Figure 7b). The profiles corresponding to the adsorption of argon are not shown, since the amount of argon is very small and therefore the profile does not show a significant average population in any position.

Adsorption of quaternary mixtures

Adsorption isotherms in Cu-BTC for a mixture of oxygen, nitrogen, argon and carbon tetrachloride molecules were computed at 298 K (Figure 8). To model a sample of air containing carbon
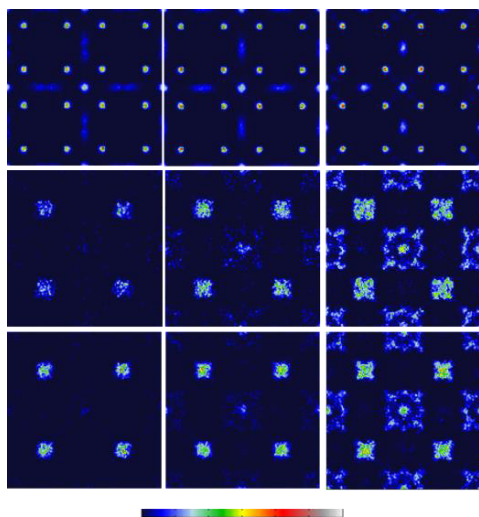
Figure 9. Average occupation profiles for carbon tetrachloride (top), oxygen (middle) and nitrogen (bottom) from the quaternary mixture at 100 kPa (left), 1000 kPa (centre) and 10 000 kPa (right) at 298 K. The same colour gradation (from dark to light) is employed in all figures, although the total number of molecules present in the unit cell is different for each calculation.

tetrachloride as contaminant we used a mixture with a composition of 20.979% O_2, 77.922% N_2, 0.999% Ar and 0.1% CCl_4. The highest adsorption selectivity is found for carbon tetrachloride molecules, with absolute values that almost equal those obtained for the binary mixtures with a composition in the bulk of 0.1% carbon tetrachloride and 99.9% of nitrogen (Figure 5) or 99.9% of oxygen (Figure A2 in Appendix 3).

Figure 9 shows the average occupation profiles for carbon tetrachloride, oxygen and nitrogen molecules taken from the adsorption of the quaternary mixture in Cu-BTC. The profiles for carbon

tetrachloride obtained from the adsorption of the mixture are very similar to those obtained in the case of the adsorption of the single component. However, oxygen and nitrogen molecules are now highly influenced by the presence of carbon tetrachloride and they cannot be adsorbed at the windows that communicate the octahedral cages with the main cages -blocked by the carbon tetrachloride molecules- nor at the main cages -filled with carbon tetrachloride molecules-. For the four components mixture studied in this work argon adsorption in Cu-BTC is negligible.

Adsorption of five-component mixtures

In order to analyse the effect with water as competing molecule we performed simulations in a range of different air models, with relative humidity spanning from 0% (0% of water vapour at 298 K and 10^5 Pa) to 100% (4% of water vapour at 298 K and 10^5 Pa). The results obtained show a preferential adsorption of carbon tetrachloride over water, oxygen, nitrogen and argon molecules for all percentages of air relative humidity (Figure 10). Although the selectivity values are always in favour of carbon tetrachloride we observe different trends depending on the air relative humidity. Hence, carbon tetrachloride adsorption selectivity over oxygen, nitrogen and argon is slightly higher in dry air than in air with 10% relative humidity. In these conditions, the presence of water in the structure (around 45 molecules per unit cell) reduces the number of molecules of carbon tetrachloride from 56 to 37
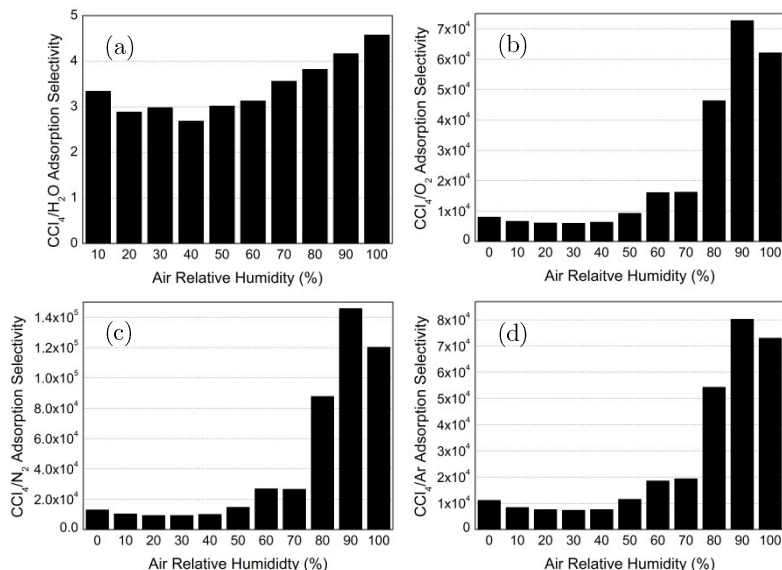
Figure 10. Adsorption selectivity of carbon tetrachloride over water (a), oxygen (b), nitrogen (c) and argon (d), from the five-component mixture at different percentages of relative humidity.

molecules per unit cell, whereas the number of molecules of oxygen, nitrogen and argon molecules remains constant. In a previous work we found that water has a large affinity for the metal centre in Cu-BTC, compared to non-polar molecules like nitrogen, oxygen or argon[9]. Consequently, water molecules preferentially adsorb in the neighbourhood of the copper atoms, at the central cages, competing with the molecules of carbon tetrachloride for this adsorption site. The preferential adsorption site for nitrogen, oxygen and argon is the interior of the octahedral cages, so, at low percentages of air relative humidity, the loading of these molecules is unaffected. These differences in preferential adsorption sites explain the slight decrease on the carbon tetrachloride selectivity for air relative humidity within the range of 10% to 40%. Once the neighbourhood of the copper atoms is fully occupied, the water molecules populate the octahedral cages. The direct competition for the adsorption sites between water and the molecules of nitrogen, oxygen, and argon reduces (for air relative humidity between 50% and 70%) and eventually excludes (for air relative humidity between 80%-100%) the last three molecules from the structure (Figure 11). This explains the exponential increase of the adsorption selectivity of carbon tetrachloride over oxygen, nitrogen and argon for percentages of air relative humidity higher than 70%. It is interesting to note that these results are in agreement with recent experimental and simulation studies, which have also reported an enhancement of selectivity of CO_2 with water content in this structure[18].
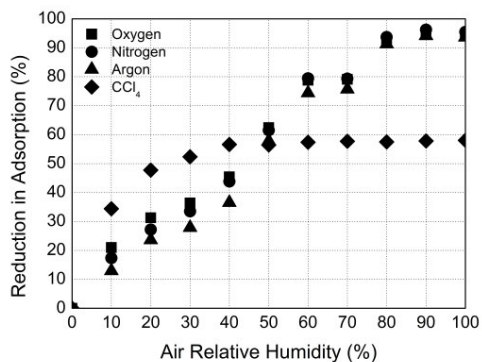
Figure 11. Effect of air relative humidity on the adsorption of a five-component mixture of carbon tetrachloride in air at 298 K. The figure shows the % reduction in the adsorption of oxygen (squares), nitrogen (circles), argon (triangles) and carbon tetrachloride (rhombus).

10% ARH   20% ARH   90% ARH
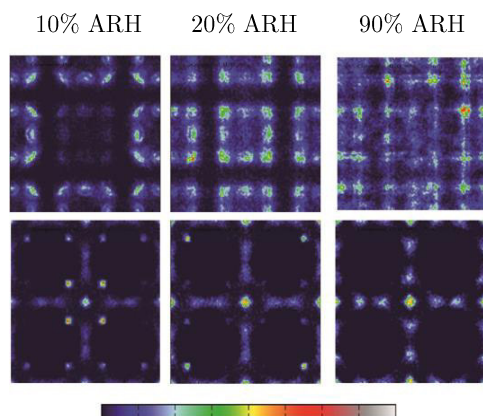
Figure 12. Average occupation profiles of water (top) and carbon tetrachloride (bottom) in Cu–BTC at 298 K. The profiles were obtained from the molecular simulations of five-component mixtures of carbon tetrachloride in air with relative humidity 10% (left), 20% (medium) and 90% (right). The same colour gradation (from dark to light) is employed in all figures, although the total number of molecules present in the unit cell is different for each calculation.

The average occupation profiles in Cu-BTC obtained for water and carbon tetrachloride during the adsorption of the five-component mixture illustrate the large affinity of water for the metal centre in Cu-BTC and the subsequent adsorption of these molecules in the windows and octahedral cages. As shown in Figure 12, for the five-component mixture with air relative humidity of 10% water adsorbs in the neighbourhood of the copper atoms and carbon tetrachloride adsorbs preferentially in the centre of the big cages and in an additional site at the big cages, blocking the access to the windows that communicate them with the octahedral cages. In the adsorption of mixtures with air relative humidity values higher than 10% the molecules of water displace carbon tetrachloride from this additional site to the centre of the big cages and finally, once the big cages are completely full the molecules of water also populate the octahedral cages. Figure 12 shows the average profiles at 10%, 20%, and 90% of air relative humidity, the rest can be found in Appendix 3 (Figure A3).

Self-diffusivities

Table 3 lists the computed self-diffusivities values obtained for oxygen, nitrogen and carbon tetrachloride as pure component, and from the quaternary mixture, at the loading corresponding to 1000 kPa and 298 K (3 oxygen molecules per unit cell, 7 nitrogen molecules per unit cell and 59 carbon tetrachloride molecules per unit cell). We also compare these results with those obtained from a binary equimolar mixture O_2/N_2, with 7 oxygen

Table 3. Self-diffusivities (m^2 s^{-1}) computed for oxygen and nitrogen as pure components, binary equimolar O_2/N_2 mixture and from the quaternary mixture. These values were computed for the loading corresponding to 10^5 Pa and 298 K.

	Pure components	Binary equimolar Mixture	Quaternary mixture
O_2	1.4 ± 0.02 10^{-8}	1.6 ± 0.02 10^{-8}	4.0 ± 0.1 10^{-11}
N_2	1.9 ± 0.04 10^{-8}	2.0 ± 0.01 10^{-8}	1.6 ± 0.1 10^{-11}

Table 4. Self-diffusivities (m^2 s^{-1}) computed for oxygen, nitrogen and water molecules, for the five component mixtures with air relative humidity spanning from 0% to 100%. These values were computed for the loading corresponding to 10^5 Pa and 298 K.

ARH %	O_2	N_2	H_2O
0	4.0 ± 0.1 10^{-11}	1.6 ± 0.1 10^{-11}	-
10	8.2 ± 0.2 10^{-10}	1.2 ± 0.1 10^{-9}	1.2 ± 0.2 10^{-10}
20	2.8 ± 0.1 10^{-10}	2.0 ± 0.2 10^{-10}	1.6 ± 0.2 10^{-10}
30	2.4 ± 0.1 10^{-10}	9.5 ± 0.3 10^{-11}	2.2 ± 0.1 10^{-10}
40	-	7.5 ± 0.2 10^{-11}	2.8 ± 0.2 10^{-10}
50	-	-	4.0 ± 0.3 10^{-10}
60	-	-	5.0 ± 0.3 10^{-10}
70	-	-	5.1 ± 0.4 10^{-10}
80	-	-	4.9 ± 0.3 10^{-10}
90	-	-	5.1 ± 0.3 10^{-10}
100	-	-	5.4 ± 0.4 10^{-10}

molecules per unit cell and 6 nitrogen molecules per unit cell. The self-diffusivity of nitrogen as pure component is slightly higher than the one obtained for oxygen, while the self-diffusivity for carbon tetrachloride is very low in comparison with both of them. Comparing the pure component diffusion values to those in the binary mixture, we observe that they are quite

similar. This behaviour reverses in the quaternary mixture, though the diffusion coefficients for the two components decrease by three orders of magnitude. The slopes of the mean-squared displacements obtained for the 59 molecules of carbon tetrachloride at long times are almost zero, indicating a very low self-diffusivity for this molecule compared with the other two components (see Figure A4 in Appendix 3).

The computed self-diffusivities for the five-component mixtures are compiled in Table 4. It is interesting to note that the presence of water in the structure enhances diffusivities in Cu-BTC. This enhancement reaches a maximum for around 10% air relative humidity and decays when we progressively increase the amount of water in the structure. This decay might be attributed to the surprising behaviour of water in the structure, which diffuses faster at higher values of air relative humidity.

Conclusions

We used Monte Carlo and Molecular Dynamics simulations to evaluate the performance of Cu-BTC metal-organic frameworks for carbon tetrachloride removal from air, at 298 K. According to our results, this material shows extremely high adsorption selectivity in favour of carbon tetrachloride. We demonstrate that this selectivity can be further enhanced in humid air. Self-diffusivity values for carbon tetrachloride are extremely low for the pure component and for the quaternary mixture formed by this component and the main components of dry air.

However, our simulations results for five component mixtures involving humid air revealed diffusion values for carbon tetrachloride up to three orders of magnitude larger than those obtained in dry air. Molecular separations are based not only on the adsorption selectivity but also on the difference between the diffusivities of the components of the mixture. However, we are unable to accurately estimate the diffusion of carbon tetrachloride for the studied systems using Molecular Dynamics and new and more sophisticated methods will need to be developed to bypass this impediment.

Bibliography

(1) Li, H.; Eddaoudi, M.; O'Keeffe, M.; Yaghi, O. M. *Nature* **1999**, *402*, 276.

(2) Britt, D.; Tranchemontagne, D.; Yaghi, O. M. *Proceedings of the National Academy of Sciences of the United States of America* **2008**, *105*, 11623.

(3) Ma, S. Q.; Zhou, H. C. *Chemical Communications* **2010**, *46*, 44.

(4) Mueller, U.; Schubert, M.; Teich, F.; Puetter, H.; Schierle-Arndt, K.; Pastre, J. *Journal of Materials Chemistry* **2006**, *16*, 626.

(5) Garcia-Perez, E.; Gascon, J.; Morales-Florez, V.; Castillo, J. M.; Kapteijn, F.; Calero, S. *Langmuir* **2009**, *25*, 1725.

(6) Krishna, R.; van Baten, J. A. *Langmuir* **2010**, *26*, 3981.

(7) Yazaydin, A. O.; Snurr, R. Q.; Park, T. H.; Koh, K.; Liu, J.; LeVan, M. D.; Benin, A. I.; Jakubczak, P.; Lanuza, M.; Galloway, D. B.; Low, J. J.; Willis, R. R. *Journal of the American Chemical Society* **2009**, *131*, 18198.

(8) Martin-Calvo, A.; Garcia-Perez, E.; Castillo, J. M.; Calero, S. *Physical Chemistry Chemical Physics* **2008**, *10*, 7085.

(9) Castillo, J. M.; Vlugt, T. J. H.; Calero, S. *Journal of Physical Chemistry C* **2008**, *112*, 15934.

(10) Babarao, R.; Hu, Z. Q.; Jiang, J. W.; Chempath, S.; Sandler, S. I. *Langmuir* **2007**, *23*, 659.

(11) Cavenati, S.; Grande, C. A.; Rodrigues, A. E. *Industrial & Engineering Chemistry Research* **2008**, *47*, 6333.

(12) Calero, S.; Martin-Calvo, A.; Hamad, S.; Garcia-Perez, E. *Chemical Communications* **2011**, *47*, 508.

(13) Nicholson, T. M.; Bhatia, S. K. *Journal of Physical Chemistry B* **2006**, *110*, 24834.

(14) Dubbeldam, D.; Galvin, C. J.; Walton, K. S.; Ellis, D. E.; Snurr, R. Q. *Journal of the American Chemical Society* **2008**, *130*, 10884.

(15) Hartmann, M.; Kunz, S.; Himsl, D.; Tangermann, O.; Ernst, S.; Wagener, A. *Langmuir* **2008**, *24*, 8634.

(16) Wu, H.; Simmons, J. M.; Liu, Y.; Brown, C. M.; Wang, X. S.; Ma, S.; Peterson, V. K.; Southon, P. D.; Kepert, C. J.; Zhou, H. C.; Yildirim, T.; Zhou, W. *Chemistry-a European Journal* **2010**, *16*, 5205.

(17) Xiang, S. C.; Zhou, W.; Gallegos, J. M.; Liu, Y.; Chen, B. L. *Journal of the American Chemical Society* **2009**, *131*, 12415.

(18) Yazaydin, A. O.; Benin, A. I.; Faheem, S. A.; Jakubczak, P.; Low, J. J.; Willis, R. R.; Snurr, R. Q. *Chemistry of Materials* **2009**, *21*, 1425.

(19) Millward, A. R.; Yaghi, O. M. *Journal of the American Chemical Society* **2005**, *127*, 17998.

(20) Yang, Q. Y.; Zhong, C. L.; Chen, J. F. *Journal of Physical Chemistry C* **2008**, *112*, 1562.

(21) Yang, Q. Y.; Zhong, C. L. *Journal of Physical Chemistry B* **2006**, *110*, 655.

(22) Babarao, R.; Jiang, J. W.; Sandler, S. I. *Langmuir* **2009**, *25*, 5239.

(23) Liu, B.; Smit, B. *Langmuir* **2009**, *25*, 5918.

(24) Yang, Q. Y.; Zhong, C. L. *Chemphyschem* **2006**, *7*, 1417.

(25) Karra, J. R.; Walton, K. S. *Langmuir* **2008**, *24*, 8620.

(26) Dathe, H.; Jentys, A.; Lercher, J. A. *Physical Chemistry Chemical Physics* **2005**, *7*, 1283.

(27) Peterson, G. W.; Wagner, G. W.; Balboa, A.; Mahle, J.; Sewell, T.; Karwacki, C. J. *Journal of Physical Chemistry C* **2009**, *113*, 13906.

(28) Keskin, S.; Liu, J. C.; Johnson, J. K.; Sholl, D. S. *Microporous and Mesoporous Materials* **2009**, *125*, 101.

(29) Skoulidas, A. I. *Journal of the American Chemical Society* **2004**, *126*, 1356.

(30) Skoulidas, A. I.; Sholl, D. S. *Journal of Physical Chemistry B* **2005**, *109*, 15760.

(31) Seehamart, K.; Nanok, T.; Krishna, R.; van Baten, J. M.; Remsungnen, T.; Fritzsche, S. *Microporous and Mesoporous Materials* **2009**, *125*, 97.

(32) Chui, S. S. Y.; Lo, S. M. F.; Charmant, J. P. H.; Orpen, A. G.; Williams, I. D. *Science* **1999**, *283*, 1148.

(33) Liu, Y.; Brown, C. M.; Neumann, D. A.; Peterson, V. K.; Kepert, C. J. *Journal of Alloys and Compounds* **2007**, *446*, 385.

(34) Calero, S.; Dubbeldam, D.; Krishna, R.; Smit, B.; Vlugt, T. J. H.; Denayer, J. F. M.; Martens, J. A.; Maesen, T. L. M. *Journal of the American Chemical Society* **2004**, *126*, 11377.

(35) Garcia-Perez, E.; Parra, J. B.; Ania, C. O.; Dubbeldam, D.; Vlugt, T. J. H.; Castillo, J. M.; Merkling, P. J.; Calero, S. *Journal of Physical Chemistry C* **2008**, *112*, 9976.

(36) Mayo, S. L.; Olafson, B. D.; Goddard, W. A. *Journal of Physical Chemistry* **1990**, *94*, 8897.

(37) Rappe, A. K.; Casewit, C. J.; Colwell, K. S.; Goddard, W. A.; Skiff, W. M. *Journal of the American Chemical Society* **1992**, *114*, 10024.

(38) Babarao, R.; Eddaoudi, M.; Jiang, J. W. *Langmuir* **2010**, *26*, 11196.

(39) Babarao, R.; Jiang, J. W. *Energy & Environmental Science* **2009**, *2*, 1088.

(40) Chen, Y. F.; Babarao, R.; Sandler, S. I.; Jiang, J. W. *Langmuir* **2010**, *26*, 8743.

(41) Jiang, J. W. *Aiche Journal* **2009**, *55*, 2422.

(42) Stogryn, D. E.; Stogryn, A. P. *Molecular Physics* **1966**, *11*, 371.

(43) Murthy, C. S.; Singer, K.; Klein, M. L.; McDonald, I. R. *Molecular Physics* **1980**, *41*, 1387.

(44) Rick, S. *Journal of Chemical Physics* **2004**, *120*, 6085.

(45) Garcia-Sanchez, A.; Ania, C. O.; Parra, J. B.; Dubbeldam, D.; Vlugt, T. J. H.; Krishna, R.; Calero, S. *Journal of Physical Chemistry C* **2009**, *113*, 8814.

(46) Dubbeldam, D.; Calero, S.; Vlugt, T. J. H.; Krishna, R.; Maesen, T. L. M.; Smit, B. *Journal of Physical Chemistry B* **2004**, *108*, 12301.

(47) Mellot, C.; Lignieres, J. *Molecular Simulation* **1996**, *18*, 349.

(48) Makrodimitris, K.; Papadopoulos, G. K.; Theodorou, D. N. *Journal of Physical Chemistry B* **2001**, *105*, 777.

(49) Lofti, A.; Vrabec, J.; Fischer, J. *Molecular Physics* **1992**, *76*, 1319.

(50) NIST database.

(51) Dubbeldam, D.; Smit, B. *Journal of Physical Chemistry B* **2003**, *107*, 12138.

(52) Liu, J. C.; Culp, J. T.; Natesakhawat, S.; Bockrath, B. C.; Zande, B.; Sankar, S. G.; Garberoglio, G.; Johnson, J. K. *Journal of Physical Chemistry C* **2007**, *111*, 9305.

(53) Chowdhury, P.; Bikkina, C.; Meister, D.; Dreisbach, F.; Gumma, S. *Microporous and Mesoporous Materials* **2009**, *117*, 406.

(54) Wang, Q. M.; Shen, D. M.; Bulow, M.; Lau, M. L.; Deng, S. G.; Fitch, F. R.; Lemcoff, N. O.; Semanscin, J. *Microporous and Mesoporous Materials* **2002**, *55*, 217.

(55) Liang, Z. J.; Marshall, M.; Chaffee, A. L. *Energy & Fuels* **2009**, *23*, 2785.

(56) Xue, C. Y.; Yang, Q. Y.; Zhong, C. L. *Molecular Simulation* **2009**, *35*, 1249.

(57) Garberoglio, G.; Skoulidas, A. I.; Johnson, J. K. *Journal of Physical Chemistry B* **2005**, *109*, 13094.

(58) Walton, K. S.; Millward, A. R.; Dubbeldam, D.; Frost, H.; Low, J. J.; Yaghi, O. M.; Snurr, R. Q. *Journal of the American Chemical Society* **2008**, *130*, 406.

Understanding Carbon Monoxide Capture Using Metal-Organic Frameworks

5

Ana Martín-Calvo, Francisco D. Lahoz-Martín
and Sofía Calero

We use molecular simulations to analyse the effect of water on the adsorption of carbon monoxide in metal-organic frameworks. We have developed a model for carbon monoxide that reproduces not only the required experimental properties more accurately than previous models, but also takes into account the effect of the dipole moment on the interaction of the molecule with water and with the metal organic framework. Our simulations were performed for Cu-BTC and IRMOF-1 with different contents of water, up to the highest water loading that each metal-organic framework can contain without losing stability. To carry out this study we computed entropies and energies of adsorption, Henry coefficients, adsorption isotherms in the dry and hydrated structures and the molecular distribution of carbon monoxide based on the topology of the framework and on the interactions with the molecules of water. Our results show that the adsorption of carbon monoxide can be increased or reduced by controlling the amount of water in the structures.

1. Introduction

Metal-organic frameworks (MOFs) are porous materials consisting on metallic centres linked by organic ligands. Their variety of pores and cavities with different sizes and shapes make these materials good candidates for storage and separation processes. Among metal-organic frameworks, Cu-BTC and IRMOF-1 are two of the most studied structures[1-3]. Cu-BTC was firstly synthesised by Chui *et al.*[4] as a metal coordination polymer based on copper centres and 1,3,5-benzenetricarboxilate (BTC) linker molecules. That conformation generates a cubic structure characterised by small and big cages connected by windows. There are two alternated types of big cages, one

with its inner surface conformed by benzene rings from the BTC with their 6-fold axis pointing towards the centre of the pore and other cavity which inner surface is not formed by the rings of BTC[5].

IRMOF-1 is the smallest structure from the family of the isoreticular metal-organic frameworks (IRMOFs) and was firstly reported by the group of Yaghi[6,7]. This structure is formed by $Zn_4O(CO_2)_6$ units linked by phenylene ligands. The linkage of the Zn_4O complexes is forced to alternate between linkers pointing outwards and inwards, resulting in a structure with two alternating types of cavities: small cavities of around 11 Å and large cavities of about 15 Å in diameter[7].

The aim of this work is to analyse the effect that the presence of water exerts in the prvious structures regarding the capture of carbon monoxide. Therefore it is important to firstly evaluate the stability of Cu-BTC and IRMOF-1 in presence of water. The stability of Cu-BTC in water is still an open subject. Li and Yang reported that Cu-BTC is stable after water adsorption[8]. Liang *et al.*[9] reported the opposite and mentioned that the stability found by Li and Yang might possibly be attributed to relatively rapid adsorption/desorption cycles used in their experiments. Following the same line of thought, Liu *et al.* suggested that the hydrothermal stability of Cu-BTC is prone to degradation after heat treatment and water vapour adsorption[10]. On the other hand Henninger *et al.*[11] showed water loading capacities in Cu-BTC about 324 g/kg for higher desorption temperatures. In a very recent work Gul-E-Noor *et al.*[12] reported that the presence of water in Cu-BTC ends up leading to a decomposition of the structure. Küsgens *et al.* concluded that despite of the instability of Cu-BTC upon direct exposure to water, this is a promising material in trace water removal[13]. In a theoretical study Grajciar *et al.*[14] observed that the structure of Cu-BTC with one or two molecules of water per paddle wheel remains relatively unchanged. However, they also showed that the stability varies for different water contents and different decomposition products. From this works we can finally conclude that Cu-BTC can be considered relatively stable upon hydration/dehydration at room temperature and for the water contents considered in this work[8,15,16].

Regarding IRMOF-1, it is well known that this structure is very sensitive to water, losing its high surface area after prolonged exposure to humid air[17]. An important point is that at low water content the structure is maintained despite a decrease of the lattice parameter. Only water quantities higher than 4% make the structure clearly unstable[18]. Recent studies provide evidences that at low water contents, the molecules of water are isolated in the lattice, but at around 6.6% water weight the basicity of water after solvation and the large coordination spheres of zinc, provoke an irreversible lattice disruption by displacement of the organic ligand[19,20].

Several works have studied adsorption and separation processes in Cu-BTC and IRMOF-1 for gases of environmental interest such as carbon dioxide, nitrogen or hydrocarbons, as well as for their mixtures[21-33]. These studies remark the importance of performing adsorption analysis searching for an optimal separation or storage of these gases. However despite of the importance of carbon monoxide, as by-product from an incomplete combustion of gasoline, oil, gas, or carbon, between others, only a few works have provided insights on the capture or separation of this molecule using MOFs[34-43].

There are only two models of carbon monoxide described in literature. The first model was proposed by Piper *et al.* in 1984 for the study of solid CO-Ar

systems[44]. The second model was developed by Straub and Karplus seven years latter for the analysis of photo-dissociation of carbon monoxide from myoglobin[45]. These models have been applied to other studies with reasonable agreement with experimental data[36,39,40,42]. However none of them are able to reproduce the experimental vapour-liquid equilibrium curve of the molecules and this is a crucial property to accurately reproduce adsorption in confined systems[46-51]. An additional option to these models is the use of the UFF generic force field[52] to mimic the molecule. Sirjoosingh *et al.* employed this strategy for the separation of carbon monoxide from carbon dioxide using ZIF-68 and ZIF-69 structures[36]. The use of the generic force field to mimic carbon monoxide is limited by the point charges that must be assigned to the atoms and that are not included in the UFF force field. The point charges used with this force field were computed using the Mulliken analysis and correspond to 0.107 e^- for the carbon atom, and -0.107 e^- for the oxygen atom. These charges lead to a dipole moment of 0.58 D whereas the experimental value for carbon monoxide is 0.112 D[53].

In this work we analyse the effect that water exerts on the adsorption of carbon monoxide in Cu-BTC and IRMOF-1. Since water is a very polar molecule (1.85 D), a model for carbon monoxide with the correct dipole moment seems important. Therefore, we developed a new model for the carbon monoxide molecule that not only reproduces the vapour-liquid equilibrium curve, the vapour pressure

curve and the bulk density for a wide range of temperatures, but also provides a dipole moment of 0.112 D. Using this model we analyse the adsorption properties of carbon monoxide in Cu-BTC and IRMOF-1 as dehydrated and hydrated structures. This model and the methodology used for our study are detailed in section 2. The obtained results are discussed in section 3 and we summarize the most relevant conclusions in section 4.

2. Simulation methods and models

We use Gibbs ensemble Monte Carlo simulations to compute the vapour-liquid equilibrium curve of carbon monoxide. During the simulations, the Lennard-Jones parameters of the carbon monoxide model were fitted to reproduce the experimental curve[54]. This is the first and the most important step to further perform adsorption studies in porous systems[46-51]. We mimic the carbon monoxide molecules with a rigid model characterised by a bond length of 1.128 Å between the carbon and the oxygen atoms. The atoms have partial charges of -0.2424 and -0.2744 e^-, respectively. A dummy atom with a point charge of 0.517 e^- is located at 0.6443 Å from the carbon atom, to reproduce the experimental dipole moment of the molecule (0.112 D)[53]. In addition, we performed Gibbs ensemble MC simulations with the models proposed by Piper *et al.*[44] and by Straub and Karplus[45]. The first model is characterised by four interaction centres: carbon and oxygen atoms -with positive and null partial charges respectively- and two sites that provide negative charges to the molecule,

Table 1. Lennard-Jones parameters, partial charges and bond lengths for the models of carbon monoxide considered in this work.

Model	Atom type	σ [Å]	ε/k_B [K]	Charge [e^-]	L [Å]
	C	3.385	39.89	0.831	-0.6446
Ref. 44	O	2.885	61.57	0	0.4836
	site 1	-	-	-0.636	-1.0820
	site 2	-	-	-0.195	0.3256
	C	3.83	13.18	-0.75	0
Ref. 45	O	3.12	80.06	-0.85	1.128
	site	-	-	1.6	0.6443
Ref. 36	C	3.43	52.888	0.107	0
	O	3.12	30.219	-0.107	1.140
	C	3.636	16.141	-0.2424	0
This work	O	2.979	98.014	-0.2744	1.128
	site	-	-	0.5168	0.6443

getting a dipole moment of 0.43 D. The model reported by Straub and Karplus is similar to the model proposed in this work. It is based on three interaction centres: carbon and oxygen atoms, both of them with negative charges, and a dummy to compensate these charges, resulting in a dipole moment of 0.35 D. Details of these models are listed in Table 1.

To simulate the molecule of water we use Tip5pEw. This model was parameterized for being used with the Ewald summation method, and it has been successfully applied in previous works, providing results for water that are in good agreement with experimental data[16,55].

Cu-BTC and IRMOF-1 frameworks were considered rigid. They interact with carbon monoxide by Lennard-Jones and Coulombic potentials. The Lennard-Jones parameters are taken from DREIDING generic force field[56]

except for cooper and zinc that were taken from UFF force field[52]. The charges for IRMOF-1 were obtained from Frost *et al.*[57]. As the goal of this study is to analyse the effect of the presence of water in the structure for carbon monoxide capture, we use a set of charges previously validated for Cu-BTC that provides the best agreement with experimental values of water adsorption in this structure[16]. Simulations were performed for one unit cell of a = b = c = 26.343 Å (Cu-BTC) and a = b = c = 25.832 Å (IRMOF-1). The computed helium void fractions are 0.76 for Cu-BTC and 0.82 for IRMOF-1. The full set of parameters and charges used in this work for the frameworks are listed in Appendix 4 (Table A1).

The interactions adsorbate-adsorbate and adsorbate-framework were modelled with Lennard-Jones parameters and Coulombic potentials. The Lennard-Jones parameters were obtained from Lorentz-Berthelot mixing rules, except for the interactions between carbon monoxide and Cu-BTC, which Lennard-Jones parameters are listed in the Table A2 in Appendix 4. Coulombic potentials are obtained by using the Ewald summation method.

To compute adsorption isotherms we use grand canonical Monte Carlo (GCMC) simulations fixing the chemical potential, volume and temperature. Pressure is obtained from fugacity using the Peng-Robinson equation of state. As MC moves we used translation, rotation, regrow at a random position, and reinsertion. To compare our results with available experimental isotherms,

absolute adsorptions were converted to excess adsorptions by the following expression[58]:

$$Ads_{Exc} = Ads_{Abs} - \frac{PV}{zRT}$$

were P is the pressure of the system, V the pore volume of the structure, z the compressibility of the gas, R the constant of gases and T the temperature of the system.

Henry coefficients and heats of adsorption at zero coverage were computed using Monte Carlo in NVT ensemble. The Henry coefficient is related to the excess chemical potential, which is computed using the Widom´s test particle method. Detailed information about these methods can be found elsewhere[59].

3. Results

We computed adsorption isotherms of carbon monoxide in metal-organic frameworks at 298 K for a range of pressure that spans from 1 to 10^5 kPa. The adsorption isotherms comparing the different models of carbon monoxide in Cu-BTC and IRMOF-1 are shown in Figure 1. The model proposed by Piper *et al.* provides the highest adsorption, followed by our model and the generic model from UFF and finally by the one proposed by Straub and Kaplus. These discrepancies can be attributed to the different topologies of the frameworks. The sensitiveness on the adsorption by the different models seems to be directly related to the shape and size of the pores. To validate this theory we performed additional simulations in MIL-47. This structure is characterised
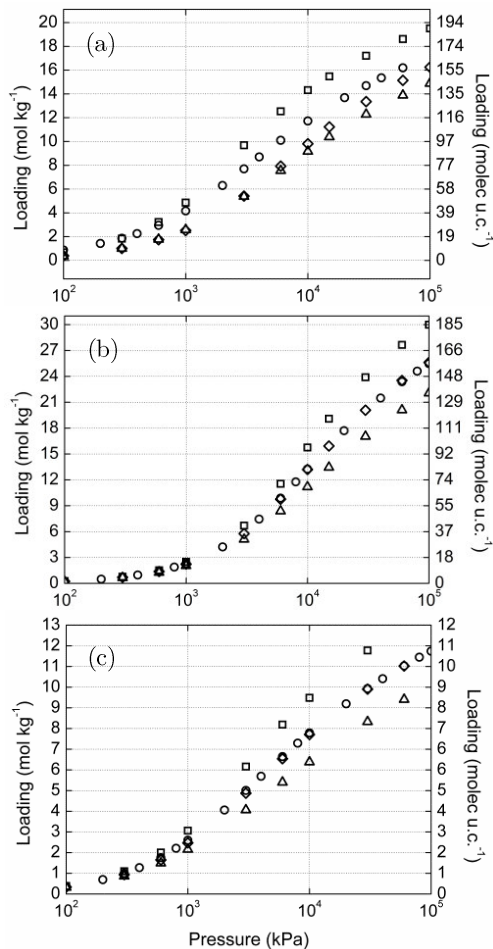
Figure 1. Adsorption isotherms of carbon monoxide in (a) Cu-BTC, (b) IRMOF-1 and (c) MIL-47 at 298K. The isotherms were computed using the models provided by Piper *et al.*[44] (squares), Straub and Karplus[45] (triangles), the UFF-based force field[36] (rhombus) and the model developed in this work (circles). The error bars are smaller than the symbol size.

by channels with diamond shape in one direction, generated by vanadium metallic centres linked by organic ligands 1,4-benzenedicarboxilate. The group of Feréy was the first reporting this framework from the family of

Table 2. Henry coefficients, energies and entropies of adsorption computed for carbon monoxide in Cu-BTC, IRMOF-1 and MIL-47 using different models. Numbers in brackets give the statistical errors in the last digit.

	K_H (mol/kg/Pa)	dU (kJ/mol)	dH (kJ/mol)	dA (kJ/mol)	dG (kJ/mol)	dS (J/K/mol)
Cu-BTC						
Ref. 44	$7.4\ 10^{-6}$ (1)	-15.75 (1)	-18.23 (1)	-6.90 (3)	-9.38 (3)	-29.68 (5)
Ref. 45	$4.0\ 10^{-6}$ (2)	-11.88 (1)	-14.36 (1)	-5.36 (1)	-7.84 (1)	-21.88 (1)
Ref. 36	$4.4\ 10^{-6}$ (2)	-12.48 (3)	-14.96 (3)	-5.62 (1)	-8.09 (1)	-23.04 (2)
This work	$1.4\ 10^{-5}$ (1)	-17.35 (3)	-19.83 (3)	-8.43 (2)	-10.91 (2)	-29.93 (1)
IRMOF-1						
Ref. 44	$2.6\ 10^{-6}$ (1)	-6.59 (1)	-9.06 (1)	-3.33 (1)	-5.81 (1)	-10.91 (8)
Ref. 45	$2.2\ 10^{-6}$ (4)	-6.15 (1)	-8.63 (1)	-2.93 (5)	-5.41 (5)	-10.79 (4)
Ref. 36	$2.4\ 10^{-6}$ (8)	-6.11 (1)	-8.59 (1)	-3.08 (8)	-5.56 (8)	-10.18 (7)
This work	$2.5\ 10^{-6}$ (4)	-6.44 (1)	-8.91 (1)	-3.21 (4)	-5.69 (4)	-10.81 (5)
MIL-47						
Ref. 44	$4.0\ 10^{-6}$ (2)	-10.49 (2)	-12.97 (2)	-5.66 (1)	-8.13 (1)	-16.22 (9)
Ref. 45	$3.3\ 10^{-6}$ (1)	-10.29 (1)	-12.77 (1)	-5.24 (1)	-7.72 (1)	-16.93 (7)
Ref. 36	$3.5\ 10^{-6}$ (1)	-10.10 (8)	-12.58 (8)	-5.32 (6)	-7.80 (6)	-16.03 (5)
This work	$3.8\ 10^{-6}$ (3)	-10.45 (3)	-12.93 (3)	-5.53 (2)	-8.01 (2)	-16.49 (2)

hybrid structures denominated MIL (Materials of the Institut Lavoisier)[60]. For the simulations we use the crystal structure from Alaerts *et al.*[61]. The simulation cell consists on a supercell of a = 27.27 Å, b = 32.29 Å and c = 27.88 Å. The force field was taken from DREIDING[56], except for vanadium which is taken from the UFF generic force field[52]. The atomic charges for MIL-47 are taken from previous works[62,63]. All these parameters are compiled in Appendix 4 (Table A1).

Adsorption properties at zero coverage for carbon monoxide in Cu-BTC, IRMOF-1 and MIL-47 are summarized in Table 2. It is interesting to highlight that, not only at zero coverage but also at low and intermediate values of pressure (Figure 1), the model seems rather insensitive to the adsorption except for Cu-BTC. The computed Henry coefficients, energies and entropies of adsorption in the low coverage regime are very much dependent on the size of the cages. We observe differences of up to 30% in the heat of adsorption for the structure with small cages (Cu-BTC). However, these differences are negligible for structures with larger cages such as IRMOF-1 and MIL-47.

At high pressure (Figure 1) the adsorption obtained for the different models is directly related to the size of the cage, the critical temperature, the vapour pressure and the liquid density of the adsorbate. Hence, we obtain the higher values of adsorption for the structure with larger cages, i.e. IRMOF-
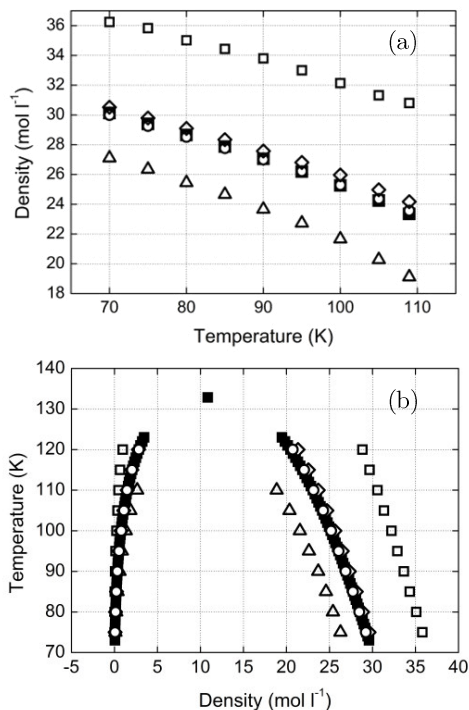
Figure 2. Comparison of experimental[54] (full squares) and simulation data obtained for (a) the liquid density of carbon monoxide at 1 MPa and (b) the vapour-liquid equilibrium curve. Simulations were performed using the models of Piper *et al.*[44] (empty squares), Straub and Karplus[45] (empty triangles), the UFF-based force field[36] (empty rhombus) and the model developed in this work (empty circles). Error bars are smaller than the symbols size.

1. This structure also gives the larger differences in adsorption depending on the model used for the adsorbate. Although the big cages of Cu-BTC are larger in diameter than these for MIL-47, we find that differences in adsorption due to variations in the carbon monoxide models are similar. This interesting result evidences that the adsorption in the structure is
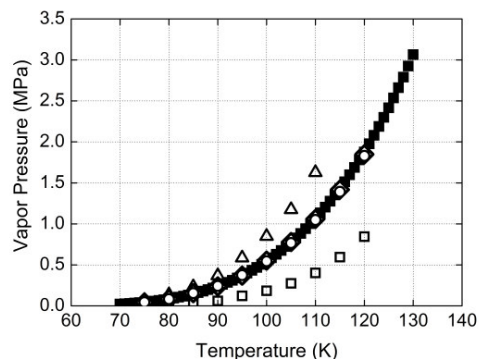
Figure 3. Vapour pressure curve obtained for carbon monoxide with the new model (empty circles) and the models proposed by Piper *et al.*[44] (empty squares) and Straub and Karplus[45] (empty triangles) and the UFF-based force field[36] (empty rhombus) The error bars are smaller than the symbol size. Experimental data are included for comparison[54] (full squares).

governed by the combination of the size and shape of the pore.

Among the different models, the one reported by Piper *et al.* gives the highest values for the liquid density and the critical temperature (Figure 2), leading to the higher adsorption in the three structures. This model overpredicts the liquid density of carbon monoxide at 1 MPa by 15%. On the contrary, the model of Straub and Karplus underpredicts this density by 10% for all range of temperatures computed. These two models are also unable to reproduce the experimental vapour pressure curve (Figure 3) and the experimental critical parameters. The critical parameters were obtained for all the models using the law of rectilinear diameters[64-67] and are compiled in Table 3. It is interesting to note that the UFF-based model reproduces the vapour-liquid

equilibrium curve, vapour pressures and the liquid density of carbon monoxide at 1 MPa as shown in Figures 2 and 3.

In order to compare with experimental data, excess adsorption isotherms of carbon monoxide in Cu-BTC and IRMOF-1 were computed with the models that reproduce the experimental properties of the fluid. The isotherms obtained with the new model are in very good agreement with the experiment (Figure 4). The isotherms computed with the model based on the UFF force field underpredict experimental data in Cu-BTC. To estimate the effect in the adsorption of both, dipole moment and van der Waals interactions we have performed additional simulations using (a) the UFF-based model with the experimental dipole and (b) our new model with a dipole of 0.58 D. As shown in Figure A1 in Appendix 4, the adsorption of carbon monoxide using the UFF-based model does not depend on the effect of the dipole. However, simulations provide higher adsorption when we increase the dipole moment of our model. Since the UFF-based model is able to reproduce the vapour liquid equilibrium curve of carbon monoxide with both set of charges, we can conclude that the van der Waals interactions shield the effect of the dipole moment in this model.

The two types of cages in Cu-BTC create different adsorption sites that are very sensitive to small variations in the polarity of the adsorbate[16,23,47,48]. As this model, based on the UFF generic force field, is not able to reproduce the experimental adsorption of carbon monoxide in Cu-BTC or the

Table 3. Comparison of the experimental critical parameters of carbon monoxide with the values obtained for all the models using the law of rectilinear diameters[64-67].

	T_C (K)	D_C (mol/l)	P_C (MPa)
Experimental	132.850	10.850	3.494
This work	134.098	10.815	3.528
Ref. 44	150.742	12.117	6.871
Ref. 45	121.275	9.955	3.095
Ref. 35	135.131	11.052	3.587
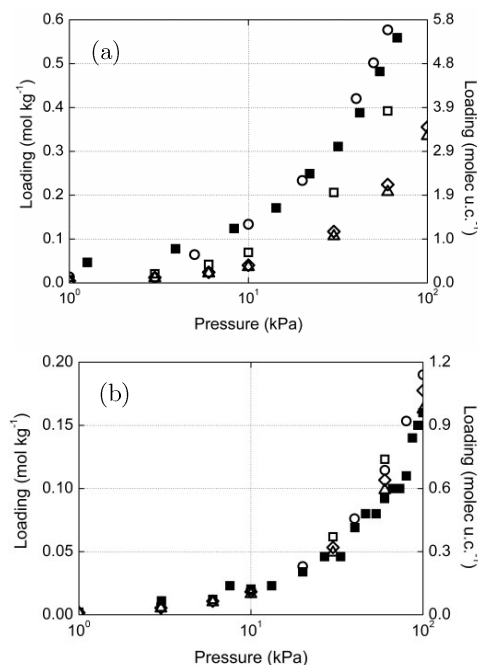
Figure 4. Excess adsorption obtained for carbon monoxide at 298 K in (a) Cu-BTC and (b) IRMOF-1. The isotherms were computed using the new model (empty circles), the UFF-based force field[36] (empty rhombus), the model proposed by Piper *et al.*[44] (empty squares) and the model proposed by Straub and Karplus[45] (empty triangles). The error bars are smaller than the symbol size. Experimental data[38,41] are included for comparison (full squares).

experimental dipole of the molecule, the remaining part of this work will be focus on the results obtained with the new model.

To proper reproduce adsorption one should be able to predict not only experimental isotherms but also the preferential sites for carbon monoxide in the structure. Hence, we analysed the preferential adsorption sites of the molecules in Cu-BTC and IRMOF-1. We considered for Cu-BTC the following different preferential sites of adsorption: (1) small cages S1, as spheres with 9.5 Å in diameter located at the centre of the small pore; (2) big cages L2, as an sphere centred at the pore with inner surface conformed by the benzene rings and 12 Å in diameter; (3) big cages L3, as spheres located at the pores with the hydrogen atoms of BTC pointing to the centre of the pore, also with 12 Å in diameter and (4) windows that communicate S1 and L3 are defined as a crowns surrounding sites S1 with radius of 1.8 Å larger than S1. The rest of the molecules would be considered as located at the windows that communicate the big cages (L2 and L3). In IRMOF-1 we considered three preferential adsorption sites, defining L1 and L2 as spheres located in both types of cavities -differenced by the orientation of the linkers- and with radius of 5.5 and 7.5 Å respectively. We

also considered communicating windows between cages.

Detailed analysis on the distribution of the molecules in the different cavities of each structure, shows that for Cu-BTC and low pressures most of the molecules are adsorbed in the small cages S1 (42.61%) and in the L2 cages (30.42%), followed by the L3 cages (12.23 %) with a similar percentage of occupancy than the windows (14.73%). The computed Henry coefficients and heats of adsorption for this system prove S1 to be the preferential adsorption site at low pressure (Table 4). An increase of the pressure leads to an increase on the adsorption in all sites. However, the percentage of molecules that fill the cages follows different trend. This percentage decreases for S1, remains constant for L2, and decreases for L3. Tables and histograms with detailed information on these occupancies can be found in Appendix 4 (Figure A2).

According to Henry coefficients and heats of adsorption listed in Table 4, carbon monoxide preferentially goes to L2 in IRMOF-1. The preference of this molecule for L2 is also observed for all the range of pressures considered in this work. On the other hand, an increment of pressure provokes the increase of the percentage of molecules that fill cages L1 and the decrease of the percentage in L2 (see Figure A3 in Appendix 4).

Table 4. Henry coefficients, energies and entropies of adsorption at zero coverage computed for carbon monoxide in Cu-BTC and IRMOF-1. The properties were also computed for each site (including the windows) by blocking the rest of cavities. Numbers in brackets give the statistical errors in the last digit.

	K_H (mol/kg/Pa)	dU (kJ/mol)	dH (kJ/mol)	dA (kJ/mol)	dG (kJ/mol)	dS (J/K/mol)
Cu-BTC	$1.4\ 10^{-5}$ (1)	-17.33 (3)	-19.80 (3)	-8.42 (2)	-10.90 (2)	-29.88 (1)
S1	$1.1\ 10^{-5}$ (2)	-19.75 (1)	-22.23 (1)	-7.78 (4)	-10.25 (4)	-40.19 (1)
L2	$2.3\ 10^{-6}$ (5)	-10.03 (1)	-12.51 (1)	-4.01 (5)	-6.49 (5)	-20.18 (4)
L3	$1.4\ 10^{-6}$ (7)	-8.17 (2)	-10.65 (2)	-2.76 (1)	-5.24 (1)	-18.15 (1)
windows	$2.9\ 10^{-7}$ (5)	-9.71 (2)	-12.19 (2)	1.18 (4)	-1.30 (4)	-36.53 (2)
IRMOF-1	$2.5\ 10^{-6}$ (4)	-6.43 (1)	-8.90 (1)	-3.21 (4)	-5.69 (4)	-10.80 (5)
L1	$4.8\ 10^{-7}$ (1)	-4.42 (1)	-6.90 (1)	0.87 (6)	-1.61 (6)	-17.75 (8)
L2	$2.0\ 10^{-6}$ (7)	-6.92 (5)	-9.40 (5)	-2.70 (8)	-5.18 (8)	-14.15 (4)
windows	$4.0\ 10^{-8}$ (6)	-5.66 (3)	-8.14 (3)	6.99 (4)	4.51 (4)	-42.47 (2)

The uptake capacity of Cu-BTC and IRMOF-1 for carbon monoxide was analysed using dehydrated and hydrated structures. Regarding the hydrated structures, we considered the highest water loading that each metal-organic framework is able to adsorb without losing stability[12,18-20,48]. For Cu-BTC we generated different structures attending to the number of molecules of water per atom of copper. Following the work reported by Gul-E-Noor *et al.*[12], we analysed four systems with 35.3%wt, 17.7%wt, 8.9%wt and 4.5%wt of water in the structure that correspond to 0.5, 1, 2 and 4 molecules of water per atom of copper. As the structure of IRMOF-1 collapses at water contents higher than 3.9%[18], we considered a system with 3.5%wt as the one with the highest water content being stable. We also analyse this percentage of water (3.5%wt) in Cu-BTC to compare the results in both structures. To study the behaviour of carbon monoxide capture using the IRMOF-1 structure with a lower quantity of water we considered another system with 1.7%wt. We have computed Henry coefficients, energies, and entropies of adsorption for all these systems (Table 5). At low water contents the Henry coefficients obtained for carbon monoxide in Cu-BTC and IRMOF-1 are not sensitive to the presence of water in the structure. The heats of adsorption obtained for IRMOF-1 are also independent on the presence of water in the structure. However, we observe differences on the energies of adsorption of carbon monoxide in the L3 cages of Cu-BTC. These differences progressively increase with the amount of water in the structure (see Appendix 4 Figure A4). The preferential adsorption site for water is L3. As shown in Figure 5 the presence and mobility, of water in these cages gradually hinders the adsorption of molecules of carbon monoxide, though the heats of adsorption computed in L3 are slightly higher for the structures containing water as a result of the interaction of carbon monoxide with the molecule of water located in the cavities. The presence of water in Cu-BTC also affects the

adsorption of carbon monoxide in cages S1 and L2, though to a lower extent. At a fixed value of pressure, low contents

of water seem to favour adsorption in S1. The reason is that the molecules of water, preferentially adsorbed in L3,

Tables 5. Henry coefficients, energies and entropies of adsorption at zero coverage computed for carbon monoxide in Cu-BTC and IRMOF-1 at different water contents. Simulations were performed for the whole structure and for the different cages. Numbers in brackets give the statistical errors in the last digit.

	K_H (mol/kg/Pa)	dU (kJ/mol)	dH (kJ/mol)	dA (kJ/mol)	dG (kJ/mol)	dS (J/K/mol)
Cu-BTC						
Cu-BTC (3.5%wt)	$1.4\ 10^{-5}$ (5)	-17.73 (2)	-20.21 (2)	-8.58 (1)	-11.06 (1)	-30.72 (1)
S1	$1.1\ 10^{-5}$ (1)	-19.92 (2)	-22.40 (2)	-7.99 (2)	-10.47 (2)	-40.03 (1)
L2	$2.4\ 10^{-6}$ (1)	-10.31 (1)	-12.79 (1)	-4.22 (1)	-6.70 (1)	-20.43 (7)
L3	$1.2\ 10^{-6}$ (5)	-8.76 (3)	-11.24 (3)	-2.45 (1)	-4.93 (1)	-21.18 (1)
windows	$3.1\ 10^{-7}$ (5)	-10.28 (3)	-12.76 (3)	0.88 (4)	-1.60 (4)	-37.47 (2)
Cu-BTC (4.5%wt)	$1.4\ 10^{-5}$ (1)	-17.86 (5)	-20.34 (5)	-8.62 (2)	-11.10 (2)	-30.99 (2)
S1	$1.1\ 10^{-5}$ (1)	-19.98 (2)	-22.46 (2)	-8.06 (3)	-10.53 (3)	-40.01 (1)
L2	$2.4\ 10^{-6}$ (8)	-10.38 (8)	-12.86 (8)	-4.25 (8)	-6.72 (8)	-20.58 (5)
L3	$1.1\ 10^{-6}$ (9)	-8.92 (2)	-11.40 (2)	-2.35 (2)	-4.83 (2)	-22.03 (1)
windows	$3.1\ 10^{-7}$ (2)	-10.40 (2)	-12.88 (2)	0.89 (1)	-1.58 (2)	-37.89 (1)
Cu-BTC (8.9%wt)	$1.5\ 10^{-5}$ (9)	-18.41 (2)	-20.89 (2)	-8.82 (1)	-11.30 (1)	-32.18 (7)
S1	$1.2\ 10^{-5}$ (7)	-20.37 (1)	-22.85 (1)	-8.28 (1)	-10.76 (1)	-40.57 (1)
L2	$2.6\ 10^{-6}$ (3)	-10.69 (8)	-13.17 (8)	-4.49 (3)	-6.97 (3)	-20.79 (4)
L3	$1.1\ 10^{-6}$ (3)	-9.52 (1)	-12.00 (1)	-2.00 (6)	-4.48 (6)	-25.23 (8)
windows	$3.3\ 10^{-7}$ (2)	-10.86 (2)	-13.34 (2)	0.60 (2)	-1.88 (2)	-38.47 (1)
Cu-BTC (17.7%wt)	$1.5\ 10^{-5}$ (3)	-19.21 (9)	-21.69 (9)	-8.99 (5)	-11.47 (5)	-34.30 (4)
S1	$1.2\ 10^{-5}$ (2)	-21.03 (5)	-23.50 (5)	-8.50 (4)	-10.98 (4)	-42.04 (3)
L2	$2.6\ 10^{-6}$ (6)	-11.19 (3)	-13.67 (3)	-4.67 (6)	-7.15 (6)	-21.88 (3)
L3	$6.3\ 10^{-7}$ (1)	-10.25 (6)	-12.73 (6)	-1.20 (7)	-3.68 (7)	-30.35 (4)
windows	$2.9\ 10^{-7}$ (8)	-11.55 (8)	-14.03 (8)	0.75 (7)	-1.73(7)	-41.27 (5)
Cu-BTC (35.3%wt)	$1.4\ 10^{-5}$ (5)	-20.26 (8)	-22.73 (8)	-9.30 (8)	-11.77(8)	-36.78 (5)
S1	$1.3\ 10^{-5}$ (5)	-21.44 (9)	-23.92 (9)	-8.97 (1)	-11.45(1)	-41.87 (7)
L2	$1.9\ 10^{-6}$ (2)	-11.88 (4)	-14.35 (4)	-4.22 (3)	-6.70 (3)	-25.69 (2)
L3	$2.4\ 10^{-7}$ (2)	-13.43 (1)	-15.91 (1)	0.86 (2)	-1.62 (2)	-47.96 (1)
windows	$1.7\ 10^{-7}$ (7)	-13.51 (3)	-15.99 (3)	1.75 (1)	-0.73 (1)	-51.20 (1)
IRMOF-1						
	K_H (mol/kg/Pa)	dU (kJ/mol)	dH (kJ/mol)	dA (kJ/mol)	dG (kJ/mol)	dS (J/K/mol)
IRMOF-1 (1.7%wt)	$2.4\ 10^{-6}$ (4)	-6.52 (1)	-9.00 (1)	-3.21 (4)	-5.69 (4)	-11.13 (6)
L1	$4.8\ 10^{-7}$ (2)	-4.48 (1)	-6.96 (1)	0.82 (1)	-1.65 (1)	-17.80 (9)
L2	$2.0\ 10^{-6}$ (6)	-7.03 (1)	-9.51 (1)	-2.69 (7)	-5.16 (7)	-14.59 (6)
windows	$4.1\ 10^{-8}$ (4)	-5.79 (4)	-8.26 (4)	6.91 (2)	4.43 (2)	-42.61 (2)
IRMOF-1 (3.5%wt)	$2.4\ 10^{-6}$ (3)	-6.62 (6)	-9.09 (6)	-3.20 (3)	-5.68 (3)	-11.45 (3)
L1	$4.7\ 10^{-7}$ (1)	-4.62 (7)	-7.10 (7)	0.81 (7)	-1.66 (7)	-18.23 (5)
L2	$1.9\ 10^{-6}$ (5)	-7.11 (9)	-9.59 (9)	-2.68 (7)	-5.16 (7)	-14.86 (5)
windows	$3.8\ 10^{-8}$ (6)	-5.79 (2)	-8.26 (2)	7.04 (4)	4.56 (4)	-43.04 (2)

displace the molecules of carbon monoxide to the small cages. The additional increase on the water content induce firstly the presence of some traces of water in S1 and L2 (10-20%wt) and secondly the displacement of all the molecules to L3 forming clusters (20-35%wt). It is for this reason that the adsorption of carbon monoxide is reduced at medium water contents, increasing again for the structures with larger water contents (see Appendix 4 Table A3).
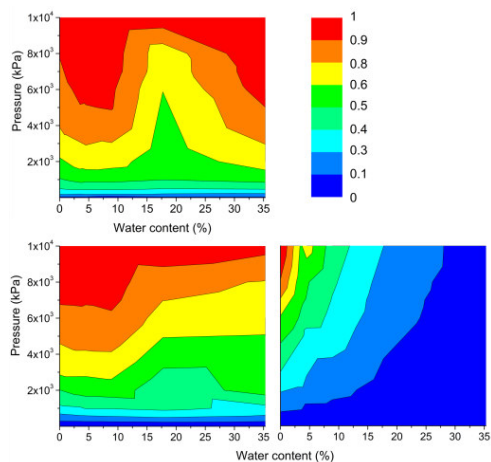

Figure 5. Carbon monoxide adsorbed in the cages S1 (top), L2 (bottom left) and L3 (bottom right) of Cu-BTC as a function of pressure and water content. The values of the maxima have been normalized to 1.
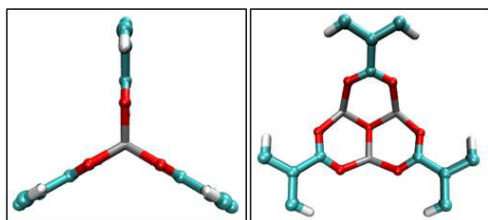
Figure 6. View of the metallic centers of IRMOF-1 from the inside of cage L1 (left) and L2 (right). The different atoms from the figure are: carbon (blue), oxygen (red), hydrogen (white) and zinc (grey).

In IRMOF-1 both, water and carbon monoxide are preferentially adsorbed in cavity L2. This is the larger of the two types of cavities of the structure and has the metal centres more exposed than in L1 (Figure 6). Due to this distribution, the interactions of molecules of water and carbon monoxide with the metal atoms of the framework are stronger in this cage. As the water content in IRMOF-1 is low (up to 3.5% wt), the adsorption of carbon monoxide in the structure is not influenced by the molecules of water (see Figures A5 and A6 and Table A4 in Appendix 4).

Conclusions

This work points out the differences on adsorption of carbon monoxide when using hydrated or dehydrated metal-organic frameworks. For the correct analysis of these differences an accurate and realistic model for carbon monoxide is needed. We have developed a model that reproduces the experimental dipole moment and bulk properties of the molecule such as vapour-liquid equilibrium curve, vapour pressures and liquid densities at 1MPa. Using this model, we have demonstrated that the presence of water can be used to enhance or to hinder the adsorption of carbon monoxide in the structure. This seems especially important in structures formed by cages of different size and shape. According to our results, it is possible to combine the topology of the framework and the polarity of the adsorbed molecules in order to obtain higher loadings. These findings could be further exploited to increase the efficiency of current adsorption and separation processes.

Bibliography

(1) Rowsell, J. L. C.; Yaghi, O. M. *Microporous and Mesoporous Materials* **2004**, *73*, 3.

(2) Li, J. R.; Kuppler, R. J.; Zhou, H. C. *Chemical Society Reviews* **2009**, *38*, 1477.

(3) Czaja, A. U.; Trukhan, N.; Muller, U. *Chemical Society Reviews* **2009**, *38*, 1284.

(4) Chui, S. S. Y.; Lo, S. M. F.; Charmant, J. P. H.; Orpen, A. G.; Williams, I. D. *Science* **1999**, *283*, 1148.

(5) Getzschmann, J.; Senkovska, I.; Wallacher, D.; Tovar, M.; Fairen-Jimenez, D.; Duren, T.; van Baten, J. M.; Krishna, R.; Kaskel, S. *Microporous and Mesoporous Materials* **2010**, *136*, 50.

(6) Eddaoudi, M.; Kim, J.; Rosi, N.; Vodak, D.; Wachter, J.; O'Keeffe, M.; Yaghi, O. M. *Science* **2002**, *295*, 469.

(7) Li, H.; Eddaoudi, M.; O'Keeffe, M.; Yaghi, O. M. *Nature* **1999**, *402*, 276.

(8) Li, Y. W.; Yang, R. T. *Aiche Journal* **2008**, *54*, 269.

(9) Liang, Z. J.; Marshall, M.; Chaffee, A. L. *Greenhouse Gas Control Technologies 9* **2009**, *1*, 1265.

(10) Liu, J.; Wang, Y.; Benin, A. I.; Jakubczak, P.; Willis, R. R.; LeVan, M. D. *Langmuir* **2010**, *26*, 14301.

(11) Henninger, S. K.; Schmidt, F. P.; Henning, H. M. *Applied Thermal Engineering* **2010**, *30*, 11.

(12) Gul-E-Noor, F.; Jee, B.; Pöppl, A.; Hartman, M. R.; Himsl, D.; Bertmer, M. *Phys. Chem. Chem. Phys.* **2011**.

(13) Kusgens, P.; Rose, M.; Senkovska, I.; Frode, H.; Henschel, A.; Siegle, S.; Kaskel, S. *Microporous and Mesoporous Materials* **2009**, *120*, 325.

(14) Grajciar, L.; Bludsky, O.; Nachtigall, P. *Journal of Physical Chemistry Letters* **2010**, *1*, 3354.

(15) Prestipino, C.; Regli, L.; Vitillo, J. G.; Bonino, F.; Damin, A.; Lamberti, C.; Zecchina, A.; Solari, P. L.; Kongshaug, K. O.; Bordiga, S. *Chemistry of Materials* **2006**, *18*, 1337.

(16) Castillo, J. M.; Vlugt, T. J. H.; Calero, S. *Journal of Physical Chemistry C* **2008**, *112*, 15934.

(17) Huang, L. M.; Wang, H. T.; Chen, J. X.; Wang, Z. B.; Sun, J. Y.; Zhao, D. Y.; Yan, Y. S. *Microporous and Mesoporous Materials* **2003**, *58*, 105.

(18) Greathouse, J. A.; Allendorf, M. D. *Journal of the American Chemical Society* **2006**, *128*, 13312.

(19) Bellarosa, L.; Calero, S.; Lopez, N. **2011**, *submitted*.

(20) Bellarosa, L.; Castillo-Sanchez, J. M.; Vlugt, T. J. H.; Calero, S.; Lopez, N. **2011**, *submitted*.

(21) Krishna, R.; van Baten, J. A. *Langmuir* **2010**, *26*, 3981.

(22) Yazaydin, A. O.; Snurr, R. Q.; Park, T. H.; Koh, K.; Liu, J.; LeVan, M. D.; Benin, A. I.; Jakubczak, P.; Lanuza, M.; Galloway, D. B.; Low, J. J.; Willis, R. R. *Journal of the American Chemical Society* **2009**, *131*, 18198.

(23) Martin-Calvo, A.; Garcia-Perez, E.; Castillo, J. M.; Calero, S. *Physical Chemistry Chemical Physics* **2008**, *10*, 7085.

(24) Yazaydin, A. O.; Benin, A. I.; Faheem, S. A.; Jakubczak, P.; Low, J. J.; Willis, R. R.; Snurr, R. Q. *Chemistry of Materials* **2009**, *21*, 1425.

(25) Millward, A. R.; Yaghi, O. M. *Journal of the American Chemical Society* **2005**, *127*, 17998.

(26) Yang, Q. Y.; Zhong, C. L.; Chen, J. F. *Journal of Physical Chemistry C* **2008**, *112*, 1562.

(27) Babarao, R.; Hu, Z. Q.; Jiang, J. W.; Chempath, S.; Sandler, S. I. *Langmuir* **2007**, *23*, 659.

(28) Babarao, R.; Jiang, J. W.; Sandler, S. I. *Langmuir* **2009**, *25*, 5239.

(29) Keskin, S.; Sholl, D. S. *Journal of Physical Chemistry C* **2007**, *111*, 14055.

(30) Alaerts, L.; Seguin, E.; Poelman, H.; Thibault-Starzyk, F.; Jacobs, P. A.; De Vos, D. E. *Chemistry-a European Journal* **2006**, *12*, 7353.

(31) Walton, K. S.; Millward, A. R.; Dubbeldam, D.; Frost, H.; Low, J. J.; Yaghi, O. M.; Snurr, R. Q. *Journal of the American Chemical Society* **2008**, *130*, 406.

(32) Yang, Q. Y.; Zhong, C. L. *Journal of Physical Chemistry B* **2006**, *110*, 17776.

(33) Liu, J. C.; Culp, J. T.; Natesakhawat, S.; Bockrath, B. C.; Zande, B.; Sankar, S. G.; Garberoglio, G.; Johnson, J. K. *Journal of Physical Chemistry C* **2007**, *111*, 9305.

(34) Britt, D.; Tranchemontagne, D.; Yaghi, O. M. *Proceedings of the National Academy of Sciences of the United States of America* **2008**, *105*, 11623.

(35) Deng, H. X.; Doonan, C. J.; Furukawa, H.; Ferreira, R. B.; Towne, J.; Knobler, C. B.; Wang, B.; Yaghi, O. M. *Science* **2010**, *327*, 846.

(36) Sirjoosingh, A.; Alavi, S.; Woo, T. K. *Journal of Physical Chemistry C* **2010**, *114*, 2171.

(37) Valenzano, L.; Civalleri, B.; Chavan, S.; Palomino, G. T.; Arean, C.; Bordiga, S. *Journal of Physical Chemistry C* **2010**, *114*, 11185.

(38) Wang, Q. M.; Shen, D. M.; Bulow, M.; Lau, M. L.; Deng, S. G.; Fitch, F. R.; Lemcoff, N. O.; Semanscin, J. *Microporous and Mesoporous Materials* **2002**, *55*, 217.

(39) Karra, J. R.; Walton, K. S. *Langmuir* **2008**, *24*, 8620.

(40) Wang, S.; Yang, Q. Y.; Zhong, C. L. *Separation and Purification Technology* **2008**, 30.

(41) Saha, D.; Deng, S. G. *Journal of Chemical and Engineering Data* **2009**, *54*, 2245.

(42) Karra, J. R.; Walton, K. S. *Journal of Physical Chemistry C* **2010**, *114*, 15735.

(43) Xu, Q.; Zhong, C. L. *Journal of Physical Chemistry C* **2010**, *114*, 5035.

(44) Piper, J.; Morrison, J. A.; Peters, C. *Molecular Physics* **1984**, *53*, 1463.

(45) Straub, J. E.; Karplus, M. *Chemical Physics* **1991**, *158*, 221.

(46) Garcia-Sanchez, A.; Ania, C. O.; Parra, J. B.; Dubbeldam, D.; Vlugt, T. J. H.; Krishna, R.; Calero, S. *Journal of Physical Chemistry C* **2009**, *113*, 8814.

(47) Calero, S.; Martin-Calvo, A.; Hamad, S.; Garcia-Perez, E. *Chemical Communications* **2011**, *47*, 508.

(48) Martin-Calvo, A.; Garcia-Perez, E.; Garcia-Sanchez, A.; Bueno-Perez, R.; Hamad, S.; Calero, S. *Phys. Chem. Chem. Phys.* **2011**.

(49) Garcia-Perez, E.; Gascon, J.; Morales-Florez, V.; Castillo, J. M.; Kapteijn, F.; Calero, S. *Langmuir* **2009**, *25*, 1725.

(50) Calero, S.; Dubbeldam, D.; Krishna, R.; Smit, B.; Vlugt, T. J. H.; Denayer, J. F. M.; Martens, J. A.; Maesen, T. L. M. *Journal of the American Chemical Society* **2004**, *126*, 11377.

(51) Dubbeldam, D.; Calero, S.; Vlugt, T. J. H.; Krishna, R.; Maesen, T. L. M.; Smit, B. *Journal of Physical Chemistry B* **2004**, *108*, 12301.

(52) Rappe, A. K.; Casewit, C. J.; Colwell, K. S.; Goddard, W. A.; Skiff, W. M. *Journal of the American Chemical Society* **1992**, *114*, 10024.

(53) Burrus, C. A. *Journal of Chemical Physics* **1959**, *31*, 1270.

(54) http://webbook.nist.gov/chemistry/.

(55) Rick, S. W. *Journal of Chemical Physics* **2004**, *120*, 6085.

(56) Mayo, S. L.; Olafson, B. D.; Goddard, W. A. *Journal of Physical Chemistry* **1990**, *94*, 8897.

(57) Frost, H.; Snurr, R. Q. *Journal of Physical Chemistry C* **2007**, *111*, 18794.

(58) Duren, T.; Sarkisov, L.; Yaghi, O. M.; Snurr, R. Q. *Langmuir* **2004**, *20*, 2683.

(59) Myers, A. L.; Monson, P. A. *Langmuir* **2002**, *18*, 10261.

(60) Barthelet, K.; Marrot, J.; Riou, D.; Ferey, G. *Angewandte Chemie-International Edition* **2001**, *41*, 281.

(61) Alaerts, L.; Kirschhock, C. E. A.; Maes, M.; van der Veen, M. A.; Finsy, V.; Depla, A.; Martens, J. A.; Baron, G. V.; Jacobs, P. A.; Denayer, J. E. M.; De Vos, D. E. *Angewandte Chemie-International Edition* **2007**, *46*, 4293.

(62) Bueno-Perez, R.; Garcia-Perez, E.; Gutierrez-Sevillano, J. J.; Merkling, P. J.; Calero, S. *Adsorption Science & Technology* **2010**, *28*, 823.

(63) Castillo, J. M.; Vlugt, T. J. H.; Calero, S. *Journal of Physical Chemistry C* **2009**, *113*, 20869.

(64) Martin, M. G.; Siepmann, J. I. *Journal of Physical Chemistry B* **1998**, *102*, 2569.

(65) Rowlinson, J. S.; Widom, B. *Molecular Theory of Capillarity*; Oxford University Press: New York, 1989.

(66) Rowlinson, J. S.; Swinton, F. L. *Liquids and Liquid Mixtures*; 3rd ed.; Butterworth: London, 1982.

(67) Atkins, P. W. *Physical Chemistry*; Oxford Higher Education: New York, 1990.

(68) Chowdhury, P.; Bikkina, C.; Meister, D.; Dreisbach, F.; Gumma, S. *Microporous and Mesoporous Materials* **2009**, *117*, 406.

(69) Garberoglio, G.; Skoulidas, A. I.; Johnson, J. K. *Journal of Physical Chemistry B* **2005**, *109*, 13094.

(70) Skoulidas, A. I. *Journal of the American Chemical Society* **2004**, *126*, 1356.

(71) Skoulidas, A. I.; Sholl, D. S. *Journal of Physical Chemistry B* **2005**, *109*, 15760.

(72) Yang, Q. Y.; Xue, C. Y.; Zhong, C. L.; Chen, J. F. *Aiche Journal* **2007**, *53*, 2832.

Insights on the Anomalous Adsorption of Carbon Dioxide in LTA Zeolites

Ana Martín-Calvo, José B. Parra, Conchi O. Ania
and Sofía Calero

6

We use a combination of experiments and molecular simulations to address the discrepancies of the force fields available in the literature to accurately reproduce CO_2 adsorption in zeolites with high density of aluminium atoms and extra-framework cations. We attribute these discrepancies to the fact that previous force fields are not parameterized to take into account the formation of carbonate-like complexes in these zeolites during CO_2 adsorption. Our data show that the formation of carbonate-like complexes has a marked effect on the accessible porous structure of the zeolite and the strength is controlled by the density and nature of extra framework cations. Strong carbonate-like complexes are formed in zeolite topologies containing high density of sodium, whereas bivalent cations give rise to more labile complexes. We provide a new set of parameters capable to reproduce the experimental adsorption in these systems. Our approach consists on the modification of the partial charges of the atoms of the zeolite that are directly involved in the formation of the surface complexes (oxygen atoms and cations). The new set of charges combined with our previous transferable force field reproduces the experimental adsorption in structures containing carbon dioxide-cation complexes.

1. Introduction

Carbon dioxide adsorption and separation over porous solids has received much attention in the last decades. In part this has been driven by the need to develop cost-efficient CO_2 capture technologies to mitigate the consequences of climate change and the improvement of gas separation processes of industrial interest (i.e., natural gas cleaning, CO_2 separation in coal combustion processes). Among porous solids, different materials have been extensively investigated for the adsorption and selective separation of carbon dioxide, being activated carbons and zeolites the most effective structures due to their thermal stability and large surface areas[1-3].

Zeolites are molecular sieves formed by TO_4 tetrahedra (T can be either Si or Al) that are connected to each other generating 3D structures with different topologies. The charge imbalance due to the presence of aluminium in the framework is compensated by extra-framework cations. The nature, number and distribution of the extra-framework cations affect the ion exchange properties of the zeolites, the basicity and the electric field in the cavities of the zeolites. These parameters tend to vary inversely with the Si/Al ratio of the framework. Besides other experimental conditions (such as pressure, temperature and moisture), the topology and composition of the zeolite govern the forces involved in the adsorption process and the overall

adsorption efficiency. For instance, at low pressure the amount of CO_2 adsorbed appears to be highly influenced by the nature and density of the cations inside the zeolite pores[4,5], whereas the pore shape and volume appear to control the adsorption capacity at high pressures[6].

Molecular simulation is a powerful tool to accurately predict adsorption and diffusion processes in crystalline porous materials[7] and has been extensively used for predicting the adsorption of carbon dioxide in zeolites[5,8-15]. A number of force fields modelling the adsorption of carbon dioxide in zeolites can be found in literature, most of them only applicable to all-silica structures ($Si/Al=\infty$)[8,11,16,17] and fewer to structures containing aluminium and extra-framework cations (mostly sodium). In a previous work we addressed the lack of transferability between the available force fields to different zeolite framework types and Si/Al ratios, providing a force field transferable to structures with Si/Al ratio ranging from 1 to ∞. This force field accurately reproduces CO_2 adsorption in structures with different aluminium content (FAU, MFI and MOR) and sodium. However, some discrepancies with experimental data were found for LTA-type structures[16]. With this information in mind, the following step is to understand the mechanism that governs CO_2 adsorption in zeolites with high aluminium content. Therefore the goal of this paper is to elucidate the factors that influence this adsorption behaviour of carbon dioxide in zeolites with high aluminium content such as LTA and NaX and to describe

the methodology for the development of additional force field parameters for these structures based on the combination of simulation techniques and experimental data.

2. Experimental details

Zeolites with faujasite, FAU, (NaY, NaX) and Linde Type A, LTA, (LTA4A, LTA5A) topology were purchased from Zeolyst Int. and Fluka, respectively. CO_2 adsorption isotherms at temperatures near ambient (i.e., 253-323 K) were performed in a volumetric analyser (ASAP 2020, Micromeritics) in the pressure range from 10^{-2} up to 120 kPa. The instrument was equipped with a turbo molecular vacuum pump and three pressure transducers (0.13, 1.33, and 133 kPa, uncertainty within 0.15% of each reading) to enhance the sensitivity in the low pressure range. Before the adsorption measurements, the zeolites were *in situ* degassed at 623 K (1 K/min) under high vacuum (ca. 10^{-3} kPa) for 17 h to remove moisture.

For the experiments carried out after exposure in carbon dioxide, the zeolites were degassed as indicated above and then put in contact with CO_2 at 298 K at 120 kPa for 24 h to allow the saturation of the zeolite with the gas and the formation of surface carbonates[18,19]. Subsequently the samples were evacuated at 273 K for 2 hours under the turbomolecular pump vacuum and then hydrogen adsorption isotherms at 77 K were measured. This experimental protocol allowed assuring that the carbonate species formed during the saturation in CO_2 are not removed during the subsequent

physisorption measurements with H_2 at 77 K. By doing this, we can explore the effect of the carbonates formed on the porosity of the zeolites. The choice of hydrogen as the gas probe for the adsorption isotherms on the samples previously exposed to CO_2 was based on its accessibility to the porous structure of all studied zeolites at cryogenic temperatures (i.e., nitrogen or argon have kinetic restrictions to enter LTA4A at such low temperatures)[20-22].

All of the isotherms were done in triplicate and the data is reproducible with an error below 0.1%. The temperature of the isotherms was controlled using a liquid nitrogen bath (77 K) and a thermostatic circulating oil bath (253-323 K). Ultrahigh purity gases (i.e., 99.999 and 99.995 % for H_2 and CO_2, respectively) were supplied by Air Products.

3. Simulation methods and models

Adsorption isotherms were obtained using Monte Carlo simulations in the grand canonical ensemble, where chemical potential, volume, and temperature are imposed. From the chemical potential we obtain the fugacity and this is directly related to pressure by the fugacity coefficient. During the simulations, random moves were performed in cycles finding the most favourable energy configuration of the system and allowing one of the following trial moves in each cycle: rotation, translation and reinsertion. To compare simulated and experimental isotherms, absolute adsorption is converted to excess adsorption[23,24]. The excess adsorption (n_{exc}) is obtained by

relation of the absolute adsorption (n_{abs}) with the pore volume of the adsorbent (V^g) and the molar density of the bulk gas phase (ρ^g), using the following expression:

$$n_{exc} = n_{abs} - V^g \, \rho^g$$

Isosteric heats of adsorption and Henry coefficients were calculated using Monte Carlo simulations in the canonical ensemble fixing the number of particles, the volume and the temperature. The simulations were carried out in the limit of zero loading, providing important information about the strength of the interaction of the adsorbate with the structure. These energies were computed using the Widom test particle method[7]. Simulations were performed with the in-house RASPA code developed by D. Dubbeldam, S. Calero, D. E. Ellis and R. Q. Snurr[25]. This code has been extensively tested and validated with a large number of experimental and simulation data[16,26-28].

Zeolites were modelled as rigid frameworks composed by silicon, aluminium and oxygen atoms and using their crystallographic positions. The zeolite structure is considered rigid, as previous studies demonstrated that flexibility of the framework has a minor effect on the adsorption of small molecules for the range of temperatures used in this work[6,29]. LTA and FAU zeolites have a cubic unit cell dimension of 24.555 Å and 25.028 Å, respectively[30,31]. They are formed by sodalite cages connected to each other by prisms that are hexagonal in FAU and cubic in LTA. In both structures sodalites describe supercages surrounded

by 10 and 8 sodalites in FAU and LTA, respectively. FAU-type zeolites have been labelled either X or Y depending on their framework aluminium density. Zeolite X contains between 96 and 77 aluminium atoms per unit cell, whereas zeolite Y contains fewer than 77 aluminium atoms per unit cell. The initial distribution of the extra-framework cations in the structure has an important role into the adsorption process[29]. Therefore for LTA we use the experimental position of the cations reported by Pluth and Smith for sodium[30] and by Firor and Seff for calcium[32]. According to these works the cations from LTA4A are located in the supercages of the zeolite, coordinated by three types of aluminosilicate rings and distributed among three different sites: a) at the centre of the 6-member-rings of the sodalites, b) at the 8-member-rings windows between supercages and c) opposite to the 4-member-rings of the cubic prisms. In the case of LTA5A the cations can be found either in the supercages or in the sodalites leading to four possible sites: a) at the 8-member-rings windows, b) at the centre of the 6-member-rings of the sodalites and two more sites resulting from the displacement of the latter to the supercages (c) or to the sodalites (d). However calcium cations are only coordinated to the 6-rings of the sodalites and not to the windows between supercages (8-member-rings). Regarding the extra-framework cations distribution in FAU, their precise crystallographic location remains uncertain[31,33,34]. The distribution of these cations highly depends on different factors such as humidity or the nature of the adsorbate. Six sites have been
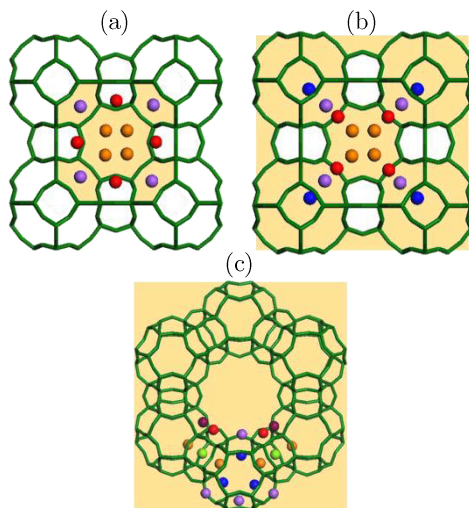
Figure 1. Positions of the cations in (a) LTA4A, (b) LTA5A and (c) FAU. In LTA4A cations are located at the 6-rings of the sodalites (purple), at the 8-rings windows between supercages (orange) and opposite to 4-rings of the cubic prisms (red). In LTA5A cations can be found at the 8-rings windows between supercages (orange), at the 6-rings of the sodalities (purple) and the latter but displaced to the supercages (red) or to the sodalites (blue). In FAU cations are distributed at the center of the hexagonal prisms (green), inside the sodalites (orange and blue) and inside the supercages at the center of the hexagonal prisms but displaced into the supercage (red), on a twofold axis opposing a 4-ring between two 12-rings (purple) and at the center of the sodalite but displaced to the supercage (violet).

identified for sodium cations: one site located at the centre of the hexagonal prisms, two sites inside the sodalites, and other three sites inside the supercages of the structure. The sites inside the supercages are (1) at the centre of the hexagonal prisms but displaced into the supercage, (2) on a twofold axis opposing a 4-member-ring

(from the hexagonal prism and the sodalite) between two 12-member-rings (window between supercages) and (3) at the centre of the sodalite but displaced to the supercage. A representation of the positions of the cations in LTA and FAU zeolites is shown in Figure 1.

In order to ensure the influence of the alumina atoms and the cations distribution inside the structures we have studied the adsorption of carbon dioxide on NaY (with 54 Na$^+$/u.c.) in a variety of five different random configurations. The results obtained show that there are no differences on the adsorption values obtained. These results agree with previous studies on the adsorption of small gases where the insensitiveness of NaY to the amount and positions of the alumina atoms (and sodium cations) is studied[35,36].

Carbon dioxide is modelled as a rigid molecule with three Lennard-Jones sites and point charges at each atom to reproduce the polarity of the molecule. The Lennard Jones parameters of the carbon and oxygen atoms were fitted to reproduce the experimental vapour-liquid phase equilibrium, while their combination (C-O) is obtained by Lorentz-Berthelot mixing rules.[16]

We use Lennard-Jones and Coulombic potentials to define the interactions of the structure with the extra-framework cations and with the adsorbates. These potentials are cut at 12 Å and shifted to zero. Coulombic interactions are computed with the Ewald summation method with a relative precision of 10^{-6}. For adsorbate-adsorbent, adsorbate-sodium and sodium-adsorbent, we use

Table 1. Lennard-Jones parameters used in this work.

Atom 1	Atom 2	ε/k_B (K)	σ (Å)
C_co2	C_co2	29.933	2.745
O_co2	O_co2	85.671	3.017
C_co2	O_zeo	37.595	3.511
O_co2	O_zeo	78.980	3.237
Na	O_zeo	23.000	3.400
Ca	O_zeo	18.000	3.450
C_co2	Na	362.292	3.320
O_co2	Na	200.831	2.758
C_co2	Ca	362.292	3.320
O_co2	Ca	200.831	2.758

the set of parameters previously developed by Calero et al., as this set is transferable for different zeolites[16]. The interactions involving calcium as extra framework cations were obtained in this work. The Lennard-Jones parameters for all interactions used in this work are collected in Table 1.

4. Results

As mentioned above, the force field reported by Calero et al. accurately reproduces CO_2 adsorption in zeolites with different aluminium content (FAU, MFI and MOR) and sodium cations. However, some discrepancies with experimental data were found for structures with high density of aluminium atoms and extra-framework cations such as LTA4A and NaX[16].

FAU and LTA type zeolites contain both silicon and aluminium atoms. The Si/Al ratio generates different FAU structures (zeolite X and Y for Si/Al ratio of 1-1.5 and >1.5, respectively)[37], while for LTA this ratio is always 1. Not only topological and composition

differences but also the density and nature of the extra framework cations are important. While FAU structures (NaX and NaY) only have sodium as extra framework cation, LTA zeolites (4A and 5A) can combine both sodium and calcium. These differences result in the above-mentioned discrepancy in predicting carbon dioxide adsorption.

According to the literature, the molecular mechanism that explains CO_2 adsorption in zeolites involves both physical and chemical adsorption, the latter through the interactions of carbon dioxide molecules with the extra-framework cations and the oxygen of the zeolite. The formation of linear and/or bent configurations of bridged adsorption complexes has been reported for different alkali-metal cations, where the oxygen atoms of CO_2 interact with the cation sites[2,38-42]. For instance, carbonate-like species in various configurations have been reported for NaX zeolite[43-45] and attributed to the basic character of the oxygen atoms of the structure. The phenomenon seems to be less perceptible in NaY zeolite, likely as a result of its lower but yet non negligible aluminium content[46]. The linear complexes Na-CO_2 formed in NaY are easily removed by degassing at room temperature. More recently Montanari and Busca[2,47] demonstrated the formation of CO_2-Na^+ complexes in Na-LTA that induce a perturbation of the Si-O-Al bonds. They also reported that linear CO_2-complexes desorb completely by degassing at room temperature, while other carbonate species resist degassing at 420 K. A similar behaviour has been observed for Ca,Na-LTA (LTA5A) but with less formation of

carbonate species. Combining IR spectroscopy, gas adsorption and theoretical approaches, Zukal et $al.$[19] showed that interactions between CO_2 molecules and Na-LTA zeolite depend on the gas loading. At low coverage carbon dioxide forms complexes by interaction with three sodium cations, whereas at higher loadings only two cations interact with each molecule of carbon dioxide.

In this work we show that the formation of carbonate-like complexes during CO_2 adsorption has an effect on the porous structure of the zeolite and on the gas-host interactions. This effect is not taken into account in previous force fields and therefore they are unable to predict the adsorption capacity of carbon dioxide in this type of structures.

To quantify the likely effect of the CO_2-complexes on the accessible pore void of the zeolites, physisorption measurements (hydrogen at 77 K) were performed on the samples previously exposed to CO_2. We have selected NaX and LTA4A with 96 sodium cations per unit cell, NaY with 54 sodium cations per unit cell, and LTA5A with 32 sodium cations and 32 calcium cations per unit cell. This experimental approach was designed to assure the formation of carbonates and avoid their decomposition in the degassing step at 273 K preceding the measurements of the adsorption isotherms. Also, hydrogen was chosen as the gas probe due to its smaller molecular diameter compared to the usual gases employed for textural characterisation (i.e., nitrogen or argon have kinetic

restrictions to enter Na-LTA at cryogenic temperatures).

Figure 2 shows the adsorption isotherms of hydrogen in FAU zeolites (NaY and NaX) at 77 K. For each structure we compare the results obtained in the bare structure and after saturation in CO_2 atmosphere. No differences are observed for NaY with the adsorption isotherms corresponding to the bare and CO_2-saturated structure completely overlapping in the whole range of pressure. This indicates that CO_2 adsorption does not alter the accessible pore volume of the zeolite, either because surface-complexes are not formed or are removed during the degassing step at low temperature before the measurements. For NaX the loading of hydrogen in the bare structure is significantly higher than this after exposure to carbon dioxide. This drop in the hydrogen uptake accounts for the amount of carbon

dioxide that remains in the pores of the zeolite due to the formation of carbonate-like complex that are not easily removed. Several experimental evidences for the formation of these complexes in NaX and NaY structures have been reported[43-45]. Our work supports these studies pointing out that the Si/Al ratio regulates the strength of the complexes. In structures with low aluminium content (i.e., NaY, Si/Al >1.5), the complexes can be easily removed by degassing at low temperature, thus they cannot be quantified by physisorption measurements. Contrariwise for Si/Al=1 (NaX) the interactions of carbon dioxide with the cations are stronger, resisting higher degassing temperatures and allowing us to quantify a ca. 8% drop in the accessible pore volume of the zeolite after CO_2 exposure, due to the formation of the carbonate-like complexes.
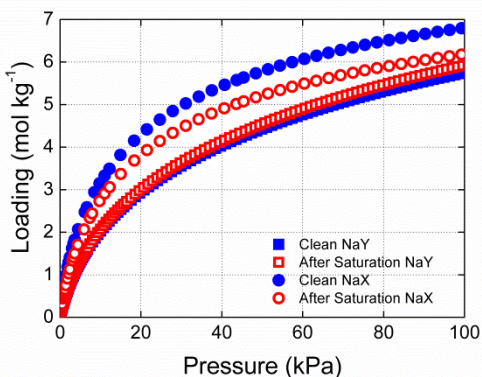
Figure 2. Adsorption isotherms of hydrogen in NaY with 54 Na^+/u.c. (squares) and NaX with 96 Na^+/u.c. (circles) at 77 K. The isotherms were measured in the bare structures (full symbols) and in the structures resulting from carbon dioxide saturation and degassing (empty symbols).
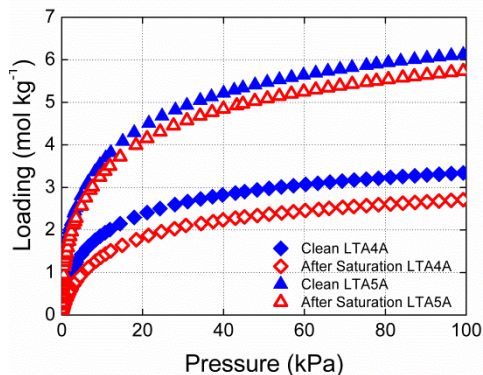
Figure 3. Adsorption isotherms of hydrogen in LTA4A with 96 Na^+/u.c. (diamonds) and LTA5A with 32 Na^+/u.c. and 32 Ca^{2+}/u.c. (triangles) at 77 K. The isotherms were measured in the bare structures (full symbols) and in the structures resulting from carbon dioxide saturation and degassing (empty symbols).

The adsorption isotherms of hydrogen in LTA structures (Figure 3) follow similar behaviour than in NaX, with a fall in the gas uptake after CO_2 exposure that evidences the formation of strong carbonate-like complexes in both LTA4A and LTA5A zeolites. Interestingly, the decrease in the amount of hydrogen adsorbed in the bare and CO_2-exposed structures was larger for LTA4A (ca. 18%) than for LTA5A (ca. 6%). As both structures have the same Si/Al ratio (Si/Al=1), this finding confirms the outstanding influence of the amount and nature of the extra framework cation. Due to the different polarity of sodium and calcium cations, the density of extra framework cations is higher in LTA4A (96 Na^+/u.c.) than in LTA5A (64 cations per unit cell), therefore, the amount of carbonate-like complexes is expected to be larger in the former than the latter. This is in agreement with the different hydrogen uptake shown in Figure 3. Since differences between both LTA structures also concern the charge of the extra-framework cations (LTA5A with 32 Na^+/u.c. and 32 Ca^{2+}/u.c.), it may be inferred that bivalent cations reduce the formation of carbonate-complexes and those formed are more labile, thus easily desorbed upon degassing.

Figure 4 shows our experimental and computed adsorption isotherms of carbon dioxide in LTA4A at 273 K. Available adsorption data were also added for comparison[19]. Simulations were performed using our previous force field[16]. This force field is expected to be transferable between zeolite topologies and can also be applied to all possible
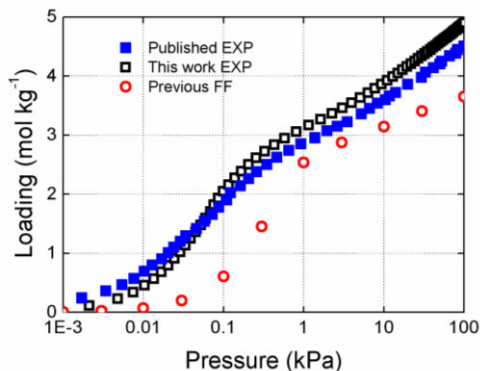
Figure 4. Experimental (squares) and simulated (circles) adsorption isotherms of CO_2 at 273 K in LTA4A (96 Na^+/u.c.). Simulations were performed using our previous force field[16]. The results obtained in this work (empty symbols) are compared with experimental data taken from the literature for validation[19] (full symbols).

Si/Al ratios with sodium as extra-framework cation. However, as shown in Figure 4, it fails to reproduce the experimental adsorption isotherms of carbon dioxide in LTA4A in the whole range of pressure. Simulations underpredict experimental adsorption, especially at low pressure and at saturation. We attribute these discrepancies to the fact that the force field was not parameterized to take into account the formation of CO_2-Na^+ complexes in a zeolitic structure. The strong interaction of the carbonate-like complexes in NaX and LTA structures, confirmed by the need of high temperatures for their complete removal, could explain the higher carbon dioxide uptake and the need of lower values of pressure to adsorb a given amount of carbon dioxide in experiments.

According to literature, the strong interactions inside structures with Si/Al = 1 lead to variations in the polarity of the framework and to perturbations of the Si-O-Al bonds[2,47]. Thus, these variations need to be taken into account in order to reproduce the adsorption of carbon dioxide when complexes are formed. A straight-forward approach consists on the modification of the partial charges of the atoms of the adsorbent that are directly involved in the formation of the complexes. Hence, the point charge of the oxygen atoms of the zeolite has been increased slightly (more negative), while increasing the point charge of the extra-framework cations in order to compensate the negative net charge of the system (Table 2). As shown in Figure 5, the previous transferable force field with this new set of charges successfully reproduces experimental adsorption of carbon dioxide in LTA4A zeolite not only at 273 K but also at 298 K. In addition, the isosteric heat of adsorption of carbon dioxide in LTA4A computed with the new set of charges is 44.2 kJ/mol, in excellent agreement with the heat of adsorption that we obtained from experimental measurements (43.3 kJ/mol).

Figure 6 shows an Arrhenius plot of the dependence of Henry coefficients with temperature in LTA4A. The experimental and simulation data obtained in this work were compared with experimental values available in the literature[19]. Considering the sensitiveness of the methods used for the obtainment of Henry coefficients, our simulation data are in reasonable agreement with our experimental data.

Table 2. Partial charges of the atoms used in this work when complexes are formed in presence of only Na^+ or Na^+ and Ca^{2+} cations. In absence of complexes we use the set of charges previously reported by Calero et al.[16].

Atoms	Na-LTA Charge (e-)	Ca, Na-LTA Charge (e-)
C_co2	0.6512	0.6512
O_co2	-0.3266	-0.3266
O_zeo	-0.4838	-0.4372
Al	0.4859	0.4859
Si	0.7859	0.7859
Na	0.6633	0.4767
Ca	-	0.9534

Figure 5. Experimental (full symbols) and computed (empty symbols) adsorption isotherms of carbon dioxide at 273 K (squares) and 298K (circles) in LTA4A (with 96 Na^+).

However, both sets of data (experiment and simulation) are one order of magnitude higher than these previously reported[19]. A possible explanation to these discrepancies could be that the authors evaluated the Henry coefficients on the isotherms measured after saturation in CO_2 and degassing at 293 K. Under these conditions carbonate-like structures are already formed and
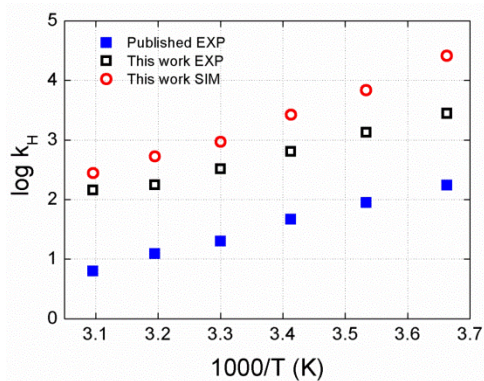
Figure 6. Henry coefficients of carbon dioxide as a function of temperature in LTA4A zeolite. Experimental and simulation values obtained in this work (empty squares and circles, respectively) are compared with previous experiments[19] (full squares).

the calculated Henry coefficients account just for the physisorbed gas. In this work Henry coefficients were obtained from the bare structures (evacuated at high temperature), thus they also account for the gas-framework interactions at low coverage where carbon dioxide chemisorption occurs. Consequently, our experimental values are consistently higher than those of Zukal *et al.*[19].

To analyse the effect exerted by the nature of the extra-framework cations, we have computed adsorption isotherms of carbon dioxide in LTA5A (Figure 7). To our knowledge there is a lack of force field parameters defining the specific interactions for calcium cations with carbon dioxide in zeolites. Previous works used generic mixing rules[48] of individual Lennard-Jones parameters reported for calcium cations in clays and carbon slits[49] and carbon dioxide[50]. As shown in Figure 7 the experimental
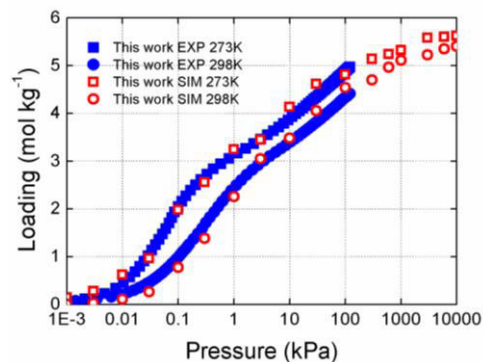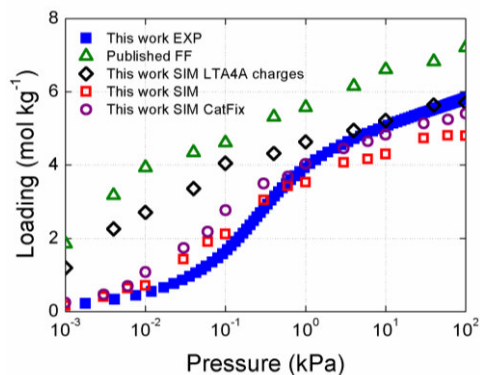

Figure 7. Experimental (full symbols) and computed (empty symbols) adsorption isotherms of carbon dioxide at 273 K in LTA5A (with 32 Na^+/u.c. and 32 Ca^{2+}/u.c.). Simulations were performed using the set of charges developed for LTA4A (black prisms) and that for LTA5A zeolites (red squares). Simulations with the latter set of charges but keeping fixed the extra framework cations are also added for comparison (purple circles). Additionally we compare with the results obtained with the previously published parameters for calcium[49] (green triangles).

results are overestimated with this set of parameters.

Our approach assumes that sodium and calcium are chemically similar and then we used for calcium-carbon dioxide interactions the same Lennard-Jones parameters that we developed for sodium-carbon dioxide interaction (Table 1). However, as shown in Figure 7 the set of charges used for LTA4A overestimates the experimental results obtained for LTA5A, probably due to the lower amount of complexes formed in structures containing calcium as well as to the higher mobility of calcium[51]. Assuming that the formation of carbonates is mainly dominated by the

amount of sodium extra-framework cations and as this is three times lower in LTA5A than in LTA4A (96 Na^+/u.c. LTA4A; 32 Na+/u.c. and 32 Ca^{2+}/u.c. LTA5A), we have performed additional simulations reducing the partial charges of the atoms involved into the complex formation by 2/3 respect to the previous increase needed for LTA4A zeolite (Table 2). As shown in Figure 7, the computed adsorption isotherm using this set of charges reproduces the experimental curve obtained at low pressure and up to 10 kPa, but underestimates the amount adsorbed at saturation. This is most likely attributed to the mobility of the cations at saturation conditions in the simulations. It should be recalled that from an experimental point of view, the mobility of the cations is hindered by the CO_2-complexes formed and the molecules of carbon dioxide already physisorbed in the structure. Indeed, as seen in Figure 7 this effect can be reproduced, at high pressure, by molecular simulation keeping the cations fixed.

Finally, we want to emphasize that the new set of parameters developed in this work is a first approach to consider the presence of complexes in zeolites. Since there are no evidences about the number or position of the complexes formed on each system, our approach averages the effect of the complexes in the whole structure. In order to predict the irreversible behaviour of the hysteresis, future experimental and theoretical work needs to be performed.

Conclusions

We have explored the mechanisms governing the CO_2 adsorption in zeolites with different aluminum content and density and nature of extra framework cations. We have shown that the accessible pore volume of the zeolite is affected by the amount and strength of carbonate-like complexes formed upon carbon dioxide adsorption; both aspects depend on the Si/Al ratio of the zeolite, as well as the nature and mobility of the extra framework cations. The strong interaction of carbonate-like complexes in zeolite structures with high amount of cations (NaX and LTA4A) explains the limitations of our previous force field to reproduce CO_2 adsorption in such structures. The experimental findings were validated with molecular simulation using transferable force fields to reproduce the adsorption of carbon dioxide in structures with high Si/Al ratio. We also provide new set of charges that accurately reproduces the experimental adsorption in structures containing carbon dioxide-cation complexes, reinforcing our previous force field.

Bibliography

(1) Yang, H.; Xu, Z.; Fan, M.; Gupta, R.; Slimane, R. B.; Bland, A. E.; Wright, I. *Journal of Environmental Sciences-China* **2008**, *20*, 14.
(2) Montanari, T.; Finocchio, E.; Salvatore, E.; Garuti, G.; Giordano, A.; Pistarino, C.; Busca, G. *Energy* **2011**, *36*, 314.

(3) Triebe, R. W.; Tezel, F. H. *Canadian Journal of Chemical Engineering* **1995**, *73*, 717.

(4) Krishna, R.; van Baten, J. M.; Garcia-Perez, E.; Calero, S. *Chemical Physics Letters* **2006**, *429*, 219.

(5) Plant, D. F.; Maurin, G.; Jobic, H.; Llewellyn, P. L. *Journal of Physical Chemistry B* **2006**, *110*, 14372.

(6) Garcia-Perez, E.; Dubbeldam, D.; Maesen, T. L. M.; Calero, S. *Journal of Physical Chemistry B* **2006**, *110*, 23968.

(7) Frenkel, D.; Smit, B. *Undesrtanding Molecular Simulation: From Algorithms to Applications*; Academic Press: San Diego. C.A., 2002.

(8) Akten, E. D.; Siriwardane, R.; Sholl, D. S. *Energy & Fuels* **2003**, *17*, 977.

(9) Hirotani, A.; Mizukami, K.; Miura, R.; Takaba, H.; Miya, T.; Fahmi, A.; Stirling, A.; Kubo, M.; Miyamoto, A. *Applied Surface Science* **1997**, *120*, 81.

(10) Jia, W.; Murad, S. *Journal of Chemical Physics* **2004**, *120*, 4877.

(11) Maurin, G.; Llewellyn, P. L.; Bell, R. G. *Journal of Physical Chemistry B* **2005**, *109*, 16084.

(12) Chen, H.; Xi, H.; Cai, X.; Qian, Y. *Microporous and Mesoporous Materials* **2009**, *118*, 396.

(13) Liu, B.; Smit, B. *Langmuir* **2009**, *25*, 5918.

(14) Madison, L.; Heitzer, H.; Russell, C.; Kohen, D. *Langmuir* **2011**, *27*, 1954.

(15) Garcia-Perez, E.; Parra, J. B.; Ania, C. O.; Garcia-Sanchez, A.; Van Baten, J. M.; Krishna, R.; Dubbeldam, D.; Calero, S. *Adsorption-Journal of the International Adsorption Society* **2007**, *13*, 469.

(16) Garcia-Sanchez, A.; Ania, C. O.; Parra, J. B.; Dubbeldam, D.; Vlugt, T. J. H.; Krishna, R.; Calero, S. *Journal of Physical Chemistry C* **2009**, *113*, 8814.

(17) Jaramillo, E.; Chandross, M. *Journal of Physical Chemistry B* **2004**, *108*, 20155.

(18) Busca, G. *Chemical Reviews* **2010**, *110*, 2217.

(19) Zukal, A.; Arean, C. O.; Delgado, M. R.; Nachtigall, P.; Pulido, A.; Mayerova, J.; Cejka, J. *Microporous and Mesoporous Materials* **2011**, *146*, 97.

(20) Arkharov, A. M.; Bering, B. P.; Kalinnikova, I. A.; Serpinskii, V. V. *Russian Chemical Bulletin* **1972**, *21*, 1389.

(21) Eagan, J. D.; Anderson, R. B. *Journal of Colloid and Interface Science* **1975**, *50*, 419.

(22) Wang, Z. M.; Arai, T.; Kumagai, M. *Energy & Fuels* **1998**, *12*, 1055.

(23) Duren, T.; Snurr, R. Q. *Journal of Physical Chemistry B* **2004**, *108*, 15703.

(24) Duren, T.; Sarkisov, L.; Yaghi, O. M.; Snurr, R. Q. *Langmuir* **2004**, *20*, 2683.

(25) Dubbeldam, D.; Calero, S.; Ellis, D. E.; Snurr, R. Q. *RASPA, version 1.0; Northwestern University: Evanston, IL* **2008**.

(26) Calero, S.; Martin-Calvo, A.; Hamad, S.; Garcia-Perez, E. *Chem. Commun.* **2011**, *47*, 508.

(27) Martin-Calvo, A.; Lahoz-Martin, F. D.; Calero, S. *Journal of Physical Chemistry C* **2012**, *116*, 6655.

(28) Gutierrez-Sevillano, J. J.; Dubbeldam, D.; Rey, F.; Valencia, S.; Palomino, M.; Martin-Calvo, A.; Calero, S. *Journal of Physical Chemistry C* **2010**, *114*, 14907.

(29) Calero, S.; Dubbeldam, D.; Krishna, R.; Smit, B.; Vlugt, T. J. H.; Denayer, J. F. M.; Martens, J. A.; Maesen, T. L. M. *J. Am. Chem. Soc.* **2004**, *126*, 11377.

(30) Pluth, J. J.; Smith, J. V. *J. Am. Chem. Soc.* **1980**, *102*, 4704.

(31) Olson, D. H. *Zeolites* **1995**, *15*, 439.

(32) Firor, R. L.; Seff, K. *J. Am. Chem. Soc.* **1978**, *100*, 3091.

(33) Mortier, W. J.; Vandenbossche, E.; Uytterhoeven, J. B. *Zeolites* **1984**, *4*, 41.

(34) Fitch, A. N.; Jobic, H.; Renouprez, A. *J. Phys. Chem.* **1986**, *90*, 1311.

(35) Garcia-Perez, E.; Dubbeldam, D.; Liu, B.; Smit, B.; Calero, S. *Angew. Chem.-Int. Edit.* **2007**, *46*, 276.

(36) Perez-Carbajo, J.; Gomez-Alvarez, P.; Bueno-Perez, R.; Merkling, P. J.; Calero, S. *Physical Chemistry Chemical Physics* **2014**, *16*, 5678.

(37) Szostak, R. *Molecular Sieves: Principles of Synthesis and Identification*; Springer, 1997.

(38) Bertsch, L.; Habgood, H. W. *J. Phys. Chem.* **1963**, *67*, 1621.

(39) Gallei, E.; Stumpf, G. *Journal of Colloid and Interface Science* **1976**, *55*, 415.

(40) Mirodatos, C.; Pichat, P.; Barthomeuf, D. *J. Phys. Chem.* **1976**, *80*, 1335.

(41) Bonelli, B.; Onida, B.; Fubini, B.; Arean, C. O.; Garrone, E. *Langmuir* **2000**, *16*, 4976.

(42) Loera, S.; Llewellyn, P. L.; Lima, E. *Journal of Physical Chemistry C* **2010**, *114*, 7880.

(43) Jacobs, P. A.; Vancauwe.Fh; Vansant, E. F.; Uytterho.Jb *Journal of the Chemical Society-Faraday Transactions I* **1973**, *69*, 1056.

(44) Jacobs, P. A.; Vancauwe.Fh; Vansatn, E. F. *Journal of the Chemical Society-Faraday Transactions I* **1973**, *69*, 2130.

(45) Martra, G.; Coluccia, S.; Davit, P.; Gianotti, E.; Marchese, L.; Tsuji, H.; Hattori, H. *Research on Chemical Intermediates* **1999**, *25*, 77.

(46) Coluccia, S.; Marchese, L.; Martra, G. *Microporous and Mesoporous Materials* **1999**, *30*, 43.

(47) Montanari, T.; Busca, G. *Vibrational Spectroscopy* **2008**, *46*, 45.

(48) Peng, X.; Cao, D. *Aiche Journal* **2013**, *59*, 2928.

49) Ohba, T.; Kojima, N.; Kanoh, H.; Kaneko, K. *Journal of Physical Chemistry C* **2009**, *113*, 12622.

(50) Peng, X.; Zhao, J.; Cao, D. *Journal of Colloid and Interface Science* **2007**, *310*, 391.

(51) Beerdsen, E.; Dubbeldam, D.; Smit, B.; Vlugt, T. J. H.; Calero, S. *Journal of Physical Chemistry B* **2003**, *107*, 12088.

Transferable Force Fields for Adsorption of Small Gases in Zeolites: Effect of Low Temperature

Ana Martín-Calvo, Juan José Gutiérrez-Sevillano, José B. Parra,
Conchi O. Ania and Sofía Calero

7

We provide transferable force fields for oxygen, nitrogen and carbon monoxide that are able to reproduce experimental adsorption in both pure silica and alumino-substituted zeolites. The force field parameters can be combined with these previously reported for carbon dioxide, methane and argon, opening the possibility of studying mixtures of interest containing the six components. Using these force field parameters we analyse the effect of low temperature on the adsorption in a variety of topologies, highlighting the difficulties that occur due to the sensitiveness of the equipment or kinetic impedimenta that can induce to erratic results. Additional problems can be found during simulations when extra-framework cations are present in the system as their lack of mobility at low temperatures could lead to kinetic effects that hinder adsorption.

1. Introduction

The lack of accurate force fields to define the interactions of guest molecules in zeolites remains an impeding factor from the simulation point of view. To use molecular simulation as predictive tool requires reliable models as well as effective force fields able to reproduce experimental data. The main difficulty of defining interactions between adsorbates and zeolites is that generic mixing rules fail for these systems. Therefore, specific parameters for the atoms of both adsorbates and adsorbents are needed. To date there are many works describing these interactions but most of them are developed for specific purposes and molecular models and they are not transferable to other structures or to different working conditions. One of the most studied adsorbates in zeolites is carbon dioxide. For this molecule a

variety of force fields are reported in the literature in both pure silica[1-4] and alumino-silicate crystals[5-7]. Among this force fields only one of them has been proven to be transferable to all zeolitic topologies, reproducing accurately experimental adsorption under different conditions[8]. Regarding diffusion of carbon dioxide in zeolites, most of the simulation studies focus in pure silica structures[9-13] and it has been demonstrated that small differences on the host-guest parameters lead to similar adsorption but have large influence on diffusion[14].

The adsorption and diffusion of alkanes have also been widely studied in both pure silica and alumino-substituted zeolites[13,15,16]. While the adsorption of hydrocarbons is well reproduced in all-silica zeolites using force fields such as TraPPE[17] or this of Dubbeldam *et al.*[18],

important differences can be found in diffusion studies[14,19-23].

The adsorption and diffusion of other small gases such as nitrogen, argon, oxygen or carbon monoxide have also been reported in zeolites but in lesser amount[2,4,9,13,16,24-31].

In this work we provide a transferable force field for light gases in zeolites with different topologies and Si/Al ratio and with sodium as extra-framework cation. We rely on reported transferable force fields for argon[24] and methane[18] and we develop new parameters for nitrogen, oxygen and carbon monoxide to reproduce experimental adsorption in zeolites for a variety of temperatures. Note that these force fields are compatible with these previously published for CO_2[8], argon[24] and methane[18]. This fact is of high relevance as it makes possible to compute adsorption in zeolites of a variety of mixtures with industrial and environmental impact (i.e. natural gas, tail gases from Fisher Tropsch processes, greenhouse gases, or pollutant removal from air). Usually available force fields are optimized at room temperature, but in this work we fit the force field parameters at 77 K and 120 K (depending on the adsorbate) in order to guarantee their validity for a wider range of temperatures. The fact of working at low temperature adds an interesting dimension to this work as the adsorption behaviour at high and low temperature could be quite different due to kinetic restrictions.

In the next sections we detail the experimental and simulation

methodology, we discuss the results obtained and finally we summarize our main findings of this work.

2. Experimental details

Zeolites with faujasite topology were purchased from Zeolyst International (CBV100 and CBV901). All silica MFI (RSIL) and ITQ-29 (pure silica LTA structure) were kindly supplied by ITQ (CSIC) and both correspond to a pure porous crystalline silicon dioxide. Experimental gas adsorption isotherms at cryogenic temperatures (i.e., 70-90-120 K) were performed in a volumetric analyser (ASAP 2020 HD, Micromeritics) in the pressure range between 10^{-2} and 120 kPa. The instrument was equipped with a turbo molecular vacuum pump and three pressure transducers (0.13, 1.33 and 133 kPa, uncertainty within 0.15% of each reading) to enhance the sensitivity in the low pressure range. Cryogenic temperatures were obtained using a helium cryocooler (Gifford-McMahon) coupled to the volumetric analyser that allows a fine temperature control between $25-325$ K with a stability of ± 0.1 K. Adsorption isotherms at 77 and 90 K were also measured using a liquid nitrogen and oxygen (respectively) bath to control the temperature; both sets of experimental data (cryocooler *vs* liquid nitrogen/oxygen) were found to be reproducible. Before the analysis, all zeolite powders were outgassed under dynamic vacuum at 623 K (1K/min) for overnight. All of the isotherms were done in triplicate and the data are reproducible with an error below 0.1%. All the gases were supplied by Air

Products with an ultrahigh purity (i.e., 99.995%).

3. Simulation methods and models

To obtain the amount of adsorbed molecules in the zeolites we perform Monte Carlo simulations (MC) using the grand canonical ensemble where chemical potential, volume and temperature are kept fixed. Fugacity is obtained from the chemical potential, and it is directly related to pressure by the fugacity coefficient. To compare with experimental data, simulated absolute adsorption isotherms are converted to excess adsorption isotherms as proposed by Duren et al.[32] Simulations are performed using the in-house code RASPA[33].

The zeolites used for the development and validation of the force fields are the pure silica versions of LTA (ITQ-29), FAU and MFI and the aluminosilicate NaY with 54 sodium extra-framework cations. The frameworks are considered rigid. ITQ-29 was firstly synthesized by Corma et al.[34] with a cubic unit cell of 11.87 Å of side. For the pure silica FAU zeolite, we use the crystallographic position of the atoms reported by Hriljac et al.[35] with a cubic unit cell of a = b = c = 24.26 Å. Both ITQ-29 and FAU are formed by sodalites connected to each other. To compare with other zeolite topology, pure silica MFI is also employed. This structure is characterized by the combination of longitudinal and zig-zag channels forming a 3D network. It is well known that MFI zeolite experiences phase transitions with loading and/or temperature[24,36-38]. These studies showed

that the zeolite adopts a monoclinic configuration at temperature below 300 K, while above this temperature the symmetry changes to orthorhombic. For this reason and due to the fact that this study focuses on adsorption at low temperatures we use the monoclinic version of MFI zeolite as reported by van Koningsveld et al.[39] with unit cell of a = 20.12 Å, b = 19.88 Å and c = 13.37 Å and $\alpha = \gamma = 90°$ and $\beta = 90.67°$. To incorporate the effect of the presence of extra-framework cations and to parameterize the interactions of the cations with the adsorbates we compute adsorption in NaY (with 54 aluminium atoms and sodium cations per unit cell) using the crystallographic positions reported by Olson[40]. The low content of aluminium of this structure (54 per unit cell) avoids the possible formation of complexes between the cations and the adsorbates[41-44]. NaY has a cubic unit cell with side size of 25.09 Å and the distribution of the aluminium atoms in our simulation cell obeys the Löwenstein rule that establish that the same oxygen atom cannot be connected to two aluminium atoms.

Regarding adsorbates we use reported models for argon[45], methane[18], nitrogen[45], oxygen[45] and carbon monoxide[46]. Argon and methane are described as united atom models with Lennard-Jones parameters on a single interaction centre[18,45]. Nitrogen, oxygen and carbon monoxide are modelled with Lennard-Jones parameters, point charges in all their atoms[45,46] and charged dummy atoms without mass to reproduce the polarity of the molecules. All these models have been fitted to reproduce experimental properties such

as the vapour-liquid coexistence, vapour pressure or liquid densities.

Guest-guest and host-guest interactions are modelled through Lennard-Jones and Coulombic interactions. Coulombic interactions are computed with the Ewald summation method with a relative precision of 10^{-6}. Lennard-Jones potentials are cut and shifted with a cut-off distance of 12 Å. Van de Waals interactions between molecules are obtained from Lorentz-Berthelot mixing rules using already published parameters for the adsorbates[18,45,46]. As mentioned before adsorbate-adsorbent interactions in zeolites do not obey generic mixing rules, therefore specific interactions need to be used. Usually, the dispersive interactions of silicon or aluminium atoms are considered through the oxygen atoms, acting these atoms as Lennard-Jones interacting centres. Nevertheless all the atoms of the system have partial charges assigned. In this work we use a set of charges for the structures that was previously reported by the group[8]. To define the Lennard-Jones interactions of the molecules with the structures, we use published values for argon and methane[18,24] and we define new ones for nitrogen, oxygen and carbon monoxide.

4. Results

To obtain the parameters for the interactions of oxygen, nitrogen and carbon monoxide with the zeolites, the first step is to reproduce the interaction of the gases in pure silica zeolites (gas-

Table 1. Lennard-Jones parameters for guest-host interactions.

Atom 1	Atom 2	ε/k_B (K)	σ (Å)
Ar	O_{zeo}	107.69	3.15
CH_4	O_{zeo}	115	3.47
N_2	O_{zeo}	60.58	3.261
O_2	O_{zeo}	65.189	3.129
C_{CO}	O_{zeo}	40.109	3.379
O_{CO}	O_{zeo}	98.839	3.057
Ar	Na	262	2.396
CH_4	Na	553.061	2.176
N_2	Na	225.568	2.766
O_2	Na	241.284	2.06
C_{CO}	Na	369.343	2.332
O_{CO}	Na	579.793	2.212

O_{zeo}). With this aim in mind we computed adsorption isotherms in ITQ-29 for all gases at 77 K, 90 K and 120 K. The Lennard-Jones parameters between the oxygen atoms (O_{zeo}) and the adsorbates were fitted to reproduce the experimental isotherms at the lowest temperature (77 K for oxygen and nitrogen and 120 K for carbon monoxide). In addition we compute adsorption isotherms at several temperatures to validate the fitted parameters that are collected in Table 1. Figure 1 compares our experimental and computed isotherms for oxygen (Figure 1a), nitrogen (Figure 1b) and carbon monoxide (Figure 1c) in ITQ-29. As observed from the figures the isotherms obtained with our new set of parameters accurately reproduce the experimental values of adsorption for all temperatures studied.

The force field parameters for argon and methane taken from the literature[18,24] have also been validated to reproduce experimental adsorption at low temperature (120 K). As shown in Figure A1 from Appendix 5 simulations reproduce experimental adsorption accurately.

To analyse the transferability of the new set of parameters, adsorption isotherms were computed for other pure silica zeolites. Figure 2 shows the adsorption isotherms computed for pure silica FAU zeolite, compared to experimental data obtained in CBV901 (nearly pure silica FAU zeolite) at different temperatures. As observed in this figure the results obtained from simulations successfully reproduce experimental data at low and medium values of pressure. The main discrepancies are observed at high pressure, where the experimental adsorption is lower than the simulated. This is due to the fact that the zeolite used in the experimental measurements (CBV901) has a surface area of 700 m^2/g while the theoretical structure has a surface area of 885 m^2/g. Therefore the saturation capacity of the theoretical structure is larger than this of the experimental structure. To validate this reasoning a correction factor of 0.79 is applied to the simulated results, obtaining the proper agreement with the experimental values.

Figure 1. Experimental (full symbols) and computed (empty symbols) adsorption isotherms of (a) oxygen, (b), nitrogen and (c) carbon monoxide in ITQ-29 at 77 K (rhombus), 90 K (squares) and 120 K (circles). The inset in Fig. 1c shows isotherms at 258 K, 278 K and 298 K (up-, down- and right-triangles, respectively).

Figure 2. Experimental (full symbols) and computed (empty symbols) adsorption isotherms for (a) oxygen, (b) nitrogen and (c) carbon monoxide in pure silica FAU at 77 K (rhombus), 90 K (squares) and 120 K (circles). Crosses indicate theoretical adsorption after the correction applied as a result of the different surface areas.
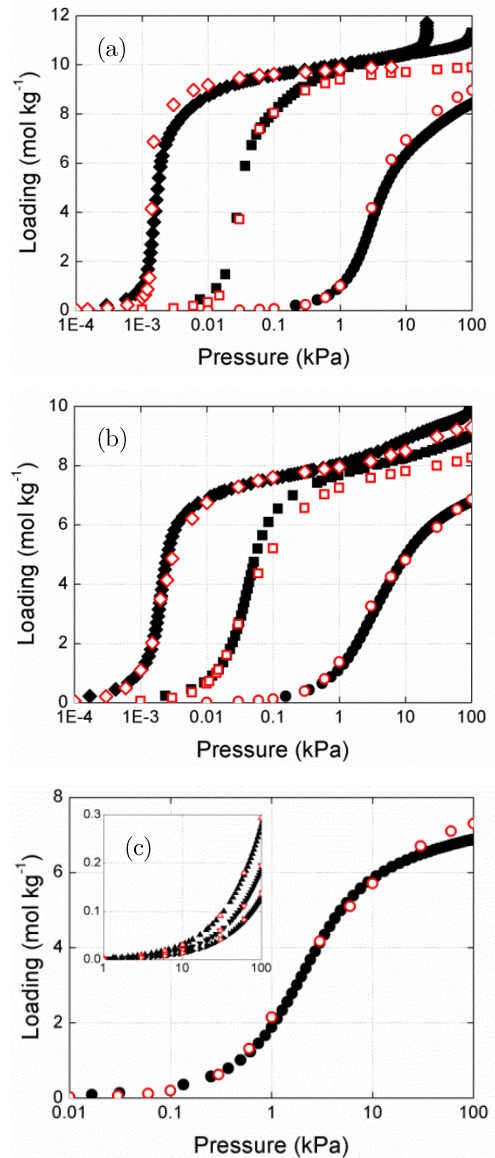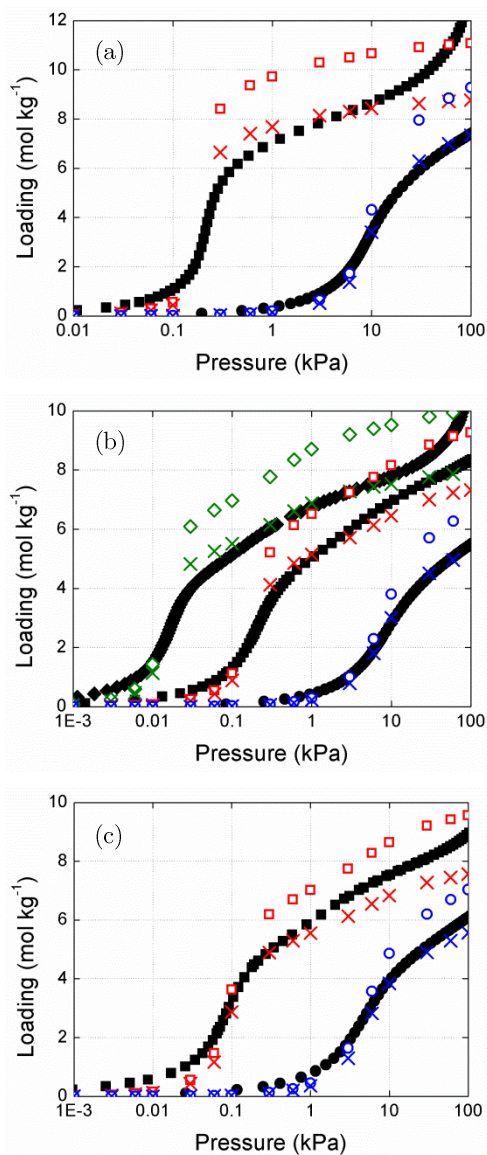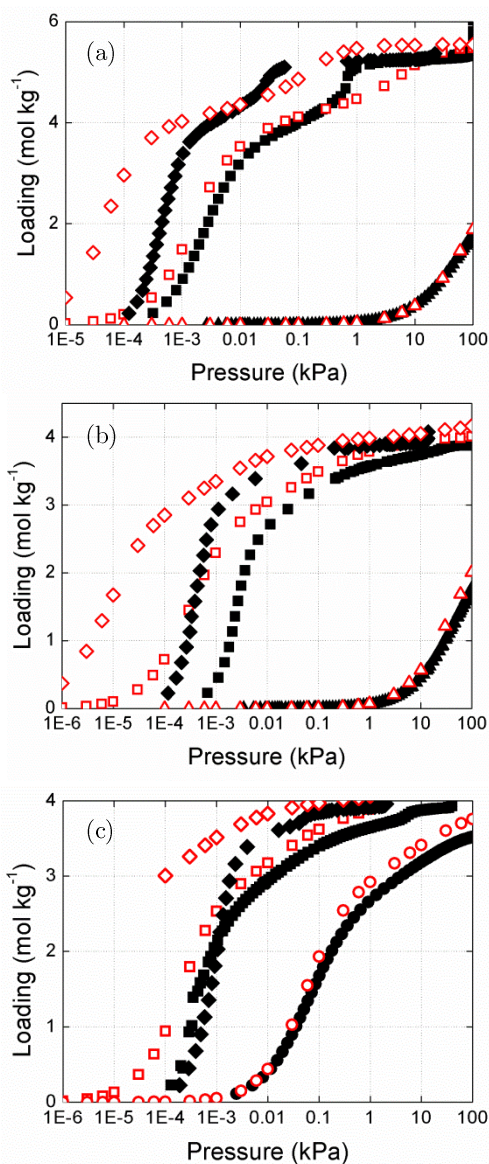
Figure 3. Experimental (full symbols) and computed (empty symbols) adsorption isotherms for (a) oxygen, (b) nitrogen and (c) carbon monoxide in pure silica MFI at 77 K (rhombus), 90 K (squares), 120 K (circles) and 196 K (triangles).

ITQ-29 and FAU contain sodalite cages connected to each other. Therefore, to check the transferability of our parameters to other topologies, adsorption isotherms have also been obtained for pure silica MFI zeolite. Figure 3 compares experimental and computed adsorption isotherms obtained for oxygen, nitrogen and carbon monoxide in pure silica MFI zeolite (experimental RSIL). As can be noted the lowest temperature brings some discrepancies since it is difficult to reach real equilibrium and there is disagreement between different authors. As an example, Figure 4 shows the adsorption isotherms of nitrogen in pure silica MFI at 77 K. As it can be seen, our experimental isotherm is in agreement with that previously reported by Hammond et al.[47], but shows a large discrepancy with that of Nakai et al.[48], though the three of them exhibit the same saturation capacity. Back to Figure 3, depending on the adsorbate, differences between experiments and simulations can be found at temperature below 77 K (oxygen) or 90 K (nitrogen and carbon monoxide). Discrepancies observed in this structure were not found in previous zeolites (ITQ-29 and FAU). These discrepancies could be due to phase transition on the MFI structure as well as to differences on the size of the crystals used in the experimental samples. The changes on the zeolite may affect to the limiting effective size of the structure, being the effect more visible on the adsorption of the largest molecules (nitrogen and carbon monoxide). Additional comparison with previous works in MFI for nitrogen, carbon monoxide and argon at high temperature (305-343
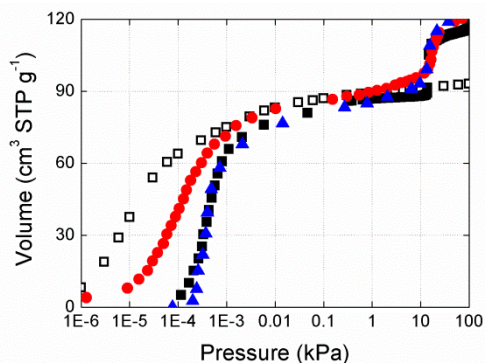
Figure 4. Adsorption isotherms of nitrogen in pure silica MFI at 77 K. The experimental data obtained in this work (squares) are compared with available data provided by Nakai et al.[47] (circles) and Hammond et al.[48] (triangles). Empty squares correspond to the adsorption isotherm that we have obtained from simulations.
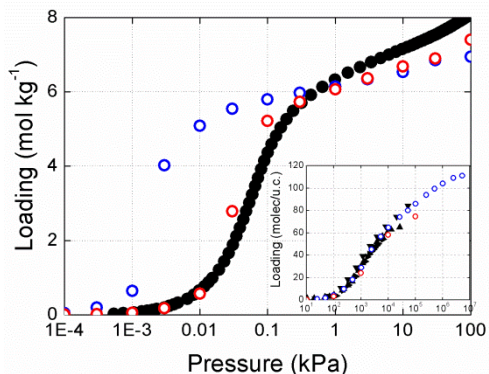
Figure 5. Experimental (full symbols) and computed (empty symbols) adsorption isotherms of methane in NaY (54 Na$^+$/u.c.) at 120 K. Blue symbols correspond to the results obtained using the parameters reported by Calero et al.[54] and red symbols to the ones obtained after fitting these parameters. The inset shows a comparison of methane adsorption isotherms in FAU (48 Na$^+$/u.c.) at 323 K with experimental values from Rowlinson, Fuchs and Talu as shown in the publication of Calero et al.[54]

K)[49,50] are shown in Figures A2-A4 in Appendix 5.

The presence of aluminium in the structures (location and density) and the type of extra-framework cation highly influences adsorption. In structures with Si/Al ratio close to 1, such as LTA, the basicity of the oxygen atoms and the number of sodium extra-framework cations lead to the formation of carbonate-like-species during the adsorption of molecules such as carbon dioxide and carbon monoxide[44,51]. These complexes affect the accessible volume of the structure and the interactions with the molecules. We have recently reported a work dealing with the formation of these complexes when carbon dioxide is adsorbed in this type of zeolites[44]. On the one hand we are currently working on the development of a set of parameters for carbon monoxide in LTA, but this implies additional difficulties that are out of the scope of this work. In addition, molecules such as nitrogen, argon, methane or oxygen are not able to enter the LTA structure due to kinetic restrictions[52,53]. Hence, to study the effect of the presence of cations avoiding the problems afore mentioned we focus on NaY zeolite with 54 sodium cations per unit cell (u.c). Using similar procedure as for pure silica zeolites we use our experimental isotherms to fit the Lennard-Jones parameters between the adsorbates and sodium cations and to validate these parameters.

Unfortunately, there is still a big lack of force fields in zeolites containing non-framework cations. Among the gases under study and to the best of our knowledge, there is only one set of parameters for methane[54]. These parameters were optimized and validated for adsorption in FAU-type zeolites at temperatures spanning from 298 K to 330 K. As shown in Figure 5 these parameters fail to reproduce adsorption at 120 K, since it overestimates the uptake at low pressures. However the saturation obtained by simulation is in reasonably good agreement with the experimental data. Amazingly enough, slight variations on the epsilon and sigma parameters lead to reproduce the experimental adsorption isotherms at low and high temperatures. This evidences the large sensitivity of the Lennard-Jones parameters when the adsorption isotherm is computed at low temperature. In addition, it is possible to find disagreements between experiments and simulations at low and medium values of pressure due to another two factors (Figure 6). On the one hand, we can find experimental restrictions similar to these observed at 77 K for pure silica structures. On the other hand the lowest uptake obtained in the experiments could be also attributed to kinetic effects. At low temperatures the reduced mobility of the cations could lead them to block the windows that communicate the α-cages of faujasite. Therefore higher pressures are needed for the molecule to enter the structure. This kinetic restriction disappears at higher temperatures allowing good agreement between experiments and simulations at temperatures above 90 K.

To avoid these impedimenta, the Lennard-Jones parameters that describe
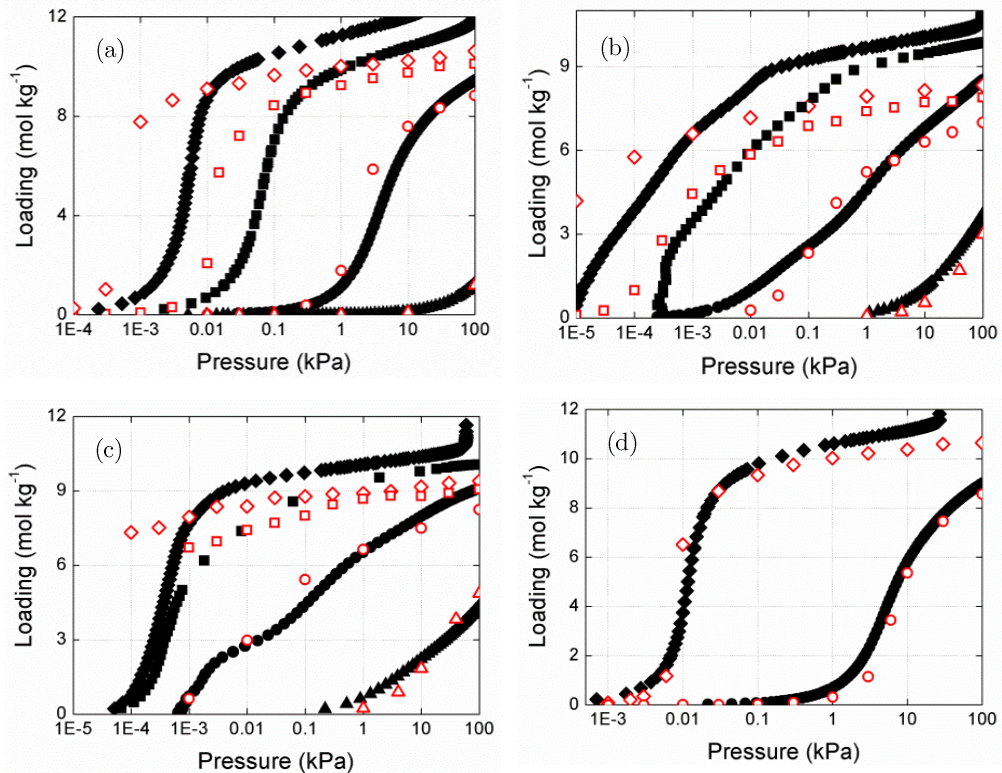
Figure 6. Experimental (full symbols) and computed (empty symbols) adsorption isotherms of a) oxygen, b) nitrogen, c) carbon monoxide and d) argon in NaY (54 Na$^+$/u.c.) at 77 K (rhombus), 90 K (squares), 120 K (circles) and 196 K (triangles).

de interactions of nitrogen, oxygen, carbon monoxide and argon with the sodium cation were fitted to the experimental isotherms obtained at 120 K and validated at higher and lower temperatures.

As shown in Figure 6, the experimental and simulated adsorption isotherms at temperatures above 90 K for oxygen (6a), nitrogen (6b) and carbon monoxide (6c) are in very good agreement. However, simulation fails to reproduce experiment at lower temperatures. These discrepancies do not apply to argon (Figure 6d) since the interaction of this gas with the cations

is not so strong and therefore its adsorption is not affected by kinetic restrictions.

Conclusions

We analyzed the effect of temperature on the adsorption behavior of argon, methane, nitrogen, oxygen, and carbon monoxide in both pure silica and aluminosilicate zeolites. To this aim the development of new sets of transferable parameters was needed. These parameters are of key importance to perform adsorption studies by molecular simulation as generic mixing rules fail to reproduce

adsorption in zeolitic systems and previous works with specific parameters are scarce. The new sets of parameters are compatible to these previously reported for carbon dioxide, methane and argon opening the possibility of studying mixtures of all components. We found that some systems need very low pressures to reach equilibrium and experimental devices are not always able to reach such pressures leading in this case to erroneous isotherms. When cations are involved in the system the low temperature affects their mobility being needed higher pressures to allow molecules to enter the structures. This kinetic effect cannot be mimic using Monte Carlo simulations being therefore more difficult to reproduce experimental results.

Bibliography

(1) Goj, A.; Sholl, D. S.; Akten, E. D.; Kohen, D. *Journal of Physical Chemistry B* **2002**, *106*, 8367.

(2) Makrodimitris, K.; Papadopoulos, G. K.; Theodorou, D. N. *Journal of Physical Chemistry B* **2001**, *105*, 777.

(3) Hirotani, A.; Mizukami, K.; Miura, R.; Takaba, H.; Miya, T.; Fahmi, A.; Stirling, A.; Kubo, M.; Miyamoto, A. *Applied Surface Science* **1997**, *120*, 81.

(4) Li, P.; Tezel, F. H. *Journal of Chemical and Engineering Data* **2008**, *53*, 2479.

(5) Jaramillo, E.; Chandross, M. *Journal of Physical Chemistry B* **2004**, *108*, 20155.

(6) Akten, E. D.; Siriwardane, R.; Sholl, D. S. *Energy & Fuels* **2003**, *17*, 977.

(7) Maurin, G.; Llewellyn, P. L.; Bell, R. G. *Journal of Physical Chemistry B* **2005**, *109*, 16084.

(8) Garcia-Sanchez, A.; Ania, C. O.; Parra, J. B.; Dubbeldam, D.; Vlugt, T. J. H.; Krishna, R.; Calero, S. *Journal of Physical Chemistry C* **2009**, *113*, 8814.

(9) Madison, L.; Heitzer, H.; Russell, C.; Kohen, D. *Langmuir* **2011**, *27*, 1954.

(10) Babarao, R.; Jiang, J. *Langmuir* **2008**, *24*, 5474.

(11) Krishna, R.; van Baten, J. M. *Journal of Membrane Science* **2010**, *360*, 323.

(12) Krishna, R.; van Baten, J. M. *Microporous and Mesoporous Materials* **2008**, *109*, 91.

(13) Garcia-Perez, E.; Parra, J. B.; Ania, C. O.; Garcia-Sanchez, A.; Van Baten, J. M.; Krishna, R.; Dubbeldam, D.; Calero, S. *Adsorption-Journal of the International Adsorption Society* **2007**, *13*, 469.

(14) Garcia-Sanchez, A.; van den Bergh, J.; Castillo, J. M.; Calero, S.; Kapteijn, F.; Vlugt, T. J. H. *Microporous and Mesoporous Materials* **2012**, *158*, 64.

(15) Garcia-Sanchez, A.; Garcia-Perez, E.; Dubbeldam, D.; Krishna, R.; Calero, S. *Adsorption Science & Technology* **2007**, *25*, 417.

(16) Pillai, R. S.; Sethia, G.; Jasra, R. V. *Industrial & Engineering Chemistry Research* **2010**, *49*, 5816.

(17) Martin, M. G.; Siepmann, J. I. *Journal of Physical Chemistry B* **1998**, *102*, 2569.

(18) Dubbeldam, D.; Calero, S.; Vlugt, T. J. H.; Krishna, R.; Maesen, T. L. M.;

Smit, B. *Journal of Physical Chemistry B* **2004**, *108*, 12301.

(19) Krishna, R.; van Baten, J. M.; Garcia-Perez, E.; Calero, S. *Chemical Physics Letters* **2006**, *429*, 219.

(20) Fritzsche, S.; Haberlandt, R.; Hofmann, G.; Karger, J.; Heinzinger, K.; Wolfsberg, M. *Chemical Physics Letters* **1997**, *265*, 253.

(21) Leroy, F.; Jobic, H. *Chemical Physics Letters* **2005**, *406*, 375.

(22) Zimmermann, N. E. R.; Jakobtorweihen, S.; Beerdsen, E.; Smit, B.; Keil, F. J. *Journal of Physical Chemistry C* **2007**, *111*, 17370.

(23) Dubbeldam, D.; Smit, B. *Journal of Physical Chemistry B* **2003**, *107*, 12138.

(24) Garcia-Perez, E.; Parra, J. B.; Ania, C. O.; Dubbeldam, D.; Vlugt, T. J. H.; Castillo, J. M.; Merkling, P. J.; Calero, S. *Journal of Physical Chemistry C* **2008**, *112*, 9976.

(25) Cho, H. S.; Miyasaka, K.; Kim, H.; Kubota, Y.; Takata, M.; Kitagawa, S.; Ryoo, R.; Terasaki, O. *Journal of Physical Chemistry C* **2012**, *116*, 25300.

(26) Pillai, R. S.; Sebastian, J.; Jasra, R. V. *Journal of Porous Materials* **2012**, *19*, 683.

(27) Sethia, G.; Pillai, R. S.; Dangi, G. P.; Somani, R. S.; Bajaj, H. C.; Jasra, R. V. *Industrial & Engineering Chemistry Research* **2010**, *49*, 2353.

(28) Sebastian, J.; Pillai, R. S.; Peter, S. A.; Jasra, R. V. *Industrial & Engineering Chemistry Research* **2007**, *46*, 6293.

(29) Mellot, C.; Lignieres, J. *Molecular Simulation* **1996**, *18*, 349.

(30) Nour, Z.; Berthomieu, D.; Yang, Q.; Maurin, G. *Journal of Physical Chemistry C* **2012**, *116*, 24512.

(31) Wang, Y.; Helvensteijn, B.; Nizamidin, N.; Erion, A. M.; Steiner, L. A.; Mulloth, L. M.; Luna, B.; LeVan, M. D. *Langmuir* **2011**, *27*, 10648.

(32) Duren, T.; Sarkisov, L.; Yaghi, O. M.; Snurr, R. Q. *Langmuir* **2004**, *20*, 2683.

(33) Dubbeldam, D.; Calero, S.; Donald, E.; Snurr, R. Q. *Molecular Simulation* **2015**, *DOI:10.1080/08927022.2015.1010082*.

(34) Corma, A.; Rey, F.; Rius, J.; Sabater, M. J.; Valencia, S. *Nature* **2004**, *431*, 287.

(35) Hriljac, J. A.; Eddy, M. M.; Cheetham, A. K.; Donohue, J. A.; Ray, G. J. *Journal of Solid State Chemistry* **1993**, *106*, 66.

(36) Hay, D. G.; Jaeger, H. *Journal of the Chemical Society-Chemical Communications* **1984**, 1433.

(37) Fyfe, C. A.; Strobl, H.; Kokotailo, G. T.; Kennedy, G. J.; Barlow, G. E. *Journal of the American Chemical Society* **1988**, *110*, 3373.

(38) Wu, E. L.; Lawton, S. L.; Olson, D. H.; Rohrman, A. C.; Kokotailo, G. T. *Journal of Physical Chemistry* **1979**, *83*, 2777.

(39) Vankoningsveld, H.; Jansen, J. C.; Vanbekkum, H. *Zeolites* **1990**, *10*, 235.

(40) Olson, D. H. *Zeolites* **1995**, *15*, 439.

(41) Jacobs, P. A.; Vancauwe.Fh; Vansant, E. F.; Uytterho.Jb *Journal of the Chemical Society-Faraday Transactions I* **1973**, *69*, 1056.

(42) Jacobs, P. A.; Vancauwe.Fh; Vansatn, E. F. *Journal of the Chemical Society-Faraday Transactions I* **1973**, *69*, 2130.

(43) Martra, G.; Coluccia, S.; Davit, P.; Gianotti, E.; Marchese, L.; Tsuji, H.; Hattori, H. *Research on Chemical Intermediates* **1999**, *25*, 77.

(44) Martin-Calvo, A.; Parra, J. B.; Ania, C. O.; Calero, S. *Journal of Physical Chemistry C* **2014**, *118*, 25460.

(45) Martin-Calvo, A.; Garcia-Perez, E.; Garcia-Sanchez, A.; Bueno-Perez, R.; Hamad, S.; Calero, S. *Physical Chemistry Chemical Physics* **2011**, *13*, 11165.

(46) Martin-Calvo, A.; Lahoz-Martin, F. D.; Calero, S. *Journal of Physical Chemistry C* **2012**, *116*, 6655.

(47) Hammond, K. D.; Tompsett, G. A.; Auerbach, S. M.; Conner, W. C., Jr. *Langmuir* **2007**, *23*, 8371.

(48) Nakai, K.; Sonoda, J.; Yoshida, M.; Hakuman, M.; Naono, H. *Adsorption-Journal of the International Adsorption Society* **2007**, *13*, 351.

(49) Dunne, J. A.; Mariwals, R.; Rao, M.; Sircar, S.; Gorte, R. J.; Myers, A. L. *Langmuir* **1996**, *12*, 5888.

(50) Golden, T. C.; Sircar, S. *Journal of Colloid and Interface Science* **1994**, *162*, 182.

(51) Arean, C. O.; Delgado, M. R.; Bauca, C. L.; Vrbka, L.; Nachtigall, P. *Physical Chemistry Chemical Physics* **2007**, *9*, 4657.

(52) Eagan, J. D.; Anderson, R. B. *Journal of Colloid and Interface Science* **1975**, *50*, 419.

(53) Arkharov, A. M.; Bering, B. P.; Kalinnikova, I. A.; Serpinskii, V. V. *Russian Chemical Bulletin* **1972**, *21*, 1389.

(54) Calero, S.; Dubbeldam, D.; Krishna, R.; Smit, B.; Vlugt, T. J. H.; Denayer, J. F. M.; Martens, J. A.; Maesen, T. L. M. *Journal of the American Chemical Society* **2004**, *126*, 11377.

Adsorption of Polar Enantiomers in Achiral Zeolites

8

Ana Martín-Calvo, Sofía Calero, Johan A. Martens
and Titus S. van Erp

We use molecular simulation techniques to analyse the enantioselective adsorption of chiral polar molecules in achiral zeolite. As a representative chiral molecule, CHClFBr is used in this study. We analyse the adsorption of racemic and scalemic mixtures of these molecules into different zeolites topologies such as MFI or MEL, both structures with intersecting channels and FER and TON, frames with non-intersecting channels. In contrast with previous findings on apolar molecules, cations are not essential to inflict heteroselective adsorption, while homoselective adsorption is never observed. We derived the mechanism behind the selectivity, which turns out to be fundamentally different from the one observed for apolar adsorbates. Our model is able to explain why apparently similar zeolite topologies can still have strong differences in their adsorption behaviour.

1. Introduction

Molecular simulations have proven to be a useful tool for studying the chiral separation of enantiomeric mixtures. From the industrial point of view, this separation is extremely important because, in many cases, just one of the enantiomers has the desired effect[1-3]. The use of zeolites as adsorbents has been considered because of their favourable characteristics. For this purpose, synthesis studies have focused on the creation of chiral zeolites[4-7], but most of them have been found to be thermally unstable. Because not many chiral zeolites are available, the recently reported enantioselectivity in achiral zeolites opens the door to propitious alternatives for separation processes using these zeolites. The approach seems to contradict the general idea that an adsorbent needs to be chiral

itself to separate a chiral mixture. However, the essential symmetry-breaking aspect is provided here not by the adsorbent but by the adsorbate because it considers mixtures in which one of the enantiomers appears in a higher concentration than its mirror image (scalemic mixture).

The simulation results on this effect have been improved thanks to a Monte Carlo (MC) scheme newly developed by van Erp *et al.*[8] for studying chiral mixtures in nanoporous materials. Using this technique, Caremans *et al.*[9] and van Erp *et al.*[10] demonstrated that chiral amplification of scalemic mixtures is possible as a result of adsorption in achiral aluminium-substituted zeolites. If one type of enantiomer is already present in a higher concentration than its counterpart in the gas phase, this relative concentration might either

increase (homoselective), decrease (heteroselective), or remain the same (aselective) upon adsorption. The type of adsorption depends on the zeolite topology, the aluminium distribution, and the type of cations used to balance the net charge of the system. Technological applications of this effect will mainly lie in chiral purification rather than separation, but in some circumstances, chiral separation of racemic mixtures is possible as well[11].

The occurrence of enantioselective adsorption of chiral alkanes was explained by the "chiral cell" model[9,10]. In this model, the molecules do not interact directly, but rather interact indirectly through the mobile cations that are interconnected through their long-range Coulombic force. The "chiral cell" model could rationalize the absence of selectivity and the occurrence of either homo- or heteroselective adsorption in all studied aluminosilicate frameworks.

In this work, we aimed to study the effect of polarity. Chlorofluorobromomethane, CHClFBr, was our test molecule for this study. It is one of the simplest chiral organic molecules and isomers of this molecule have previously been used to study adsorption in chiral zeolites.[12] The achiral zeolite topologies that we considered are (a) MFI and MEL, structures characterised by longitudinal channels interconnected by zigzag channels and (b) FER and TON, characterised by being formed only by longitudinal channels. In Figure 1, energy grids of the two types of topologies are depicted.
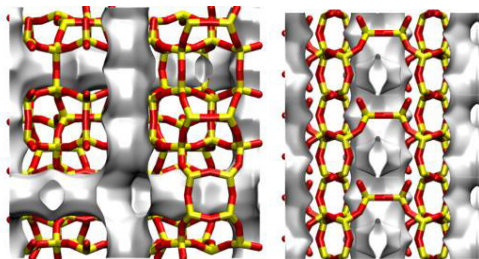
Figure 1. Energy grid representation of the different topologies considered in this work: (left) Intersecting channels (MFI and MEL) and (right) longitudinal channels (FER and TON). The interior of the energy surface (grey) delimits the pore volume where molecules can be adsorbed. Oxygen and silicon atoms of the zeolite are represented in red and yellow, respectively.

In addition, we analysed several aluminium-substituted forms of MFI (Al-1 Al-2, Al-3, Al-4, Al-5, Al-6, Al-8 and Al-11)[9] using calcium as extra-framework cation. Note that these substitutions do not induce chirality into the zeolite crystal. It turns out that the enantioselective adsorption behaviour of chiral polar molecules and the mechanisms behind it are very different from these of apolar molecules.

2. Simulation methods and models

Adsorption isotherms were computed by Monte Carlo simulations in the grand canonical ensemble (GCMC) in which chemical potential, volume and temperature are fixed. Pressure is related through fugacity by the Peng–Robinson equation[13]. The zeolites structures were considered to be rigid. The crystallographic positions for the different zeolites under study were taken from previous publications by van Koningsveld *et al.*[14] for MFI, Fyfe *et*

Table 1. Lennard-Jones parameters and partial charges used in this work. Interactions between non-identical atoms are defined by Lorentz-Bertheloz mixing rules. Oa corresponds to the oxygen atoms of the zeolites that are connected to aluminium atoms.

Atoms	ε/k_B (K)	σ (Å)	Charge (e-)
O_{zeo}	48.208	48.208	-1.025
Oa_{zeo}	48.208	48.208	-1.200
Si	156.161	3.804	2.050
Al	156.161	3.911	1.750
Ca	25.187	3.093	2.000
C	25.137	3.600	0.307
H	15.034	2.500	0.102
Cl	133.743	3.470	-0.115
F	40.772	2.750	-0.189
Br	198.088	3.650	-0.105

al.[15] for MEL, Morris *et al.*[16] for FER and Marler[17] for TON. The CHClFBr molecule was considered to be rigid as well and was modelled using the OPLS force field[18]. Coulombic interactions were computed by using Ewald summations with a relative accuracy of 10^{-6}. The dispersive interactions of the adsorbate with the zeolite were modelled by Lennard-Jones (LJ) interactions between the atoms of the adsorbate and the atoms of the zeolite framework using Lorentz-Berthelot mixing rules. LJ interactions were truncated and shifted at 12 Å. The polarity of the molecules and zeolites was modelled by partial charges on the atoms. Table 1 lists all LJ parameters and partial charges. In addition to the standard Monte Carlo moves, rotation, translation, regrow, reinsertion and identity change, we also included ξ replica exchange moves and chiral inversion moves[8], which considerably improve the statistics for the adsorption of chiral and multicomponent mixtures.

All simulations were performed at 298 K and at constant pressures of 10^2 Pa for MEL, 10^{-2} Pa for TON and 10 Pa for MFI and MEL, which correspond to the saturation pressures for the various structures.

To analyse the energetics of our simulations, we made some comparative studies in vacuum of minimized clusters. These minimizations were calculated using the Baker method with a root-mean-square (RMS) and maximum (MAX) gradient tolerance of 10^{-6}.

3. Results

The computed adsorption isotherms of enantiopure CHClFBr in the four structures under study are shown in Figure 2. MEL, MFI and FER zeolites exhibited the highest loadings at around 2 mol/kg, whereas TON zeolite reached saturation at approximately 1.2 mol/kg.

Figure 3 shows the enantiospecific adsorption isotherms for chiral mixtures of CHClFBr in the same zeolite structures at the fixed values of pressure mentioned before. This implies that all zeolites were saturated and that the total number of CHClFBr molecules remained more or less constant during the runs, although the relative fractions of S and R enantiomers could still fluctuate significantly. The data presented in Figure 3 show the fraction of S enantiomers in the adsorbed phase as function of the same fraction in the gas phase. Naturally, these curves must go through the points (0,0) and (1,1), as well as (1/2, 1/2). The latter is a result of the symmetry of the system. If all
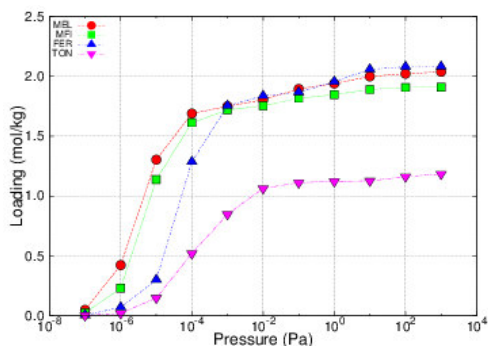
Figure 2. Computed adsorption isotherms of the *S*- enantiomers of CHClFBr as pure component in MEL (circles), MFI (squares), FER (up triangles) and TON zeolites (down triangles), at 298 K.

Figure 3. Representation of the fractional adsorbed phase of *S*-CHClFBr in the zeolites against the fractional content of the same component in the bulk phase. Solid line represents the results from MEL, dotted line show the values obtained for MFI, FER is represented by dashed line and double dot line is used for the results of TON.

atom coordinates were mirrored into a plane of symmetry of the zeolite, all of the chiral guest molecules would change identity. Because the energy of the system does not change as a result of this operation and the chemical potentials of the *S* and *R* enantiomers are identical for racemic mixtures, this mirror configuration must have exactly the same probability as its original. Hence, there cannot be an enantiomeric excess at this point.

MEL, MFI and FER show straight lines, indicating that the two components, *R* and *S*, are adsorbed at the same ratio as in the gas phase. This selective adsorption corroborates previous results on apolar molecules showing that pure silica zeolites are not selective[9,10]. However differently from the apolar molecule studies, CHClFBr in TON does show a heteroselective deviation from the straight line. A rationalization of this difference is that the polar CHClFBr molecules have long-range interactions. For apolar

molecules, the long-range interaction is established indirectly through the cations in the Al-substituted frameworks. Of course, having long-range interactions between enantiomers is not sufficient. These interactions should also be very specific, within the environment of the zeolite, to discriminate between $R-R$ (or $S-S$) and $S-R$ molecular interactions. Apparently, only TON is able to establish this distinction, in contrast to MEL, MFI and even FER, which is very similar to TON.

We also analysed the effect of Al substitutions. To quantify the enantioselective effect, we applied the adapted enantiomeric excess, ee*, as defined in ref 9, which graphically corresponds to the maximum vertical displacement, either positive or negative, from the diagonal in Figure 3. Homoselective adsorption results in
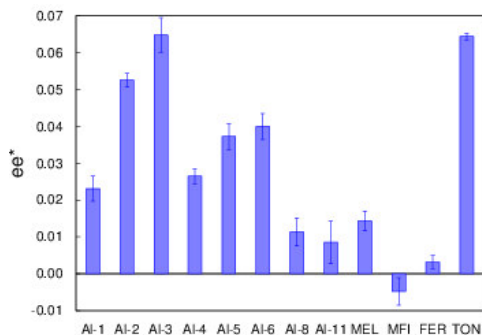
Figure 4. Enantiomeric excess values ee*, for all 8 Al-substituted MFI systems using calcium as extra-framework cation and the pure silica structures considered in this work.

Figure 5. Carbon-carbon distance between CHClFBr enantiomers. The solid line (red) represents the distances of S-S dimers, results from R-R dimers are plotted with a dashed line (green) and by a dotted line (blue) the distances for S-R dimers.

negative value, whereas heteroselective adsorption gives a positive value. Figure 4 shows that Al substitutions and concurrent inclusion of extra-framework cations increases the selectivity in MFI, as in studies of apolar molecules. However, all ee* values are strictly positive (except for a small negative value for pure silica MFI), indicating that heteroselective adsorption is the only type of enantioselectivity for CHClFBr. For apolar chiral molecules, both homoselectivity and heteroselectivity were observed[9,10]. To understand the mechanism of heteroselective adsorption with small polar molecules, we further focus on pure silica TON. We will try to rationalize why it is selective whereas the similar FER structure is aselective. For this purpose, we determined the carbon−carbon distance distribution for the different enantio pair combinations by averaging over all simulations, that is, for different S fractions in the gas phase.

In Figure 5, one can distinguish three main distances between the carbon atoms, at around 4, 5.5 and 7 Å, which correspond to the separation of cage centres in TON. Naturally, at large distances, there is no significant difference in the histograms of pairs having the same chirality, $R−R/S−S$ *versus* the histogram for pairs of opposite chirality, $S−R$. However, at small distances, there is a noticeable difference. The $S−R$ pair is able to get much closer than the $R−R$ or $S−S$ pair inside the TON zeolite. Related to this is the considerably higher occurrence of configurations with a C · · · C distance of less than 4 Å in $S−R$ pairs as compared to $R−R/S−S$ pairs, which is of sufficient magnitude to account for the observed heteroselective effect in Figure 3.

To isolate the possible energetic origin of this effect, we analysed minimum-energy dimer configurations in vacuum using the Baker optimization scheme starting from several randomized initial

conditions. As result, we obtained the global minima of the $S-R$ and $R-R$ (or $S-S$) dimers in addition to many local minima. Considering the global minima, we detected that the energy of the $R-R$ dimer is lower than this of the $S-R$ dimer (-1253.19 *versus* -1228.93 k_BK). From these data alone, one would rather predict homoselective behaviour instead of the observed heteroselectivity. However, based on a simple geometrical argument, one can exclude both global minimum configurations when considering the zeolite as well. Carbon–bromine is the longest bond in the CHClFBr molecule. One can consider the channels of TON as cylinders with a small radius of the same size. Then, it is evident that the dimer configurations, minimized in vacuum, can fit in the zeolite channels only if the carbon–bromine bonds of the two molecules are almost parallel to the carbon–carbon intermolecular axis. This is not the case for the global minimum configurations, as one can see in Figure 6.

This hypothesis can be quantified by analysing the angular distribution of the molecules inside TON zeolite. We considered the angle between the C–Cl, C–H, C–F and C–Br bonds and the Cartesian axes, with the Z axis parallel to the zeolite channel. As before, we averaged over all simulations. The distribution shown in Figure 7 confirms our geometrical argument. The cosine of the angle between the carbon–bromine bond and the Z axis is peaked around 1, indicating that the carbon–bromine bond is almost always parallel to the axis of channel. Interestingly, the angular distribution of the C–H bond
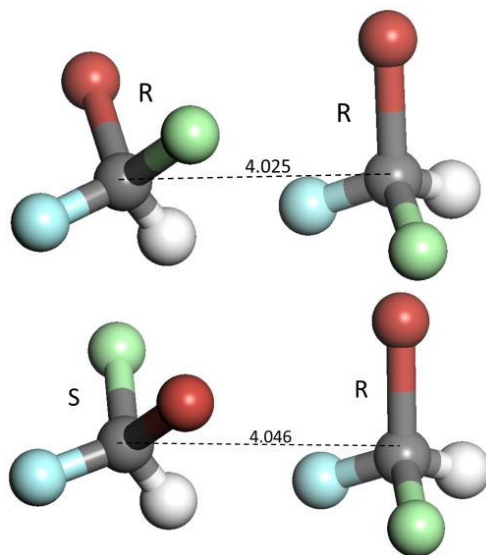
Figure 6. Snapshot of the optimized dimeric configurations R-R (top) and S-R (bottom) in vacuum. Carbon atoms are represented in grey, hydrogen atoms in white, bromine atoms in red, chlorine atoms in green and fluorine in blue. Carbon-carbon distances are given in angstroms.

with the X axis is even more peaked. This is due to the shape of the channel having a cross section that is not completely cylindrical but rather elliptical. The cylindrical pore is narrower along the X axis, making its direction accessible only by the smallest bond.

Based on these findings, we re-examined our set of minimized dimer configurations considering only the local minima having bromine as the outer atoms. If viewed from the top along the Br–C$\cdots$C–Br axis, the two types of configurations can be characterised as what we call triangular and hexagonal. The first type has an $R-R$ enantiomer as a minimum, whereas the second has $S-R$ as the minimum (see Figure 8).
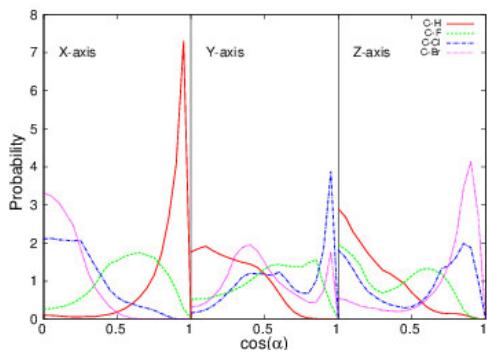
Figure 7. Angular orientation of CHClFBr in TON (α is the angle described by C-X vector and the Cartesian axis). Solid (red), dashed (green), dash-dotted (blue) and dotted (pink) lines show the results of carbon-hydrogen, carbon-chlorine and carbon-bromine respectively.

Figure 8. Snapshot of the optimized dimeric configurations R-R (top) and S-R (bottom) in vacuum with the Br-C...C-Br distributions. Carbon atoms are represented in grey, hydrogen atoms in white, bromine atoms in red, chlorine atoms in green and fluorine atoms in blue. Distances between atoms are given in angstroms.

Figure 9 shows a cartoon representation of the top view of the $R-R$ dimer that looks like a triangle, where the atoms are "superimposed" (their separation is mainly along the Z axis, which is perpendicular to the page). The two molecules show a small inclination that results in a larger separation distance between the two chlorine atoms with respect to the separation of the oppositely charged hydrogen and fluorine atoms. On the other hand, the $S-R$ configuration viewed from the top looks hexagonal. By considering solely the Coulombic energy due to partial charges of neighbouring atoms, one can decipher why these configurations are the lowest in energy for the triangular and hexagonal dimer configurations. If one considers all possible permutations of the atoms in the lower molecule with the atoms in the upper molecule held fixed, the energy always goes up. There are two negative charges and only one positive charge. For the triangular case, it is clear that, to obtain the lowest

energy, one should superimpose the atoms with the positive charge on the most negatively charged atoms. This gives the highest possible negative Coulombic energy term twice and the smallest possible positive energy term (by the pairing of the smallest negatively charged atoms) once. Similarly, for the hexagonal structure, one should position the positively charged atom of the lower molecule between the negatively charged atoms of the upper one. In addition, the most negatively charged atoms should be kept away from each other. This simple reasoning explains why the triangular configuration has an $R-R$ (or $S-S$) dimer as the minimum energy structure, whereas the minimum-energy structure is an $S-R$ dimer for the hexagonal structure. Again, the $R-R$ triangular dimer energy is lower than the $S-R$
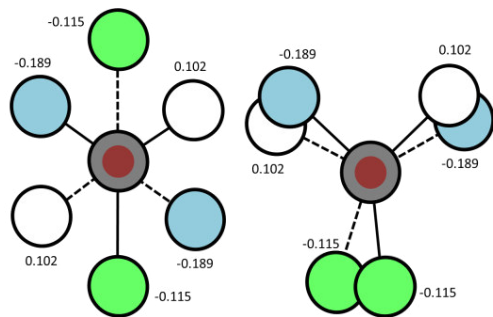
Figure 9. Schematic representation of the top view of *R-R* (left) and *S-R* (right) dimeric configurations, with the R enantiomer on top. The partial charges (e⁻) of each atom are also indicated. Carbon atoms are represented in grey, bromine atoms in red, chlorine atoms in green, fluorine atoms in blue and hydrogen atoms in white. Dashed bonds refer to the bonds of the lowest molecule.

hexagonal dimer, in contradiction to what one would expect because the adsorption is heteroselective. However, only the hexagonal structures were actually found in the MC simulations of CHClFBr molecules inside the zeolite. As expected, some of the structures were hexagonal $R-R$ or $S-S$ dimers, but the majority, were $S-R$ dimers. Hence, only hexagonal dimer configurations fit in the zeolite channel and the lowest energy for these types of dimer configurations is obtained by the enantio pair $S-R$. These two facts together explain why $S-R$ molecules can be much closer inside TON than $R-R$ or $S-S$ dimers and why the adsorption isotherm is heteroselective. Regarding this aspect, the only question remaining is: Why do the triangular dimer configurations not fit?

To understand this situation, considering the zeolite channel as a cylinder with an elliptical cross-sectional area is insufficient. The smallest possible imaginary ellipse that encapsulates all atoms of Figure 9 is not smaller for the hexagonal structure than it is for the triangular structure. To understand the fact that no triangular configurations occur inside the zeolite, we performed the following analysis. We took a snapshot of one of the MC simulations in which a hexagonal $S-R$ dimer configuration was detected (with a C · · · C distance of less than 4 Å). We eliminated all of the other molecules and minimized the structure. The minimization resulted in only small reorientations (e.g., C · · · C changed from 3.62 to 3.64 Å) and a lower energy compared to the initial energy (-22644 *versus* -23514 k_BK). Then, we took a triangular R−R dimer from the vacuum minimization and translated and rotated this configuration into an empty zeolite to obtain approximately the same orientation inside the zeolite as the hexagonal $S-R$ dimer. That is, the C · · · C midpoint was matched, as well as the C · · · C angular orientation.

Finally, a rotation along the C · · · C axis was performed to obtain the same angle between the C−H bond of the R enantiomer and the X axis. The geometry and energy of this artificially created zeolite−dimer configuration was then analysed before and after energy minimization. The minimization caused a significant deviation from the initial conditions. The C · · · C distance increased from 3.8 to 4.8 Å and the energy decreased from +1264 to −21061 k_BK, indicating that the triangular

configuration does not allow the two molecules to remain close when positioned inside the zeolite. This minimized structure was therefore disregarded in the further analysis.

Figure 10 shows the top and side views of the minimized hexagonal $S-R$ configuration inside the channel of TON and of the initial triangular $R-R$ configuration. Regarding the top views, it is far from obvious why the triangular configuration does not fit. None of the atoms in the triangular configuration seem to be much closer to the "cylinder wall" than the atoms in the hexagonal configuration. Only if one inspects the side views of the configurations inside the channel can a major mismatch be detected. The initial value of one of the chlorine−oxygen distances is 2.38 Å for the triangular $R-R$ configuration, which is in the repulsive region of their LJ interactions. In the top view, all chlorine atoms seem to be equally close

to the oxygens of the zeolite, but this is deceptive because the relative orientations along the Z direction are not visible. The hexagonal structure with C−Cl bonds pointing in the positive and negative Y directions avoids Cl−O distances that are too small by having the two Cl atoms at different Z values with respect to the closest oxygen inside the zeolite ring. The triangular configuration, with both chlorine atoms pointing in the positive Y direction, is not able to do the same. One of the Cl atoms will meet a nearby oxygen inside the cylindrical wall having approximately the same positioning along the Z axis, which causes a high penalty to the total energy of the system. Hence, the cylindrical model is not sufficient to describe the observed enantioselectivity. Both the elliptical shape of the cross-sectional area and the corrugation of the potential energy field along the channel are important parameters to
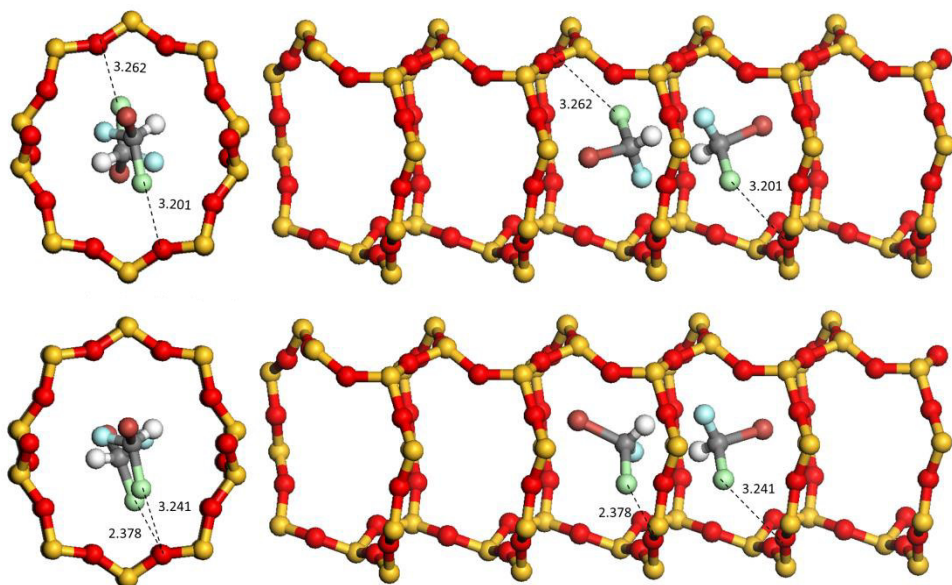
Figure 10. Top and side views of CHClFBr molecules in the optimized *S-R* (top) and initial *R-R* (bottom) dimeric configurations. Distances between atoms are given in angstroms.
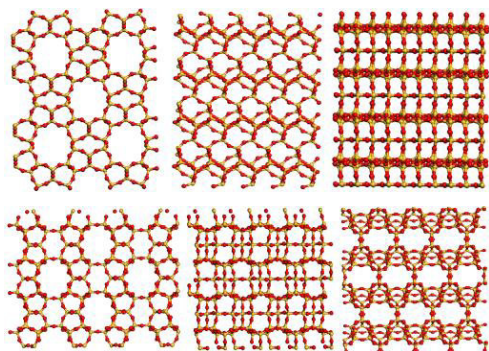
Figure 11. Comparison of TON (top) and FER (bottom) zeolites, including views of the X-Y (left), Y-Z (center) and X-Z (right) planes.

understand the heteroselectivity of this system.

Finally, we briefly discuss why enantioselectivity is absent in FER even though it has a similar channel-type structure with even narrower pores. Naively, one would expect that the smaller channel diameter would enhance the subtle packing differences between $R-R$ (or $S-S$) and $S-R$ dimers. However, although the top view indeed suggests that FER has narrower pores than TON (see Figure 11), the side view shows more open windows at the sides of the principal channels in the $X-Z$ plane. This particular topology gives too much rotational freedom to the CHClFBr molecules, thereby destroying any possible enantiospecific packing effect.

Conclusions

In this work, we have shown the enantioselective capacities of achiral zeolites when adsorbing small polar molecules. The previous studies with nonpolar molecules were the first proof of principle that achiral zeolites can have chiral discrimination power, but it is difficult to exploit this effect for industrial applications. Doing so requires a special siting of aluminium atoms in the framework that is not yet under control in the synthesis processes of zeolites. Moreover, chiral alkanes presumably have very low diffusion constants in MFI zeolites. In contrast, the small chiral polar molecules studied in this work do not depend on Al substitutions to show enantioselectivity and diffuse much more rapidly. This brings technological applications closer to reality. The effect of selectivity has a strong dependence on topology, because zeolites that are assumed to be similar can show different adsorption behaviours. For instance, both TON and FER are zeolites containing nonintersecting channels, but only TON is selective for the studied molecule. The molecular mechanism responsible for heteroselectivity in TON is fundamentally different from that of chiral apolar molecules in Al-substituted zeolites. The reason for the difference is that polar molecules have long-range interactions and, therefore, do not need to rely on indirect interactions through extra-framework cations. The mechanism is explained by the fact that enantiomers of opposite chirality are able to approach each other at much smaller distances than enantiomers of identical chirality within the TON zeolite channel. The standard representation of the channel of the zeolite as a simple cylinder is not sufficient to explain this effect. The ellipticity of the cross section and corrugation of the potential field along

the channel's axis are additional parameters that are needed to describe this enantioselective packing effect. This understanding allows for the rationalization of the best material and conditions for the optimal enantiopurification and separation of chiral mixtures.

Bibliography

(1) Maier, N. M.; Franco, P.; Lindner, W. *Journal of Chromatography A* **2001**, *906*, 3.

(2) Guebitz, G.; Schmid, M. G. *Journal of Chromatography A* **2008**, *1204*, 140.

(3) Breuer, M.; Ditrich, K.; Habicher, T.; Hauer, B.; Kesseler, M.; Sturmer, R.; Zelinski, T. *Angew. Chem.-Int. Edit.* **2004**, *43*, 788.

(4) Blaser, H. U.; Muller, M. *Stud. Surf. Sci. Catal.*, 1991; Vol. 59, 73-92.

(5) Li, Y.; Yu, J. H.; Wang, Z. P.; Zhang, J. N.; Guo, M.; Xu, R. R. *Chemistry of Materials* **2005**, *17*, 4399.

(6) Tang, L.; Shi, L.; Bonneau, C.; Sun, J.; Yue, H.; Ojuva, A.; Lee, B.-L.; Kritikos, M.; Bell, R. G.; Bacsik, Z.; Mink, J.; Zou, X. *Nature Materials* **2008**, *7*, 381.

(7) Sun, J.; Bonneau, C.; Cantin, A.; Corma, A.; Diaz-Cabanas, M. J.; Moliner, M.; Zhang, D.; Li, M.; Zou, X. *Nature* **2009**, *458*, 1154.

(8) van Erp, T. S.; Dubbeldam, D.; Caremans, T. P.; Calero, S.; Martens, J. A. *Journal of Physical Chemistry Letters* **2010**, *1*, 2154.

(9) Caremans, T. P.; van Erp, T. S.; Dubbeldam, D.; Castillo, J. M.; Martens, J. A.; Calero, S. *Chemistry of Materials* **2010**, *22*, 4591.

(10) van Erp, T. S.; Caremans, T. P.; Dubbeldam, D.; Martin-Calvo, A.; Calero, S.; Martens, J. A. *Angew. Chem.-Int. Edit.* **2010**, *49*, 3010.

(11) van Erp, T. S.; Dubbeldam, D.; Calero, S.; Martens, J. A. *Chemical Engineering Science* **2010**, *65*, 6478.

(12) Castillo, J. M.; Vlugt, T. J. H.; Dubbeldam, D.; Hamad, S.; Calero, S. *Journal of Physical Chemistry C* **2010**, *114*, 22207.

(13) Robinson, D. B.; Peng, D. Y.; Chung, S. Y. K. *Fluid Phase Equilibria* **1985**, *24*, 25.

(14) Vankoningsveld, H.; Vanbekkum, H.; Jansen, J. C. *Acta Crystallographica Section B-Structural Science* **1987**, *43*, 127.

(15) Fyfe, C. A.; Gies, H.; Kokotailo, G. T.; Pasztor, C.; Strobl, H.; Cox, D. E. *Journal of the American Chemical Society* **1989**, *111*, 2470.

(16) Morris, R. E.; Weigel, S. J.; Henson, N. J.; Bull, L. M.; Janicke, M. T.; Chmelka, B. F.; Cheetham, A. K. *Journal of the American Chemical Society* **1994**, *116*, 11849.

(17) Marler, B. *Zeolites* **1987**, *7*, 393.

(18) CostanteCrassous, J.; Marrone, T. J.; Briggs, J. M.; McCammon, J. A.; Collet, A. *Journal of the American Chemical Society* **1997**, *119*, 3818.

Enantiomeric Adsorption of Lactic Acid in Achiral Zeolites

Ana Martín-Calvo, Sofía Calero, Johan A. Martens
and Titus S. van Erp

9

We studied the adsorption of chiral mixtures of lactic acid in several zeolites. All zeolite systems showed either no selectivity or heteroselectivity in which the minority enantiomer is adsorbed by a higher fraction than its fraction in the reservoir. Analysis of the mechanism showed that none of the previously identified origins of enantioselective adsorption of scalemic mixtures applies to lactic acid. However, based on the lack of any ordered distribution in the adsorbed phase we postulate a new mechanism that is likely to be very generic for chiral adsorption processes that proceed via chaotic packing of the adsorbate molecules. The new mechanism can explain several characteristics of the adsorption data and hints on new prospective separation methods with a high potential for pharmaceutical applications.

1. Introduction

There is a strong need for alternatives to conventional petrochemical processes using renewable sources. On the search for substitutes to the conventional plastic production from petroleum oil, lactic acid (LA) represents a reliable alternative as it is used for the production of bio-plastics[1]. Monomers of this molecule and its cyclic di-esters (lactide) are used to produce polylactic acid (PLA) which has applications as biodegradable plastics with low emissions of carbon dioxide. Condensation and polymerization are the procedures involved for monomers of lactic acid and lactide, respectively. For the production of PLA the stereo-purity of the lactic acid is of key importance. The mechanical properties and the thermal- and hydrolysis-resistance of the resulting materials are enhanced if a stereo-complexation of

enantio-pure S-PLA and R-PLA is used in the procedure[2]. Mixtures of both enantiomers result in amorphous PLA which can be only used for the production of plastics of low quality. Additionally lactic acid is also used in the production of added-value chemicals and intermediate building blocks[1,3] while its R-form has also medical applications as a marker for bacterial infections[4]. Lactic acid can be obtained in two different ways: 1) by microbial fermentation of sugarcane or corn starch, among other sources, or 2) by chemical synthesis. The fermentation procedure mainly results in S-LA, while the chemical synthesis leads to racemic mixtures of the S- and R- enantiomers of lactic acid. The main problem for making these biomaterials commercially attractive is the extremely high cost of obtaining pure R-LA. For this reason the separation of enantiomers from racemic mixtures of lactic acid seems as

an alternative for the production of the pure enantiomers.

Zeolites contain channels and/or cages of molecular dimensions and are hence ideally suited for molecular separation. However, enantioselective adsorption generally requires chiral adsorbents while only 8 chiral zeolite topologies are known today[5-8]. In addition, these structures are often thermally unstable and show asymmetry that is developed on a length scale of several nanometres. This makes them less appropriate for recognition by the smaller enantiomers. Given the richness of symmetric zeolites the chance of finding an ideal match between adsorbent and adsorbate would be much higher if we could use achiral zeolite structures for enantioselective adsorption. In previous publications[9-13] we showed that this is indeed possible under certain conditions provided that the adsorbate is a scalemic mixture of the enantiomers. Enantio-enhancement or even enantioseparation[11] is possible whenever there is a right match between adsorbate mixture, zeolite-topology and the possible presence of extra-framework cations.

Caremans *et al.*[9] and van Erp *et al.*[10,13] were the first to demonstrate this potential for enantioseparation of non-polar alkanes (4,4-ethylmethyloctane) in achiral aluminium-substituted MFI zeolites. The mechanism behind this selectivity is remarkable since the enatiomers have only short-range interaction and adsorb at the intersections of the MFI channels that are relatively far away from each other. Each intersection can only be occupied by a single enantiomer, so it seems impossible for molecules to feel each other inside the zeolite, let alone recognize their mutual chirality. The phenomena was explained by the so-called "chiral cell" model[9,10,13] in which the extra-framework cations with their long-range Coulombic interaction can mediate an indirect interaction between the enantiomers. Depending on the aluminium distribution and the type of cations used to balance the net charge of the system, different adsorption behaviours are observed: a) homoselective, if the presence of an enantiomer in the zeolite favours the adsorption of the same type of enantiomer; b) heteroselective, when the adsorption of an enantiomer is reduced by the presence of the same type of enantiomers in the zeolite; and c) aselective, if both enantiomers adsorb in the zeolite with the same ratio than in the reservoir. In order to tune this behaviour for practical applications, it would be required a high control of positioning aluminium atoms at specific sites, which is yet beyond present zeolite synthesis technology. Moreover, the packing of enantiomers in the zeolite needs to be tight in order to give a difference between the adsorption of the left- and right-handed molecules. As a consequence, diffusion coefficients might be very low which also reduces its practical implementation. However, we recently showed that the enantioselective effect can also exist for the adsorption of small polar molecules, such as chlorofluorobromomethane[11]. The polarity of the molecules creates stronger direct interactions between the molecules which makes the presence of cations and specific aluminium frameworks unnecessary. The case of

chlorofluorobromomethane showed only heteroselective adsorption, besides aselective adsorption and its mechanism is completely different from that of the chiral alkanes in aluminium-substituted zeolites. In the CHClFBr case the formation of pairs of enantiomers with opposite chirality, creating energetically stable structures, are causing the heteroselective effect. Pairs of identical enantiomers were in even lower energy when considered in vacuum. However, these pairs did not fit inside the channels of the zeolite without breaking the favourable configuration.

In this work we study by computer simulations the adsorption behaviour of mixtures of lactic acid, using MFI and its aluminium-substituted forms as molecular sieves. We analyse the effect of the type and number of cations as well as the influence of the temperature into the process. This is the first study to this enantioselective effect in achiral zeolites for lactic acid that in its enantiopure form has high potential for industrial and medical applications. The relatively large availability of enantiopure S-LA, via fermentation[3,14], and racemic LA mixtures, via catalysis[15], makes possible to create large amounts of scalemic mixtures in which the S-form is in excess. Therefore, the above-described mechanism for enantioseparation in achiral zeolites becomes very interesting since it requires an initial feed that is scalemic (not 50/50). However, in order to get the enantiopure R-form, which cannot be obtained from fermentation, we would in principle need homoselective adsorption. In such a case the S-form, which is in majority, would completely

adsorb excluding the R-form in its enantipure form from the zeolite. This work shows that the heteroselective behaviour seems far more easily to obtain when considering polar molecules. We provide an analysis for this phenomenon and postulate a new mechanism, the "random cell" model, which is fundamentally different from previously studied cases. The model explains the heteroselective trend and the steep slopes in isotherms at the enantiopure limits.

2. Simulation methods and models

We use Configurational Bias Monte Carlo (CBMC) simulations in the grand canonical ensemble to compute adsorption isotherms. In this ensemble chemical potential, volume and temperature are fixed. The zeolites are considered as rigid structures using the crystallographic positions of the atoms of MFI zeolite reported by van Koningsveld et $al.$[16]. The enantiomers of lactic acid have been modelled as flexible full atom models using harmonic potentials for bonds and bends and TraPPE dihedrals for proper and improper torsions. The parameters of these potentials are based on CVFF force fields[17,18]. A representation of the enantiomers is depicted in Figure 1.

The interactions between the atoms of the system are defined by Lennard-Jones and Coulombic potentials. Partial charges of the structure are taken from a previous publication of Calero et $al.$[19] while Lennard-Jones parameters are obtained from DREIDING generic force field[20]. Lennard-Jones parameters of lactic acid are also from CVFF force

fields[17,18]. These parameters are collected in Table 1.

Coulombic interactions are computed using the Ewald summation method with a relative precision of 10^{-6}. The Lennard-Jones interactions adsorbate-absorbent and adsorbate-adsorbate are obtained from Lorentz-Berthelotz mixing rules using a cut off of 12 Å. Besides standard Monte Carlo moves such as rotation, translation, reinsertion and identity change, we also include ξ-replica exchange and chiral inversion moves[13] to improve the statistics of the adsorption in multicomponent mixtures.
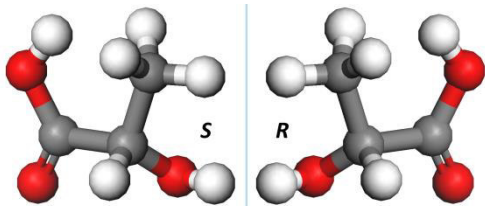
Figure 1. Representation of the two enantiomers (S and R) of lactic acid. Carbon atoms are colored in grey, oxygen atoms in red and hydrogen atoms in white.

Table 1. Lennard-Jones parameters and partial charges of the atoms used in this work. *Corresponds to the oxygen atoms of the zeolite connected to aluminium atoms.

Atom	ε/k_B	σ(Å)	Charge (e-)
O_{zeo}	48.208	3.033	-1.025
Oa_{zeo}*	48.208	3.033	-1.200
Si	156.161	3.804	2.050
Al	156.161	3.911	1.750
Na	251.872	2.800	1.000
Ca	25.187	3.093	2.000
C_{COOH}	74.476	3.617	0.240
C_{chiral}	19.625	3.875	-0.070
C_{CH3}	19.625	3.875	-0.030
Ola	114.734	2.859	-0.380
H_{CH}	19.122	2.449	0.100
H_{OH}	-	-	0.300

Simulations were performed using the in-house RASPA code developed by Dubbeldam *et al.*[21].

3. Results

Experimental adsorption data of lactic acid from fermentation on zeolite molecular sieves, show the capacity of MFI zeolite to adsorb lactic acid up to 46.10 g/kg (ca. 4 molec/uc) from aqueous solution at room temperature[14]. In computer simulations the conditions of the reservoir are determined by the fugacity and the ratio of left- and right-handed molecules in the bulk. Lactic acid is difficult to get into a gas-phase for which the fugacity would be close to the gas-pressure, but in principle this fugacity is directly related to the chemical potential and to the activity coefficient of the solvent that could be matched to the experimental value. Another more practical approach that we applied is to fix the total number of lactic acid molecules in the zeolite to 4 molecules per unit cell, which would correspond to lactic acid adsorption from the aqueous phase. In addition we focussed on the hypothetical case for which we can increase the fugacity in a similar way as we can do for gas-phase adsorption to investigate the limit of maximal loading. In that situation we expect to find strongest effects regarding enantioselectivity since the packing becomes crucial here. By increasing the fugacity we discovered that our force field model of MFI and lactic acid shows a saturation capacity of 173 mg/g or 11 molecules lactic acid per unit cell. Therefore, in our analysis we compare the enantioselective effect

of both loadings: 4 and 11 molecules per unit cell.

A method to quantify the effect of the enantioselectivity is to obtain the adapted enantiomeric excess, *ee** as proposed by Caremans *et al.*[9] (Figure 2). A graphical representation of this *ee** corresponds to the maximum vertical displacement, either positive or negative, from the diagonal (aselective behaviour) in a plot where the fraction of *S*-molecules adsorbed is given as function of the fraction of *S*-molecules in the reservoir (see Figure 3). Since the adsorbent is not chiral, a curve like this has to be point-symmetric passing through the (0.5, 0.5) point. A positive or negative deviation in the first half of the curve indicates heteroselective and homoselective adsorption, respectively. Figure 2 compares the enantiomeric excess for both loadings of lactic acid in

pure silica MFI and its 8 aluminium-substituted version using both Na$^+$ and Ca^{2+} cations. The aluminium-substituted structures have been obtained by exchanging eight silicon atoms of the structure by aluminium in T-Site positions 1, 2, 3, 4 5, 6, 8 and 11. Positions 7, 9, 10 and 12 were disregarded due to violation of the Löwenstein´s rule[22]. Additionally we compare the results obtained for MFI systems with these obtained for saturated pure silica zeolites FER and TON (with 4 and 2 molec/uc, respectively).

As observed in Figure 2 all calculated *ee** values are positive or close to zero. This indicates that enantioselectivity, if it occurs, is mainly heteroselective. The selectivity for the aluminium-free zeolites is not very significant as found in previous studies on chiral
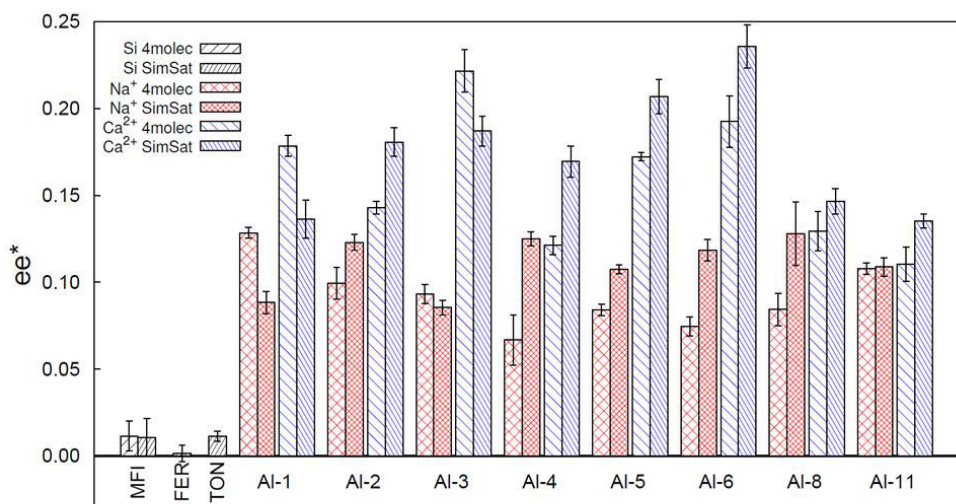
Figure 2. Comparison of the enantiomeric values, ee*, for pure silica MFI, FER and TON (black) and the eight Al-substituted derivate of MFI using both sodium (red) and calcium (blue) as extra-framework cation. We compare the results obtained for the maximum average loading of each structure (11 molec/uc in MFI, 4 molec/uc in FER and 2 molec/uc in TON) and MFI systems with 4 molec /uc.

alkanes[9,10,12,13]. The total absence of any homoselective system is in disagreement with the alkanes systems, but similar behaviour was found for other small polar molecules like CHClFBr[11]. On the other hand, CHClFBr showed also significant heteroselective adsorption for some pure silica zeolites like TON, which is not selective when considering lactic acid.

Overall, the zeolites with calcium seem to give stronger selectivities compared to sodium. This could be attributed to a higher degree of asymmetry due to an asymmetric positioning of Ca^{2+} between two aluminium atoms[9,10,12,13]. On the other hand, the difference in selectivity between 4 or 11 molecules per unit cell is smaller than one would expect. This suggests that the selectivity is mainly driven by specific lactic acid-cation packing rather than packing effects between the adsorbing molecules. Since the MFI framework having aluminium in T-Site 5 with Ca^{2+} was the model system that was best understood regarding homoselectivity of alkanes, we further focus on this system (Al-5). In Figure 3 we show isotherms for maximum loading (11 molec/uc on average) in which we plot the fraction of S-molecules adsorbed versus its fraction in the reservoir. When considering the room temperature curve (300 K) the steepness of the curves near the enantiopure limit is in particular interesting. For separation purposes this implies that the system should be very effective in removing the enantiomer in lower amount in an almost enantiopure mixture. This is usually the most expensive step in pharmaceutical enantioseparation-processes, which

requires very high degrees of enantiopurity. In other words, if we have mixtures with only a small fraction of S-lactic acid, this zeolite system should be very effective in removing the remaining S-fraction from the reservoir within a single step batch process. The process seems less suitable for getting such a mixture in the first place. From the racemic mixtures obtained from synthesis and enantiopure amounts of S-lactic acid from fermentation we are able to create scalemic sources in which the S-enantiomer is in excess. However, we would need a homoselective adsorption process in order to extract from such a solution a mixture in which the R-enantiomer is in excess. The applications of the zeolitic systems discussed here would, therefore, still require an external source such as a chiral-catalytic process or another homoselective zeolite that we have not discovered yet.
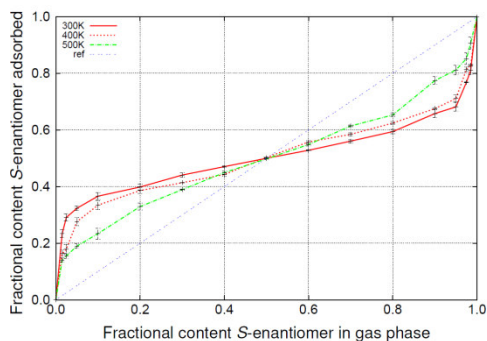
Figure 3. Representation of the fractional adsorbed phase of S-LA against the fractional content of the same component in the bulk phase, at 300 K (red line), 400K (dashed red line) and 500 K (green dashed line).

Figure 3 shows the fraction of *S*-lactic acid adsorbed in the Al-5(Ca^{2+}) zeolite *versus* the fraction of *S*-lactic acid in the reservoir for temperatures of 400 and 500 K. Besides giving the temperature-dependence of the enantioselective strength, high-temperature simulations were carried out in order to investigate possible ergodicity problems of the sampling at low temperature. For instance the acceptance of an identity-change move is only 0.0038% at 300 K. As a consequence we needed to perform a massive number of MC moves up to 800 thousand cycles in which we try to change the enantiomeric identity. In addition, the replica exchange and chiral inversion moves[12] support the enantiomeric conversion even further. Still, it is not impossible that configuration space is not well sampled under such conditions. This acceptance move increases till 0.0087% at 500 K.

Figure 3 shows that the adsorption selectivity decreases for increasing temperatures. Still, even at 500K the heteroselective behaviour is significant. This suggests that the origin of the selectivity is energetic rather than entropic. In addition, the fact that the heteroselectivity remains even after many *R*-*S* exchange moves is reassuring for the behaviour found at 300 K.

To see the effect of the number of cations on the heteroselective strength of the adsorption, we generate structures with different aluminium content (always in T-Site position 5). Figure 4 shows the adsorption behaviour of four different structures with 2, 4, 6 and 8 aluminium atoms, using calcium as extra-framework
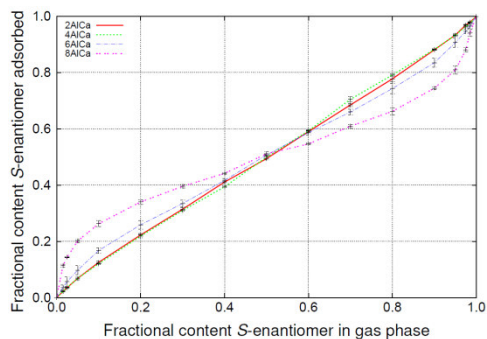
Figure 4. Representation of the fractional adsorbed phase of *S*-LA against the fractional content of the same component in the bulk phase, at 500K. Comparison of structures with 2 (red line), 4 (dashed green line), 6 (dashed blue line) and 8 aluminum per unit cell (dashed pink line).

cation. Results obtained for systems with sodium can be found in Appendix 6. For efficiency reasons (higher acceptance rate), we made this analysis at 500 K, where heteroselective adsorption is still high. For the structures with less than 8 aluminium atoms per unit cell, we generate a set of different random configurations. The results shown in Figure 4 are averaged out over these different structures.

Figure 4 shows that small amount of aluminium in the structure (and therefore few cations), up to 4 atoms/uc, are not enough to induce chiral modification for scalemic mixtures. Only with 6 Al/uc this effect becomes significant. The presence of only heteroselectivity and no homoselectivity regardless the zeolitic system is similar to our study of CHClFBr adsorption. For these systems[11], the reason for heteroselectivity was found in the

formation of molecular pairs in the zeolite that consist of enantiomers with opposite chirality. The paired enantiomers form energetically favourable conformations with short centre-of-mass distances. Pairs of identical enantiomers were even lower in energy regarding the gas phase. However, these did not fit into the zeolite as was shown by the distribution of separation distances between the different enantiomers in the zeolite. In order to examine whether the same mechanism applies to lactic acid, we computed the carbon-carbon distance distribution for the different enantiomeric pairs. The average distribution over all simulation results of Al-5 (Ca^{2+}) is given in Figure 5.

Clearly, the distribution seems not to give any indication for enhanced pair-formation for R-S versus R-R or S-S pairs as was found for CHClFBr[11]. Below 4 Å the distribution function drastically drops and there is no significant difference between R-S pairs versus S-S/R-R pairs. At larger distances there seems to be some deviation which must be attributed to statistical errors since the R-R and S-S curves should in principle coincide at infinite simulation time. So the differences between the two curves are only indicative for the inaccuracy or not complete ergodic sampling. With this in mind we cannot distinguish between the distance-distribution of opposite *versus* identical enantiopairs. Henceforth, the mechanism that causes heteroselective adsorption in lactic acid must be different from that of CHClFBr. Additionally the distributions between the two enantiomers and the calcium
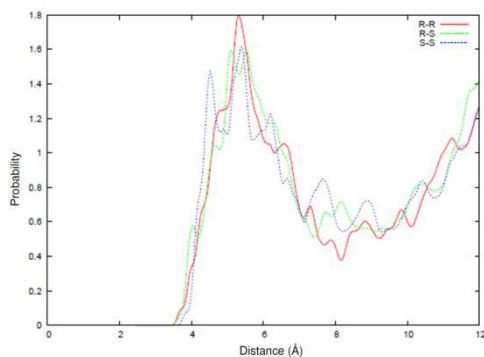
Figure 5. Carbon-carbon distance between lactic acid enantiomers. The solid (red), dashed (green) and dotted (blue) lines represent the distances of R-R, R-S and S-S dimers, respectively.

cations have also been computed, averaged and for a fixed ratio, but they did not reveal a significant difference that could explain the heteroselective effect.

Since the heteroselectivity seems not to be related to the lactic acid intermolecular orientation, we can assume that it originates from the interaction between lactic acid at one side and the zeolite and extra-framework cations at the other side. In this respect it would resemble the alkane adsorption in aluminium substituted MFI[9,10,12,13]. There, the mechanism was induced to a highly ordered packing of alkanes and cations into the zeolite intersections. The cation positions alternated between the upper and lower aluminium at the entrance of the zigzag-channels making a motif that resembles the knight jumps on a chessboard[9,10,12,13]. The packing of the lactic acid and cations in Al-5 (Ca^{2+}) is, however, completely different. While the inclusion of the branched alkanes is
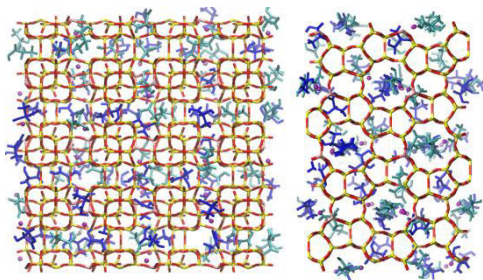
Figure 6. Snapshots of the distribution of the molecules of lactic acid in MFI-Al5 (Ca^{2+}) equimolar system at 300 K. Comparison of *X-Y* (left) and *Z-X* (right) views. *S*-LA is represented in light blue, *R*-LA in dark blue and calcium cations in purple.

confined to the intersections of the zeolite channels, lactic acid can be found in both the channels and the intersections as shown in Figure 6. The calcium ions remain more or less between the aluminium atoms since they establish an effective negative charge into the zeolite network. However, the polar lactic acid shows a much higher capacity than apolar alkanes in decoying the cations away from their zero-loading ground state positions. As a result, the alternating pattern of the cations is lost and also the packing of the lactic acid molecules seems highly chaotic compared the 4,4-ethylmethyloctane packing in the same zeolite.

Even after intensive searches for patterns, we were not able to identify a very specific packing mechanism, as we found for CHClFBr and 4,4-ethylmethyloctane, that could explain the significant enantioselective effect. However, we observe that, when we investigate more complex systems or systems with stronger short-range interactions, heteroselectivity occurs much more often than homoselectivity[11]. Homoselectivity requires a highly ordered packing while heteroselectivity can occur in ordered or in chaotic systems. On second thought, we can postulate reasonable conjectures why this is so. In fact, after all our searches for patterns it might well be that exactly, the absence of order causes the heteroselective adsorption effect. We can explain this as follows. Consider an enantiomeric mixture in the reservoir that is close to the enantiopure limit. Once this mixture starts to adsorb into the zeolite the majority enantiomer will be dominant in the zeolite as well. However, if these enantiomers fail to create a highly structured packing in the confined spaces it will leave, at some point, all type of cavities of all type of shapes. For instance, if the zeolite is filled up to 80% of full loading, the remaining space forms potential adsorption sites for the non-adsorbed reservoir enantiomers. These adsorption sites can be more or less spherically symmetric with no specific preference for left- or right-handed molecules, or can be asymmetric with preference to receive either the majority or minority enantiomer. The majority enatiomer will fill up the first two types of cavities, but then there might well be a significant fraction of adsorption sites left that are only accessible by the minority enantiomer. Hence, we expect a strong heteroselective effect whenever this last fraction of chiral adsorption cavities is much larger than the fraction of the minority enantiomer in the reservoir. This model, which we name as the "random cell" model, explains very well

the steepness of the slopes in Figures 3 and 4 at the enatiopure limits. From the fact that these curves always pass through the (x,y)=(0,0), (0.5,0.5) and (1,1) points, one expects the largest deviation from the straight diagonal line, if any, somewhere in the middle of these points at the x-values 0.25 or 0.75. This is true for most packings that occur in an ordered fashion[9,10,12,13], but not for this or similar cases.

One point of caution needs to be made. Chaotic packing in a MC simulation does not necessarily imply that nature will be chaotic as well. Besides systematic uncertainties as force field parameters, ergodic sampling is also very difficult in these systems. In retrospect, it is not surprising that our initial results of the chiral alkanes in aluminium substituted MFI zeolites showed heteroselective behaviour before we developed our improved MC moves[13]. Once we improved our MC sampling, the system found a highly ordered packing and changed completely from heteroselective to homoselective (see Fig. 2 in ref 13). It is therefore not impossible that we do not reach the right highly ordered packing due to the limitations of our MC method. Parallel tempering might be helpful to improve the ergodicity of the sampling[23] but it would require a lot of additional simulations at elevated temperatures. Maybe more promising is the Continuous Fractional Component Monte Carlo method[24,25], that can in some cases drastically increase the ergodicity of the sampling. Another point to realize is that for some systems even reality might not be ergodic due to molecules not being able to pass each other inside the zeolite or leave the zeolite once they are inside. In such cases the reality might not mimic the equilibrium distribution which a MC method always aims for, though not always achieves.

Conclusions

In this work we have shown that lactic acid possesses enantiospecific adsorption characteristics in several achiral zeolites when considering adsorption of scalemic mixtures. The only type of selectivity was heteroselective adsorption in which the minority enantiomer is adsorbed more easily than the majority enantiomer. This is in agreement with other studies on polar molecules, but different from chiral alkane adsorption which shows both homoselectivity and heteroselectivity. None of the previously reported mechanisms for enantioselectivity did apply to the lactic acid case. However, based on the exclusion of mechanisms that involve some kind of ordered packing phenomena, like pair-formation or the chiral cell model, we postulate a new conjecture. This conjecture states that it is actually the lack of order that causes the enantioselectivity in this case. The reasoning is that an unordered packing leaves free all kinds of spaces of asymmetric shapes. These spaces will be filled up by the molecules that are not yet adsorbed. This implies that at some point the minority enantiomer might be the only type of molecule fitting into the remaining adsorption cavities. Therefore, even if this minority enantiomer only contains a marginal fraction of the mixture in the reservoir, they might end up with a much higher

fraction in the zeolite. The model, that we coined the "random cell" model, explains nicely the very steep slopes in adsorption curves where the fraction of one enantiomer in the zeolite is plotted against the same fraction in the reservoir and the relative scarcity of homoselectivity compared to heteroselectivity. The new mechanism might well be very generally applicable in describing enantioselective adsorption which involves a more or less chaotic packing of molecules. These insights might prove to be very valuable for pharmaceutical applications which usually require a very high degree of enantipurity. Our results give the surprising suggestion that the best way to remove the minority enatiomer is to use a nanoporous material in which the adsorbate can only pack chaotically rather than in a well ordered fashion.

Bibliography

(1) Dusselier, M.; Van Wouwe, P.; Dewaele, A.; Makshina, E.; Sels, B. F. *Energy & Environmental Science* **2013**, *6*, 1415.

(2) Tsuji, H. *Macromolecular Bioscience* **2005**, *5*, 569.

(3) Wee, Y. J.; Kim, J. N.; Ryu, H. W. *Food Technology and Biotechnology* **2006**, *44*, 163.

(4) Smith, S. M.; Eng, R. H. K.; Buccini, F. *Journal of Infectious Diseases* **1986**, *154*, 658.

(5) Rouse, R. C.; Peacor, D. R. *American Mineralogist* **1986**, *71*, 1494.

(6) Harrison, W. T. A.; Gier, T. E.; Stucky, G. D.; Broach, R. W.; Bedard, R. A. *Chemistry of Materials* **1996**, *8*, 145.

(7) Tang, L.; Shi, L.; Bonneau, C.; Sun, J.; Yue, H.; Ojuva, A.; Lee, B.-L.; Kritikos, M.; Bell, R. G.; Bacsik, Z.; Mink, J.; Zou, X. *Nature Materials* **2008**, *7*, 381.

(8) Sun, J.; Bonneau, C.; Cantin, A.; Corma, A.; Diaz-Cabanas, M. J.; Moliner, M.; Zhang, D.; Li, M.; Zou, X. *Nature* **2009**, *458*, 1154.

(9) Caremans, T. P.; van Erp, T. S.; Dubbeldam, D.; Castillo, J. M.; Martens, J. A.; Calero, S. *Chemistry of Materials* **2010**, *22*, 4591.

(10) van Erp, T. S.; Caremans, T. P.; Dubbeldam, D.; Martin-Calvo, A.; Calero, S.; Martens, J. A. *Angewandte Chemie-International Edition* **2010**, *49*, 3010.

(11) Martin-Calvo, A.; Calero, S.; Martens, J. A.; van Erp, T. S. *Journal of Physical Chemistry C* **2013**, *117*, 1524.

(12) van Erp, T. S.; Dubbeldam, D.; Calero, S.; Martens, J. A. *Chemical Engineering Science* **2010**, *65*, 6478.

(13) van Erp, T. S.; Dubbeldam, D.; Caremans, T. P.; Calero, S.; Martens, J. A. *Journal of Physical Chemistry Letters* **2010**, *1*, 2154.

(14) Aljundi, I. H.; Belovich, J. M.; Talu, O. *Chemical Engineering Science* **2005**, *60*, 5004.

(15) Dakka, J.; Goris, H. *Catalysis Today* **2006**, *117*, 265.

(16) Vankoningsveld, H.; Vanbekkum, H.; Jansen, J. C. *Acta Crystallographica Section B-Structural Science* **1987**, *43*, 127.

(17) Dauberosguthorpe, P.; Roberts, V. A.; Osguthorpe, D. J.; Wolff, J.; Genest, M.; Hagler, A. T. *Proteins-Structure Function and Genetics* **1988**, *4*, 31.

(18) Gaedt, K.; Holtje, H. D. *Journal of Computational Chemistry* **1998**, *19*, 935.

(19) Calero, S.; Dubbeldam, D.; Krishna, R.; Smit, B.; Vlugt, T. J. H.; Denayer, J. F. M.; Martens, J. A.; Maesen, T. L. M. *Journal of the American Chemical Society* **2004**, *126*, 11377.

(20) Mayo, S. L.; Olafson, B. D.; Goddard, W. A. *Journal of Physical Chemistry* **1990**, *94*, 8897.

(21) Dubbeldam, D.; Calero, S.; Ellis, D. E.; Snurr, R. Q. RASPA, version 1.0; Northwestern University: Evanston, IL **2008**.

(22) Loewenstein, W. *American Mineralogist* **1954**, *39*, 92.

(23) Qiao, Z.; Torres-Knoop, A.; Dubbeldam, D.; Fairen-Jimenez, D.; Zhou, J.; Snurr, R. Q. *Aiche Journal.* **2014**, *60*, 2324-2334.

(24) Dubbeldam, D.; Torres-Knoop, A.; Walton, K. S. *Molecular Simulation* **2013**, *39*, 1253.

(25) Shi, W.; Maginn, E. J. *Journal of Chemical Theory and Computation* **2007**, *3*, 1451.

10

Conclusions

This work emphasizes the need of using realistic force fields in order to reproduce adsorption and diffusion properties in porous materials. Available models have been validated and new force fields have been developed.

To understand the differences exerted by single components and mixtures on the adsorption behaviour the topology of the structures, their composition and the nature of the gases are key factors.

Regarding the influence of the topology in adsorption and separation processes of greenhouse gases and pollutants, the main conclusions of this work are:

1.- Adsorption isotherms of the components of natural gas (small hydrocarbons, N_2 and CO_2) in Cu-BTC and IRMOF-1 show that the former structure is the best adsorbent at low pressure, while the latter is better at high pressure. (Chapter 2)

2.- From the analysis of mixtures of natural gas and as a result of the competition of the molecules for the small cavities of the structure, Cu-BTC shows the highest selectivity for CO_2, being this structure a good candidate to separate CO_2 from the other components of the mixture. (Chapter 2)

3.- The adsorption and diffusion of the components of air ($O_2/N_2/Ar$) in Cu-BTC is drastically reduced by the presence of carbon tetrachloride, as a result of the competition of the molecules for the same adsorption sites. (Chapter 3)

4.- As a consequence of the distribution of the molecules inside the cavities of Cu-BTC, a selective blockage of the small cages leads to an increase of the selective adsorption of CCl_4 over the other components from air. (Chapter 3)

5.- Structures with large cavities as IRMOF-1 were proved to be suitable materials for storage processes. On the other hand, structures combining different size of cavities such as Cu-BTC show promising results in separation processes. Depending on the distribution of the molecules inside the structure and considering the competition of the molecules for specific adsorption sites, it is possible to enhance or to dismiss the selectivity of a framework for certain gases blocking specific adsorption sites of the structure.

The conclusions concerning the effect of humidity into adsorption and separation processes are:

6.- Water molecules have different adsorption sites inside Cu-BTC than air compounds. For this reason their adsorption at low percentages of air relative humidity is unaffected. (Chapter 4)

7.- When the amount of water adsorbed in the structure increases it populates other sites of the structures reducing the adsorption of O_2, N_2 and argon and excluding them eventually, while the adsorption of CCl_4 is almost unaffected. This explains the exponential increase of CCl_4 adsorption selectivity in the Cu-BTC structure. (Chapter 4)

8.- The presence of low amounts of water enhances diffusivities in Cu-BTC, with a maximum at about 10% of air relative humidity. The diffusivity of the molecules decays at larger water content. (Chapter 4)

9.- It is possible to enhance or to hinder the adsorption capacity of a structure by combining the topology of the framework and the polarity of the adsorbed molecules. Structures with cages of different sizes and shapes (Cu-BTC) are more affected by the presence of water than structures with one single type of cavities (IRMOF-1). (Chapter 5)

10.- An interesting option to modify the behaviour of a given porous material is by taking into account the humidity of the environment. The water stability of porous materials is a delicate point as some of them lose their crystallinity when water attacks the metallic centres. For this reason it is important to quantify the maximal water uptake of a given framework without affecting its structure. Combining different contents of water with the topology and the polarity of the molecule under study it is possible to increase or to reduce the adsorption.

Related to the adsorption of gases in presence of extra-framework cations, the most relevant concluding remarks are:

11.- In structures containing extra-framework cations such as LTA or FAU zeolites the Si/Al ratio, as well as the type, amount and distribution of the cations determine the strength of the interactions of the molecules with the structure. These interactions in structures with Si/Al ratio close or equal one lead to the formation of strong complexes between adsorbates, extra-framework cations and structures, which are difficult to eliminate. (Chapter 6)

12.- The number and mobility of the cations influence the strength of the complexes formed. These complexes induce changes on the structure that need to be considered during the simulations. (Chapter 6)

13.- Transferable force fields for molecules adsorbed in zeolites are limited by the type of molecule, the topology, the extra-framework distribution and the working conditions. (Chapter 7)

14.- Adsorption at low temperature implies some technical difficulties on the experimental approach since temperature restricts the mobility of both adsorbates and extra-framework cations. (Chapter 7)

15.- The presence of extra-framework cations in the structures increases even more the need of detailed studies of the systems. It is important to understand the effect that density, chemical potential and mobility of the cations exert on the adsorption.

The main conclusions obtained from the enantiomeric separation studies are:

16.- The polarity of the molecules is crucial for enantiomeric separation. The mechanism that explains selective adsorption behaviour of achiral zeolites for non-polar molecules is completely different to the mechanism for small polar molecules. Enantiomeric separation of non-polar molecules can be attributed to the distribution of the aluminium and the extra-framework cations. On the other hand, the mechanism that rules the adsorption of polar enantiomers is highly influenced by the topology of the structure. (Chapter 8)

17.- In the case of bulky polar molecules, the chaotic distribution of the first adsorbed molecules leaves empty spaces inside the structure, favouring the adsorption of the opposite enantiomer. (Chapter 9)

18.- Achiral zeolites can be used for the separation of chiral compounds (scalemic mixtures). The separation of enantiomeric mixtures is very sensitive to the presence of extra-framework cations, their distribution inside the structures and the topology of the zeolites as a function of the size, shape and polarity of the adsorbates.

Molecular simulation techniques have been proved to be very useful tools to understand adsorption and diffusion mechanisms. This knowledge can be used to determine the best materials and conditions in order to enhance the efficiency of a variety of processes with environmental or industrial relevance.

Resumen (Summary in Spanish)

En este trabajo de tesis, se usa la simulación molecular para el estudio de las propiedades de adsorción y difusión de diversos gases en materiales nanoporosos. Para ello, se han elegido gases con importancia ambiental y se han estudiado procesos que pueden ser utilizados para reducir las emisiones de ciertos contaminantes. Los estudios se centran en zeolitas y MOFs, ambos tipos de materiales son bien conocidos y tienen numerosas aplicaciones industriales, convirtiéndolos en buenos candidatos para su uso en los procesos de estudio. Para las simulaciones se han usado tanto campos de fuerza disponibles en la literatura, como modelos nuevos desarrollados durante el trabajo. Se han estudiado los mecanismos que guían los procesos de adsorción y difusión, así como la distribución de las moléculas dentro de las estructuras.

Influencia de la topología en el proceso de adsorción/separación de gases de efecto invernadero y otros contaminantes (Capítulos 2 y 3)

En el capítulo 2 se utilizan campos de fuerzas y modelos previamente publicados para el estudio de la separación de una mezcla de gas natural en diferentes MOFs. Con este objetivo se estudia la adsorción de los principales componentes del gas natural (CH_4, C_2H_6, C_3H_8, CO_2, N_2) en dos estructuras metal-orgánicas cristalinas bien conocidas (Cu-BTC e IRMOF-1). De acuerdo con las diferencias topológicas y la distribución de las moléculas dentro de las estructuras, cada una de ellas será usada para una finalidad distinta.

Una vez demostrada la eficiencia del Cu-BTC en los procesos de separación, en el capítulo 3 se estudia la capacidad de dicho material para la eliminación de CCl_4 del aire. Para ello, se estudian las propiedades tanto de adsorción como de difusión de las moléculas dentro de la estructura. Además, se propone un bloqueo selectivo de parte de la estructura con el fin de aumentar la selectividad del material en el proceso de separación.

Efecto de la humedad en los procesos de adsorción y separación (Capítulos 4 y 5)

Para profundizar en el estudio de la eliminación de CCl_4 del aire, en el capítulo 4, se discute el efecto que tiene la humedad relativa del aire en el proceso de separación. En primer lugar se discuten los modelos de las moléculas de estudio, y a continuación se analiza la adsorción y difusión de las mezclas para ver la influencia de distintos porcentajes de humedad relativa en la eliminación de CCl_4 usando Cu-BTC.

En el capítulo 5 se investiga el efecto del agua en la adsorción de CO en diferentes estructuras metal-orgánicas cristalinas. Tras una discusión acerca de los diferentes modelos de CO y sus propiedades de adsorción en Cu-BTC, IRMOF-1 y MIL-47, se propone un nuevo modelo de CO. Finalmente se estudia la influencia de la presencia de agua en la adsorción de CO en Cu-BTC e IRMOF-1.

Adsorción de gases en presencia de cationes (Capítulos 6 y 7)

En el capítulo 6 se estudia el proceso de adsorción de CO_2 en aluminosilicatos. Dependiendo de la relación Si/Al dentro de la estructura, se pueden formar complejos entre el CO_2 y los cationes que interaccionan con la estructura. En este trabajo se combinan técnicas experimentales y de simulación, para investigar dicho efecto en zeolitas tipo FAU y LTA. Desde el punto de vista de la simulación se usa un campo de fuerzas transferible para definir las interacciones del CO_2 con las estructuras, y se proporcionan nuevos parámetros para reproducir dichas interacciones en los casos en los que se forman complejos.

No existen muchos campos de fuerzas transferibles publicados para el estudio de adsorción en zeolitas. En el capítulo 7, se usan modelos previos para CH_4 y Ar y se diseñan algunos nuevos para O_2, N_2 y CO, con el objetivo de estudiar la adsorción de dichos gases tanto en estructuras pura sílice como en aluminosilicatos.

Separación de enantiómeros (Capítulos 8 y 9)

Otro proceso de separación de interés industrial es la separación de enantiómeros de mezclas racémicas. En el capítulo 8, se investiga el comportamiento selectivo de zeolitas durante la adsorción de pequeños enantiomeros quirales, tales como el CHClFBr. A raíz de trabajos previos con moléculas no polares, se estudia la necesidad de cationes para la inducción de selectividad en zeolitas tipo MFI. Además se estudia el efecto de la topología en el comportamiento selectivo a través de la adsorción en zeolitas tipo MEL, FER y TON.

En el capítulo 9 se usa el conocimiento adquirido en el capítulo anterior para describir el mecanismo que controla la adsorción de mezclas enantioméricas de ácido láctico en zeolitas tipo MFI.

Las principales conclusiones obtenidas a partir de los estudios realizados son:

En lo relativo a la influencia de la topología en el proceso de adsorción/separación de gases de efecto invernadero y otros contaminantes, se ha visto que estructuras con grandes cavidades como IRMOF-1 son materiales idóneos para los procesos de almacenamiento, mientras que estructuras que combinan cajas de diferente tamaño como Cu-BTC, presentan resultados prometedores en procesos de separación. Además, dependiendo de la distribución de las moléculas dentro de las estructuras y considerando su competencia por los sitios preferentes de adsorción, es posible aumentar o reducir la selectividad de un material hacia ciertos gases mediante el bloqueo selectivo de partes de la estructura.

En cuanto al estudio del efecto de la humedad en los procesos de adsorción y separación, se ha comprobado que la humedad relativa del aire es una alternativa interesante para modificar el comportamiento de un determinado material. Dado que la estabilidad de algunos materiales en presencia de agua es un tema delicado ya que en muchos casos éstos pierden su estructura cristalina cuando el agua ataca los centros metálicos, es importante saber cuál es la cantidad máxima de agua que un material puede contener sin que su estructura se vea afectada. Es posible combinar topología, diferentes contenidos de agua y polaridad de las moléculas de estudio para aumentar o reducir las capacidades de adsorción de un material.

Respecto a la adsorción de gases en presencia de cationes, se ha visto la necesidad de una buena caracterización de los sistemas, ya que el tipo, la densidad y la movilidad de dichos cationes, tienen una gran influencia en los procesos de adsorción.

En los estudios de separación de enantiómeros, se ha comprobado que mezclas escalémicas de compuestos quirales pueden ser separados usando zeolitas no quirales. Esta separación es sensible a la presencia de cationes, su distribución dentro de las estructuras y su topología dependiendo del tamaño, forma y polaridad de los adsorbatos.

Por último y como conclusión general de este trabajo, se hace evidente la utilidad de las técnicas de simulación molecular para la comprensión de mecanismos de adsorción y difusión. Para ello es imprescindible contar con modelos y campos de fuerza realistas que sean capaces de reproducir los comportamientos experimentales de los sistemas. Como consecuencia, el conocimiento adquirido puede servir para determinar los mejores materiales y condiciones para optimizar la eficiencia de una gran variedad de procesos con interés industrial y ambiental.

Samenvatting (Summary in Dutch)

In dit proefschrift gebruiken we moleculaire simulaties om adsorptie en diffusie-eigenschappen van gassen in nanoporeuze materialen te bestuderen. Wij richten ons op gassen met milieurelevantie en bestuderen processen die kunnen worden gebruikt om de emissie van bepaalde verontreinigende stoffen tegen te gaan. De studies richten zich op zeolieten en MOF's, beide soorten materialen zijn goed bekend en hebben een groot aantal industriële toepassingen. Het zijn daarom goede kandidaten voor een studie naar dit soort processen. Voor de simulaties zijn zowel krachtvelden uit de literatuur, en zelf-ontwikkelde nieuwe modellen gebruikt. We hebben de mechanismen bestudeert die het gedrag van adsorptie en diffusie, en de verdeling van moleculen binnen de structuren-bepalen.

Invloed van topologie in het proces van adsorptie / scheiding van broeikasgassen en andere vervuilende stoffen (Hoofdstukken 2 en 3)

In hoofdstuk 2 gebruiken we eerder gepubliceerde modellen en krachtvelden om de adsorptie afscheiding van aardgas mengsel in MOF's te bestuderen. Daartoe bestuderen we het adsorptie gedrag van de belangrijkste componenten van aardgas (CH_4, C_2H_6, C_3H_8, CO_2, N_2) in twee bekende metal-organic frameworks (Cu-BTC en IRMOF-1). Op basis van de verschillende topologieën en de verdeling van de moleculen in de twee structuren, hebben beide materialen verschillende toepassingen.

Om de efficiëntie van de Cu-BTC in scheidingsprocessen te bewijzen bestuderen we de prestaties van dit materiaal op de scheiding van CCl_4 uit de lucht in hoofdstuk 3. Hiertoe bestuderen we adsorptie en diffusie-eigenschappen van deze moleculen in de structuur. Verder stellen we een selectieve blokkade van de structuur voor om de selectiviteit van het scheidingsproces te verbeteren.

Effect van vocht op de adsorptie en scheiding (Hoofdstukken 4 en 5)

Om verdere vooruitgang te boeken met de studie over het verwijderen van CCl_4 uit de lucht, bespreken we in hoofdstuk 4 het effect van relatieve luchtvochtigheid op het scheidingsproces. Voor dit doel, behandelen we eerst de modellen van de moleculen in deze studie. Vervolgens analyseren we de invloed van verschillende percentages van relatieve luchtvochtigheid op het adsorptie en diffusie gedrag van het gasmengsel in Cu-BTC hetgeen kan leiden tot de verwijdering van CCl_4 uit de MOF.

In hoofdstuk 5 onderzoeken we het effect van water op de adsorptie van CO in metal-organic frameworks. Na bespreking van de beschikbare modellen van CO adsorptie en hun gedrag in Cu-BTC, IRMOF-1 en MIL-47, presenteren we een nieuw model voor CO. Tenslotte bestuderen we de invloed van het water in zowel Cu-BTC en IRMOF-1 tijdens het adsorptie proces.

Gasadsorptie in aanwezigheid van kationen (Hoofdstukken 6 en 7)

In hoofdstuk 6 bestuderen we de adsorptie van CO_2 in zeolieten die aluminium bevatten. Afhankelijk van de Si/Al-verhouding kunnen complexen tussen CO_2 en de extra-raamwerk kationen een interactie met de structuur vormen. In dit werk onderzoeken we zo'n effect bij FAU en LTA zeolieten door het combineren van experimenten en simulatietechnieken. Voor de simulaties gebruiken we een beschikbaar overdraagbaar krachtveld om de interacties van CO_2 te definiëren met de structuren, en herleiden een nieuwe set parameters om deze interacties te reproduceren wanneer complexen worden gevormd.

Er zijn niet veel overdraagbare krachtvelden in de literatuur te vinden die de adsorptie van bepaalde moleculen in zeolieten kunnen beschrijven. In hoofdstuk 7 gebruiken we eerder beschikbare modellen voor CH_4 en Ar, maar bieden nieuwe modellen aan voor de beschrijving van O_2-, N_2- en CO-adsorptie in zowel zuivere silica als aluminosilicaten.

Enantiomerenscheiding (Hoofdstukken 8 en 9)

Een scheidingswerkwijze van industrieel belang is de scheiding van enantiomeren van racemische mengsels. In hoofdstuk 8 onderzoeken we het enantioselectieve gedrag van zeolieten tijdens de adsorptie van kleine polaire moleculen zoals CHClFBr. Uit eerder werk met niet-polaire moleculen, hebben we ondervonden dat het induceren van kationen noodzakelijk is voor een selectief gedrag in het MFI zeoliet. Daarom bestuderen we hetzelfde effect samen met topologische effecten voor de adsorptie in MFI, MEL, FER en TON zeolieten.

In hoofdstuk 9 gebruiken we de verkregen kennis, over het mechanisme uit het vorige hoofdstuk, om het adsorptiegedrag van enantiomere mengsels van melkzuur in MFI zeolieten te beschrijven.

De belangrijkste conclusies uit het onderzoek zijn:

Wat betreft de invloed van topologie op de adsorptie/scheiding van broeikasgassen en andere verontreinigende stoffen, is gevonden dat structuren met grote holtes zoals IRMOF-1 geschikte materialen zijn voor opslag, terwijl structuren zoals Cu-BTC, die bestaan uit holtes van verschillende groottes, veelbelovende resultaten laten zien voor scheidingsprocessen. Bovendien herleiden we uit onze simulatie resultaten dat het mogelijk moet zijn om preferentiële adsorptie te verbeteren door selectieve blokkades in de MOF structeer te genereren.

In de studie van het effect van vochtigheid op adsorptie- en scheidingsprocessen, bleek dat deze relatieve vochtigheid een interessante parameter is om het gedrag van een gegeven materiaal te wijzigen. Aangezien de stabiliteit van sommige materialen in de aanwezigheid van water is een gevoelig punt is, in veel gevallen verliezen ze hun kristallijne structuur wanneer het water in contact komt met de metaalcentra, is het belangrijk om te weten wat de maximale hoeveelheid water is die een materiaal kan bevatten zonder dat de structuur getroffen wordt. Door verschillende water gehaltes te combineren met moleculen van verschillende vorm and polariteit is het mogelijk om de adsorptie te verhogen of te verlagen.

Wat betreft de adsorptie van gassen in aanwezigheid van kationen, is een goede karakterisering van de systemen noodzakelijk, omdat het type, dichtheid en mobiliteit van deze kationen, een grote invloed op de adsorptie hebben.

In studies van scheiding van enantiomeren, is gebleken dat scalemic mengsels van chirale verbindingen kunnen worden gescheiden met niet-chirale zeolieten. Deze scheiding is gevoelig voor de aanwezigheid van kationen, hun verdeling binnen de structuren en de topologie. Het meeste efficiente systeem voor scheiding is weer afhankelijk van de grootte, vorm en polariteit van de adsorbaten.

Tenslotte, als een algemene conclusie van dit werk, blijkt het nut van moleculaire simulatie technieken voor het begrijpen van de mechanismen van adsorptie en diffusie. Het is daarom essentieel om realistische modellen en krachtvelden te hebben die het experimentele gedrag van systemen kunnen reproduceren. Hierdoor kan de verworven kennis medebepalen wat de beste materialen en omstandigheden zijn voor het verbeteren van diverse processen die belangrijk zijn voor industriële toepassingen of het milieu.

Appendix 1
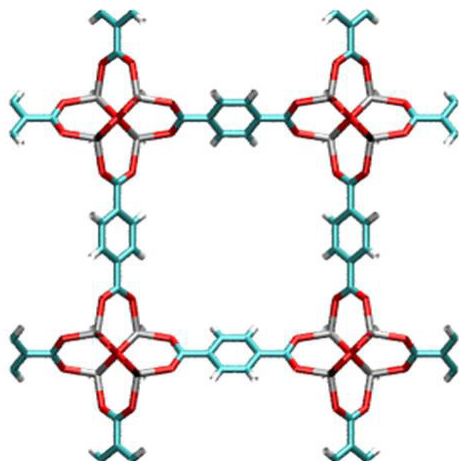
Figure A1. IRMOF-1 as reported by Yaghi and co-workers[1,2]. IRMOF-1 structure consists of a cubic array of $Zn_4O(CO_2)_6$ clusters connected by phenylene links. Each unit cell contains 8 Zn_4O tetrahedral clusters and 24 linker molecules. The linkage of the Zn_4O complexes is forced to alternate between linkers pointing outwards and inwards, resulting in a structure with two alternating type of cavities. Four small cavities of about 10.9 Å and four larger cavities of about 14.4 Å diameter[2]. Carbon atoms in blue; hydrogen in white; oxygen in red; zinc in grey.
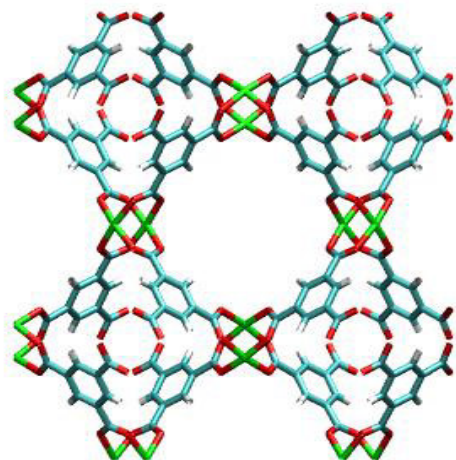
Figure A2. Cu-BTC (BTC: benzene-1,3,5-tricarboxylate) as reported by Chui and co-workers[3], where the coordinated water molecules were removed. Cu-BTC structure consists of a metal coordination polymer based on copper as the metal centre and benzene-1,3,5-tricarboxylates as the linker molecule. It is formed by primary building blocks connected to form a face-centred cubic crystal framework, and secondary building blocks -octahedral units- forming tetrahedron-shaped pockets accessible for small molecules through the small windows. Carbon atoms in blue; hydrogen in white; oxygen in red; copper in green.
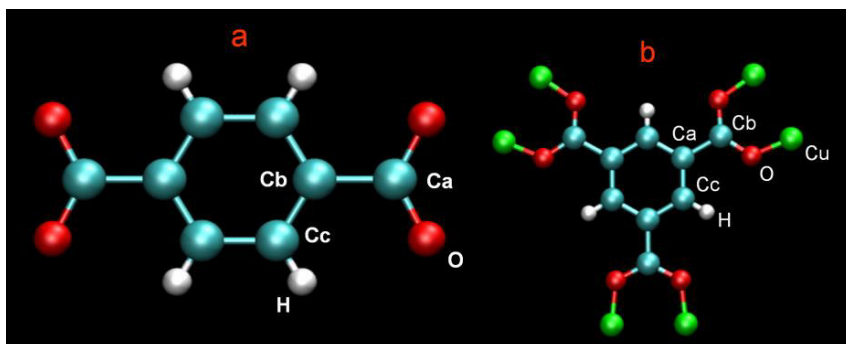
Figure A3. Definition of the different atoms in the linker molecules for (a) IRMOF-1 and (b) Cu-BTC. The crystallographically different atoms are labeled; the other labels follow by symmetry.
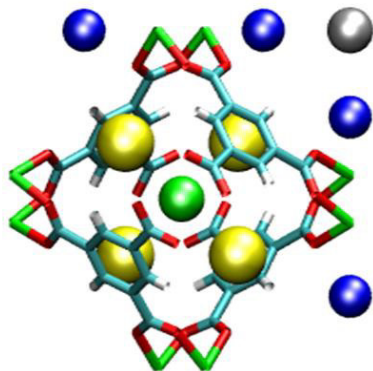
Figure A4. Preferential adsorption sites in Cu-BTC labelled I, I', II, and III. Colour spheres illustrate the positions of the different sites. Site I, region close to the Cu atoms of the framework (blue spheres); site II, centre of the octahedral side pockets (green sphere); site III, windows of the octahedral side pockets (yellow spheres); site I', centre of the big Cu-BTC cages (grey sphere).
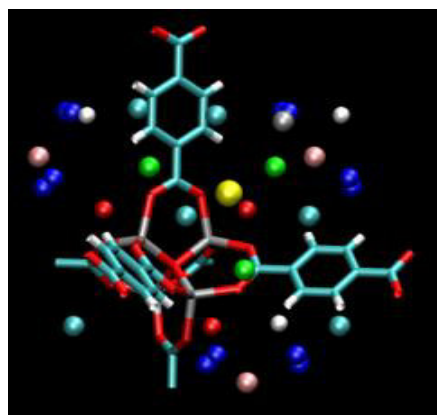
Figure A5. Preferential adsorption sites in IRMOF-1. Colour spheres illustrate the positions of the different sites. Sites I (yellow) and II (red) are located in the large and small cages, respectively. Site III (green) is located in the region that separates both types of cages. Sites IV (light blue) and V (dark blue) are close to the linker molecules, above and beneath the centre of the phenyl ring (site IV) and on the edges (site V) of it. Sites VI (grey) and VII (white) form a layer above site IV, and site VIII (pink) is located at the centre of the small cage, above site II and surrounded by site V.
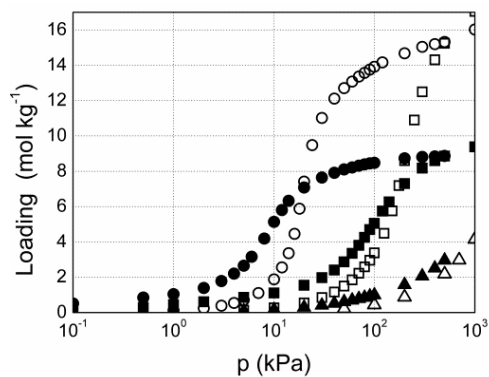
Figure A6a. Adsorption isotherms of pure methane (triangles), ethane (squares) and propane (circles) in Cu-BTC (full symbols) and IRMOF-1 (open symbols) at 298 K.
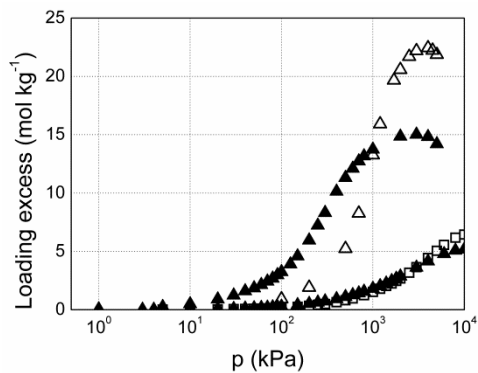
Figure A6b. Adsorption isotherms of pure CO_2 (triangles) and N_2 (squares) in Cu-BTC (full symbols) and IRMOF-1 (open symbols) at 298 K.
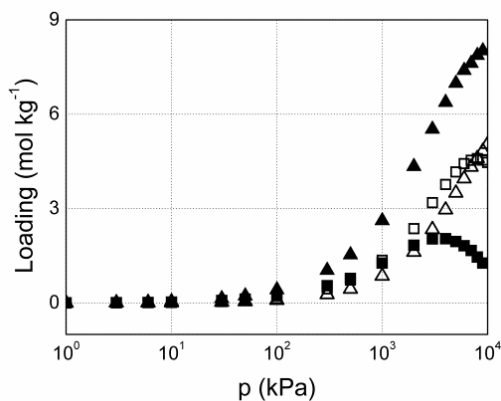
Figure A7. Excess adsorption for the 10:90 mixture of CO_2 (triangles) and N_2 (squares) mixture in Cu-BTC (full symbols) and IRMOF-1 (open symbols) at 298 K.

(a)   (b)
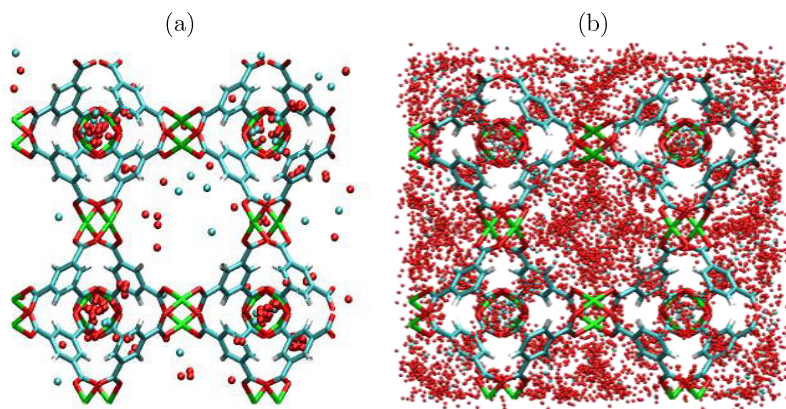
Figure A8. Centre-of-mass distributions of CO_2 (red) and methane (blue) molecules adsorbed in Cu-BTC at 298 K. (a) Low pressure (2 kPa) and (b) high pressure ($5 \cdot 103$kPa). The equilibrium snapshots are taken from two independent simulations (pure component adsorption) and combined into one figure. Snapshots were taken every 5000 steps in a simulation of one million MC steps at low pressure, and every 200000 steps in a simulation of four million MC steps at high pressure. At low pressures, methane and CO_2 preferentially adsorb in the small octahedral cages. At higher pressures, and once the octahedral cages are partially filled, the molecules adsorb in the windows (Site III) and in the big cage (Site I'). Site I remains empty for both molecules over the entire range of pressures.

(a)   (b)
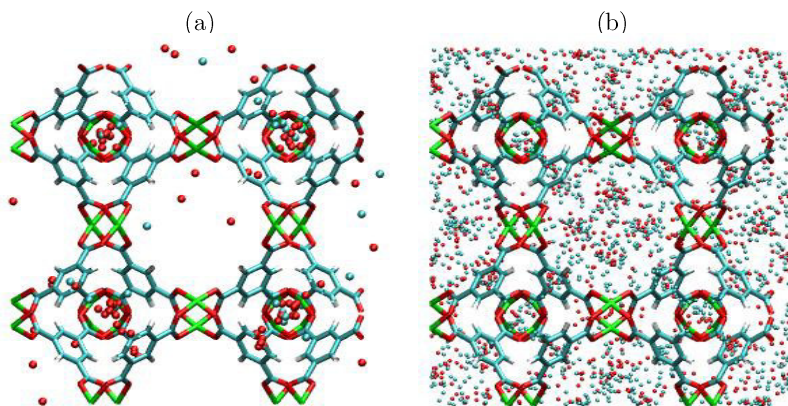
Figure A9. Centre-of-mass distributions of CO_2 (red) and methane (blue) molecules adsorbed in Cu-BTC at 298 K a) low pressure (2kPa); b) high pressure ($5 \cdot 103$kPa). The equilibrium snapshots are taken from one single simulation (50:50 mixture adsorption). Snapshots were taken every 5000 steps in a simulation of one million MC steps at low pressure, and every 200000 steps in a simulation of four million MC steps at high pressure. At low pressure, methane preferentially adsorbs in the octahedral cages displacing an important fraction of CO_2 molecules to the windows. At high pressures and once the octahedral cages are full, Site I' becomes the preferential adsorption site.

Movie 1. Centre-of-mass distribution of CO_2 adsorbed in Cu-BTC at 298 K and increasing pressure, from 2 kPa to $5 \cdot 10^3$ kPa. The equilibrium snapshots are taken from independent simulations at different pressures (pure component adsorption). Snapshots were taken every 200000 steps simulations of four million MC steps. At low pressures, CO_2 preferentially adsorbs in the small octahedral cages. At higher pressures and once the octahedral cages are partially filled, the molecules adsorb in the windows (Site III) and in the big cage (Site I'). Site I remains empty over the entire range of pressures.

http://www.rsc.org/suppdata/cp/b8/b807470d/b807470d-mov1.avi

Movie 2. Centre-of-mass distribution of methane adsorbed in Cu-BTC at 298 K and increasing pressure, from 2 kPa to $5 \cdot 10^3$ kPa. The equilibrium snapshots are taken from independent simulations at different pressures (pure component adsorption). Snapshots were taken every 200000 steps simulations of four million MC steps. At low pressures, methane preferentially adsorb in the small octahedral cages. At higher pressures and once the octahedral cages are partially filled, the molecules adsorb in the windows (Site III) and in the big cage (Site I'). Site I remains empty over the entire range of pressures.

http://www.rsc.org/suppdata/cp/b8/b807470d/b807470d-mov2.avi

Movie 3. Centre-of-mass distributions of CO_2 (red) and methane (blue) molecules adsorbed in Cu-BTC at 298 K and increasing pressure, from 2 kPa to $5 \cdot 10^3$ kPa. The equilibrium snapshots for each pressure are taken from one single simulation (50:50) mixture adsorption. Snapshots were taken every 200000 steps in simulations of four millions MC steps. At low pressures, methane preferentially adsorbs in the octahedral cages displacing an important fraction of CO_2 molecules to the windows. At higher pressures and once the octahedral cages are full, Site I' becomes the preferential adsorption site.

http://www.rsc.org/suppdata/cp/b8/b807470d/b807470d-mov3.avi

Table A1. Non-bonded van der Waals and charge parameters for the MOFs and adsorbed molecules used in this work.

IRMOF-1			
Atom type	ε/k_B [K]	σ [Å]	Charge [e^-]
Zn	27.7	4.04	1.275
Oa	48.19	3.03	-1.5
Ob	48.19	3.03	-0.6
Ca	47.86	3.47	0.475
Cb	47.86	3.47	0.125
Cc	47.86	3.47	-0.15
H	7.65	2.85	0.15
Cu-BTC			
Atom type	ε/k_B [K]	σ [Å]	Charge [e^-]
Cu	2.518	3.114	1.0
Ob	48.19	3.03	-0.6
Ca	47.86	3.47	0.7
Cb	47.86	3.47	0.0
Cc	47.86	3.47	-0.15
H	7.65	2.85	0.15
Adsorbed molecules			
Atom type	ε/k_B [K]	σ [Å]	Charge [e^-]
CH_4	158.5	3.72	-
CH_3	108.0	3.76	-
CH_2	56.0	3.96	-
C (CO_2)	27.0	2.80	0.7
O (CO_2)	79.0	3.05	-0.35
N (N_2)	36.4	3.32	-0.40484
Dummy (N_2)	-	-	0.80968

Cu-BTC and IRMOF-1 frameworks are considered rigid with Lennard-Jones parameters taken from DREIDING[4] force field, except the value for Cu, that was taken from the UFF[5] force field. Lorentz-Berthelot mixing rules were used to calculate mixed Lennard-Jones parameters and the atomic charges for the MOFs are taken from Frost *et al.* and Dubbeldam *et al.*[6]. One unit cell of the IRMOF-1 (a = b = c = 25.832 Å) and one unit cell of Cu-BTC (a = b = c = 26.343 Å) were used in our simulations. We obtained a helium void fraction of 0.82 for IRMOF-1 and of 0.76 for Cu-BTC.

Table A2. Preferential adsorption sites for pure component methane, ethane, propane, CO_2 and N_2 in Cu-BTC at 298 K.

Methane					
Pressure (kPa)	Loading (molec uc^{-1})	Site I' (%)	Site I (%)	Site II (%)	Site III (%)
2	0.34	21.6	0.1	68.8	9.5
20	2.92	25.9	0.1	63.9	10.1
200	15.38	44.9	0.0	38.0	17.1
500	28.92	59.6	0.0	21.4	19.0
Ethane					
Pressure (kPa)	Loading (molec uc^{-1})	Site I' (%)	Site I (%)	Site II (%)	Site III (%)
2	5.98	9.2	0.0	89.1	1.7
20	14.95	44.6	0.0	49.6	5.8
200	71.10	77.1	0.0	10.8	12.1
1000	90.96	78.2	0.0	8.5	13.3
Propane					
Pressure (kPa)	Loading (molec uc^{-1})	Site I' (%)	Site I (%)	Site II (%)	Site III (%)
2	13.29	40.7	0.0	58.4	0.9
20	69.23	83.4	0.0	11.5	5.1
200	84.56	85.9	0.0	9.4	4.7
500	85.59	85.3	0.0	9.1	5.6
CO_2					
Pressure (kPa)	Loading (molec uc^{-1})	Site I' (%)	Site I (%)	Site II (%)	Site III (%)
2	1.02	24.2	0.1	38.9	36.8
20	8.68	32.4	0.1	30.5	37.0
200	58.07	63.0	0.2	9.6	27.2
1000	132.83	77.6	0.2	4.2	18.0
5000	132.83	77.6	0.2	4.1	18.1
N_2					
Pressure (kPa)	Loading (molec uc^{-1})	Site I' (%)	Site I (%)	Site II (%)	Site III (%)
2	0.06	44.9	0.1	42.6	12.4
20	0.59	45.9	0.3	40.6	13.2
200	4.99	40.4	0.0	40.3	19.3
1000	17.31	60.9	0.2	23.4	15.5
6000	46.65	74.5	0.7	9.0	15.8

Table A3. Preferential adsorption sites for pure component methane, ethane, propane, CO_2 and N_2 in IRMOF-1 at 298 K.

Pressure (kPa)	Loading (molec uc^{-1})	Site I (%)	Site II (%)	Site III (%)	Site IV (%)	Site V (%)	Site VI (%)	Site VII (%)	Site VIII (%)
Methane									
5	0.13	32.7	0.8	37.1	13.4	5.4	0.6	4.8	5.2
100	2.78	32.8	0.7	36.3	13.8	5.2	0.9	4.8	5.5
500	13.36	30.0	0.8	36.9	14.1	6.0	1.1	5.0	6.1
2000	47.02	21.7	0.5	40.5	15.6	7.4	1.8	5.5	7.0
6000	81.35	16.3	1.2	41.3	12.8	7.1	3.6	6.1	11.6
Ethane									
5	0.82	46.2	0.1	31.1	11.7	3.1	0.2	4.2	3.4
100	20.52	40.9	0.1	33.2	11.2	3.7	1.0	4.9	5.0
500	93.90	18.8	0.3	40.5	8.9	6.5	4.3	5.2	15.5
1000	104.84	16.1	0.4	41.5	9.0	5.8	4.8	5.0	17.4
Propane									
5	4.51	53.8	0.0	26.8	11.1	2.0	0.3	4.0	2.0
100	85.48	24.0	0.7	35.1	6.4	7.8	4.5	5.1	16.4
500	93.25	20.6	0.8	38.4	6.0	7.7	4.3	3.2	19.0
CO_2									
5	0.28	36.1	0.8	41.9	11.7	3.0	0.4	2.9	3.2
100	5.56	34.0	0.9	41.5	12.9	3.5	0.5	3.4	3.3
500	32.60	27.2	1.3	43.0	14.4	4.3	1.4	4.1	4.3
2000	128.00	15.2	1.9	40.3	15.2	8.9	4.3	6.1	8.1
5000	135.32	12.9	2.1	40.6	16.5	7.9	4.7	6.1	9.2
N_2									
5	0.05	28.0	0.4	37.3	13.3	7.4	1.2	6.2	6.2
100	1.05	26.4	0.8	37.0	15.9	6.6	1.8	5.9	5.6
500	4.99	26.7	0.8	36.7	15.6	6.9	1.6	5.8	5.9
2000	4.99	24.6	0.9	40.5	12.5	9.4	1.3	3.4	7.4
6000	34.65	19.6	1.2	37.1	18.5	8.0	2.9	4.4	8.3

Table A4. Preferential adsorption sites for CO_2 and methane from a CH_4/CO_2 equimolar mixture in Cu-BTC at 298 K.

CO₂ 50 %					
Pressure (kPa)	Loading (molec uc⁻¹)	Site I' (%)	Site I (%)	Site II (%)	Site III (%)
1	0.22	25.1	0.2	43.4	31.3
13	2.85	26.9	0.1	34.8	38.2
100	15.71	42.9	0.1	21.0	36.0
1000	90.53	74.2	0.2	5.0	20.6
4000	120.17	78.0	0.3	4.0	17.7
Methane 50 %					
Pressure (kPa)	Loading (molec uc⁻¹)	Site I' (%)	Site I (%)	Site II (%)	Site III (%)
1	0.08	22.5	0.0	66.8	10.7
13	0.87	26.2	0.0	62.5	11.3
100	3.71	47.8	0.1	38.1	14.0
1000	14.70	76.3	0.6	9.4	13.7
4000	12.33	76.3	0.6	9.4	13.7

Table A5. Preferential adsorption sites for CO_2 and methane from a CH_4/CO_2 equimolar mixture in IRMOF-1 at 298 K.

CO₂ 50 %									
Pressure (kPa)	Loading (molec uc⁻¹)	Site I (%)	Site II (%)	Site III (%)	Site IV (%)	Site V (%)	Site VI (%)	Site VII (%)	Site VIII (%)
10	0.29	37.4	0.8	41.6	11.7	2.7	0.2	2.8	2.8
100	2.80	34.5	0.8	41.8	13.1	3.1	0.7	3.0	3.0
500	14.53	30.5	1.1	43.2	13.3	3.8	0.9	3.6	3.6
1000	31.81	26.7	1.1	39.7	15.6	6.0	2.0	4.8	4.1
4000	91.63	16.5	1.6	42.8	15.0	7.3	3.1	6.1	7.6
Methane 50 %									
Pressure (kPa)	Loading (molec uc⁻¹)	Site I (%)	Site II (%)	Site III (%)	Site IV (%)	Site V (%)	Site VI (%)	Site VII (%)	Site VIII (%)
10	0.14	31.8	0.9	35.9	15.0	4.8	0.9	5.6	5.1
100	1.37	32.2	0.7	36.4	14.0	5.6	1.0	4.7	5.4
500	6.65	27.1	0.8	38.0	14.5	6.2	1.5	5.4	6.5
1000	13.36	20.7	1.0	39.5	14.0	9.2	1.0	6.7	7.9
4000	24.28	11.8	1.1	36.6	15.9	10.0	5.4	6.5	12.7

Table A6. Preferential adsorption sites for CO_2 and methane from a CO_2/CH_4 10:90 mixture in Cu-BTC at 298 K.

CO₂ 10%					
Pressure (kPa)	Loading (molec uc⁻¹)	Site I' (%)	Site I (%)	Site II (%)	Site III (%)
1	0.05	29.6	0.0	35.9	34.5
10	0.45	26.6	0.0	36.9	36.5
100	3.24	39.0	0.1	23.8	37.1
1000	21.43	62.5	0.0	7.0	30.5
6000	45.84	75.8	0.6	4.0	19.6
Methane 90 %					
Pressure (kPa)	Loading (molec uc⁻¹)	Site I' (%)	Site I (%)	Site II (%)	Site III (%)
1	0.14	21.7	0.0	68.2	10.1
10	1.26	25.0	0.0	64.3	10.7
100	7.97	41.3	0.1	45.0	13.6
1000	38.25	70.7	0.1	13.1	16.1
6000	57.89	74.5	0.3	6.6	18.6

Table A7. Preferential adsorption sites for CO_2 and methane from a CO_2/CH_4 10:90 mixture in IRMOF-1 at 298 K.

CO₂ 10 %									
Pressure (kPa)	Loading (molec uc⁻¹)	Site I (%)	Site II (%)	Site III (%)	Site IV (%)	Site V (%)	Site VI (%)	Site VII (%)	Site VIII (%)
10	0.06	35.8	1.2	42.8	10.9	2.6	0.0	3.5	3.2
100	0.56	36.7	0.9	40.4	12.1	3.4	0.3	2.9	3.3
500	2.84	32.2	0.9	43.6	12.1	3.7	0.7	3.3	3.5
2000	10.84	26.5	0.4	42.7	13.3	6.0	3.0	4.7	3.4
6000	20.03	18.2	2.2	46.9	11.9	6.3	2.0	4.7	7.8
Methane 90 %									
Pressure (kPa)	Loading (molec uc⁻¹)	Site I (%)	Site II (%)	Site III (%)	Site IV (%)	Site V (%)	Site VI (%)	Site VII (%)	Site VIII (%)
10	0.25	33.2	0.7	34.8	15.7	4.9	0.7	4.7	5.3
100	2.45	33.0	0.7	35.4	13.8	5.5	1.0	4.9	5.7
500	12.23	29.2	0.7	37.0	14.1	6.1	1.3	5.3	6.3
2000	43.12	18.3	1.1	37.9	16.4	8.2	2.9	5.5	9.7
6000	69.04	18.3	1.1	37.9	16.3	8.2	2.9	5.5	9.8

Table A8. Preferential adsorption sites for CO_2 and N_2 from a CO_2/N_2 10:90 mixture in Cu-BTC at 298 K.

CO₂ 10 %					
Pressure (kPa)	Loading (molec uc⁻¹)	Site I' (%)	Site I (%)	Site II (%)	Site III (%)
10	0.47	26.2	0.1	39.6	34.1
100	4.03	29.0	0.1	33.4	37.5
1000	25.61	51.0	0.0	16.3	32.7
4000	61.83	67.9	0.3	7.2	24.6
8000	78.59	71.4	0.4	5.4	22.8
N₂ 90 %					
Pressure (kPa)	Loading (molec uc⁻¹)	Site I' (%)	Site I (%)	Site II (%)	Site III (%)
10	0.25	44.6	0.9	39.6	14.9
100	2.16	51.7	0.7	33.8	13.8
1000	12.54	79.9	2.1	9.0	9.0
4000	19.87	83.5	1.2	4.2	11.1
8000	19.87	83.5	1.2	4.2	11.1

Table A9. Preferential adsorption sites for CO_2 and N_2 from a CO_2/N_2 10:90 mixture in IRMOF-1 at 298 K.

CO₂ 10 %								
Pressure (kPa)	Loading (molec uc⁻¹)	Site I (%)	Site II (%)	Site III (%)	Site IV (%)	Site V (%)	Site VI (%)	Site VII (%)	Site VIII (%)
10	0.06	37.4	1.4	39.4	10.3	3.6	0.6	3.6	3.7
100	0.56	36.5	0.6	42.4	10.9	3.1	0.5	2.8	3.3
300	1.65	35.9	0.9	41.0	12.1	3.2	0.5	3.3	3.1
2000	9.89	31.9	0.9	43.1	13.4	3.7	1.4	2.3	3.3
8000	28.88	23.9	1.4	44.4	13.8	4.4	2.7	3.8	5.6
10000	30.99	24.0	1.9	38.9	15.0	5.5	2.5	4.6	7.6
N₂ 90 %								
Pressure (kPa)	Loading (molec uc⁻¹)	Site I (%)	Site II (%)	Site III (%)	Site IV (%)	Site V (%)	Site VI (%)	Site VII (%)	Site VIII (%)
10	0.10	25.8	1.2	38.7	15.1	5.9	2.5	6.1	4.7
100	0.91	28.0	0.9	36.5	15.0	7.0	1.6	5.6	5.4
300	2.71	26.2	0.9	35.7	16.4	7.3	1.6	6.2	5.7
2000	14.50	22.3	0.4	36.2	14.6	8.7	2.4	10.1	5.3
8000	27.99	15.1	2.2	35.6	16.0	10.2	3.3	6.7	10.9
10000	27.99	15.1	2.2	35.6	16.0	10.2	3.3	6.7	10.9

Table A10. Preferential adsorption sites for CO_2, ethane, methane, N_2 and propane from a five-component natural gas mixture (95:2.0:1.5:1.0:0.5) $CH_4/C_2H_6/N_2/CO_2/C_3H_8$ in Cu-BTC at 298 K.

Pressure (kPa)	Loading (molec uc^{-1})	Site I' (%)	Site I (%)	Site II (%)	Site III (%)
CO$_2$ 1%					
2	0.01	32.2	0.0	34.9	32.9
20	0.06	46.5	0.1	21.0	32.4
200	0.42	65.5	0.0	1.2	33.3
1000	1.91	72.7	0.7	0.4	26.2
6000	4.47	81.1	0.4	1.0	17.5
Ethane 2 %					
2	0.27	3.8	0.0	94.9	1.3
20	1.10	10.5	0.0	87.6	1.9
200	2.79	45.1	0.0	49.5	5.5
1000	7.77	72.6	0.0	17.7	9.8
6000	10.57	74.7	0.0	15.2	10.1
Methane 95 %					
2	0.26	25.7	0.1	64.0	10.2
20	1.54	45.7	0.1	40.8	13.4
200	9.27	72.6	0.1	9.4	17.9
1000	31.92	78.3	0.3	2.5	18.9
N$_2$ 1.5 %					
2	0.00	40.7	0.0	40.7	18.6
20	0.01	69.5	0.3	18.4	11.8
200	0.04	88.9	0.0	11.1	0.0
1000	0.12	83.9	0.0	3.2	12.9
Propane 0.5 %					
2	1.05	1.8	0.0	98.2	0.1
20	4.09	5.1	0.0	94.8	0.2
200	7.93	33.8	0.0	65.4	0.7
1000	17.70	65.7	0.1	32.1	2.1
6000	16.29	69.8	0.0	27.8	2.4

Table A11. Preferential adsorption sites for CO_2, ethane, methane, N_2 and propane from a five-component natural gas mixture (95:2.0:1.5:1.0:0.5) $CH_4/C_2H_6/N_2/CO_2/C_3H_8$ in IRMOF-1 at 298 K.

CO₂ 1 %									
Pressure (kPa)	Loading (molec uc^{-1})	Site I (%)	Site II (%)	Site III (%)	Site IV (%)	Site V (%)	Site VI (%)	Site VII (%)	Site VIII (%)
5	0.01	30.1	0.7	48.0	10.8	2.2	0.7	4.3	3.2
100	0.06	35.2	0.8	41.7	12.6	3.2	0.7	2.8	3.0
500	0.28	32.4	1.0	43.3	12.0	3.5	0.9	3.4	3.5
2000	1.09	22.5	2.5	45.8	9.8	4.7	3.4	5.5	5.8
6000	1.76	17.7	1.8	49.1	10.4	4.8	5.1	3.5	7.6

Ethane 2 %									
Pressure (kPa)	Loading (molec uc^{-1})	Site I (%)	Site II (%)	Site III (%)	Site IV (%)	Site V (%)	Site VI (%)	Site VII (%)	Site VIII (%)
5	0.02	46.0	0.1	31.8	11.3	3.1	0.4	3.7	3.6
100	0.33	46.8	0.1	31.1	11.5	2.9	0.4	3.8	3.4
500	1.77	42.9	0.1	32.8	11.2	3.5	0.6	4.6	4.3
2000	7.47	28.9	0.1	36.6	11.2	5.8	2.9	6.3	8.2
6000	10.39	21.8	0.4	41.3	9.6	6.0	3.2	4.3	13.4

Methane 95 %									
Pressure (kPa)	Loading (molec uc^{-1})	Site I (%)	Site II (%)	Site III (%)	Site IV (%)	Site V (%)	Site VI (%)	Site VII (%)	Site VIII (%)
5	0.13	33.8	0.7	35.6	14.4	4.9	0.9	4.6	5.1
100	2.62	32.4	0.7	36.3	13.9	5.5	0.9	4.9	5.4
500	12.95	28.7	0.8	37.6	13.6	6.2	1.4	5.3	6.4
2000	44.08	18.7	1.5	40.0	12.5	8.4	3.6	5.9	9.4
6000	62.61	13.5	1.8	42.1	12.0	8.4	4.7	5.5	12.0

N₂ 1.5 %									
Pressure (kPa)	Loading (molec uc^{-1})	Site I (%)	Site II (%)	Site III (%)	Site IV (%)	Site V (%)	Site VI (%)	Site VII (%)	Site VIII (%)
5	0.01	23.6	0.9	37.7	21.7	8.5	0.0	3.8	3.8
100	0.02	25.6	0.9	37.6	15.3	6.9	2.0	5.5	6.2
500	0.07	23.4	0.9	37.3	15.5	7.9	2.4	5.9	6.7
2000	0.17	10.7	1.8	42.9	16.1	7.1	1.8	12.5	7.1
6000	0.09	10.7	1.8	42.9	16.1	7.1	1.8	12.5	7.1

Propane 0.5 %									
Pressure (kPa)	Loading (molec uc^{-1})	Site I (%)	Site II (%)	Site III (%)	Site IV (%)	Site V (%)	Site VI (%)	Site VII (%)	Site VIII (%)
5	0.02	55.4	0.1	26.1	11.0	2.3	0.1	3.5	1.5
100	0.37	53.8	0.0	26.8	11.6	2.0	0.2	3.9	1.7
500	2.23	51.8	0.0	27.3	11.2	2.5	0.3	4.4	2.5
2000	10.81	38.4	0.1	32.3	10.8	4.6	1.5	6.2	6.1
6000	12.35	32.9	0.3	33.4	9.9	5.6	2.7	5.9	9.3

(1)   Eddaoudi, M.; Kim, J.; Rosi, N.; Vodak, D.; Wachter, J.; O'Keeffe, M.; Yaghi, O. M. *Science* **2002**, *295*, 469.

(2)   Li, H.; Eddaoudi, M.; O'Keeffe, M.; Yaghi, O. M. *Nature* **1999**, *402*, 276.

(3)   Chui, S. S. Y.; Lo, S. M. F.; Charmant, J. P. H.; Orpen, A. G.; Williams, I. D. *Science* **1999**, *283*, 1148.

(4)   Mayo, S. L.; Olafson, B. D.; Goddard, W. A. *Journal of Physical Chemistry* **1990**, *94*, 8897.

(5)   Rappe, A. K.; Casewit, C. J.; Colwell, K. S.; Goddard, W. A.; Skiff, W. M. *Journal of the American Chemical Society* **1992**, *114*, 10024.

(6)   Dubbeldam, D.; Walton, K. S.; Ellis, D. E.; Snurr, R. Q. *Angew. Chem.-Int. Edit.* **2007**, *46*, 4496.

Appendix 2

Table A1. Lennard-Jones parameters and point charges used in this work

Cu-BTC			
Atom	ε/k_B [K]	σ [Å]	Charge [e⁻]
Cu	2.518	3.114	1.0
O_b	48.19	3.03	-0.6
C_a	47.86	3.47	0.7
C_b	47.86	3.47	0.0
C_c	47.86	3.47	-0.15
H	7.65	2.85	0.15
Adsorbed Molecules			
Atom	ε/k_B [K]	σ [Å]	Charge [e⁻]
O (O_2)	53.023	3.045	-0.112
Dummy (O_2)	-	-	0.224
N (N_2)	38.298	3.306	-0.405
Dummy (N_2)	-	-	0.810
Ar	124.070	3.380	-
CCl_4	519.730	5.140	-

Figure A1 compares our computed adsorption values of carbon tetrachloride with experimental adsorption previously reported in several materials[1]. As shown in the figure, the amount of carbon tetrachloride that we obtain at saturation on Cu-BTC is higher than the obtained for other materials such as activated carbon BPL, hydrophobic zeolite Y and silicalite-1 and only comparable with the obtained for MCM-41. However, we can indicate two main reasons to prioritize Cu-BTC over MCM-41. The first reason is that saturation on Cu-BTC is reached at lower pressures than on MCM-41. The second reason is that Cu-BTC is stable upon hydration/dehydration[2], whereas MCM-41 collapses upon rehydration at room temperature and also when it is left in air for three months[3].
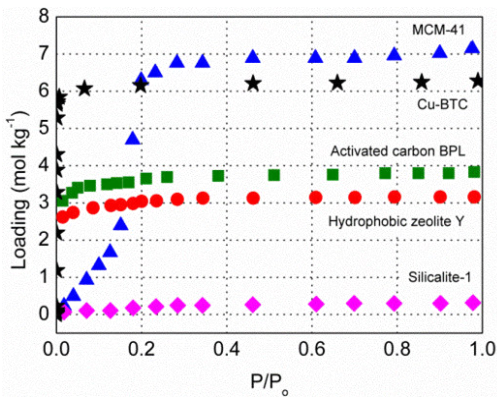
We have performed additional simulations to check the effect with water as competing molecule. Simulations were performed in what we think could be one of the worst of the scenarios, i.e. 100% relative air humidity (4% of water at room conditions). The obtained results show preferential adsorption of carbon tetrachloride over water (Figure A2) and demonstrate that carbon tetrachloride selectivity over N_2, O_2, and Ar increases even more with ambient humidity. It is also interesting to note that recent experimental and simulation studies have also reported an enhancement of selectivity of CO_2 with water content in this structure[4].
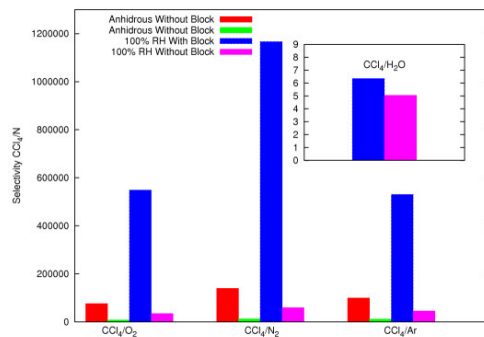

Figure A2. Adsorption selectivity of carbon tetrachloride over the main components of air in anhydrous conditions and for air relative humidity 100%. Comparison between the values obtained for the blocked and for the non-blocked structures.

Figure A1. Adsorption isotherms of carbon tetrachloride over several adsorbents.

(1)   Zhao, X. S.; Ma, Q.; Lu, G. Q. M. *Energy & Fuels* **1998**, *12*, 1051.

(2)   Castillo, J. M.; Vlugt, T. J. H.; Calero, S. *Journal of Physical Chemistry C* **2008**, *112*, 15934.

(3)   Zhao, X. S.; Audsley, F.; Lu, G. Q. *Journal of Physical Chemistry B* **1998**, *102*, 4143.

(4)   Yazaydin, A. O.; Benin, A. I.; Faheem, S. A.; Jakubczak, P.; Low, J. J.; Willis, R. R.; Snurr, R. Q. *Chem. Mat.* **2009**, *21*, 1425.

Appendix 3

Table A1. Computed surface area of Cu-BTC using different molecules. The surface area is given in m^2/g.

Hydrogen	Oxygen	Nitrogen	Argon	CCl_4	Experimental[1]
2563.92	2513.30	2344.28	2296.84	1432.47	1958

Table A2. Lennard-Jones parameters and partial charges used for Cu-BTC. The Lennard-Jones parameters were taken from the DREIDING generic force field[2], except copper that was taken from the UFF force field[3]. The atomic charges for Cu-BTC were taken from reference 4.

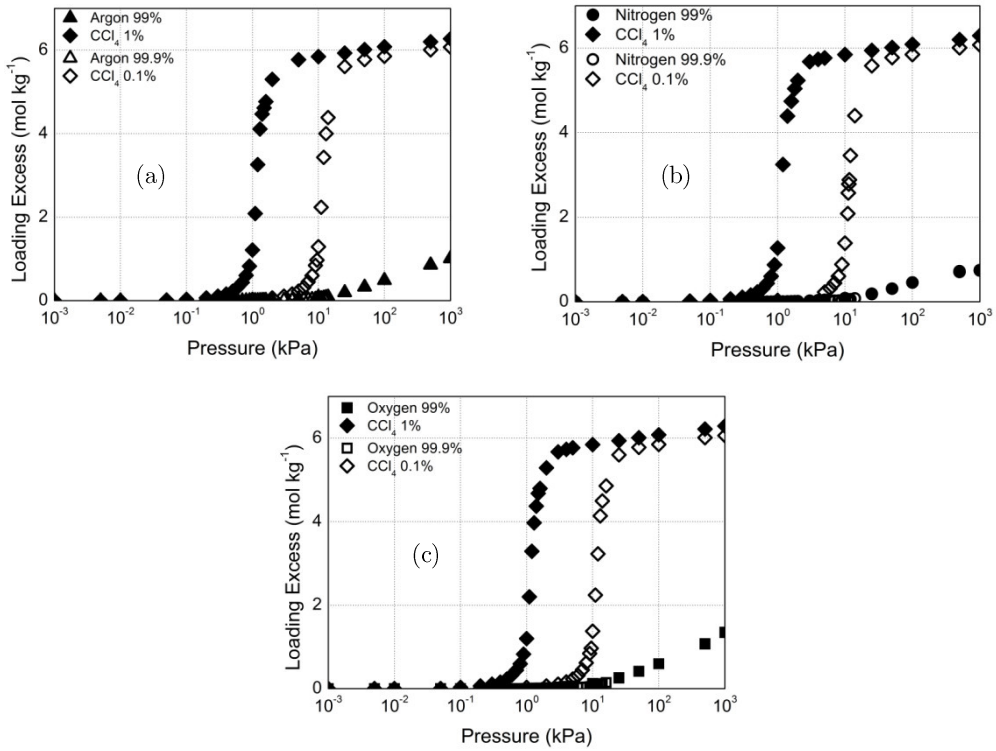| Cu-BTC			
Atom	ε/k_B [K]	σ [Å]	Charge [e⁻]
Cu	2.518	3.114	1.0
Ob	48.19	3.03	-0.6
Ca	47.86	3.47	0.7
Cb	47.86	3.47	0.0
Cc	47.86	3.47	-0.15
H	7.65	2.85	0.15

Figure A1. Adsorption isotherms of (a) Ar/CCl$_4$, (b) N$_2$/CCl$_4$ and (c) O$_2$/CCl$_4$ binary mixtures in Cu-BTC. The adsorption isotherms of argon (triangles), nitrogen (circles), oxygen (squares) and carbon tetrachloride (rhombus) were computed at 298 K and at bulk partial fugacity ratio of 99:1 (full symbols) and 99.9:0.1 (empty symbols). Computed error bars are within the symbol size.
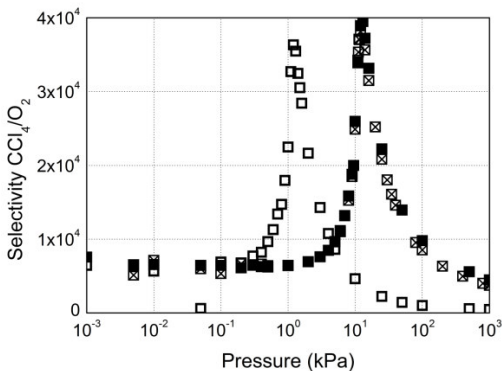

Figure A2. Adsorption selectivity of carbon tetrachloride over oxygen obtained from the computed adsorption isotherms of O$_2$/CCl$_4$ mixtures at a bulk partial fugacity ratio of 99:1 (empty symbols), 99.9:0.1 (full symbols) and 20.979:0.1 (crossed symbols).

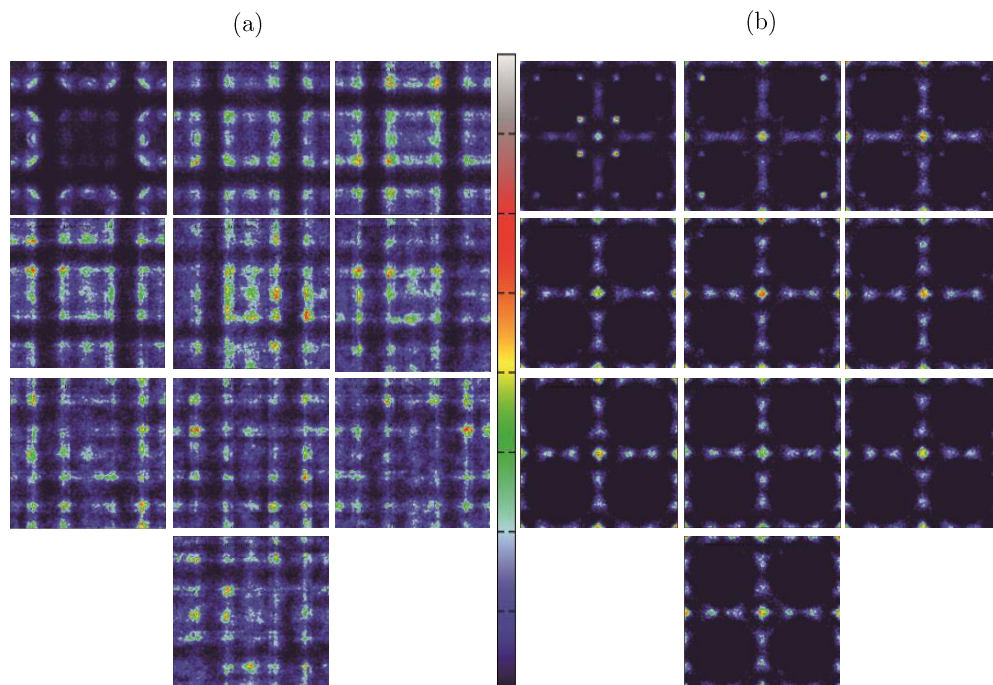(a)   (b)

Figure A3. Average occupation profiles of (a) water and (b) carbon tetrachloride in Cu-BTC. The profiles were obtained from the molecular simulations of five-component mixtures of carbon tetrachloride in air with relative humidity from 10%-30% (top left-top right) to 100% (bottom). The same colour gradation (from dark blue to white) is employed in all figures, although the total number of molecules present in the unit cell is different for each calculation.
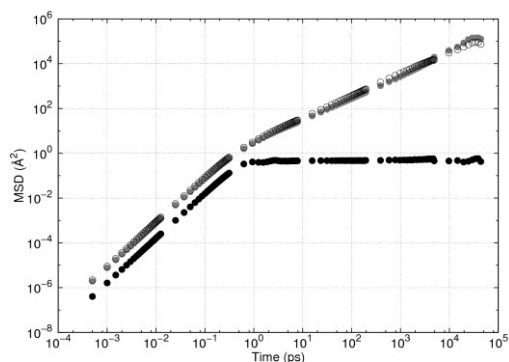

Figure A4. Representation of the Mean Square Displacement (MSD) of oxygen (grey circles), nitrogen (empty circles) and carbon tetrachloride (black circles) as pure components.

(1) Ma, S. Q.; Zhou, H. C. *Chemical Communications* **2010**, *46*, 44.

(2) Mayo, S. L.; Olafson, B. D.; Goddard, W. A. *Journal of Physical Chemistry* **1990**, *94*, 8897.

(3) Rappe, A. K.; Casewit, C. J.; Colwell, K. S.; Goddard, W. A.; Skiff, W. M. *Journal of the American Chemical Society* **1992**, *114*, 10024.

(4) Farrusseng, D.; Daniel, C.; Gaudillere, C.; Ravon, U.; Schuurman, Y.; Mirodatos, C.; Dubbeldam, D.; Frost, H.; Snurr, R. Q. *Langmuir* **2009**, *25*, 7383.

Appendix 4

Table A1. Lennard-Jones parameters and partial charges used for Cu-BTC, IRMOF-1 and MIL-47[1-5]. We consider different types of carbon atoms: C_a, linked to oxygen atoms, C_b, linked to other carbon atoms and C_c, linked to hydrogen atoms. We also define two types of oxygen atoms: O_a, linked to atoms of zinc or vanadium and O_b, linked to carbon atoms C_a.

Cu-BTC			
Atom	ε/k_B [K]	σ [Å]	Charge [e⁻]
Cu	2.518	3.114	1.248
O_b	48.19	3.03	-0.624
C_a	47.86	3.47	0.494
C_b	47.86	3.47	0.13
C_c	47.86	3.47	-0.156
H	7.65	2.85	0.156
IRMOF-1			
Atom	ε/k_B [K]	σ [Å]	Charge [e⁻]
Zn	27.7	4.04	1.275
O_a	48.19	3.03	-1.5
O_b	48.19	3.03	-0.6
C_a	47.86	3.47	0.475
C_b	47.86	3.47	0.125
C_c	47.86	3.47	-0.15
H	7.65	2.85	0.15
MIL-47			
Atom	ε/k_B [K]	σ [Å]	Charge [e⁻]
V	8.059	2.801	1.68
O_a	48.19	3.03	-0.6
O_b	48.19	3.03	-0.52
C_a	47.86	3.47	0.56
C_b	47.86	3.47	0.0
C_c	47.86	3.47	-0.15
H	7.65	2.85	0.12

Table A2. Lennard-Jones parameters used in this work to define the interactions between the molecule of carbon monoxide and Cu-BTC metal-organic framework.

Atom type	Atom type	ε/k_B [K]	σ [Å]
Cu	C_co	7.650	3.386
O_a	C_co	33.468	3.344
O_b	C_co	33.353	3.564
C_a	C_co	33.353	3.564
C_b	C_co	33.353	3.564
H	C_co	13.334	3.254
Cu	O_co	18.852	3.0465
O_a	O_co	82.471	3.0045
O_b	O_co	82.189	3.2245
C_a	O_co	82.189	3.2245
C_b	O_co	82.189	3.2245
H	O_co	32.859	2.9145

Table A3. Amount of molecules of carbon monoxide per unit cell adsorbed in each site for Cu-BTC at 298 K as a function of pressure and water content.

3.5 %wt			S1		L2		L3		Windows S1-L3		Windows L2-L3	
Pressure (kPa)	Total	CO	CO	H_2O	CO	H_2O	CO	H_2O	CO	H_2O	CO	H_2O
10	20.29	1.29	0.92	0.04	0.23	0.00	0.05	17.87	0.07	0.94	0.03	0.16
100	27.69	8.69	5.31	0.01	1.95	0.00	0.58	18.31	0.46	0.51	0.39	0.18
1000	60.26	41.26	14.63	0.02	14.40	0.00	5.63	18.17	3.31	0.66	3.30	0.16
10000	127.47	108.47	26.08	0.01	38.76	0.00	24.35	18.38	8.38	0.44	10.91	0.17
4.5 %wt			S1		L2		L3		Windows S1-L3		Windows L2-L3	
Pressure (kPa)	Total	CO	CO	H_2O	CO	H_2O	CO	H_2O	CO	H_2O	CO	H_2O
10	25.29	1.29	0.99	0.08	0.19	0.00	0.04	22.24	0.03	1.47	0.05	0.22
100	32.73	8.73	5.29	0.03	2.03	0.00	0.52	22.50	0.43	1.21	0.47	0.26
1000	65.16	41.16	14.64	0.04	14.87	0.01	4.93	22.33	3.25	1.41	3.48	0.22
10000	130.99	106.99	26.39	0.02	38.60	0.01	22.97	22.89	8.02	0.81	11.01	0.27
8.9 %wt			S1		L2		L3		Windows S1-L3		Windows L2-L3	
Pressure (kPa)	Total	CO	CO	H_2O	CO	H_2O	CO	H_2O	CO	H_2O	CO	H_2O
10	49.38	1.38	1.05	0.24	0.22	0.01	0.03	39.54	0.02	7.47	0.05	0.75
100	56.90	8.90	5.43	0.22	2.15	0.01	0.42	39.41	0.37	7.53	0.54	0.83
1000	87.41	39.41	14.41	0.18	15.30	0.01	3.71	39.80	2.37	7.16	3.62	0.86
10000	147.53	99.53	26.38	0.08	38.85	0.01	17.50	41.45	6.00	5.26	10.81	1.20
17.7 %wt			S1		L2		L3		Windows S1-L3		Windows L2-L3	
Pressure (kPa)	Total	CO	CO	H_2O	CO	H_2O	CO	H_2O	CO	H_2O	CO	H_2O
10	96.52	1.52	1.11	1.16	0.31	0.22	0.05	68.38	0.02	20.61	0.04	4.64
100	103.99	8.99	5.70	0.81	2.40	0.22	0.23	68.14	0.15	20.51	0.52	5.33
1000	130.79	35.79	13.10	1.47	16.06	0.13	2.14	68.82	0.94	19.93	3.56	4.65
10000	182.60	87.60	25.70	0.45	39.59	0.15	10.26	73.62	2.99	14.97	0.91	5.83
35.3 %wt			S1		L2		L3		Windows S1-L3		Windows L2-L3	
Pressure (kPa)	Total	CO	CO	H_2O	CO	H_2O	CO	H_2O	CO	H_2O	CO	H_2O
10	191.26	1.26	0.95	11.63	0.28	7.01	0.00	124.22	0.00	23.57	0.03	23.57
100	197.42	7.42	4.96	8.67	2.03	20.23	0.07	118.29	0.07	20.80	0.30	22.03
1000	220.91	30.91	14.75	1.21	13.38	25.55	0.35	121.33	0.67	17.89	1.76	24.03
10000	258.54	68.54	26.77	1.39	36.55	8.44	0.47	135.73	1.09	15.31	3.67	29.14

Table A4. Amount of molecules of carbon monoxide per unit cell adsorbed in each site for IRMOF-1 at 298 K as a function of pressure and water content.

1.7 %wt			L1		L2		Windows	
Pressure (kPa)	Total	CO	CO	H_2O	CO	H_2O	CO	H_2O
10	6.12	0.12	0.03	0.67	0.09	4.65	0.00	0.69
100	7.51	1.51	0.26	0.53	1.19	4.86	0.07	0.61
1000	20.15	14.15	2.66	0.92	10.76	4.35	0.73	0.73
10000	86.55	80.55	19.05	1.06	56.29	4.05	5.21	0.90
3.5 %wt			L1		L2		Windows	
Pressure (kPa)	Total	CO	CO	H_2O	CO	H_2O	CO	H_2O
10	12.13	0.13	0.02	0.47	0.11	10.62	0.01	0.91
100	13.59	1.59	0.25	1.11	1.26	9.79	0.08	1.10
1000	25.50	13.50	2.44	1.68	10.40	9.27	0.66	1.05
10000	91.20	79.20	18.67	2.36	55.34	8.40	5.19	1.25
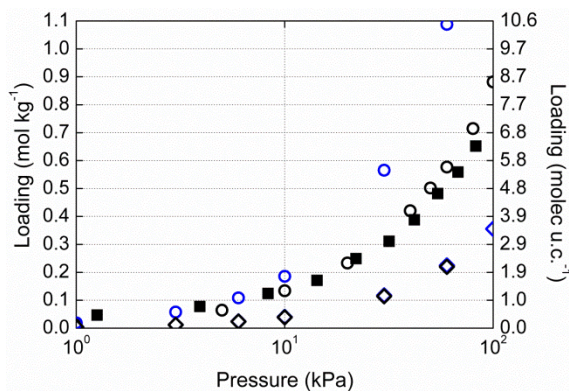
Figure A1. Adsorption isotherms of carbon monoxide in Cu-BTC at 298 K using the model developed in this work (circles) and the UFF-based model (rhombus). Simulations were performed using a dipole moment of 0.112 D (black symbols) and 0.58 D (blue symbols). Experimental data (squares) are included for comparison.
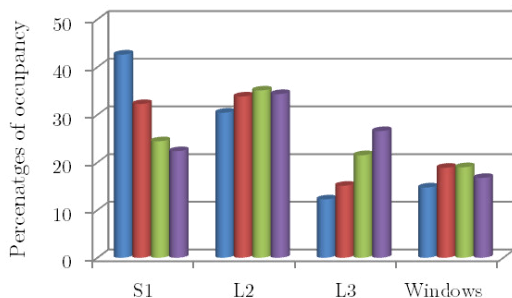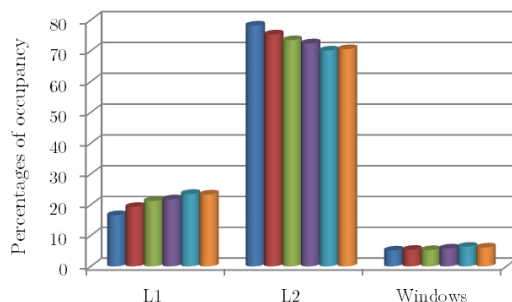
Figure A2. (top) Percentage of adsorption in the different cavities of Cu-BTC at 298K and 0.4 MPa (blue), 1 MPa (red), 4 MPa (green) and 10 MPa (purple). (bottom) Amount of molecules per unit cell adsorbed in each site as a function of pressure.

Pressure (MPa)	Total (molec uc⁻¹)	S1 (molec uc⁻¹)	L2 (molec uc⁻¹)	L3 (molec uc⁻¹)	S1-L3 (molec uc⁻¹)	L2-L3 (molec uc⁻¹)
0.4	21.99	9.37	6.69	2.69	1.99	1.25
1	40.49	13.05	13.69	6.11	4.36	3.28
4	82.47	20.15	28.93	17.73	8.42	7.24
10	111.62	24.95	38.33	29.65	8.83	9.86

Figure A3. (top) Percentage of adsorption in the different cavities of IRMOF-1 at 298K and 1 MPa (blue), 2 MPa (red), 4 MPa (green), 6 MPa (purple), 8 MPa (light blue) and 10 MPa (orange). (bottom) Amount of molecules per unit cell adsorbed in each site as a function of pressure.

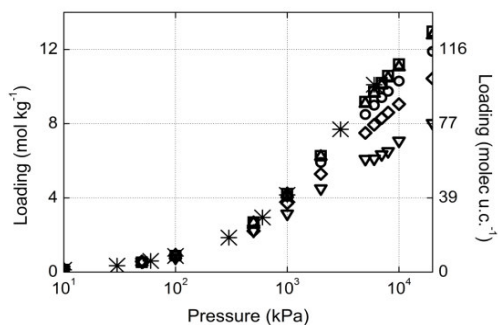| Pressure (Mpa)	Total (molec uc⁻¹)	L1 (molec uc⁻¹)	L2 (molec uc⁻¹)	Windows (molec uc⁻¹)
1	13.95	2.32	10.91	0.72
2	26.73	5.16	20.13	1.44
4	45.83	9.74	33.66	2.43
6	60.36	13.14	43.71	3.51
8	72.4	17.04	50.74	4.62
10	81.98	19.13	57.83	5.02

Figure A4. Adsorption isotherms computed for carbon monoxide in Cu-BTC at 298K. The results are obtained for the structures with 35.3%wt (triangles), 17.7%wt (rhombus), 8.9%wt (circles), 4.5%wt (up triangles) and 3.5%wt (squares). The computed results for the dehydrated structure (asterisks) are included for comparison. Error bars are smaller than the symbol size.
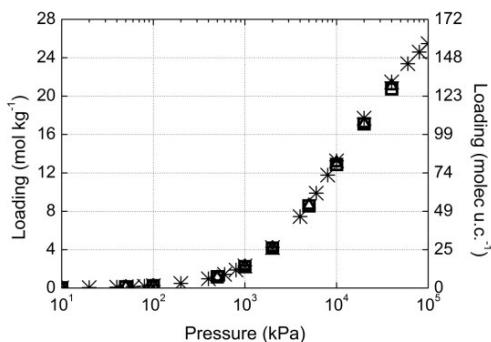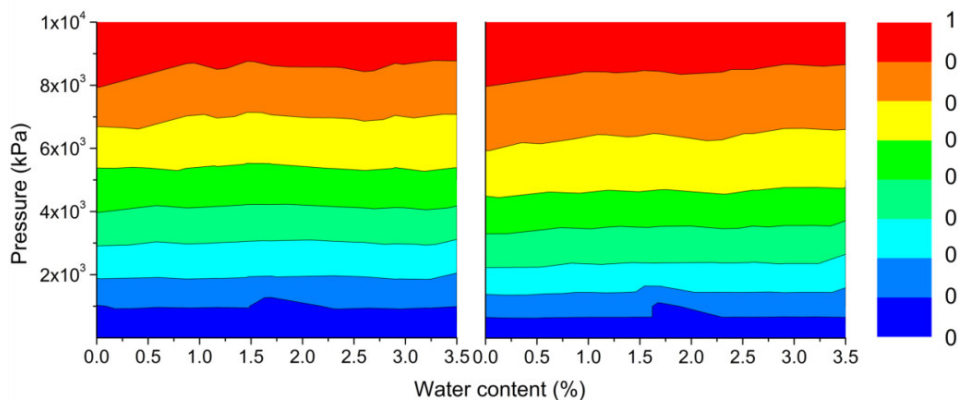
Figure A5. Adsorption isotherms computed for carbon monoxide in IRMOF-1 at 298K. The results are obtained for the structures with 3.5%wt (squares), 1.7 %wt (triangles). The computed results for the dehydrated structure (asterisks) are included for comparison. Error bars are smaller than the symbol size.

Figure A6. Carbon monoxide adsorbed in the cages L1 (left), L2 (right) of IRMOF-1 as a function of pressure and water content. The values of the maxima have been normalized to 1.

(1) Mayo, S. L.; Olafson, B. D.; Goddard, W. A. *Journal of Physical Chemistry* **1990**, *94*, 8897.

(2) Rappe, A. K.; Casewit, C. J.; Colwell, K. S.; Goddard, W. A.; Skiff, W. M. *Journal of the American Chemical Society* **1992**, *114*, 10024.

(3) Frost, H.; Snurr, R. Q. *Journal of Physical Chemistry C* **2007**, *111*, 18794.

(4) Castillo, J. M.; Vlugt, T. J. H.; Calero, S. *Journal of Physical Chemistry C* **2008**, *112*, 15934.

(5) Bueno-Perez, R.; Garcia-Perez, E.; Gutierrez-Sevillano, J. J.; Merkling, P. J.; Calero, S. *Adsorption Science & Technology* **2010**, *28*, 823.

Appendix 5
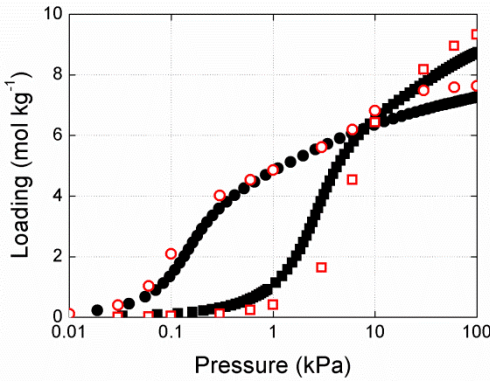
Figure A1: Comparison of experimental (full symbols) and simulated (empty symbols) adsorption isotherms of argon (squares) and methane (circles) at 120 K in ITQ-29.
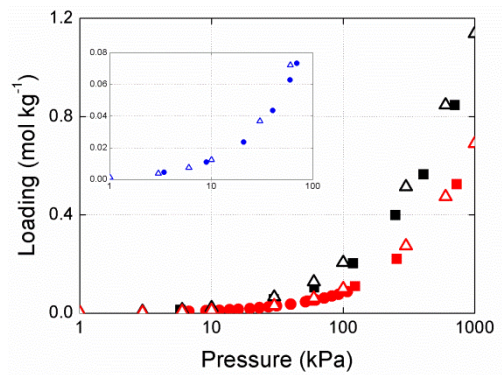

Figure A2: Comparison of experimental (full symbols) and simulated (empty triangles) adsorption isotherms of nitrogen at 305 K (black), 334 K (blue) and 343 K (red) in silicalite. Previous works from Dunne *et al.*[2] (circles) and Golden and Sircar[1] (squares) are used for comparison.
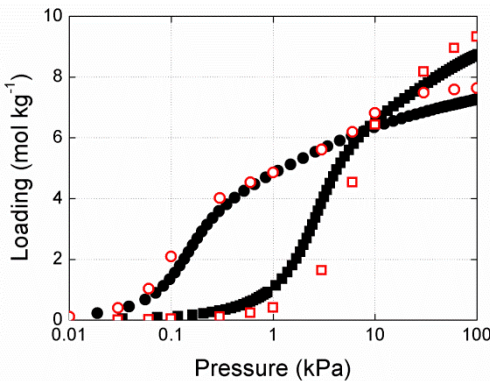

Figure A3: Comparison of experimental (full symbols) and simulated (empty triangles) adsorption isotherms of carbon monoxide at 305 K (black) and 341 K (red) in silicalite. A previous work from Golden and Sircar[1] (squares) is used for comparison.
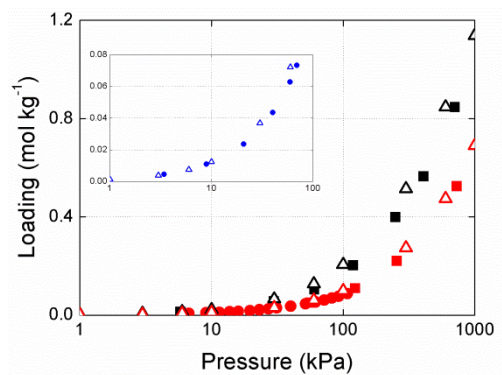

Figure A4: Comparison of experimental (full symbols) and simulated (empty triangles) adsorption isotherms of argon at 305 K (black), 325 K (green) and 342 K (red) in silicalite. Previous works from Dunne *et al.*[2] (circles) and Golden and Sircar[1] (squares) are used for comparison.

(1) Golden, T. C.; Sircar, S. *Journal of Colloid and Interface Science* **1994**, *162*, 182.

(2) Dunne, J. A.; Mariwals, R.; Rao, M.; Sircar, S.; Gorte, R. J.; Myers, A. L. *Langmuir* **1996**, *12*, 5888.
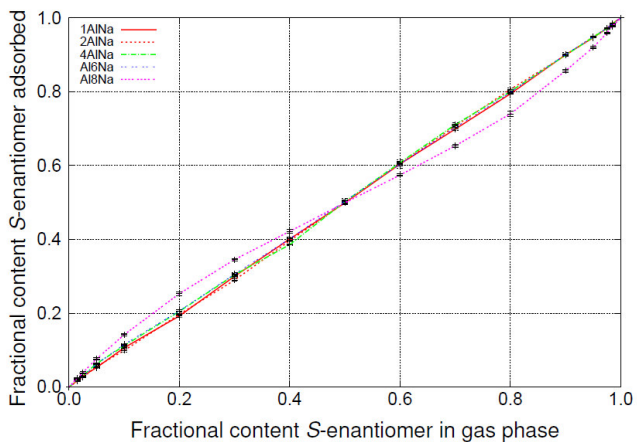
Appendix 6

Figure A1. Representation of the fractional adsorbed phase of S-LA against the fractional content of the same component in the bulk phase, at 500K. Comparison of structures with 1 (red line), 2 (dotted red line), 4 (dashed green line), 6 (dashed blue line) and 8 aluminium per unit cell (dashed pink line).

List of publications

The following publications are directly related with this Thesis

Peer reviewed journals

- **A. Martín-Calvo**, J. J. Gutiérrez-Sevillano, J. B. Parra, C. O. Ania and S. Calero, "Transferable Force Fields for Adsorption of Small Gases in Zeolites: Effect of Low Temperature" *Journal of Physical Chemistry C*, 2015, (submitted).

- **A. Martín-Calvo**, J. B. Parra, C. O. Ania and S. Calero, "Insights on the Anomalous Adsorption of Carbon Dioxide in LTA Zeolites" *Journal of Physical Chemistry C*, 2014, 118 (44), 25460-25467.

- R. Bueno-Pérez, **A. Martín-Calvo**, P. Gómez-Álvarez, J. J. Gutiérrez-Sevillano, P. J. Merkling, T. J. H. Vlugt, T. S. van Erp, D. Dubbeldam and S. Calero, "Enantioselective Adsorption of Ibuprofen and Lysine in Metal-Organic Frameworks" *Chemical Communications*, 2014, 50 (74), 10849-10852.

- **A. Martín-Calvo**, S. Calero, J. A. Martens and T. S. van Erp. "Enantiomeric Adsorption of Lactic Acid Mixtures in Achiral Zeolites" *Journal of Physical Chemistry C*, 2014, 118 (27), 14991-14997.

- F. D. Lahoz-Martín, **A. Martin-Calvo** and S. Calero. "Selective Separation of BTEX Mixtures Using Metal-Organic Frameworks", *Journal of Physical Chemistry C*, 2014, (24), 13126-13136.

- I. Matito-Martos, **A. Martín-Calvo**, J. J. Gutiérrez-Sevillano, M. Haranczyk, M. Doblaré, J. B. Parra, C. O. Ania and S. Calero. "Zeolite Screening for the Separation of Gas Mixtures Containing SO_2, CO_2 and CO". *Physical Chemistry Chemical Physics*, 2014, 16 (37), 19884-19893.

- S. R. Bajpe, E. Breynaert, **A. Martín-Calvo**, D. Mustafa, S. Calero, C. E. A. Kirschhok and J. A. Martens. "COK-16: A Cation-Exchanging Metal-Organic Framework Hybrid". *Chem. Plus. Chem.*, 2013, 87 (5), 402-406.

- **A. Martín-Calvo**, S. Calero, J. A. Martens and T. S. van Erp. "Adsorption of Polar Enantiomers in Achiral Zeolites" *Journal of Physical Chemistry C*, 2013, 117 (3), 1524-1530.

- J. J. Gutiérrez-Sevillano, **A. Martín-Calvo**, D. Dubbeldam, S. Calero and S. Hamad. "Adsorption of Hydrogen Sulphide on Metal-Organic Frameworks". *RSC Advances*, 2013, 3 (34), 14737-14749.

- X. Liu, **A. Martín-Calvo**, E. McGarrity, S. K. Schnell, S. Calero, J. M. Simon, D. Bedeauxk, S. Kjelstrup, A. Bardow and T. J. H. Vlugt. "Fick Diffusion Coefficients in Ternary Liquid Systems from Equilibrium Molecular Dynamics Simulations". *Industrial & Engineering Chemical Research*, 2012, 51 (30), 10247-10258.

- **A. Martín-Calvo**, F. D. Lahoz-Martín and S. Calero. "Understanding Carbon Monoxide Capture Using Metal-Organic Frameworks". *Journal of Physical Chemistry C*, 2012, 116 (11), 6655-6663.

- **A. Martín-Calvo**, E. García-Pérez, A. García-Sánchez, R. Bueno-Pérez, S. Hamad and S. Calero. "Effect of Air humidity on the removal of Carbon Tetrachloride from Air Using Cu-BTC Metal-Organic Frameworks". *Physical Chemistry Chemical Physics*, 2011, 13 (23), 11165-11174.

- S. Calero, **A. Martín-Calvo**, S. Hamad and E. García-Pérez, "On the Performance of Cu-BTC Metal Organic Frameworks for Carbon Tetrachloride Gas Removal". *Chemical Communications*, 2011, 47 (1), 508-510.

- J. J. Gutiérrez-Sevillano, D. Dubbeldam, F. Rey, S. Valencia, M. Palomino, **A. Martín-Calvo** and S. Calero. "Analysis of the ITQ-12 Zeolite Performance in Propane-Propylene Separation Using a Combination of Experimental and Molecular Simulations" *Journal of Physical Chemistry C*, 2010, 114 (35), 14907-14914.

- T. S. van Erp, T. P. Caremans, D. Dubbeldam, **A. Martín-Calvo**, S. Calero and J. A. Martens, "Enantioselective adsorption in achiral zeolites". *Angewandte Chemie*, 2010, 49 (17), 3010-3013.

- **A. Martín-Calvo**, E. García-Pérez, J. M. Castillo and S. Calero, "Molecular Simulations for Adsorption and Separation of Natural Gas in IRMOF-1 and Cu-BTC Metal-Organic Frameworks" *Physical Chemistry Chemical Physics*, 2008, 10 (47), 7085-7091.

Non-peer reviewed journals

- **A. Martín-Calvo**, J. J. Gutiérrez-Sevillano and S. Calero, "Estudio por Simulación de la Adsorción y Difusión de Gases con Impacto Ambiental Usando Cu-BTC" *Materiales en Adsorción y Catálisis* (RSEQ), Num.6, Octubre 2013.

- **A. Martín-Calvo**, J. J. Gutiérrez-Sevillano and S. Calero, "Simulations Studies on the Adsorption and Diffusion of Gasses of Environmental Impact Using Cu-BTC Metal-organic Framework" (7 pages). *Conference Proceeding*. EBA-9 & IBA-1, Recife (Brasil) 2012.

Acknowledgements/Agradecimientos

Y después de toda esta parrafada científica, llega lo más importante, esa parte que todo el mundo se lee de verdad y que ¡uy como se te escape alguien! :-P

Bromas aparte, muchas son las personas que, de una forma u otra, han formado parte de este proyecto. A todas ellas, las que están y las que no, me gustaría darles las gracias.

El día que vinieron a hablarnos de los proyectos fin de carrera, recuerdo que **Sofía** comentó: "si alguien se decide por este proyecto, que sepa que esto no va a ser un paseo, y que va a tener que trabajar duro" (transcripción no literal, ya hace tiempo de aquello y la memoria a veces falla). Y tanto que había que trabajar. Lo que ella no sabía, era que soy tan cabezota, que incluso con el proyecto terminado y sin posibilidades de financiación, yo iba a seguir trabajando. Aunque eso no fue un problema, ella me buscó varios contratos, y tras 2 intentos de FPU, a la tercera fue la vencida. Así pues, por su constante apoyo, esfuerzos y consejos: Sofía, mil gracias. Muchísimas gracias también a **Elena**, que, cuando raspa no era RASPA y nuestro logo era una raspa giratoria sacada de google, me guio en mis primeros pasos en esto de la simulación, bueno, en los primeros, en los segundos y en los terceros. This thesis wouldn´t be possible without **Johan** and **Titus**. You welcomed me at COK on my first time abroad and gave me the opportunity of doing this joint PhD. For that and all the support, thank you very much. (Titus, I can keep giving you more "nice TOCs" to use on your website).

During this time I have met many great people. Without **David** nothing, literally nothing of this would have been possible. I can nothing but thanking you for your dedication and patience with all of us. I would also like to thank **Thijs** and **Joeri** for hosting me at their groups and for showing me that there is world out of RASPA. Me gustaría agradecer también a **Conchi** y **Parra**, por sus innumerables aportaciones, discusiones y charlas.

En este tiempo, el grupo RASPA ha cambiado mucho. Empezamos siendo 4 gatos mal contados y ya casi ni cabemos en las fotos, y todos han aportado su granito de arena. Entre los más veteranos, quiero agradecer a **JuanMa**, por su ayuda incondicional, aun estando en la otra punta del mundo, a **JuanJo**, por su constante ayuda científica, scriptera y artística, la salsa y los churros navideños, a **Rocío**, por descubrirnos a los Antílopez, que tantos buenos ratos nos han hecho pasar (mucho mejor que las magdalenas, dónde va a parar), a **Said**, por no hacer "ajam" cuando la situación lo requiere, y a **Patrick**, por tener siempre un "hasta mañana". Entre los nuevos, aunque ya no lo son tanto, a **Paco**, **Ismael**, **Vicent**, **Salva**, **Julio, Paula**, **Rabdel** y **Jose "Chico"**, por los buenos ratos en el laboratorio y fuera de él (aunque se pierdan los pipirigañas, las lentejas de los martes y el sunny-tea-time).

Cómo no, a **José Luis** (alias "el otri") por tener siempre una respuesta. To the temporary RASPA guys **Katie** and **Tim**, for their friendship. Pero no solo de RASPA vive el hombre, gracias a **Vanesa**, **Idi**, **Chema**, **Paula Z**. y **Juan Antonio**, porque cuando nos juntamos nos lo pasamos genial.

Fuera de la UPO no tengo más que palabras de gratitud para mis mosqueteros, (**Julia**, **Pili** y **Ale**) por apoyarme en los buenos y en los malos momentos, y por esos montaditos del Eme. A Ale además, por prestarnos equipos nuevos a todo RASPA durante casi 2 años. Thanks to **Sneha**, for being a friend, a sister, an English teacher and a hard reviewer (no hard feelings sweetheart). A las palomas (**Cristina**, **Elenita** y **Ana**) y al equipo de alemán (**Sabo** y **JuanRa**), por estar ahí, aunque desperdigados.

Por último y especialmente, me gustaría dar las gracias a mi familia, que aunque siguen sin saber a qué me he dedicado todos estos años, siempre preguntan por cómo va todo. A mis padres, **Charo** y **Jesús**, por estar ahí los 365 días del año dando lo mejor de ellos, sin importar las circunstancias, a **We**, mi hermana, por aprenderse el título de mi tesis, aunque se lo he acortado a última hora. Con muchísimo cariño a mis abuelos (**Ana** y **Manolo**), que son mis segundos padres (Abue, ahora sí que voy a usar el bolígrafo) y a mis "tais", **Elena** y **Juan**, por acordarse siempre de su "eurosobri".

Y con esto y un bizcocho, hasta mañana a las diez.

Sed buenos.